

## Non-saturated Chloride Diffusion in Sustainable Cementitious Materials

Zhang, Yong

**DOI**

[10.4233/uuid:c3cd9297-6d49-4ed6-8979-22419b98622f](https://doi.org/10.4233/uuid:c3cd9297-6d49-4ed6-8979-22419b98622f)

**Publication date**

2018

**Document Version**

Final published version

**Citation (APA)**

Zhang, Y. (2018). *Non-saturated Chloride Diffusion in Sustainable Cementitious Materials*. [Dissertation (TU Delft), Delft University of Technology]. <https://doi.org/10.4233/uuid:c3cd9297-6d49-4ed6-8979-22419b98622f>

**Important note**

To cite this publication, please use the final published version (if applicable).  
Please check the document version above.

**Copyright**

Other than for strictly personal use, it is not permitted to download, forward or distribute the text or part of it, without the consent of the author(s) and/or copyright holder(s), unless the work is under an open content license such as Creative Commons.

**Takedown policy**

Please contact us and provide details if you believe this document breaches copyrights.  
We will remove access to the work immediately and investigate your claim.

# **Non-saturated Chloride Diffusion in Sustainable Cementitious Materials**

Proefschrift

ter verkrijging van de graad van doctor  
aan de Technische Universiteit Delft,  
op gezag van de Rector Magnificus prof.dr.ir. T.H.J.J. van der Hagen,  
voorzitter van het College voor Promoties,  
in het openbaar te verdedigen op  
donderdag 1 november 2018 om 15:00 uur

door

**Yong ZHANG**

Master of Science, Wuhan University of Technology, P.R. China  
geboren te Hubei, P.R. China

Dit proefschrift is goedgekeurd door de promotoren.

Samenstelling promotiecommissie bestaat uit:

Rector Magnificus,	voorzitter
Prof.dr.ir. K. van Breugel	Technische Universiteit Delft, promotor
Dr. G. Ye	Technische Universiteit Delft, promotor

Onafhankelijke leden:

Prof.dr.ir. H.E.J.G. Schlangen	Technische Universiteit Delft
Prof.dr. Z.W. Jiang	Tongji University, China
Prof.dr. M.R. Geiker	Norwegian University of Science and Technology, Norway
Prof.dr. L.P. Tang	Chalmers University of Technology, Sweden
Dr. K.H.A.A. Wolf	Technische Universiteit Delft
Prof.dr.ir. P.L.J. Zitha	Technische Universiteit Delft, reservelid

ISBN: 978-94-6366-097-6

Keywords: Supplementary cementitious materials; Pore structure; Degree of water saturation; Relative humidity; Chloride diffusion; Service life

Printed by: Gildeprint

Cover design: Yong Zhang

Copyright © 2018 by Yong Zhang

All rights reserved. No part of the material protected by this copyright notice may be reproduced or utilized in any form or by any means, electronic or mechanical, including photocopying, recording or by any information storage and retrieval system, without written permission from the author.

Printed in the Netherlands.

The best of man is like water,  
Which benefits all things, and does not contend with them,  
Which flows in places that others disdain,  
Where it is in harmony with the Way.

So the sage:  
Lives within nature,  
Thinks within the deep,  
Gives within impartiality,  
Speaks within trust,  
Governs within order,  
Crafts within ability,  
Acts within opportunity.

He does not contend, and none contend against him.

*Chapter 8 of Tao te Ching by Laozi*



## Acknowledgements

This thesis is the result of a research project funded by the Chinese Scholarship Council (CSC). The research was conducted in the Microlab, Section of Materials and Environment at the Faculty of Civil Engineering and Geosciences, Delft University of Technology (TU Delft). There are many people who have contributed to the research project from different angles. I would like to express sincere gratitude to all of them.

My promotor Prof. Klaas van Breugel. Your invaluable advice and constructive comments are of paramount importance to improve the quality of the thesis. Discussion with you is always inspiring. Your wisdom, endless patience, profound erudition, and strong sense of humor made me feel nothing is impossible.

My promotor Dr. Guang Ye. Your significant guidance and sufficient supervision throughout my entire PhD study are the essential ingredients for the thesis. You gave me freedom to explore whatever interested me. Your persistent encouragement, solution-oriented thinking and time management have ignited my creativity and passion for research. You promoted my researchability by many different kinds of cooperation and activity. 'Thanks' appears a word too little for a mountain of efforts you made for me.

Prof. Erik Schlangen. Your considerable support in the Microlab is the key to carry out the research project. A special note of appreciation goes to Prof. Rob Polder for his illustration and help on resistivity measurement, a technique of uttermost importance in the thesis. Discussions with Prof. Geert de Schutter of Gent University are very helpful for the ideas in this research.

Prof. Haiqing Yuan, Prof. Ji Wang, Prof. Shaopeng Wu, Prof. Wei Chen and Prof. Zhonghe Shui at Wuhan University of Technology. With your recommendations I got the great opportunity to do research in Delft, which is also a fantastic place for life.

My thesis committee members. Your time and efforts on the thesis assessment are highly appreciated. Appreciation also goes to the anonymous reviewers for their valuable comments on the journal papers linked to the thesis.

All staff and members in Materials and Environment made me feel fruitful and prosperous. Fulfilled in the Microlab are smiles, supports, inspiring discussions, great achievements..... Dr. Henk Jonkers, Dr. Oguzhan Copuroglu and Dr. Dessi Koleva, your courses substantially deepened and extended my understanding of concrete. Dr. Marc Ottele, your time on the summary translation was really a significant help for me.

Ms. Claire de Bruin, Ms. Iris Batterham, Ms. Claudia Baltussen, Ms. Melanie Holtzapffel and Ms. Nynke Verhulst. Without any of you, I would have got lost over the past years. Special thanks must go to Ms. Franca Post at the CICAT of TU Delft for her strong management support.

Mr. Gerrit Nagtegaal, Mr. Maiko van Leeuwen, Mr. Ton Blom, Mr. Arjan Thijssen and Mr. John van den Berg. Your assistances with the experimental work are gratefully acknowledged. Cynthia, I am pretty grateful for your help with the moisture measurements.

Thank you, Zhengxian Yang, for your great care and significant support to my life all over these years. I am very thankful to Jian Zhou, Mingzhong Zhang and Zhiwei Qian for their advice on my research but also for their suggestions on my career development. Particular thanks to my officemates Haoliang Huang (1<sup>st</sup> year), Nguyen van Tuan (2<sup>nd</sup> year), Senot

Sangadji (3<sup>rd</sup> year) and Zhichao Pan (4<sup>th</sup> year) for the colorful and pleasant moment spent together. Branko Šavija and Mladena Lukovic, you are always so sweet and supportive that I can hardly find the right words to describe how grateful I am.

Deeply anchored in my heart is the precious friendship with previous colleagues: Balqis Md Yunus, Chunping Gu, Damian Palin, Hua Dong, Jie Hu, Junfeng Su, Jie Zhao, Jure Zlopasa, Lupita Sierra Beltran, Lelang Lu, Lourdes Maria, Peng Gao, Quantao Liu, Qi Zhang, René Veerman, Virginie Wiktor, Xiaowei Ouyang, Yuwei Ma, Ying Wang, Zhuqing Yu.....

I will forever be grateful to the help and happy times given by all my current fantastic colleagues: Albina Kostiuhenko, Agus Susanto, Bei Wu, Boyu Chen, Claudia Romero Rodriguez, Farhad Pargar, Gabriel Hoder, Hongzhi Zhang, Jeannette van den Bos, Jiayi Chen, Hao Huang, Marc Ottele, Nader Sadeghi, Marija Nedeljkovic, Natalie Carr, Renee Mors, Stefan Chaves Figueiredo, Shi Xu, Shizhe Zhang, Tianshi Lu, Wenjuan Lyu, Xuliang Hou, Xu Ma, Yidong Gan, Yading Xu, Yibing Zuo, Yun Zhang, Zhipei Chen, Zhenming Li.....

Dr. Fuhai Li, Dr. Jiahua Liu, Prof. Jiangxiong Wei, Dr. Yun Huang and Prof. Yingzi Yang, your visit in the Microlab broadened my horizons to a wider perspective and brought me new ideas and quite a lot of fun as well. A series of nice discussion with Dr. Jorge Sanchez Dolado deeply impressed me.

Qingliang Yu. You are like an elder brother to me. Billions and billions of thanks to you for your sincere care, help and advice on my life.

Koos van Dijk, I surely owe you a debt of gratitude for what you have done for me. You shared with me your eighty years' life stories and engineering experiences. You very often cooked nice foods for me. You have taken me to plenty of very beautiful places in the Netherlands. You were very patient and spent countless hours to have nederlands spraagen with me. My feeling of appreciation is far beyond any words.

Mandy and Max, many thanks to your friendliness and generous. I am delighted more than ever being a neighbor of you.

My friends. I can never have a better life in the Netherlands because of you: Ben Ren, Chang Wang, Dongya Ren, Feifei Xu, Gang Liu, Huarong Zheng, Jianbin Fang, Jitang Fan, Jiaguang Li, Jiang Li, Jinlong Li, Jingjing Liu, Ling Chang, Linfeng Chen, Lilan Zhou, Ming Dai, Meng Ma, Ming Ma, Mubiao Xie, Shaoguang Li, Shouqian Li, Shuhong Tan, Ping Liu and Yan Ni, Qin Liu, Tiantian Yao, Wangwang Liu, Wenhao Yuan, Wuyuan Zhang and Yi Chen, Weiming Zheng and Cuilin Wu, Xiuhan Chen, Xinhe Yao, Xuhong Qiang and Xu Jiang, Xiaoyan Wei, Xueqian Zhai, Xi Zhang, Xuan Zheng, Yifan Pan, Yihui Wang, Yuanyang Wan, Yuguang Yang and Bin Hu, Yuan Zhang, Zhiyong Wang..... Lijie Wang, Kai Wu, Yun Gao and Zhijun Tan, your kindness during my stay in Gent is highly appreciated. Only with all of you I can have such a complete and unforgettable PhD journey.

In the end, my family. It is beyond words to express my deep sense of gratitude to my parents for their endless love, long-lasting understanding, unconditional support..... I never thank you enough, my dearest sister, for your kindest care and for always being there for me..... All those my family has given me are a debt that I can never afford to pay back.

Yong Zhang

Delft, September 2018

# Table of Contents

---

List of Symbols	v
List of Abbreviations	xi
<b>Chapter 1 General Introduction</b>	<b>1</b>
1.1 Background of this project	1
1.2 Objectives and scope of this project	3
1.3 Strategy of the research	3
1.4 Outline of thesis	4
<b>Chapter 2 Chloride Diffusion in Unsaturated Cementitious Materials: A Literature Review</b>	<b>7</b>
2.1 Introduction	7
2.2 Moisture condition in hardened cementitious materials	7
2.2.1 Cement hydration and water phases .....	7
2.2.2 Determination of water content .....	8
2.3 Survey of experimental methods	10
2.3.1 Sample preconditioning for obtaining uniform moisture content .....	11
2.3.2 Measurement of chloride diffusion coefficient in unsaturated concretes .....	12
2.4 Chloride diffusion in non-saturated cementitious materials	14
2.4.1 Definition of relative chloride diffusion coefficient $D_{rc}$ .....	14
2.4.2 Factors affecting the $D_{rc}$ in unsaturated cementitious materials .....	14
2.4.3 Current expressions for relative chloride diffusion coefficient .....	21
2.5 Evaluation	23
2.6 Conclusions and outlook	23
<b>Chapter 3 Experimental Technique for Pore Structure Measurement: Intrusion-Extrusion Cyclic Mercury Porosimetry (IEC-MIP)</b>	<b>25</b>
3.1 Introduction	25
3.2 Microstructure of cementitious pastes	26
3.2.1 Structure formation due to cement hydration .....	26
3.2.2 Pore space .....	27
3.2.3 Microstructure of cement paste .....	27
3.2.4 Effect of SCMs on microstructure .....	28

3.3	Principles of mercury intrusion porosimetry (MIP)	29
3.3.1	Washburn equation.....	29
3.3.2	Test procedure of standard MIP test .....	29
3.3.3	Technique parameters .....	30
3.3.4	Evaluation of MIP technique.....	31
3.4	Intrusion-extrusion cyclic mercury porosimetry (IEC-MIP)	34
3.4.1	Test sequence .....	34
3.4.2	Analysis of measurement data.....	36
3.5	Conclusions	40
<b>Chapter 4 Analysis of Pore Structure in Blended Cement Pastes</b>		<b>41</b>
4.1	Introduction	41
4.2	Experimental program	42
4.2.1	Raw materials.....	42
4.2.2	Sample preparation.....	43
4.2.3	Pore structure measurement .....	43
4.3	Results and discussion	43
4.3.1	Porosity.....	43
4.3.2	Pore size distribution.....	47
4.3.3	Critical pore diameter $d_{cr}$ and threshold pore diameter $d_{th}$ .....	48
4.3.4	Pore connectivity and distribution of pore entrapment .....	51
4.4	Conclusions	55
<b>Chapter 5 Chloride Transport Property in Saturated Cementitious Materials: Effect of Pore Structure</b>		<b>57</b>
5.1	Introduction	57
5.2	Experimental program	58
5.2.1	Materials and samples preparation.....	58
5.2.2	Rapid chloride migration test .....	58
5.3	Experimental results	59
5.3.1	Chloride migration coefficient $D_{RCM}$ with age.....	59
5.3.2	Pore size effect on $D_{RCM}$ .....	60
5.3.3	Porosity effect on $D_{RCM}$ .....	61
5.3.4	Pore connectivity effect on $D_{RCM}$ .....	62
5.4	Discussion	62
5.4.1	Pore structure and transport property: role of small capillary pores .....	62
5.4.2	Connectivity of small capillary pores ( $0.01 \mu\text{m} < d \leq d_{th}$ ) .....	64
5.4.3	Quantitative relationship between chloride transport and connectivity of small capillary pores.....	65
5.5	Conclusions	66

## **Chapter 6 Moisture Distribution and Water Continuity in Unsaturated Cementitious Materials 67**

6.1	Introduction	67
6.2	Moisture distribution and water continuity	68
6.2.1	Effect of pore features on moisture distribution.....	68
6.2.2	Effect of pore features on water continuity .....	69
6.3	Experimental program: water vapour desorption isotherm	74
6.3.1	Materials and samples .....	75
6.3.2	Sample preconditioning for desired uniform water content.....	75
6.4	Experimental results	77
6.4.1	Water vapour desorption isotherm (WVDI) in OPC mortars .....	77
6.4.2	Water vapour desorption isotherm (WVDI) in blended cement mortars .....	77
6.5	Discussion	78
6.5.1	Moisture distribution in unsaturated cementitious materials .....	78
6.5.2	Water continuity in unsaturated cementitious materials .....	79
6.6	Conclusions	80

## **Chapter 7 Relative Chloride Diffusion Coefficient in Unsaturated Cementitious Materials 81**

7.1	Introduction	81
7.2	Mathematical description of relative chloride diffusion coefficient	82
7.2.1	Nernst-Einstein equation .....	82
7.2.2	Conductivity $\sigma$ of cementitious system.....	82
7.2.3	Relative chloride diffusion coefficient $D_{rc}$ .....	85
7.3	Experimental program	86
7.3.1	Sample preparation.....	86
7.3.2	Conductivity $\sigma_{p,s_w}$ of pore solution at various saturation levels.....	86
7.3.3	Conductivity $\sigma_{s_w}$ of mortar specimens at various saturation levels.....	87
7.4	Experimental results and discussion	88
7.4.1	Conductivity $\sigma_{p,s_w}$ of pore solution in unsaturated mortars.....	88
7.4.2	Conductivity $\sigma_{s_w}$ of unsaturated mortars .....	90
7.4.3	Relative chloride diffusion coefficient $D_{rc}$ in OPC mortars.....	91
7.4.4	Relative chloride diffusion coefficient $D_{rc}$ in blended cement mortars .....	93
7.5	Validation of the equation for relative chloride diffusion coefficient	95
7.5.1	Validation of Eq. (7.17) with experimental data derived in this work.....	95
7.5.2	Validation of Eq. (7.17) with experimental data reported in literature .....	95
7.5.3	Determination of coefficient $c$ and prediction of relative chloride diffusion coefficient $D_{rc}$ .....	96
7.6	Conclusions	98

---

<b>Chapter 8 Effect of Unsaturated Chloride Diffusion on Service Life Prediction of Reinforced Concrete Structures</b>	<b>99</b>
8.1 Introduction	99
8.2 Unsaturated chloride diffusion	100
8.3 Role of unsaturated chloride diffusion in service life	102
8.3.1 Evolution of unsaturated chloride diffusion coefficient $D(\alpha(t), S_w)$ .....	102
8.3.2 Chloride diffusion coefficient against internal relative humidity .....	105
8.4 Comparative study	107
8.4.1 Specimens and exposure condition .....	107
8.4.2 $D(t)$ by DuraCrete approach .....	107
8.4.3 $D(\alpha(t), S_w)$ by present approach .....	108
8.5 Conclusions	110
<b>Chapter 9 Retrospection, Conclusions and Prospects</b>	<b>111</b>
9.1 Retrospection	111
9.2 Conclusions	112
9.3 Contributions to science and engineering	113
9.4 Prospects	114
References	115
Summary	125
Samenvatting	127
List of Publications	131
Curriculum Vitae	133

# List of Symbols

---

## Roman lower case letters

$c$	Coefficient representing the fineness of pore size	[-]
$c_i$	Concentration of the ion $i$	[mol/L]
$d$	Equivalent pore diameter	[m]
$d_0$	Unit diameter	[nm]
$d_a$	Average pore diameter	[nm]
$d_0$	Average pore diameter at a reference age $t_0$	[nm]
$d_a(t)$	Average pore diameter at time $t$	[nm]
$d_{cr}$	Critical pore diameter	[nm]
$d_p$	The smallest drained pore diameter	[nm]
$d_{s,cr}$	The pore size smaller than, but close to, the critical pore diameter	[nm]
$d_{th}$	Threshold pore diameter	[nm]
$dP$	The change of pressure	[N/m <sup>2</sup> ]
$dV$	The change of pore volume	[m <sup>3</sup> ]
$k_e$	Environment factor	[-]
$k_{e,0}$	Effect of environment class on $k_e$	[-]
$k_{e,c}$	Effect of cement type on $k_e$	[-]
$m_b$	Mass percentage of blended cement in the binder	[%]
$m_c$	Mass percentage of ordinary cement in the binder	[%]
$m_d$	The mass of specimen dried at 105 °C	[g]
$m_h$	The mass of specimen at a particular saturation level	[g]
$m_s$	The mass of specimen at saturated state	[g]
$m_{C-S-H}$	The mass of calcium silicate hydrate	[g]
$n$	Ageing factor	[-]
$n_{H_2O}$	The number of moles of water in the pore solution	[mol]
$n_{solution}$	The number of moles of water and solute in the pore solution	[mol]
$n_K^r$	The moles of potassium ion released during cement hydration	[mol]
$n_{Na}^r$	The moles of sodium ion released during cement hydration	[mol]
$r$	Equivalent pore radius	[m]
$r_k$	Kelvin radius of the meniscus	[m]
$r_p$	Pore radius	[m]

$t$	Thickness	[m]
$t_0$	Reference time	[hr]
$x_d$	Average value of the penetration depths	[mm]

### Roman capital letters

$A$	Cross sectional area of cementitious material	[m <sup>2</sup> ]
$A_b$	Water absorption	[-]
$A_s$	Cross sectional area of the solid phase	[m <sup>2</sup> ]
$A_p$	Cross sectional area of the pore solution phase	[m <sup>2</sup> ]
$A_v$	Cross sectional area of the vapour phase	[m <sup>2</sup> ]
$C_K$	Concentration of potassium ion in the pore solution	[mol/L]
$C_{Na}$	Concentration of sodium ion in the pore solution	[mol/L]
$C(x, t)$	Chloride profiles at depth $x$ after service period $t$	[-]
$D$	Chloride diffusion coefficient	[m <sup>2</sup> /s]
$D_0$	Intrinsic chloride diffusion coefficient	[m <sup>2</sup> /s]
$D_a$	Apparent chloride diffusion coefficient	[m <sup>2</sup> /s]
$D_{Cl}$	Chloride diffusion coefficient	[m <sup>2</sup> /s]
$D(t)$	Time-dependent chloride diffusion coefficient	[m <sup>2</sup> /s]
$D_p$	Chloride diffusion coefficient in the pore solution	[m <sup>2</sup> /s]
$D_{rc}$	Relative chloride diffusion coefficient	[-]
$D_{RCM}$	Chloride diffusion coefficient from rapid chloride migration test	[m <sup>2</sup> /s]
$D_0$	Chloride diffusion coefficient at a reference age $t_0$	[m <sup>2</sup> /s]
$D_{RCM}(t)$	Time-dependent chloride migration coefficient	[m <sup>2</sup> /s]
$D_{S_w}$	Chloride diffusion coefficient at a given degree of water saturation	[m <sup>2</sup> /s]
$D_{Sat}$	Chloride diffusion coefficient at saturated state	[m <sup>2</sup> /s]
$F_0$	Formation factor	[-]
$F_{0,Sat}$	Formation factor of cementitious material at saturated state	[-]
$F_{0,S_w}$	Formation factor of cementitious material at unsaturated state	[-]
$F_I$	Force	[N]
$G_i$	Empirical coefficient for the conductivity of aqueous solution	[(mol/L) <sup>-0.5</sup> ]
$I$	Electrical current	[A]
$I_m$	Molar ionic strength	[(mol/L) <sup>0.5</sup> ]
$K_f$	Adsorption coefficient for potassium ion	[L/g]
$L$	The length of a specimen	[mm]
$N_{Sat}$	The number of transport channels at saturated state	[-]
$N_w$	The number of transport channels at unsaturated state	[-]
$P$	Applied pressure	[MPa]
$R$	Electrical resistance of cementitious material	[Ω]

$R_b$	Bulk resistance	[ $\Omega$ ]
$R_d$	Distribution ratio	[L/g]
$R_s$	Electrical resistance of the solid phase	[ $\Omega$ ]
$R_p$	Electrical resistance of the pore solution phase	[ $\Omega$ ]
$R_v$	Electrical resistance of the vapour phase	[ $\Omega$ ]
$RH_c$	Critical relative humidity	[-]
$RH_d$	Desired relative humidity	[-]
$RH_m$	Relative humidity in the middle of the specimen	[-]
$RH_s$	Relative humidity in the surface of the specimen	[-]
$RH_S$	Water activity effect caused by dissolved ions	[%]
$RH_K$	Curvature effect of menisci formed at pore solution-vapour interface	[%]
$S_{cr}$	Critical saturation	[%]
$S_t$	Total pore surface area	[m <sup>2</sup> /m <sup>3</sup> ]
$S_w$	Degree of water saturation	[-]
$S_{w,e}$	Degree of water saturation at equilibrium state	[-]
$S_w(t)$	Degree of water saturation at time $t$	[-]
$T$	Absolute temperature	[K]
$U$	Absolute value of the applied voltage	[V]
$V$	Volume of cementitious material	[m <sup>3</sup> ]
$V_{por}$	Pore volume	[m <sup>3</sup> ]
$V_m$	Molar volume of water	[L/mol]
$V_w$	Volume of water	[L]
$V_{i-1}^{cin}$	Cumulative intrusion volume at intrusion step ( $i-1$ ) of IEC-MIP test	[ml/ ml]
$V_i^{cin}$	Cumulative intrusion volume at intrusion step $i$ of IEC-MIP test	[ml/ ml]
$V_{i-1}^{cex}$	Cumulative intrusion volume at extrusion step ( $i-1$ ) of IEC-MIP test	[ml/ ml]
$V_i^{cex}$	Cumulative intrusion volume at extrusion step $i$ of IEC-MIP test	[ml/ ml]
$V_i^{ink}$	The volume of ink-bottle pores at intrusion step $i$ of IEC-MIP test	[ml/ ml]
$V_i^{th}$	The volume of throat pores at intrusion step $i$ of IEC-MIP test	[ml/ ml]
$V_s^{in}$	Cumulative throat pore volume	[ml/ml]
$V_s^{th}$	cumulative intrusion volume	[ml/ml]
$V_{sc}^{ink}$	Volume of ink-bottle small capillary pores	[ml/ml]
$V_{sc}^{th}$	Volume of throat small capillary pores	[ml/ml]
$V_s^{in}$	Volume of intruded pores	[ml/ml]
$V_p$	Volume of pore solution phase	[ml]
$V_s$	Volume of solid phase	[ml]
$V_t$	Total pore volume	[ml/ml]
$V_v$	Volume of vapour phase	[ml]
$Z$	Impedance	[ $\Omega$ ]

**Greek letters**

$\alpha$	Degree of cement hydration	[%]
$\alpha_{en}$	Pore entrapment	[%]
$\beta_i$	Structure factor of a given phase layer in cementitious material	[-]
$\beta_s$	Structure factor of solid phase	[-]
$\beta_p$	Structure factor of pore solution phase	[-]
$\beta_v$	Structure factor of vapour phase	[-]
$\gamma_m$	Surface tension of mercury	[N/m]
$\gamma_w$	Surface tension of water	[N/m]
$\lambda$	Empirical constant	[-]
$\lambda_i$	Equivalent conductivity of the ion species $i$	[cm <sup>2</sup> ·S/mol]
$\lambda_i^0$	Equivalent conductivity of an ionic species at infinite dilution	[cm <sup>2</sup> ·S/mol]
$\rho$	Electrical resistivity	[Ω·m]
$\rho_b$	Specific gravity of blended cement	[kg/m <sup>3</sup> ]
$\rho_c$	Specific gravity of ordinary cement	[kg/m <sup>3</sup> ]
$\sigma$	Electrical conductivity	[S/m]
$\sigma_p$	Conductivity of pore solution	[S/m]
$\sigma_{p,Sat}$	Conductivity of pore solution at saturated state	[S/m]
$\sigma_{p,S_w}$	Conductivity of pore solution at unsaturated state	[S/m]
$\sigma_s$	Conductivity of solid phase	[S/m]
$\sigma_{Sat}$	Conductivity of saturated cementitious material	[S/m]
$\sigma_{S_w}$	Conductivity of unsaturated cementitious material	[S/m]
$\sigma_v$	Conductivity of vapour phase	[S/m]
$\theta_a$	Advancing contact angle	[°]
$\theta_m$	Contact angle between mercury and solids	[°]
$\theta_r$	Receding contact angle	[°]
$\theta_w$	Contact angle between water and solids	[°]
$\phi_e$	Effective porosity	[%]
$\phi_{ink}$	Ink-bottle porosity	[%]
$\phi_p$	Volume fraction of pore solution phase	[%]
$\phi_s$	Volume fraction of solid phase	[%]
$\phi_v$	Volume fraction of vapour phase	[%]
$\phi_{sc}^{th}$	Volume of small capillary pores (throat type)	[ml/ml]
$\phi_{sc}^{ink}$	Volume of small capillary pores (ink-bottle type)	[ml/ml]
$\phi_t$	Total porosity	[%]
$\Delta\phi_F$	Porosity difference between pastes OPC-FA-LP and OPC-FA	[%]
$\Delta\phi_B$	Porosity difference between pastes OPC-BFS-LP and OPC-BFS	[%]
$\eta_{d_i}$	Connectivity of pores at a specific diameter $d_i$	[%]
$\eta_p$	Pore connectivity	[%]
$\eta_{sc}$	Connectivity of small capillary pores	[%]

---

$\eta_{s,cr}$	Connectivity of pores ( $0.01 \mu\text{m} < d < \text{critical pore diameter } d_{cr}$ )	[%]
$\eta_w$	Water continuity	[0-1]
$\mu_p$	Pore structure parameter	[-]
$z$	Charge number	[-]
$z_i$	Valence of the ion $i$	[-]



## List of Abbreviations

---

w/b	Water to binder ratio
w/c	Water to cement ratio
wt.	By weight
AASHTO	American Association of State Highway and Transportation Officials
AC	Alternating current
AFt	Ettringite
AFm	Calcium monosulfoaluminate
ASTM	American Society for Testing and Materials
BFS	Ground granulated blast furnace slag
C <sub>3</sub> A	Tricalcium Aluminate
Ca	Calcium
CC	Calcium carbonate
CH	Calcium hydroxide (Portlandite)
Cl <sup>-</sup>	Chloride ion
CO <sub>2</sub>	Carbon oxide
C-S-H	Calcium silicate hydrate
DC	Direct current
DTG	Differential thermogravimetric analysis
EIS	Electrochemical impedance spectroscopy
FA	Fly ash
H	Hydrotalcite
Hc	Hemicarboaluminate
HCl	Hydrogen chloride
ICP-OES	Inductively coupled plasma atomic emission spectroscopy
IEC-MIP	Intrusion-extrusion cyclic mercury porosimetry
ITZ	Interfacial transition zone
LOI	Loss on ignition
LP	Limestone powder
Mc	Monocarboaluminate
MIP	Mercury intrusion porosimetry
Ms	Monosulphate

NaCl	Sodium chloride
OPC	Ordinary Portland cement
PSD	Pore size distribution
PVC	Polyvinyl chloride
RCM	Rapid chloride migration
RH	Relative humidity
SCMs	Supplementary cementitious materials
SEM	Scanning Electron Microscopy
SD	Saturation degree
SF	Silica fume
TGA/DSC	Thermogravimetry analysis & Differential Scanning Calorimetry
WVDI	Water vapour desorption isotherm
XRD	X-ray diffraction

## Chapter 1

### General Introduction

---

#### 1.1 Background of this project

The environmental impact of the large-scale use of concrete is a serious issue in the building industry. Portland cement is a major component of concrete. Cement production nowadays accounts for approximately 5~7% of global man-made CO<sub>2</sub> emissions across the world [Benhelal et al. 2013]. Using less Portland cement would result in a huge reduction in CO<sub>2</sub> emissions. Great opportunities lie in the utilization of binders with partial replacement of Portland cement by supplementary cementitious materials (SCMs), such as blast furnace slag from steel industry, fly ash from coal-fired power plants, limestone powder, etc.

When the Portland cement is partially replaced by SCMs, the question is to what extent the concretes made with these SCMs can meet prevailing durability criteria. There is no doubt that addition of SCMs, either reactive or inert, will affect the hydration process and formation of microstructure [Juenger et al. 2011]. As a result, the durability of concrete made with SCMs might be different from that of concrete based on pure Portland cement.

One of the main durability problems of concrete structures is the chloride-induced reinforcement corrosion [Tuutti 1982], caused by chloride penetration in the cover concrete. Chloride penetration involves a variety of transport phenomena, such as diffusion, absorption and electrical migration. In most service life design and durability specifications, e.g. DuraCrete [2000] and Life-365 [2001], the chloride penetration is assumed to be dominated by chloride diffusion. Chloride ions diffuse in concrete via the water-filled pore network. A certain percentage of the chloride ions can be captured physically/chemically by the hydration products, e.g. calcium silicate hydrate (C-S-H) and calcium monosulfoaluminate hydrate (AFm). The interaction between chlorides and hydrates is known as chloride binding [Tang & Nilsson 1993].

The *chloride diffusion coefficient*  $D_{Cl}$  is a parameter widely used to indicate the capacity of concrete to resist chloride diffusion. The factors that influence the *microstructure* and *moisture condition* (i.e. moisture content and its distribution) will affect the  $D_{Cl}$ -value. These factors include:

- Type of cement
- Mix proportion, i.e. water-to-binder (w/b) ratio, replacement level, etc.
- Curing age
- Internal relative humidity or degree of water saturation
- Exposure condition, i.e. relative humidity, temperature, chemicals (CO<sub>2</sub>, SO<sub>4</sub><sup>2-</sup>, etc.)

Laboratory measurements and field data have demonstrated that the  $D_{Cl}$ -value, derived by using Fick's 2<sup>nd</sup> law to describe the chloride profiles, is not a constant but decreases with time. *Densification of the microstructure* due to continuous hydration is normally considered an explanation for the decrease of the  $D_{Cl}$ -value [Tang 1996]. It is reported, however, that the hydration process is noticeable only in the first few years [Scrivener & Nonat 2011]. This makes it essential to consider a point not explicitly addressed so far, namely that the  $D_{Cl}$ -value can decrease with *decreasing moisture content*.

Figure 1.1 shows an example of the moisture profile in the cover concrete exposed to marine environment. The near-surface part of the concrete might have a high degree of water saturation  $S_w$  because of the ingress of the moisture from the environment. The internal concrete (Zone II), however, is relatively dry and has a saturation level  $S_w$  approximately the same as that caused by self-desiccation [Persson 1997]. Hence there is a moisture gradient in zone I. In the first few years of exposure the *capillary absorption*, as a result of wetting-drying cycles, may significantly accelerate the chloride penetration in zone I. The absorption effect is strong when the moisture content of the near-surface concrete is low, but becomes increasingly weak with an increase of the number of wetting-drying cycles, since wetting-drying cycles normally lead to a continuous water supply and comparatively little evaporation [Mustafa et al. 1994, Fraj et al. 2012]. The chloride penetration in zone II is considered driven merely by diffusion.

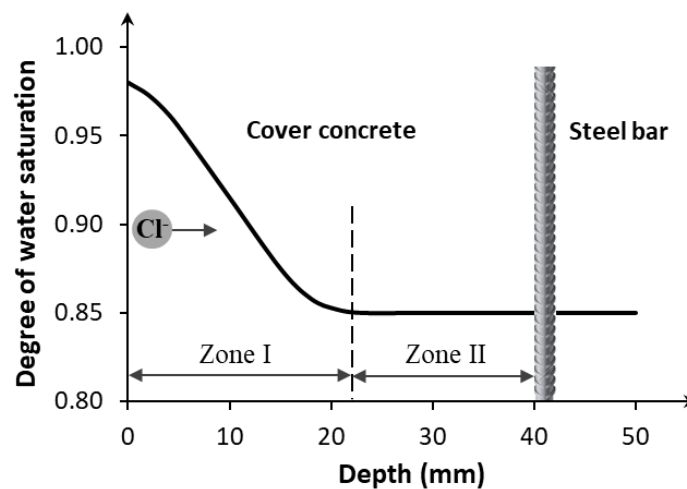


Fig. 1.1 Moisture profile in marine concrete and transport of chloride ions ( $Cl^-$ ).

In present service life calculations, e.g. DuraCrete [2000], the chloride diffusion coefficient  $D_{Cl}$  is generally determined based on chloride penetration tests performed on *saturated* concretes. The effect of the moisture content on the  $D_{Cl}$ -value is *implicitly* described with the ageing factor  $n$  and the environmental factor  $k_e$ . Attempts have been made in recent years to study the  $D_{Cl}$  in non-saturated cementitious materials [Climent et al. 2002, Nielsen & Geiker 2003, Olsson et al. 2013, Mercado-Mendoza et al. 2014, Olsson et al. 2018]. However, to what extent the moisture content does influence chloride diffusion is still a pending issue. There is no consensus about the role of the w/b ratio in the non-saturated chloride diffusion [Zhang et al. 2012, Olsson et al. 2013]. The impact of SCMs on the non-saturated chloride

diffusion is even less studied. The relationship between non-saturated chloride diffusion and pore structure is not completely clear. So far, a widely endorsed mathematical expression to predict the  $D_{Cl}$  in non-saturated cementitious materials is not available.

## 1.2 Objectives and scope of this project

The goals of this research project are, firstly, to understand the effect of SCMs on the pore structure and moisture distribution and, secondly, to develop a tool for predicting the chloride diffusion coefficient in *non-saturated* cementitious materials. Experiments are conducted in order to achieve these goals. The main objectives are outlined as follows:

- 1) To characterize the pore structure of blended cementitious materials, including porosity, pore size, pore connectivity, critical and average pore diameter;
- 2) To understand the moisture distribution in the pore structure of cementitious materials at various degrees of water saturation;
- 3) To determine the chloride diffusion coefficient at various degrees of water saturation based on theoretical considerations and experimental studies;
- 4) To discuss the role of unsaturated chloride diffusion in service life prediction of concrete structures.

The experiments conducted in this project concern the following materials and samples:

- Raw materials: CEM I 42.5 (OPC), low-calcium fly ash (FA), ground granulated blast furnace slag (BFS) and limestone powder (LP);
- Samples: paste samples (cured 28~370 days) and mortar samples (cured 28~730 days);
- W/b ratio: 0.4, 0.5 and 0.6;
- Degree of water saturation: 18~100%.

The binders contain pure OPC, binary and ternary cements. Paste samples are used for pore structure measurements. Mortar samples are used for water vapour desorption isotherm tests as well as for analyses of chloride transport properties under saturated and non-saturated conditions.

## 1.3 Strategy of the research

In cementitious materials the ionic transport is primarily dependent on the pore structure and moisture condition (i.e. moisture content and its distribution). In *saturated* condition the pore structure plays a major role in the ionic transport. In *non-saturated* condition the moisture distribution in the pore structure, especially in the small capillary pores, dominates the ionic transport. For a given moisture content the moisture distribution is, in essence, controlled by the pore structure. Figure 1.2 shows the interrelationship between these parameters.

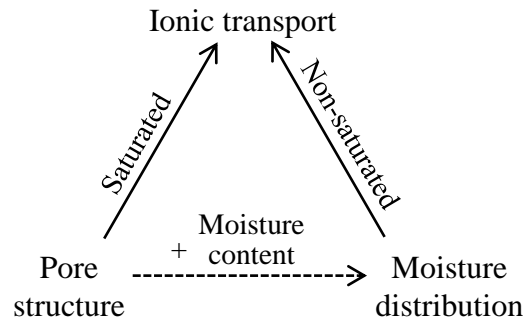


Fig. 1.2 Dependence of ionic transport on pore structure and moisture condition.

The research comprises a series of experimental studies. Based on the research framework shown in Fig. 1.2, the main strategy for the experiments is described as follows:

- 1) Step one: The pore structure, which governs the moisture distribution and ionic transport, is characterized. A novel measurement procedure, i.e. *intrusion-extrusion cyclic mercury porosimetry* (IEC-MIP), is proposed and then applied to identify the size and connectivity of small capillary pores in paste specimens made with and without SCMs.
- 2) Step two: The influence of the pore structure on the chloride diffusion coefficient in *saturated* cementitious materials is estimated by means of rapid chloride migration test [NT Build 492].
- 3) Step three: For a given pore structure the *moisture distribution* at various degrees of water saturation is investigated based on the Kelvin law and water vapour desorption isotherms of cementitious materials.
- 4) Step four: A *mathematical equation* for predicting the chloride diffusion coefficient of cementitious material at various degrees of water saturation is developed based on the Nernst-Einstein equation and conductivity of cementitious electrolyte, as well as on moisture distribution in the pore structure. Validation of the equation with experimental data is performed.
- 5) Step five: The equation developed in Step four is extended. A *formula* for determining the chloride diffusion coefficient is then proposed that explicitly considers the evolution of the pore structure and degree of water saturation with time. The role of the degree of water saturation in the long-term chloride diffusion is discussed.

## 1.4 Outline of thesis

This thesis is organized into five parts. The flowchart is shown in Fig. 1.3.

- Research background and literature review (Chapters 1, 2)
- Characterization of the pore structure and discussion on the influence of the pore structure on the chloride diffusion coefficient in saturated cementitious materials (Chapters 3, 4, 5)
- Moisture distribution in cementitious materials (Chapter 6)

- Chloride diffusion coefficient in unsaturated cementitious materials and evolution of unsaturated chloride diffusion coefficient (Chapters 7, 8)
- Conclusions and prospects (Chapter 9)

Chapter 1 outlines the research background, objectives, research scope and strategy of this research project.

Chapter 2 provides a comprehensive overview of the state of the art in the research field of chloride diffusion in non-saturated cementitious materials, including experimental methods, influencing factors and current mathematical expressions.

Chapter 3 describes the principles of the mercury intrusion porosimetry (MIP) technique based on the microstructure of hardened cement paste. An alternative measurement, i.e. *intrusion-extrusion cyclic mercury porosimetry* (IEC-MIP), is proposed and evaluated. The IEC-MIP measurement enables to distinguish between small (throat) pores and large (ink-bottle) pores, both playing different roles in the moisture-dependent ionic transport.

Chapter 4 presents the experimental results of the pore structure of paste specimens determined by IEC-MIP tests. Pore structure parameters linked to ionic transport are identified, including porosity, pore size distribution, critical pore diameter, threshold pore diameter, pore connectivity and pore entrapment. The changes of the pore structure due to the addition of SCMs are analyzed.

Chapter 5 evaluates the influence of the pore structure on the chloride diffusion in saturated cementitious mortars. The chloride diffusion process is indicated by the chloride migration coefficient obtained from rapid chloride migration test [NT Build 492].

Chapter 6 deals with the moisture distribution in unsaturated cementitious materials. The effects of pore features, i.e. porosity, pore size, pore connectivity and tortuosity, on the moisture distribution are analyzed based on the Kelvin law. In parallel, the water vapour desorption isotherms of mortar specimens are measured. A formula is then established with which the continuity of water-filled pores is expressed as a function of the degree of water saturation.

Chapter 7 investigates the chloride diffusion in unsaturated cementitious materials. Mathematical description of the *relative* chloride diffusion coefficient  $D_{rc}$  is performed according to the Nernst–Einstein equation, the microstructure-based conductivity of cementitious electrolyte and the continuity of water-filled pores. Experiments are carried out and the data obtained are used to validate the mathematical equation. The influences of SCMs on the  $D_{rc}$  are analyzed.

Chapter 8 discusses the effect of the degree of water saturation on the long-term chloride diffusion coefficient in unsaturated cementitious materials.

Chapter 9 summarizes the results, conclusions and prospects of this research.

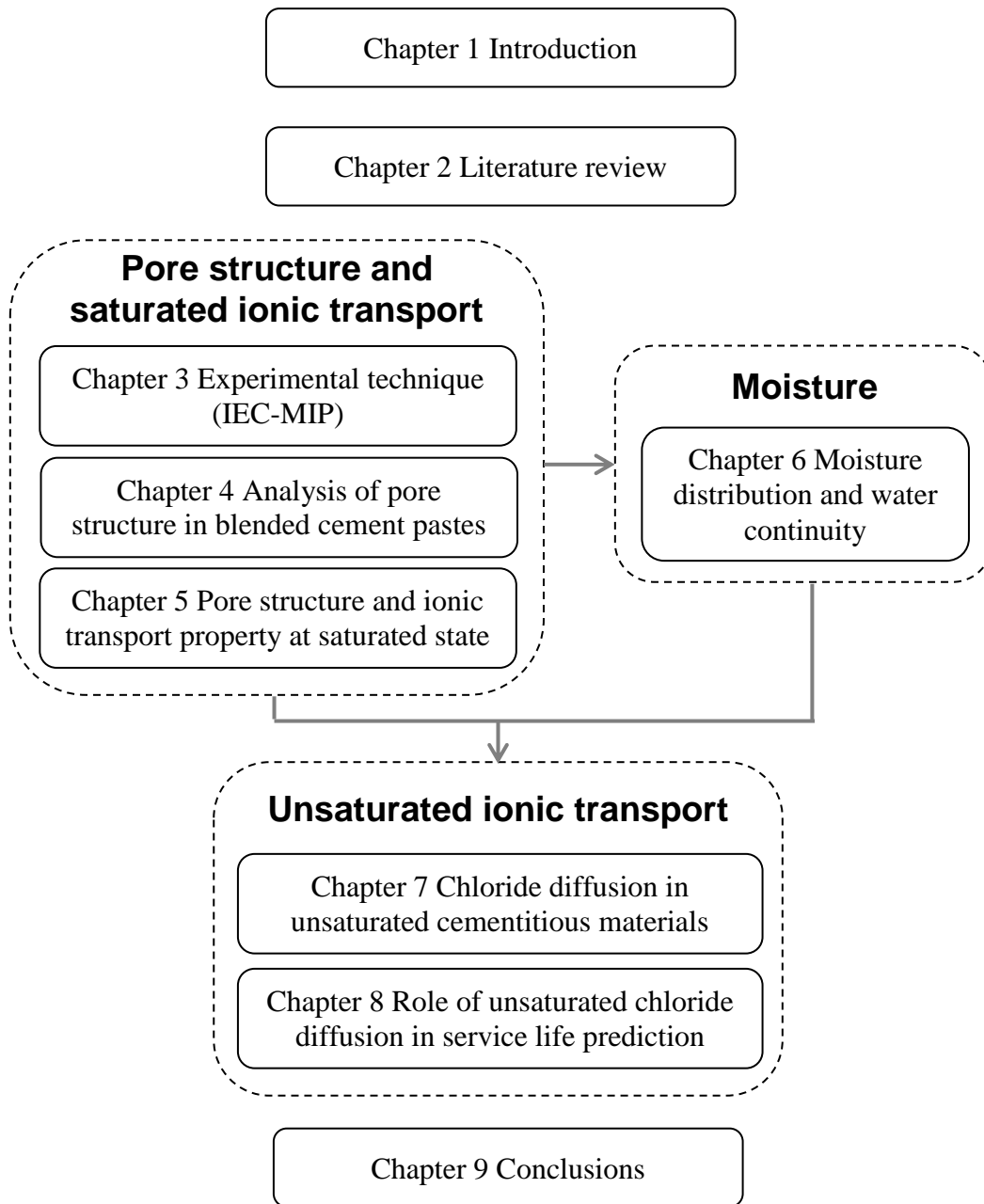


Fig. 1.3 Flowchart of this thesis.

## Chapter 2

# Chloride Diffusion in Unsaturated Cementitious Materials: A Literature Review

---

## 2.1 Introduction

Onsite concrete is rarely saturated. Even for an underwater concrete, only the outer few centimeters are saturated while the interior part is rather dry [Chatterji 1994 & 2004]. In unsaturated concrete the water phase accumulates preferentially in small pores through which ionic transport is possible. The gas phase, on the contrary, tends to fill the ‘central region’ of large pores and forms gas phase clusters that block the ionic transport [Zhang et al. 2014]. The water content and its distribution are key factors that influence the chloride diffusion in unsaturated concretes.

In this chapter the knowledge of the moisture condition in cementitious materials is briefly addressed. Previous investigations relevant to chloride diffusion in unsaturated cementitious materials are reviewed, including experimental methods, measurements and results.

## 2.2 Moisture condition in hardened cementitious materials

### 2.2.1 Cement hydration and water phases

Cement reacts with water and produces a hardened cement paste. The water phase in the cement paste can roughly be classified into three categories [Powers 1945]: capillary water, gel water and non-evaporable water, as illustrated in Fig. 2.1.

Capillary water is the water held in capillary pores. Part of the capillary water is physically adsorbed on the pore walls. The *adsorbed capillary water* is hardly available for cement hydration. The *free capillary water*, in contrast, can easily be mobilized for cement hydration. Cement grains react with the free capillary water resulting in a net reduction of the total volume of water and solid. The chemical shrinkage has been reported as 6.4 ml/100 g reacted cement [Powers 1946]. In unsaturated cement pastes some of the capillary pores are fully filled with water, some are partially water-filled, and the rest is only covered with thin water film [Neville 1981, Taylor 1990].

Gel water, also termed “interlayer water”, refers to the water between the C-S-H gel layers. 1 g hydrated products contain around 0.19 g gel water [Powers 1947]. The gel water can be removed when the cement paste is subjected to D-drying (equilibrated with dry ice at -79 °C,

vapour pressure  $0.5 \times 10^{-3}$  mm Hg) [Powers 1960].

The non-evaporable water is the water retained in hydration products after the D-drying procedure [Powers 1960]. For complete hydration of the cement, the non-evaporable water amounts to 0.22~0.25 g/g of the anhydrous cement [van Breugel 1991].

The non-evaporable water is an intrinsic component of solid phases through which ionic transport is not possible. The gel water is present in very fine pores. Ionic transport through these fine pores is negligible [Mindess & Young 1981]. In a normal concrete the ionic transport takes place predominantly via the capillary water.

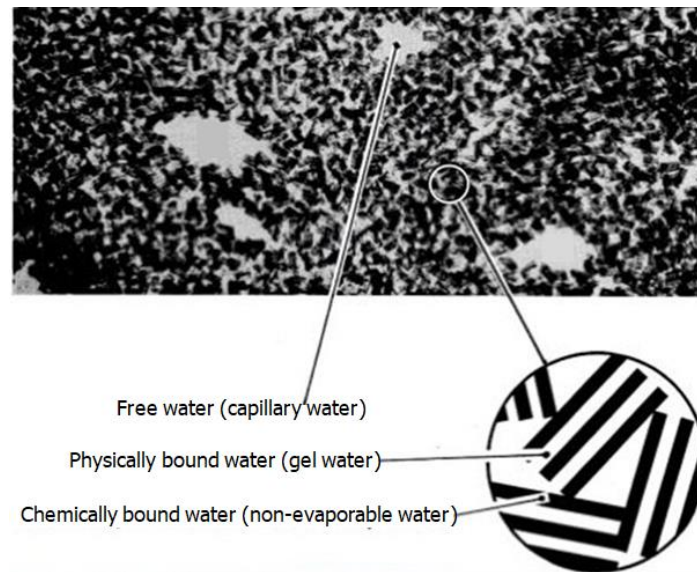


Fig. 2.1 Illustration of water phases in the cement paste [Powers 1945].

## 2.2.2 Determination of water content

Relative humidity and degree of water saturation are two different parameters that are used to determine the water content in cementitious materials at equilibrium moisture state.

### 2.2.2.1 Relative humidity

The internal relative humidity RH of cementitious material is expressed as [Köhler 1936]:

$$RH = RH_S \cdot RH_K \quad (2.1)$$

The term  $RH_S$  accounts for the decrease of water activity caused by dissolved ions. In an ideal solution  $RH_S$  is estimated with Raoult's law [Jensen 1993]:

$$RH_S = \frac{n_{H_2O}}{n_{solution}} \quad (2.2)$$

where  $n_{H_2O}$  is the number of moles of water in the pore solution and  $n_{solution}$  is the total number of moles (including water and solute) in the pore solution.

The term  $RH_K$  is associated with the curvature formed at the fluid/vapour interfaces.  $RH_K$  can be determined with the Kelvin equation [Brunauer 1943]:

$$\ln(RH_K) = -\frac{2\gamma_w \cdot V_m \cdot \cos \theta_w}{r_k \cdot R \cdot T} \quad (2.3)$$

where  $V_m$  is the molar volume of water;  $\theta_w$  is the contact angle between water and solids (if perfect wetting is assumed,  $\theta_w = 0$ );  $r_k$  is the Kelvin radius of the meniscus [m];  $R$  is the ideal gas constant (8.314 J/mol·K);  $T$  is the absolute temperature [K].  $\gamma_w$  is the surface tension of the pore solution (0.072 N/m for pure water). The presence of dissolved salts can reduce the surface tension  $\gamma_w$ . For a cementitious pore solution, a surface tension of approximately 0.055 N/m has been reported [Jensen 1993]. The Kelvin equation is able to provide a reasonable estimation of the menisci with radius as low as 4 nm, with a deviation of  $\pm 6\%$  when the radius is within 4~20 nm [Fisher 1981].

If the adsorbed water film is taken into account, as illustrated in Fig. 2.2a, the Kelvin equation is replaced by the Kelvin-Cohan equation [Neimark et al. 2003]:

$$RH_K = \exp\left(-\frac{2\gamma_w \cdot V_m \cdot \cos \theta_w}{(r_p - t) \cdot R \cdot T}\right) \quad (2.4)$$

where  $r_p$  is the radius [m] of the pores in which the meniscus surface is formed.  $d_p$  ( $d_p = 2r_p$ ) is generally assumed the *smallest drained pore diameter* in a partially saturated sample. A pore is defined as *drained* when the pore is only covered with a nano-scale water film.  $t$  [m] is the thickness of the water film and depends on internal RH [Badmann et al. 1981]:

$$t = [0.385 - 0.189 \cdot \ln(-\ln(RH))] \times 10^{-9} \quad [1\% \leq RH \leq 95\%] \quad (2.5)$$

The  $t$ -RH curve plotted from Eq. (2.5) is shown in Fig. 2.2b. Combining Eqs. (2.1) and (2.4) leads to an expression for the smallest drained pore diameter  $d_p$ .

$$d_p = -\frac{4 \cdot \gamma_w \cdot \cos \theta_w \cdot V_m}{RT \cdot \ln(RH/RH_S)} + 2t \quad (2.6)$$

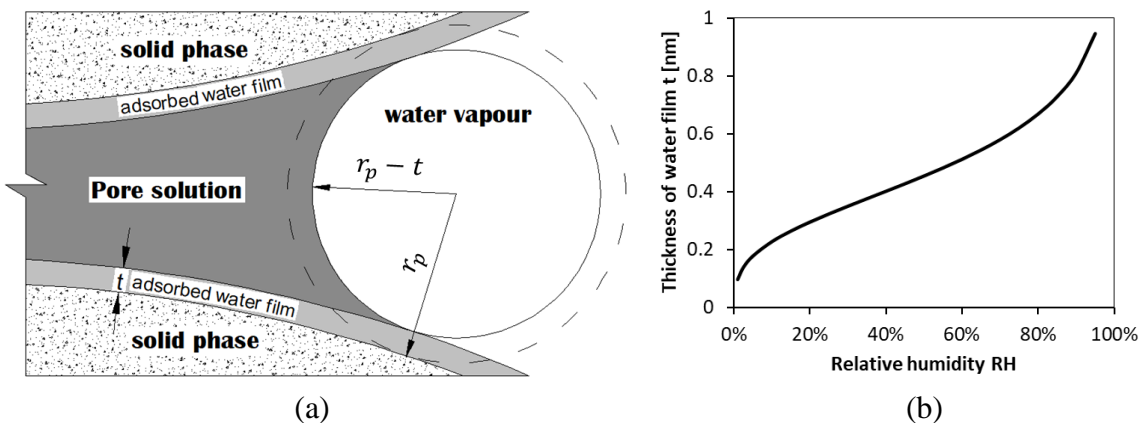


Fig. 2.2 (a) Schematic illustrations of meniscus curvature and adsorbed water film in the capillary pores. (b) Thickness  $t$  of water film versus internal RH according to Eq. (2.5).

### 2.2.2.2 Degree of water saturation

Degree of water saturation,  $S_w$ , is defined as the ratio of the volume of pore water over the total pore volume [López & González 1993].

$$S_w = \frac{m_h - m_d}{m_s - m_d} \times 100\% \quad (2.7)$$

where  $m_h$  [g] is the mass of specimen at a particular degree of water saturation,  $m_s$  [g] is the mass of specimen at saturated state, and  $m_d$  [g] is the mass of dried specimen. The parameters  $m_h$ ,  $m_s$  and  $m_d$  can be obtained by following ASTM C642-13.

The water absorption  $A_b$  of the specimen is expressed as [RILEM TC 116-PCD]:

$$A_b = \frac{m_s - m_d}{m_d} \quad (2.8)$$

From Eqs. (2.7) and (2.8), the specimen mass  $m_h$  corresponding to a particular water saturation  $S_w$  can be deduced.

$$m_h = m_s \frac{1 + A_b \cdot S_w}{1 + A_b} \quad (2.9)$$

## 2.3 Survey of experimental methods

Ionic transport in an unsaturated porous system is different from that in a saturated porous system (see Fig. 2.3). There are two major challenges in the experiments relevant for chloride diffusion in unsaturated concretes. *First*, proper sample preconditioning is required to prepare a concrete sample with uniform moisture content, i.e. desired moisture content and homogeneous moisture distribution. *Second*, it is not easy to force chloride ions into an unsaturated concrete without changing the interior moisture condition or microstructure of the concrete sample. Previous research relating to the two challenges is reviewed below.



Fig. 2.3 Transport of chloride ions ( $Cl^-$ ) in saturated (left) and unsaturated (right) porous systems.

### 2.3.1 Sample preconditioning for obtaining uniform moisture content

Two different desorption regimes are found in the literature for preparing a cementitious sample with uniform moisture content: “RH” (relative humidity) preconditioning and “SD” (saturation degree) preconditioning.

In “RH” preconditioning (Fig. 2.4a) the sample is moved stepwise to drier RH climates until it is in equilibrium with the desired RH climate. The step-by-step desorption regime guarantees minimal damage (e.g. cracking) of the specimen. The different RH climates can be controlled by saturated salt solutions [DIN 50008]. The “RH” preconditioning approach has been described by several workers [Climent et al. 2002, Nielsen et al. 2003, Olsson et al. 2013]. The “RH” preconditioning is known to be time-consuming because of the low moisture diffusivity of cementitious materials. Particularly at low RH climates it may take years for a concrete sample (10 mm thick) to reach equilibrium moisture state [Gallé 2000 & 2001].

In “SD” preconditioning (Fig. 2.4b) the sample is pre-treated in an oven at a relatively high temperature, e.g. 50 °C. The *first* step is to dry the sample until it loses a predefined amount of water. The *second* step is to keep the sample sealed until it reaches a homogeneous moisture distribution (i.e. uniform RH). The duration of the second step is required equal to at least the drying period of the first step, but should not be less than 3 days [Parrott 1994]. The “SD” preconditioning is a quick method to obtain partially saturated samples and has been used by several workers, like Guimarães et al. [2011], Antón et al. [2013], Sánchez et al. [2013], etc. Pretreatment at high temperature may nevertheless induce microstructure changes of the sample by, for example, accelerated hydration. Normally the sample is hydrated to a high degree before it is used for “SD” preconditioning.

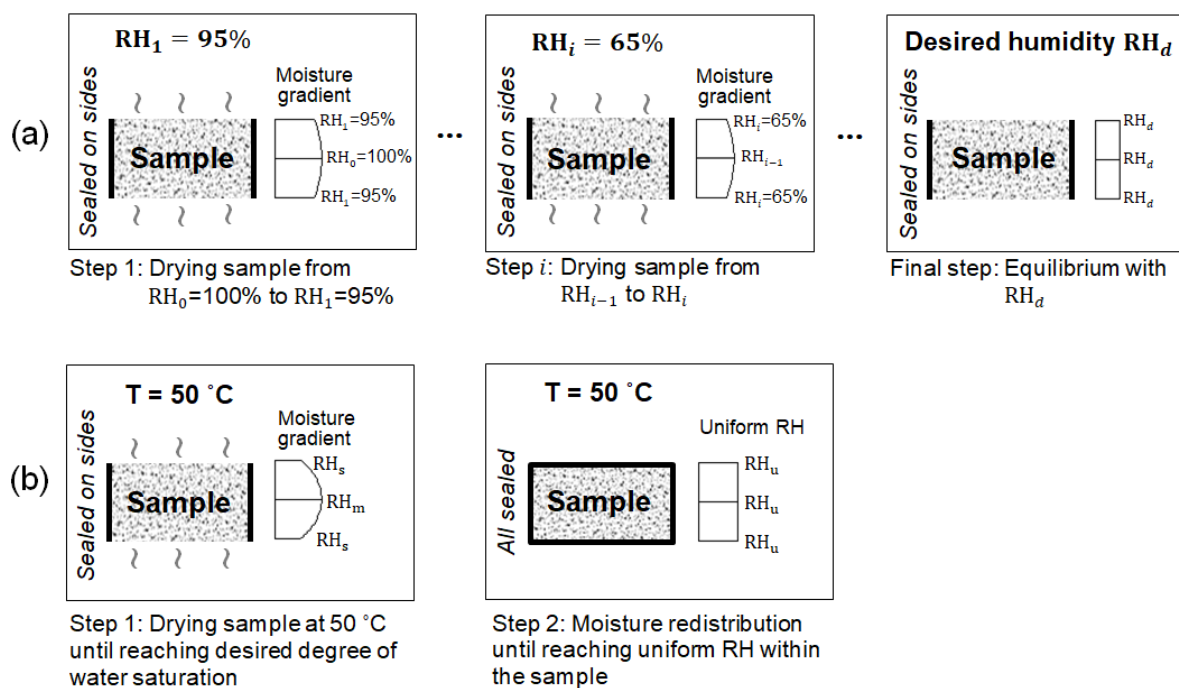


Fig. 2.4 Illustrations of “RH” preconditioning (a) and “SD” preconditioning (b).

### 2.3.2 Measurement of chloride diffusion coefficient in unsaturated concretes

At present there is no standard test available for measuring the chloride diffusion coefficient  $D_{Cl}$  in *unsaturated* concretes. Current standard tests, such as Salt Ponding Test (AASHTO T259), Diffusion Test (NT BUILD 443), Rapid Chloride Permeability Test (AASHTO T277), Rapid Chloride Migration Test (NT BUILD 492), Conductivity Technique (ASTM C 1760), etc., are designed to measure the  $D_{Cl}$  in *saturated* concretes. Among these test methods, the Diffusion Test and Conductivity Technique have been extended by a few researchers to determine the  $D_{Cl}$  in unsaturated concretes.

#### 2.3.2.1 Diffusion test

Figure 2.5 illustrates the diffusion test on a non-saturated sample. Only one side of the sample is exposed to the chloride environment. The chloride source can be an aqueous solution of sodium chloride (NaCl) [Nielsen & Geiker 2003], gaseous hydrogen chloride (HCl) [Climent et al. 2002], or solid NaCl (passing number 100 sieve) [Guimarães et al. 2011]. After a certain test period the chloride profiles are obtained by, firstly, grinding successive 2-mm parallel layers and, secondly, performing potentiometric titration on the grinded powders of each layer [NT Build 208]. The chloride diffusion coefficient of the sample is then determined mathematically by using Fick's 2<sup>nd</sup> law to fit the chloride profiles.

There are pros and cons of the different ways of imposing chlorides into non-saturated samples. Imposing a chloride source in the form of NaCl solution is convenient, but will introduce extra water that can lead to unwanted moisture redistribution of the sample. The imposition of solid NaCl results in a very slow diffusion process in the non-saturated sample. By using the HCl gas, no extra water is introduced, but it may alter the microstructure of the sample due to the acid nature of HCl.

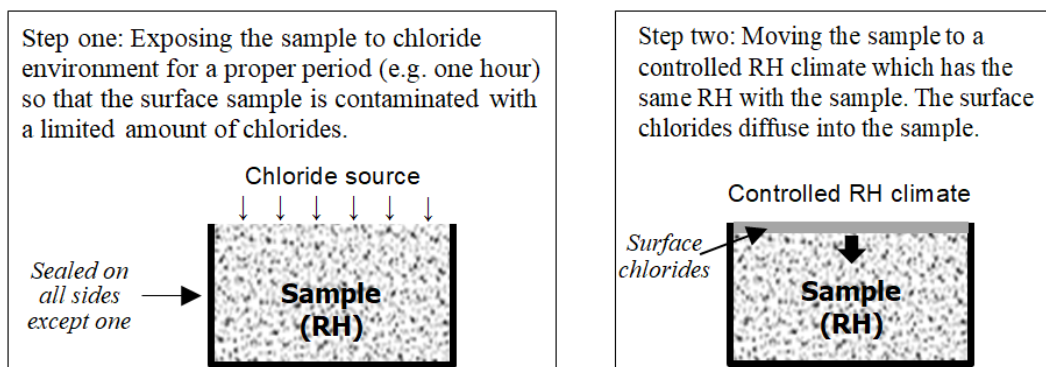


Fig. 2.5 Illustration of two-step chloride diffusion test on a non-saturated sample.

#### 2.3.2.2 Conductivity technique

Ionic conductivity and ionic diffusion coefficient can be correlated by using the Nernst-Einstein equation [McKee 1981]. The electrical conductivity measurement is based on the microstructure and moisture condition of the material under study [McCartert & Garvin 1989, Vedalakshmi et al. 2008, Weiss et al. 2013]. There are two types of measurement for

determining a conductivity value. By applying alternating current (AC) or direct current (DC), the measurement is defined as *electrochemical impedance spectroscopy* test or *resistivity* test, respectively [Rajabipour 2006 & 2007]. Both tests have been utilized to determine the chloride diffusion coefficient in non-saturated cementitious materials [Mercado-Mendoza et al. 2014, Olsson et al. 2013]. The non-destructive nature, rapid and ease of performing a conductivity experiment make it an attractive addition to the determination of chloride diffusion coefficient, although it cannot identify the chloride binding effect.

#### *Electrochemical Impedance Spectroscopy test (AC)*

In an electrochemical impedance spectroscopy (EIS) test, where the voltage can oscillate in a sinusoidal manner with a constant frequency, the *impedance* of the material is measured. The term impedance ( $Z$ ) contains a real ( $Z'$ ) and an imaginary ( $Z''$ ) component, i.e.  $Z = Z' + Z''$ . Both  $Z'$  and  $Z''$  are measured at different frequencies and can be plotted against each other in a so called Nyquist plot. Figure 2.6a presents an example of the Nyquist plot of a saturated concrete sample [Christensen et al. 1994]. At the intersection of the two arcs, the imaginary impedance ( $Z''$ ) is theoretically zero. The frequency corresponding to this point is called the “cut-off” frequency. The derived impedance  $Z$  at that point is called bulk resistance  $R_b$  [ $\Omega$ ], which is often used to determine the conductivity of the sample.

Determination of the  $R_b$ -value becomes difficult in the case of an unsaturated concrete sample, since the Nyquist plot changes drastically at low water saturation levels. An example is shown in Fig. 2.6b. To determine the bulk resistance  $R_b$ , a modified equivalent electrical model and an optimization procedure are required [Mercado-Mendoza et al. 2014].

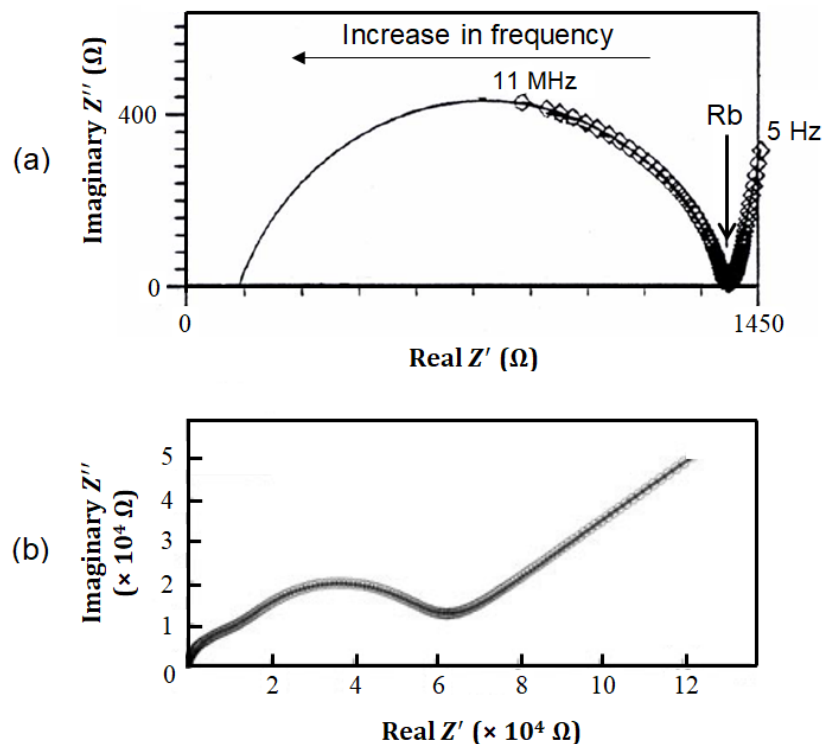


Fig. 2.6 Nyquist plot: (a) saturated concrete [after Christensen et al. 1994]; (b) unsaturated concrete with water saturation level of 67% [after Mercado-Mendoza et al. 2014].

### *Resistivity test (DC)*

In a resistivity test the electrical *resistance*  $R$  [ $\Omega$ ] of the material is measured. The conductivity, which is the inverse of resistivity, is determined as a function of the resistance  $R$  [Polder 2001]. The resistivity tests will be adopted in the present project to determine the chloride diffusion coefficient in unsaturated cementitious samples, in the light of the fact that steel corrosion is an electrochemical process involving direct current (DC) [Stratfull 1968]. More details about the resistivity theory and experiments will be given in Chapter 7.

## **2.4 Chloride diffusion in non-saturated cementitious materials**

### **2.4.1 Definition of relative chloride diffusion coefficient $D_{rc}$**

The relative chloride diffusion coefficient  $D_{rc}$  has often been used to describe the chloride diffusion in non-saturated cementitious materials. It is defined as the *ratio* of chloride diffusion coefficient  $D_{Cl}$  at a particular unsaturated state over that at saturated state.

$$D_{rc} = \frac{D_{Cl}(\text{unsaturated state})}{D_{Cl}(\text{saturated state})} \quad (2.10)$$

The unsaturated state, in the cases where equilibrium moisture content is present, can be indicated by either the degree of water saturation  $S_w$  or the relative humidity RH. The influencing factors and existing expressions on the  $D_{rc}$ -value (or  $D_{Cl}$ -value) are reviewed in the following.

### **2.4.2 Factors affecting the $D_{rc}$ in unsaturated cementitious materials**

#### *2.4.2.1 Effect of degree of water saturation on $D_{rc}$ -value*

Few studies on the  $D_{rc}$ -values are available in the literature. The details and results are summarized in Table 2.1 and Fig. 2.7, respectively.

The general trend observed in Fig. 2.7 is that the  $D_{rc}$ -value strongly depends on the degree of water saturation  $S_w$ . The dependency, however, shows a large scatter. Climent et al. [2002] and de Vera et al. [2007] reported  $D_{rc}$ -values to be slightly altered in the high saturation levels, i.e.  $S_w = 70\sim 100\%$ . Buchwald [2000] found that the  $D_{rc}$ -value decreased clearly from 1 to 0.42 when the  $S_w$  decreased from 100 to 70%. According to Mercado et al. [2014], the  $D_{rc}$ -value dropped drastically from 1 to 0.03 in this saturation range.

A satisfactory explanation for the large scatter of the  $D_{rc}$ - $S_w$  relation cannot be found in literature yet, and is an important reason for further research in this thesis.

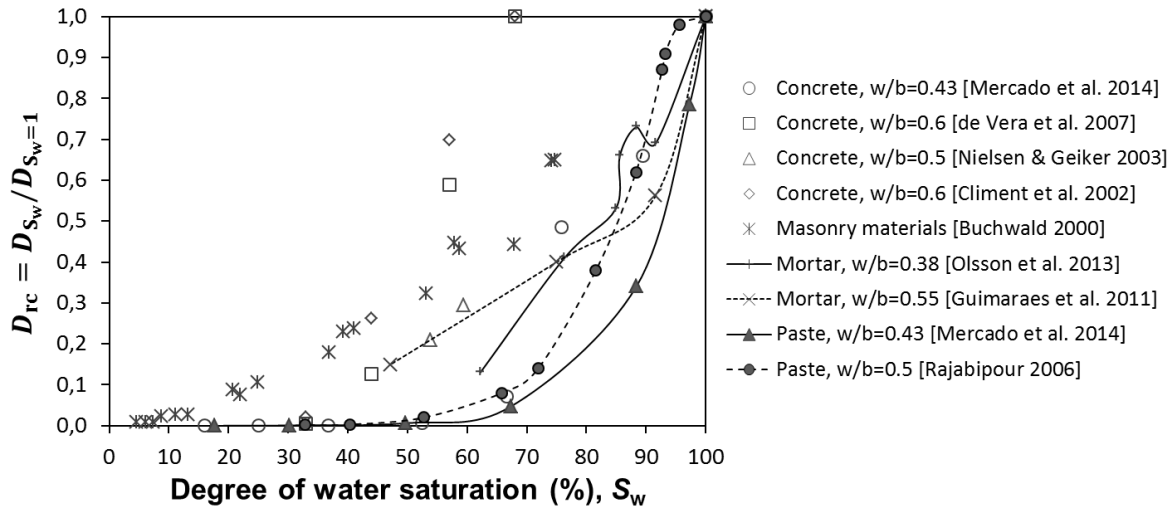


Fig. 2.7 Summary of the  $D_{rc}$ - $S_w$  relations reported by different workers.

#### 2.4.2.2 Effect of w/c ratio on $D_{Cl}$ -value and $D_{rc}$ -value

The role of the w/c ratio in the non-saturated chloride diffusion coefficient,  $D_{Cl}$ -value or  $D_{rc}$ -value, is still a point of controversy.

Based on diffusion tests, Climent et al. [2002] determined the chloride diffusion coefficient  $D_{Cl}$  as a function of the internal RH in concrete specimens. It was found that in the range of 54~98% RH the concrete with w/c = 0.5 always showed a smaller  $D_{Cl}$ -value than the concrete with w/c = 0.6. Based on resistivity tests, Olsson et al. [2013] determined the  $D_{Cl}$ -RH relation for mortar specimens and reported that compared to the mortar with w/c = 0.38 the mortar with w/c = 0.53 has a larger  $D_{Cl}$ -value at high RH (e.g. > 85%) but a smaller  $D_{Cl}$ -value at low RH (e.g. < 85%).

Olsson et al. [2013] stated that the w/c ratio has little effect on the  $D_{rc}$ - $S_w$  relation in OPC mortars (see Fig. 2.8-left). Based on a simulation study, Zhang et al. [2012] reported that in OPC pastes a higher w/c ratio leads to a higher  $D_{rc}$  at a given  $S_w$  level (see Fig. 2.8-right).

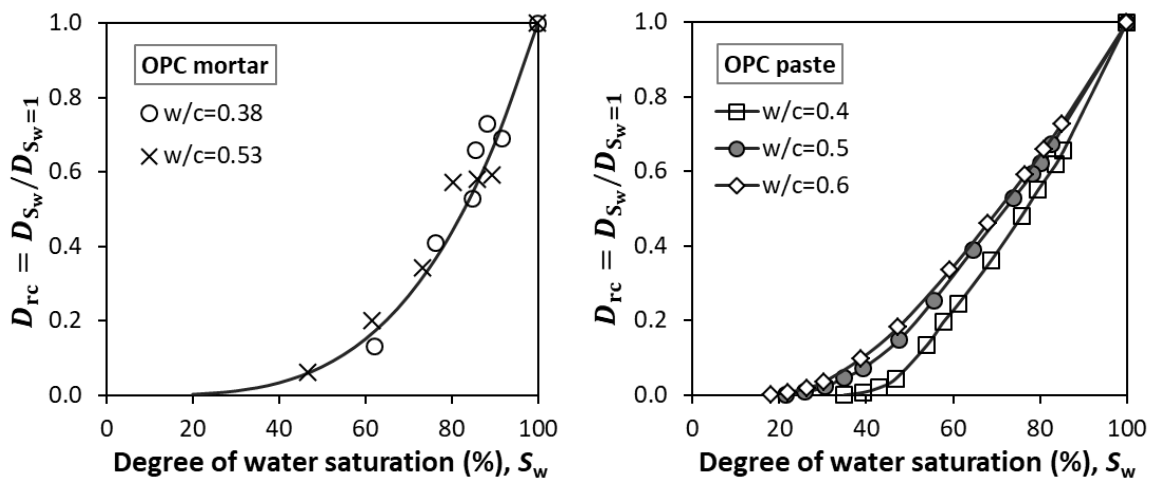


Fig. 2.8 Effect of w/c ratio on the  $D_{rc}$ - $S_w$  relation. (a) Experimental data from Olsson et al. [2013]; (b) Simulation data from Zhang et al. [2012].

Table 2.1 Experimental studies on chloride diffusion coefficient in unsaturated cementitious materials

No.	Cement type	Specimen	Curing condition	Moisture condition	Chloride source	Tests conducted	Reference
1	CEM II/A-L-32.5 R	Concrete	28 days	In equilibrium with >95%, 86%, 75%, and 54% RH	PVC combustion gases (HCl)	Diffusion	Climent et al. 2002
	CEM II/A-L-42.5 R						
2	Rapid-hardening cement	Mortar	4.6 months	In equilibrium with 85%, 65% RH	Immersion 26 % NaCl solution for 2 h, then dry to original mass	Diffusion	Nielsen 2003
3	CEM II/A-L-32.5 R	Concrete	28 days	In equilibrium with >95%, 86%, 75%, and 54% RH	PVC combustion gases (HCl)	Diffusion	De Vera et al. 2007
	CEM II/A-L-42.5 R						
4	CP VRS	Mortar		Oven drying at 50°C, $S_w=50\%$ , 75%, 90%, 100%	Solid NaCl	Diffusion	Guimaraes et al. 2011
5		Lime mortar				EIS	Buchwald 2000
6	ASTM Type I	Cement paste	18 months				Rajabipour 2007
	ASTM Type I + 5% silica fume						
7	CEM I 52.5 N PM ES	Concrete		Kept in a water tank for 3 months, oven dried progressively at 80 °C	cyclic exposure consisting of 6 h wetting periods with 30 g/l NaCl solution, and 6 h drying periods.	Diffusion	Ben Fraj et al. 2012
	CEM I 52.5 N PM ES + 30% Slag						
8	CEM I 42.5 N	Mortar	2 months	In equilibrium with 100%, 97.5%, 94%, 91%, 85%, 75%, 59% and 33% RH.		Conductivity	Olsson et al. 2013
	CEM I 42.5 N + 5% Silica fume						
	CEM I 42.5 N + 40% Slag						
9	CEM I 42.5 N + 70% Slag	Cement paste	6 months	In equilibrium with 94%, 84%, 75%, 66%, 55%, 44% and 33% RH		EIS	Mercado-Mendoza et al. 2014
	CEM ICEM V (55% Cement + 22% Slag + 23% Fly ash)						
		Concrete					

### 2.4.2.3 Effect of interfacial transition zone on $D_{rc}$ -value

The interfacial transition zone (ITZ) is usually considered as a third morphological constituent in concrete at the boundary between aggregate and cement matrix [Asbridge et al. 2001]. It comprises similar phases as the paste matrix, but has different microstructure, morphology and density [Chen et al. 2006, Gao et al. 2014]. The thickness of the ITZ varies in the range of 10~50  $\mu\text{m}$  [Sicat et al. 2014]. The chloride migration coefficient of the ITZ is about 1.5~3 times higher than that of the paste matrix [Zhang et al. 2013]. The addition of pozzolanic materials leads to a denser ITZ [Larbi 1991].

Figure 2.9 shows the experimental  $D_{rc}$ - $S_w$  data for pastes and concretes. At a given  $S_w$  level, the  $D_{rc}$ -value of paste is generally smaller than that of concrete. Especially for high  $S_w$  levels, e.g.  $S_w = 70\sim 90\%$ , big differences of the  $D_{rc}$ -values exist between OPC paste and OPC concrete. Such differences, however, are small between blended paste and blended concrete.

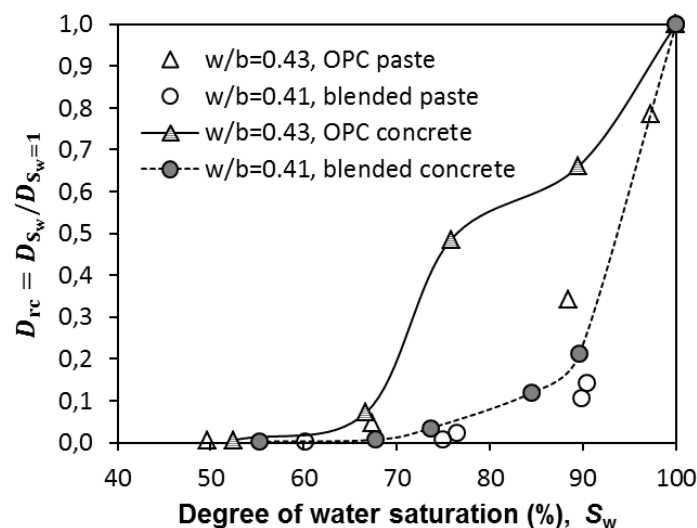


Fig. 2.9  $D_{rc}$ - $S_w$  relations in pastes and concretes with OPC binder and blended binder (55% OPC + 22% BFS + 23% FA) (after Mercado-Mendoza et al. [2014]).

### 2.4.2.4 Effect of chloride binding on $D_{Cl}$ -value

The chloride binding behavior plays an important role in the chloride diffusion process. In saturated concrete the chloride binding exists in the whole pore network. In non-saturated concrete, however, the chloride binding occurs mainly in the water-filled pores. Different chloride binding isotherms, i.e. linear, Langmuir, Freundlich, and BET binding isotherms, have been proposed to describe the relationship between free and bound chlorides in *saturated* concrete. The Langmuir isotherm is applicable at low free chloride concentration (lower than 0.05 mol/L), while the Freundlich isotherm is often applied when the free chloride concentration is higher than 0.01 mol/L [Tang et al. 1992].

Based on diffusion tests, de Vera et al. [2007] studied the chloride diffusion in unsaturated concretes. The (water-soluble) *free* chloride profile [Chaussadent & Arliguie 1999] and (acid-soluble) *total* chloride profile [Climent et al. 2004] were measured. The *bound* chloride profile represents the difference between total and free chloride profiles. The relationships

between bound and free chlorides over a range of free chloride concentrations were described with a Langmuir isotherm.

De Vera et al. [2007] also determined the chloride diffusion coefficient  $D_{Cl}$  by using Fick's 2<sup>nd</sup> law to fit both the free chloride profile and the total chloride profile. The obtained  $D_{Cl}$ -values are presented in Table 2.2. The ratio of the  $D_{Cl}$ -values between the free and the total chloride profiles varies by a factor of 0.5~1.5 when the degree of water saturation  $S_w$  changes in the range of 33~68%.

*Table 2.2 Chloride diffusion coefficient  $D_{Cl}$  in unsaturated concretes obtained by using Fick's 2<sup>nd</sup> law to fit the free and total chloride profiles (After de Vera et al. [2007])*

Degree of water saturation $S_w$ (%)	Chloride diffusion coefficient $D_{Cl}$ ( $\times 10^{-12}$ m <sup>2</sup> /s)		
	Free chloride profile	Total chloride profile	Ratio
68	5.86	3.85	1.52
57	3.45	2.21	1.56
44	0.74	1.01	0.73
33	0.03	0.06	0.50

#### 2.4.2.5 Effect of wetting-drying cycles on $D_{Cl}$ -value

Owing to wetting-drying cycles concrete structures in a marine tidal zone will suffer from severe chloride ingress. During the wetting period chloride ions penetrate into concrete by the coupled actions of ionic diffusion and capillary absorption. During the drying period the water evaporates from the concrete and leads to crystallization of dissolved salts in the pores. The wetting process is generally much faster than the drying process. Spraag et al. [2011] reported that the amount of fluid (0.8 mm<sup>3</sup>/mm<sup>2</sup>) that had evaporated after 8 days can be re-saturated by absorption within 2 hours.

Fraj et al. [2012] measured the chloride penetration in unsaturated concretes (initially with internal RH = 50, 75 and 90%) under wetting-drying climate, i.e. 6 h of wetting (exposed to NaCl solution, 60 g/l) and 18 h of drying (exposed to air, 50% RH). The chloride penetration rate [m<sup>2</sup>/s] was indicated with the chloride diffusion coefficient  $D_{Cl}$  determined by applying Fick's 2<sup>nd</sup> law to fit the penetrated chloride profiles. The  $D_{Cl}$ -values versus wetting-drying cycles are plotted in Fig. 2.10. With an increase of wetting-drying cycle, the  $D_{Cl}$ -value shows a decreasing trend for all RH levels studied. In OPC concretes the  $D_{Cl}$ -value for different RH levels differs substantially at early wetting-drying cycles, but shows a minor difference after 60 wetting-drying cycles. The same observation holds also for BFS-blended concretes. All these suggest that the effect of capillary absorption on the chloride penetration is not significant after a sufficient number of wetting-drying cycles.

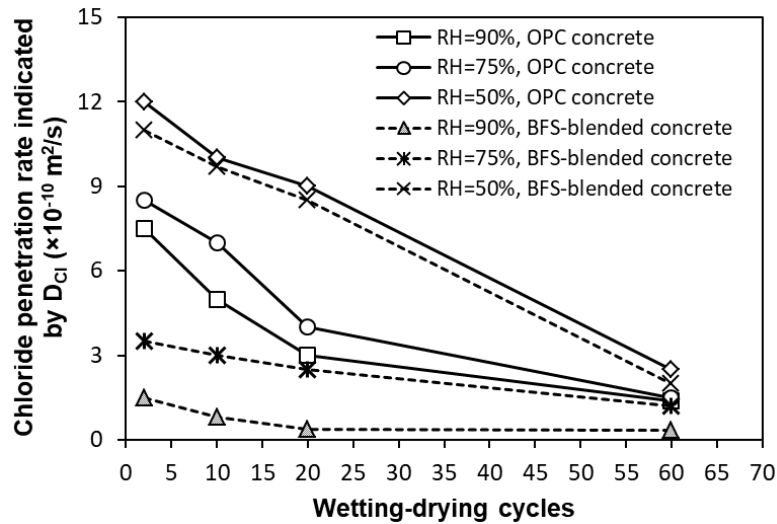


Fig. 2.10 Effect of wetting-drying cycles on chloride penetration in OPC and BFS-blended concretes ( $w/b = 0.48$ ) with internal RH of 50, 75 and 90% (after Fraj et al. [2012]).

2.4.2.6 Effect of SCMs on  $D_{rc}$ -value

Silica fume (SF)

SF is a by-product of the smelting process in the silicon and ferrosilicon industry. It mainly consists of amorphous silica. The addition of SF can result in a finer pore size distribution [Selvaraj et al. 2003]. SF reacts with calcium hydroxide and densifies the paste-aggregate interfacial transition zone. SF-blended concrete comprises a more discontinuous and impermeable pore network compared to that of OPC concrete [Khalil 1996].

It appears that the effect of SF (5 wt.%) on the  $D_{rc}$ - $S_w$  relation is not significant (see Fig. 2.11). For mixtures with  $w/b = 0.38$ , the SF-blended mortar shows a slightly lower  $D_{rc}$ -value than the OPC mortar of the same saturation level  $S_w$  (see Fig. 2.11-left). There is a minor change in the  $D_{rc}$ - $S_w$  relation between OPC and SF-blended mortars when the  $w/b$  ratio increases up to 0.53 (see Fig. 2.11-right).

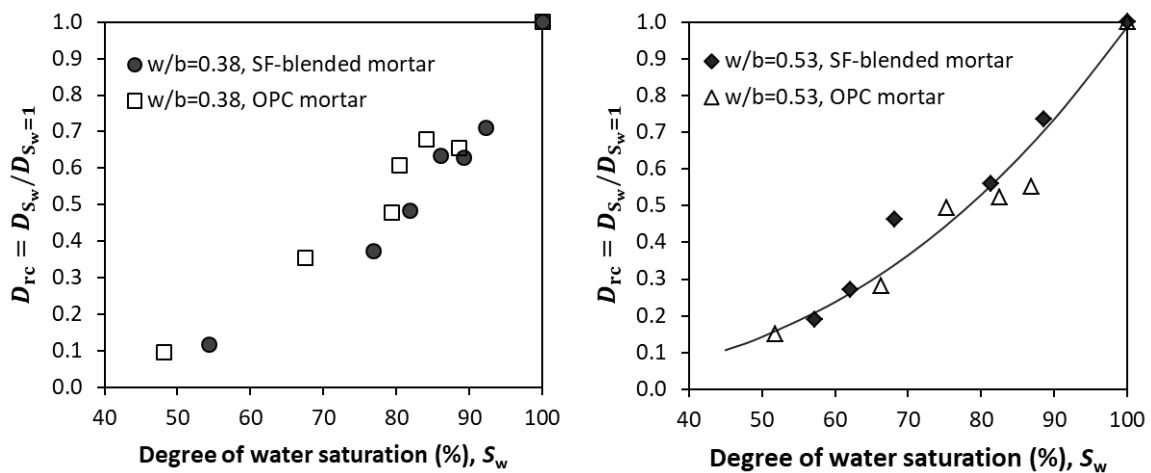


Fig. 2.11  $D_{rc}$ - $S_w$  relations in OPC and SF (silica fume 5 wt.%) -blended mortars with  $w/b = 0.38$  (left) and  $w/b = 0.53$  (right) (after Olsson et al. [2018]).

### Ground granulated blast furnace slag (BFS)

BFS is rich in CaO (calcium oxide) and contains a limited amount of crystals. BFS shows both cementitious behaviour (latent hydraulic activity) and pozzolanic characteristics (reaction with calcium hydroxide). Substantial effect of the slag content on the chloride diffusion coefficient  $D_{Cl}$  is found when the OPC is replaced by slag at high percentages, i.e. > 50%. The  $D_{Cl}$ -value of saturated slag-blended concretes, with slag content 50~80%, is reported to be a factor of 10~16 lower than that of saturated OPC concretes [Bijen 1996]. In the Netherlands, BFS-cement with slag content of 65~70% has a market share of about 60%, and it is the exclusive material used for concrete structures in marine environment [Polder 2012]. Substitution of OPC by slag increases the amount of small pores but decreases the total porosity [Ping et al. 2013].

Figure 2.12 shows the  $D_{rc}$ - $S_w$  relations in mortars blended with 0, 40 and 70% BFS. Compared to the controlled OPC binder, the addition of 40% BFS shows little influence on the  $D_{rc}$ - $S_w$  relation. While in the presence of 70% BFS, the  $D_{rc}$  is much lower than the OPC binder of the same saturation level  $S_w$ .

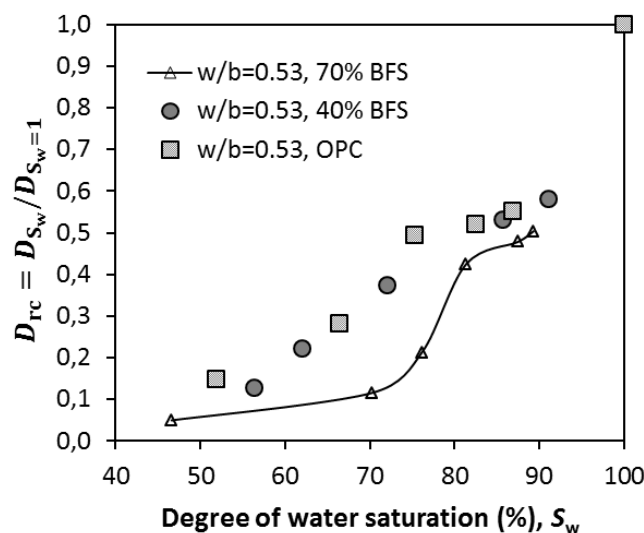


Fig. 2.12  $D_{rc}$ - $S_w$  relations in the mortars with 0, 40 and 70% BFS (after Olsson et al. [2018]).

### Fly ash (FA)

FA powders mainly consist of  $\text{SiO}_2$  and  $\text{Al}_2\text{O}_3$ , while containing much less CaO compared to OPC powders. The addition of FA increases the capillary porosity, but goes along with a decrease of the chloride diffusion coefficient in saturated concrete [Kayyali et al. 1995, Saraswathy et al. 2006]. No literature was found on the effect of FA on the chloride diffusion in non-saturated cementitious materials.

### Limestone powder

Calcite is the major component of limestone powder (LP). LP has chemical and physical binding capacity for chloride ions, depending on chloride concentration in the pore solution [CEB 1989]. The European Standard (EN 197-1) allows the use of LP up to 5% in concrete. The LP-filled ternary concretes (i.e. OPC-FA-LP and OPC-BFS-LP) have higher strengths

than the LP-free binary concretes (i.e. OPC-FA and OPC-BFS) [Weerdt et al. 2011a & 2011b]. This is attributed to the synergistic effect between LP and pozzolanic additives (FA, BFS) [Weerdt et al. 2010]. To what extent the synergistic effect influences the  $D_{rc}$ - $S_w$  relation is not known yet and needs further research.

#### *Ternary cement (BFS plus FA)*

Compared to the OPC paste the ternary paste (OPC-BFS-FA) shows a much lower relative chloride diffusion coefficient  $D_{rc}$  for a given  $S_w$  level (see Fig. 2.13). The  $D_{rc}$ -value of the ternary paste drops to 0.1 for  $S_w$ -values as high as 90%, and approaches zero at  $S_w = 75\%$ .

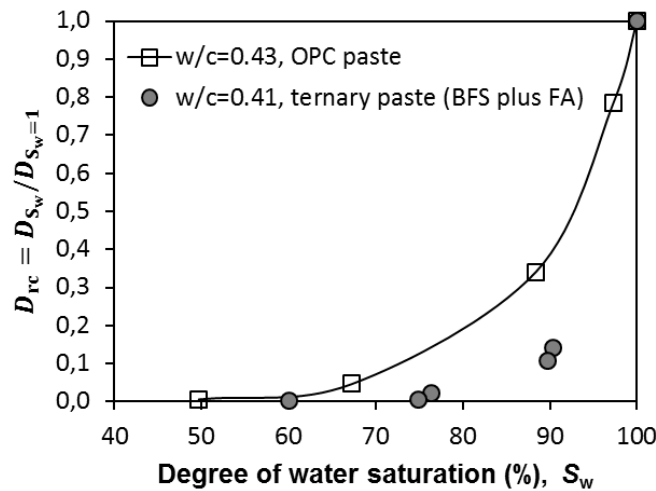


Fig. 2.13  $D_{rc}$ - $S_w$  relations in the pastes with OPC and ternary cement (55% OPC + 22% BFS + 23% FA) (after Mercado-Mendoza et al. [2014]).

### 2.4.3 Current expressions for relative chloride diffusion coefficient

#### 2.4.3.1 $D_{rc}$ -RH relationship

Based on regression analyses on the experimental data of ionic/water diffusion, Saetta et al. [1993] developed an *S-shaped* relationship with which the relative chloride diffusion coefficient  $D_{rc}$  was described as a function of the internal relative humidity RH in concrete.

$$D_{rc} = \frac{D(RH)}{D(RH = 100\%)} = \left[ 1 + \frac{(1 - RH)^4}{(1 - RH_c)^4} \right]^{-1} \quad (2.11)$$

where  $RH_c$  is defined as critical relative humidity at which  $D_{rc} = 1/2$ .  $RH_c = 75\%$  was proposed in the work of Saetta et al. [1993]. The reports from other workers, however, indicated that the  $RH_c$ -value may vary in a wide range of 75~92%, depending on the temperature and the pore structure of the samples used [Nielsen et al. 2003, Olsson et al. 2013, Zhang et al. 2015].

### 2.4.3.2 $D_{rc}$ - $S_w$ relationship

#### Power equation

Buchwald [2000] determined the ionic diffusion coefficient in masonry materials based on EIS tests. A semi-empirical *power* equation, as shown in Eq. (2.12), was put forward.

$$D_{rc} = S_w^\lambda \quad (2.12)$$

Equation (2.12) has been used by other researchers to fit experimental data produced in their works. Baroghel-Bouny et al. [2011] found  $\lambda = 6$  and Olsson et al. [2013] found  $\lambda = 4.5$ .

#### Polynomial equation

Based on simulated microstructures, Zhang et al. [2012] studied the ionic diffusion in unsaturated cement pastes with w/c ratios of 0.4, 0.5 and 0.6 by using lattice Boltzmann method. He suggested a quadratic *polynomial* equation, as shown in Eq. (2.13), with which the simulated  $D_{rc}$ - $S_w$  relations could approximately be described.

$$D_{rc} = a \cdot S_w^2 + b \cdot S_w + c \quad (2.13)$$

where  $a$ ,  $b$  and  $c$  are empirical constants.

### 2.4.3.3 Evaluation of current equations

The current equations (Eqs. (2.11), (2.12) and (2.13)) are compared with experimental data reported in literature in order to evaluate their reliability. Figure 2.14-left shows an example of the curves obtained by using Eqs. (2.12) and (2.13) to fit the data taken from Rajabipour [2006]. It is shown that Eq. (2.12) tends to underestimate the  $D_{rc}$ -value at high saturation levels (e.g.  $S_w > 85\%$ ) and overestimate the  $D_{rc}$ -value at low saturation levels (e.g.  $S_w < 85\%$ ). Equation (2.13) is applicable to describe the  $D_{rc}$ - $S_w$  data only when  $S_w \geq 64\%$ . Figure 2.14-right compares Eq. (2.11) with the  $D_{rc}$ -RH data taken from two different reports. It can be concluded that Eq. (2.11) overestimates the  $D_{rc}$ -value at high RH levels (e.g.  $RH > 85\%$ ) and underestimates the  $D_{rc}$ -value at low RH levels (e.g.  $RH < 85\%$ ).

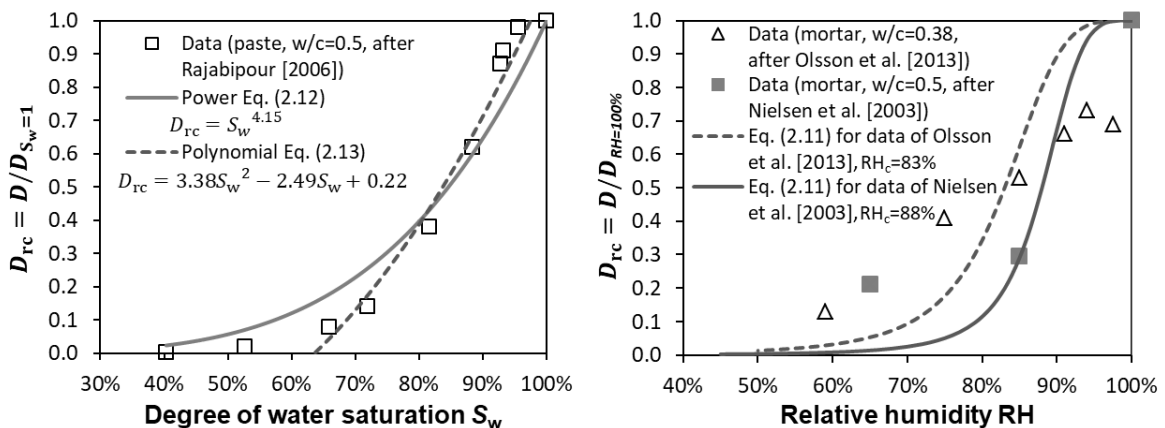


Fig. 2.14 Examples of curves obtained by using current equations (Eqs. (2.11), (2.12) and (2.13)) to fit the available experimental data: (a)  $D_{rc}$  vs.  $S_w$ ; (b)  $D_{rc}$  vs. RH.

## 2.5 Evaluation

Previous reports on the subject of non-saturated ionic diffusion have demonstrated that the relative chloride diffusion coefficient  $D_{rc}$  depends on the degree of water saturation  $S_w$  as well as on the microstructure-related parameters, such as w/b ratio, type of cement, ITZ, etc. The ITZ effect on the  $D_{rc}$ - $S_w$  relation is less pronounced in the blended systems than that in the OPC systems. The role of the chloride binding in the  $D_{rc}$  is almost negligible, compared to the role of the  $S_w$  in the  $D_{rc}$ . The influence of wetting-drying cycles on the  $D_{rc}$ - $S_w$  relation becomes increasingly weak with a continuous increase of wetting-drying cycles.

Our current knowledge about chloride diffusion in non-saturated cementitious materials is far from adequate. The effect of the w/b ratio on the  $D_{rc}$ - $S_w$  relation is still controversial. To what extent the addition of SCMs can affect the  $D_{rc}$ - $S_w$  relation is not clear yet. Current expressions cannot well describe the  $D_{rc}$  in the entire  $S_w$  range.

More detailed research has to be done in order to clearly understand the chloride diffusion in non-saturated cementitious materials. It is evident that both *moisture content* and *moisture distribution* influence the non-saturated chloride diffusion. The emphasis of previous research, however, is mainly on *moisture content*. This could be considered an important reason for the large scatter of the data ( $D_{rc}$  vs.  $S_w$ ) found in the literature. The *pore structure* is a fundamental factor influencing the moisture distribution and should be taken into account in order to reliably predict the  $D_{rc}$ - $S_w$  relation.

Partial replacement of OPC by SCMs will change the pore structure due to changes in the particle size distribution and related changes in the particle packing, and changes of the cement hydration and/or other chemical reactions, as well as changes of the development of microstructure [Stark 2011]. As a result, the moisture distribution and associated  $D_{rc}$ - $S_w$  relation in unsaturated blended concretes can differ substantially from those in pure OPC concretes.

## 2.6 Conclusions and outlook

Previous experiments and mathematical expressions regarding the relative chloride diffusion coefficient  $D_{rc}$  of unsaturated cementitious materials were reviewed and evaluated. The published results about the  $D_{rc}$ - $S_w$  relations show a large scatter and are partly controversial. More detailed research needs to be done, including:

- 1) Development of reliable and rapid method(s) to prepare unsaturated samples with uniform moisture contents;
- 2) Experimental approaches with high reproducibility to measure the relative chloride diffusion coefficient with and without chloride binding;
- 3) A comprehensive knowledge about the pore structure, especially the structure of small capillary pores, in cementitious materials made with SCMs;
- 4) Moisture distribution in non-saturated cementitious materials;
- 5) The role of w/c (w/b) ratio in the  $D_{rc}$ - $S_w$  relation;

- 6) The effect of SCMs (e.g. slag, fly ash, limestone powder) on the  $D_{rc}$ - $S_w$  relation;
- 7) A reliable numerical tool for predicting the  $D_{rc}$ -value based on the saturation level  $S_w$  and pore structure;
- 8) The role of unsaturated chloride diffusion in the service life of cementitious materials.

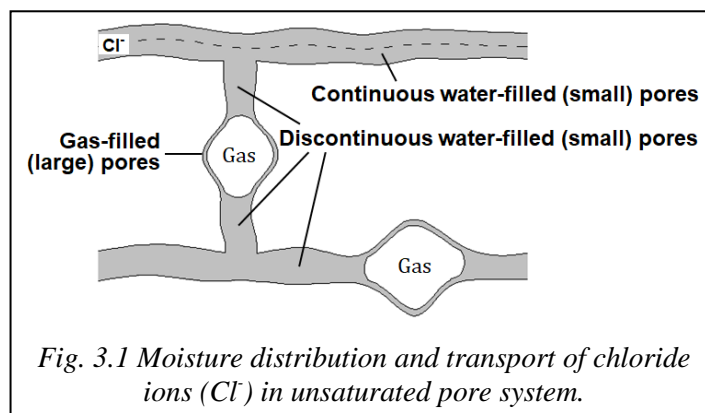
All these aspects will be addressed in the following chapters except the aspect (2).

## Chapter 3

# Experimental Technique for Pore Structure Measurement: Intrusion-Extrusion Cyclic Mercury Porosimetry (IEC-MIP)

### 3.1 Introduction

In unsaturated pore systems the *small* pores tend to be water-filled while the *large* pores tend to be gas-filled, as illustrated in Fig. 3.1. To study the chloride transport property it is a prerequisite to distinguish between *continuous* and *discontinuous* water-filled (small) pores.



For analyzing the pore structure of cementitious materials, the

mercury intrusion porosimetry (MIP) technique has been widely used. In this chapter (see Fig. 3.2) both the microstructure of cement paste and the principles of MIP technique are described. It is known that in standard MIP tests the large (ink-bottle) pores cannot be identified and the small (throat) pores are overestimated [Diamond 2000a]. To overcome these drawbacks, an alternative measurement protocol, i.e. *intrusion-extrusion cyclic mercury porosimetry* (IEC-MIP), is proposed. The IEC-MIP can distinguish between small (throat) pores and large (ink-bottle) pores and, therefore, enables to better study the ionic transport routes in unsaturated cementitious systems.

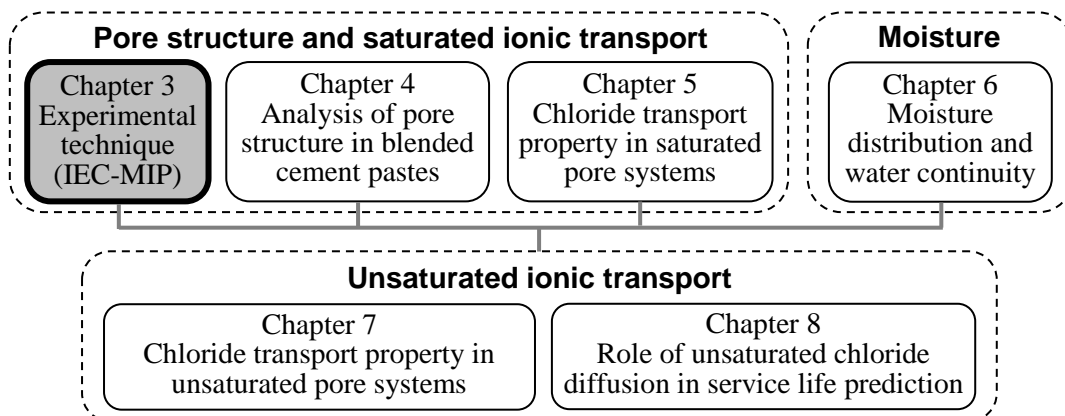


Fig. 3.2 Main chapters of the thesis.

## 3.2 Microstructure of cementitious pastes

### 3.2.1 Structure formation due to cement hydration

The “internal structure” of hardened cementitious materials can be examined with scanning electron microscopy (SEM). Figure 3.3 shows an example of a backscattered image (500 $\times$ ) of the microstructure of 28-day-old cement paste. The brightness intensity of each pixel is proportional to the measured X-ray attenuation coefficient that strongly depends on the density of the target phase. The dark areas account for the low density phases, e.g. air voids and capillary pores. The brighter areas represent the high density phases, e.g. calcium silicate hydrate (C-S-H), calcium hydroxide (CH) and anhydrous cement grain in the order of higher brightness. The distribution of different phases is marked in Fig. 3.3.

The anhydrous cement grains are surrounded by uniformly grey hydration products, named ‘inner product’ C-S-H. The ‘inner product’ C-S-H develops as hydration shells around the surface of anhydrous cement grains [Tennis & Jennings 2000]. A number of tiny deposits are precipitated far away from the anhydrous cement grains. These tiny deposits, named ‘outer product’ C-S-H, are formed by through-solution deposition in the originally water-filled space [Jennings 2008]. The ‘inner product’ C-S-H shells are non-porous at this magnification. C-S-H is the main hydration product and makes up 50~60% of the solid volume in mature cement pastes [Ramachandran et al. 2001].

The hydration product CH tends to form large crystals and mostly precipitates in between partially or fully hydrated cement grains. CH occupies 20~25% of the solid volume in mature cement pastes [Ramachandran et al. 2001]. In most cement pastes, other components, i.e. AFt (ettringite) and AFm (monosulphate), are also found. Both phases are often intimately intermingled with CH and ‘outer product’ C-S-H, and hardly recognizable at the magnification 500 $\times$  [Stark 2011]. They can constitute up to 15~20% of the solid volume in mature cement pastes [Ramachandran et al. 2001].

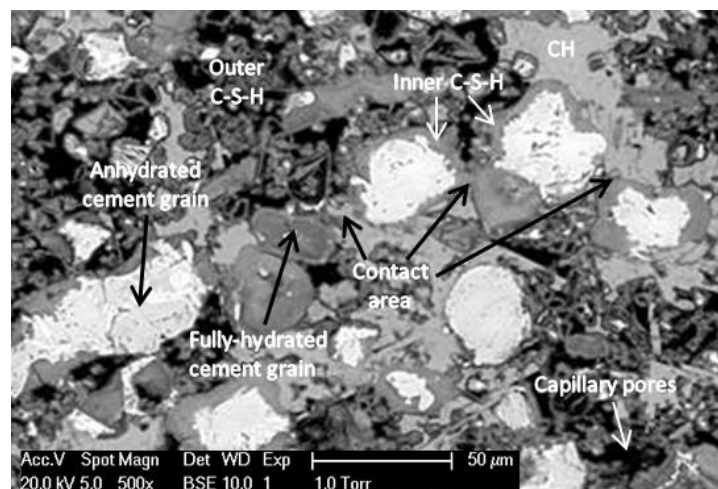


Fig. 3.3 Backscattered image (500 $\times$ ) of 28-day-old cement paste ( $w/c = 0.4$ ) [Ye 2003].

### 3.2.2 Pore space

Hardened cement paste has a broad pore size distribution, ranging from nanometers to micrometers. The main hydration product (C-S-H) consists of an irregular or kinked array of layers, which are randomly arranged to create interlayer space of different shapes and sizes (5 to 25 Å) [Feldman et al. 1970]. Apart from interlayer space, nanometric gel pores are present in between C-S-H particles [Jennings 2008].

Capillary pores are the residual unfilled spaces between hydrating cement grains, usually irregular in shape. Powers [1946] defines two types of capillary pores: small capillary pores and large capillary pores. The small capillary pores refer to the voids resulting from insufficient packing of hydration products. The large capillary pores represent the voids left outside the clusters of hydration products. The pore diameter 0.1 µm is often considered a threshold to distinguish between small and large capillary pores [Kaufmann et al. 2009].

Entrapped air voids are unavoidable in cement pastes, except for vacuum-mixing. Unlike capillary/gel pores, air voids are spherical in shape and mostly closed. Other voids, like micro-cracks, are present as well due to, for example, temperature or moisture gradients.

With a magnification of 500×, Fig. 3.3 only shows the pores larger than 0.185 µm [Ye 2003]. The pores below 0.185 µm, which are considered to be present in the clusters of hydration products, can be detected by other techniques, such as MIP [Diamond 2000a], nitrogen sorption/desorption [Ranaivomanana et al. 2011], etc.

### 3.2.3 Microstructure of cement paste

Two basic characteristics can be inferred from the microstructure of cement paste shown in Fig. 3.3. *First*, each cement grain grows outwardly with ongoing hydration. *Second*, the microstructure far away from anhydrous cement grain is more porous than that nearby. A sketch of the microstructure of cement paste formed based on the two characteristics is given in Fig. 3.4. The microstructure consists of four parts:

- Anhydrous cement grains.
- Inner product zone, which comprises the deposits of inner C-S-H. The interlayer pore space and gel pores ( $\leq 0.01$  µm) are present within C-S-H particles [Jennings 2008]. As a result of cement hydration, the inner C-S-H grows inwardly [van Breugel 1991].
- Outer product zone, which mainly comprises the deposits of outer C-S-H and CH. The deposits close to inner products are densely packed (dense outer product zone), while those far away are loosely packed (porous outer product zone). The small capillary pores are present within clusters of hydrates in outer product zone. As hydration proceeds, the outer products from one cement grain grow outwardly until they make contact with those from neighbouring cement grains, initiating the so called “contact area” [van Breugel 1991].
- Large capillary pores, which represent the void space left outside any deposits.

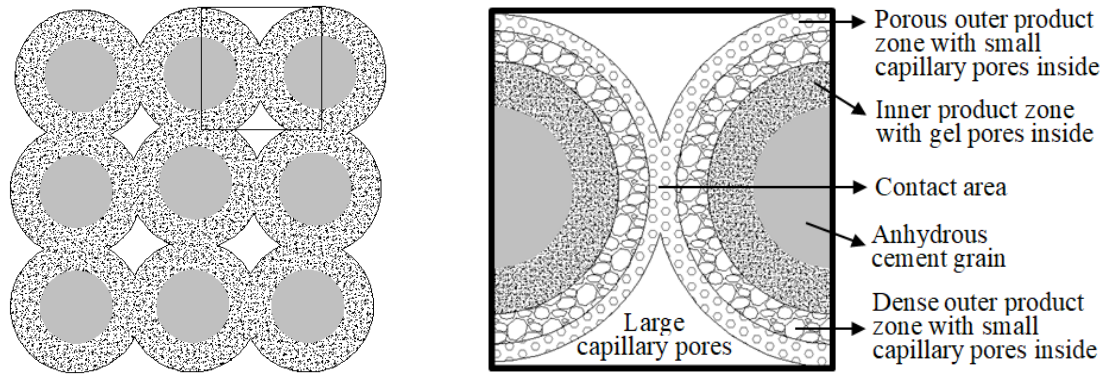


Fig. 3.4 Microstructure formed based on interactions between hydrating cement grains.

### 3.2.4 Effect of SCMs on microstructure

The microstructure of cement paste becomes more complex when the OPC is partially replaced by SCMs (e.g. FA or BFS). The silica in SCMs reacts with CH and produces secondary C-S-H hydrates [Escalante & Sharp 2004]. In many cases the role of different SCMs in the hydration and microstructure formation is similar. Compared to OPC pastes, incorporating SCMs often results in lower heat release, lower CH content, higher C-S-H content and lower Ca/Si ratio of C-S-H [Stark 2011]. Figure 3.5 shows an example of the backscattered image of a paste blended with 70 wt.% BFS. The hydrates are densely packed, and the boundary between the inner C-S-H and outer C-S-H is vague. The dark areas in Fig. 3.5 represent the large capillary pores. Their sizes are smaller and their connectivity is lower, compared to the large capillary pores in OPC pastes as indicated in Fig. 3.3.

The moisture distribution in *unsaturated* BFS-blended pastes is very different from that in *unsaturated* OPC pastes, because of the different pore sizes and different pore connectivities. The effects of the pore structure on moisture distribution will be described in more detail in Chapter 6.

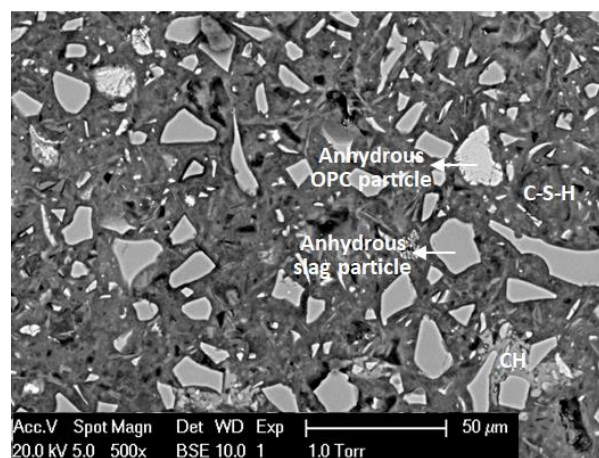


Fig. 3.5 Backscattered image of 28-day-old paste blended with 70 wt.% BFS,  $w/b = 0.4$ .

### 3.3 Principles of mercury intrusion porosimetry (MIP)

#### 3.3.1 Washburn equation

Mercury fills a pore system provided that a pressure is applied. The equilibrium of forces acting inside cylindrical pores, i.e.  $F_1 = F_2$ , is illustrated in Fig. 3.6. The Washburn equation [Washburn 1921] can be applied to determine the radius  $r_p$  [ $\mu\text{m}$ ] of the pores intruded at pressure  $P$  [MPa], as:

$$r_p = (-2\gamma_m \cos\theta)/P \quad (3.1)$$

where  $\gamma_m$  is the surface tension of mercury (0.48 kN/m) and  $\theta$  is the contact angle [ $^\circ$ ]. According to different authors [Cook 1993, Moro et al. 2002, Zhou et al. 2010], the advancing angle  $\theta_a$  ranges from 130 to 141 $^\circ$  and the receding angle  $\theta_r$  varies in the range of 104~126 $^\circ$ .

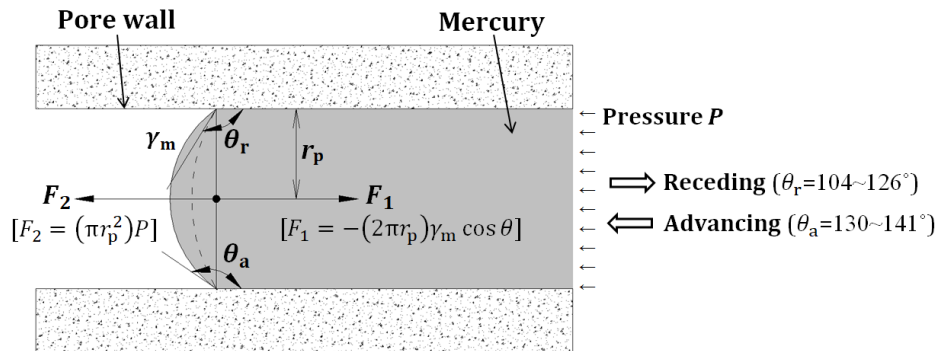


Fig. 3.6 Equilibrium of forces acting inside cylindrical pores.

#### 3.3.2 Test procedure of standard MIP test

For an MIP test the specimen is first dried to empty the pores of any existing fluid. The dried specimen is weighted and then placed into a penetrometer, which is subsequently evacuated. Mercury is forced into the specimen by increasing the pressure, which is called *pressurization*. The pressurization consists of a low pressure run (by pneumatic means) and a high pressure run (by hydraulic means). In the low pressure run, the penetrometer is filled with mercury via its stem until the specimen is completely surrounded by mercury. In the high pressure run, the mercury gradually intrudes the pores that are connected to the surface of the specimen until the maximum applied pressure is reached. This procedure is known as *intrusion*. After completion of the intrusion procedure, an *extrusion* procedure follows. When the applied pressure decreases from the maximum to the minimum, i.e. *depressurization*, the mercury is extruded out of the specimen. The intrusion and extrusion procedures in a complete cycle are commonly adopted as *standard MIP test*.

The intrusion-extrusion cycle in the standard MIP test often shows a hysteresis because of the “ink-bottle” effect [Willis et al. 1998]. The 2<sup>nd</sup> *pressurization* of MIP has little ink-bottle effect and provides a more truthful determination of small capillary pores.

### 3.3.3 Technique parameters

Figure 3.7-left shows an example of the pore size distribution (PSD) obtained from standard MIP test. Figure 3.7-right plots the differential PSD of the intrusion measurement. Various pore structure parameters can be identified, viz. porosity, PSD, threshold and critical pore diameter, total pore surface area, average pore diameter and pore connectivity.

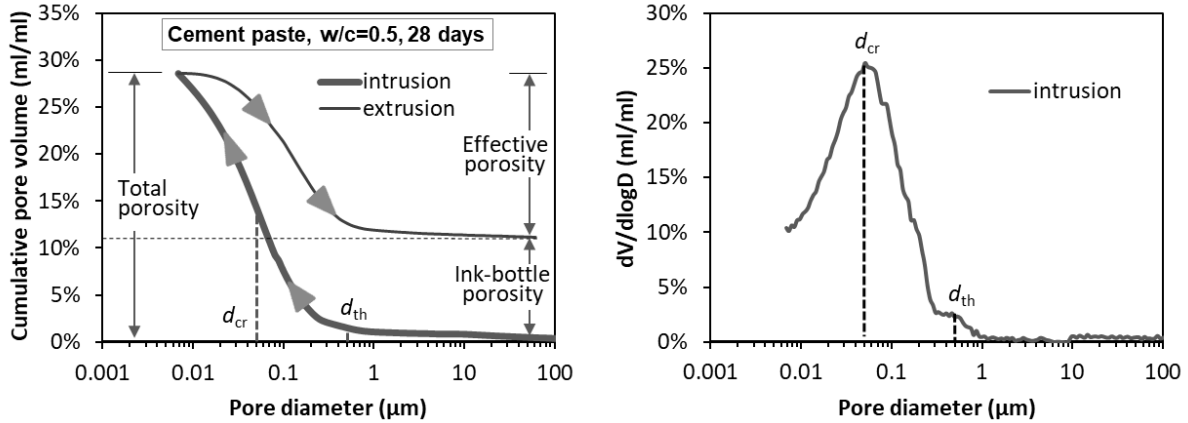


Fig. 3.7 Cumulative pore size distribution (left) and differential curve (right).

#### 3.3.3.1 Total porosity, effective porosity, and ink-bottle porosity

The total open porosity ( $\phi_t$ ), often in short *total porosity*, is determined as the cumulative volume of all open pores intruded by mercury at the maximum pressure. The  $\phi_t$ -value is independent of the size and shape of the pores. The *effective porosity* ( $\phi_e$ ) is determined as the cumulative volume of extruded pores in the extrusion procedure. The *ink-bottle porosity* ( $\phi_{ink}$ ) refers to the irreversible entrapped mercury between the intrusion and extrusion procedures. These different porosities are marked in Fig. 3.7-left.

#### 3.3.3.2 Pore size distribution (PSD)

The pore size distribution,  $dV(d)$ , is defined as the pore volume  $V_{por}$  per unit interval of pore diameter  $d$  [Ritter et al. 1945], as:

$$dV(d) = -\frac{V_{por}}{d} \cdot \frac{dV}{dP} \quad (3.2)$$

where  $dV$  [ $m^3$ ] and  $dP$  [ $N/m^2$ ] are the change of the pore volume and the applied pressure, respectively.

#### 3.3.3.3 Threshold pore diameter $d_{th}$ and critical pore diameter $d_{cr}$

The *threshold pore diameter*  $d_{th}$  refers to the pore size, above which there is comparably little mercury intrusion while immediately below this diameter significant mercury is intruded [Aligizaki 2006]. The *critical pore diameter*  $d_{cr}$  corresponds to the peak of a differential PSD curve. In the example shown in Fig. 3.7,  $d_{th} = 0.5 \mu m$  and  $d_{cr} = 0.05 \mu m$ .

### 3.3.3.4 Average pore diameter $d_a$

For total pore volume  $V_t$  [ $\text{m}^3/\text{m}^3$ ] and total pore surface area  $S_t$  [ $\text{m}^2/\text{m}^3$ ], the *average pore diameter*  $d_a$  is expressed as [Aligizaki 2006]:

$$d_a = \frac{4V_t}{S_t} \quad (3.3)$$

The total surface area  $S_t$  of cylindrical pores can be calculated as [Spitzer 1981]:

$$S_t = \frac{1}{\gamma_m \cos \theta} \int_0^V P dV \quad (3.4)$$

Since the smaller pores have lower volume-to-surface area ratio, a smaller average pore diameter  $d_a$  indicates a porous system with finer pore size distribution (PSD). It is well-known that the PSD plays a significant role in the moisture distribution. The average pore diameter  $d_a$  will be adopted to quantitatively study the effect of the PSD on the moisture distribution and ionic transport in non-saturated porous systems (see Chapters 6 and 7).

### 3.3.3.5 Pore connectivity

Figure 3.8 illustrates the typical pore geometries in hardened cement pastes. The *continuous pores* (Fig. 3.8a-b) can form a connected network relating the two opposite surfaces of a porous specimen. The *dead-end pores* (Fig. 3.8c) are discontinuous pores which are connected with only one surface of a porous specimen. The *isolated pores* (Fig. 3.8d) are surrounded by solid phases and have no connection with any surface of a porous specimen.

The *pore connectivity*  $\eta_p$  is often estimated as the ratio between the volume of continuous pores (effective porosity  $\phi_e$ ) and the total pore volume (total porosity  $\phi_t$ ) [Garboczi 1990]:

$$\eta_p = \frac{\text{effective porosity } \phi_e}{\text{total porosity } \phi_t} \times 100\% \quad (3.5)$$

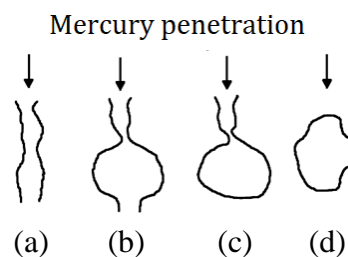


Fig. 3.8 Classification of capillary pore geometry: (a) continuous pore; (b) continuous pore with ink-bottle; (c) dead-end pore; (d) isolated pore [Ye 2003].

## 3.3.4 Evaluation of MIP technique

### 3.3.4.1 Ink-bottle effect

The Washburn equation (Eq. (3.1)) gives a correct relationship between the applied pressure

and the intrusion pore size only if all the pores are cylindrical and they are entirely and equally accessible to the outer surface of the specimen. This condition, however, is not satisfied in hydrated cement systems. The “accessibility” problem [Diamond 2000a], also known as “ink-bottle effect” [Willis et al. 1998], is illustrated in Fig. 3.9a-b.

- a) When a large pore  $d_1$  opens to the exterior mercury (Fig. 3.9a), the Washburn equation gives a correct relationship of pore volume *vs.* pore diameter.
- b) When a small pore  $d_2$  opens to the exterior mercury (Fig. 3.9b), the volume  $v_1$  cannot be recorded when the pressure  $P_1$  corresponding to the large diameter  $d_1$  is applied. At a higher pressure  $P_2$ , corresponding to the small diameter  $d_2$ , the combined volumes ( $v_2+v_1$ ) of the small and large pores will be recorded. As a result, the standard MIP test underestimates large pores and overestimates small pores, because of the “ink-bottle” effect. The mercury in the throat pore  $d_2$  can be freely removed after an extrusion procedure, but the mercury in the ink-bottle pore  $d_1$  is irreversibly entrapped.

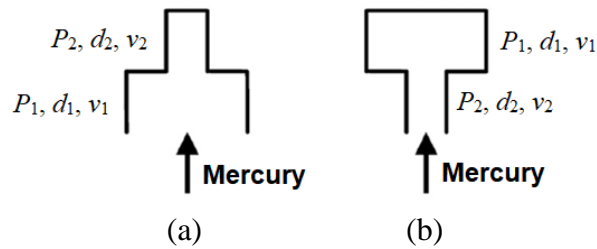


Fig. 3.9 Imaginary channels consisting of a large pore and a small pore: (a) large pore opens to the exterior mercury; (b) small pore opens to the exterior mercury [Diamond 2000a].

In order to characterize the distribution of the entrapped mercury volume as a function of pore size [Lowell et al. 1981], the term *pore entrapment*  $\alpha_{\text{en}}$  is adopted and expressed as the ratio of the entrapped volume over the intruded volume when mercury penetrates the throat pore of a specific diameter. In the example shown in Fig. 3.9b, the  $\alpha_{\text{en}}$ -value at the throat pore  $d_2$  is calculated as:

$$\alpha_{\text{en}} = \frac{\text{entrapped volume}}{\text{intruded volume}} \times 100\% = \frac{v_1}{v_1 + v_2} \times 100\% \quad (3.6)$$

It should be mentioned that the standard MIP test enables measuring the total entrapped volume of mercury (i.e. ink-bottle porosity) and the total intruded volume of mercury (i.e. total porosity), but it is not able to determine the distribution of the pore entrapment  $\alpha_{\text{en}}$  as a function of the pore diameter  $d_i$ , because standard MIP cannot distinguish between small (throat) pores and large (ink-bottle) pores. An alternative measurement, i.e. IEC-MIP, will make a difference in this respect. The details will be presented in Section 3.4.

The distribution of pore entrapment ( $\alpha_{\text{en}}$  *vs.*  $d_i$ ) is helpful to understand the continuity of water-filled pores in unsaturated porous systems.

- 1) A low  $\alpha_{\text{en}}$ -value means that the small pores  $d_i$  are highly interconnected (Fig. 3.10-I), suggesting that the small pores  $d_i$  can easily form continuous water-filled paths in the case of water loss in large pores.

- 2) A high  $\alpha_{en}$ -value means that the small pores  $d_i$  are highly connected with large pores (Fig. 3.10-II). In the case of water loss in large pores, the water in the small pores  $d_i$  is easy to become discontinuous.

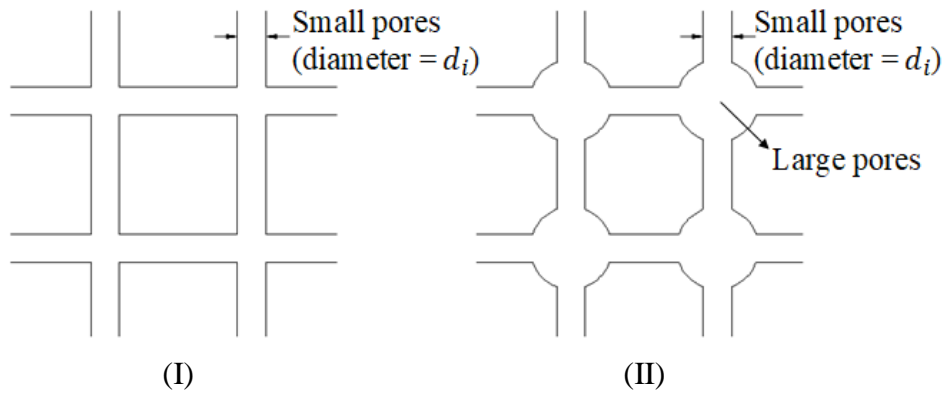


Fig. 3.10 Schematic representations of pore entrapment at a specific small pore diameter  $d_i$ : (I) Small pores (with low pore entrapment) are highly interconnected; (II) Small pores (with high pore entrapment) are connected by large pores.

### 3.3.4.2 MIP-derived pore structure and ionic transport

The standard MIP test provides estimates of the global pore structure parameters, such as total porosity  $\phi_t$  and pore connectivity  $\eta_p$ . In a *saturated* pore system (Fig. 3.11-left), all pores are water-filled. Adoption of the MIP-derived pore structure parameters, including total porosity  $\phi_t$  and pore connectivity  $\eta_p$ , to indicate the ionic transport property is meaningful.

However, both total porosity  $\phi_t$  and pore connectivity  $\eta_p$  are not effective to study the ionic transport in a *non-saturated* pore system. As indicated in Fig. 3.11-right, the pores can be categorized into three groups: (1) *Gas-filled pores*, which impede the ionic transport; (2) *Discontinuous water-filled pores*, which refer to the pores that are water-filled but cannot form a continuous path for ionic transport; (3) *Continuous water-filled pores*, which allow ionic transport. Since the water-filled pores are often small in size, the volume of small capillary pores and the pore entrapment  $\alpha_{en}$  of small capillary pores are the essential parameters for indicating the non-saturated ionic transport property.

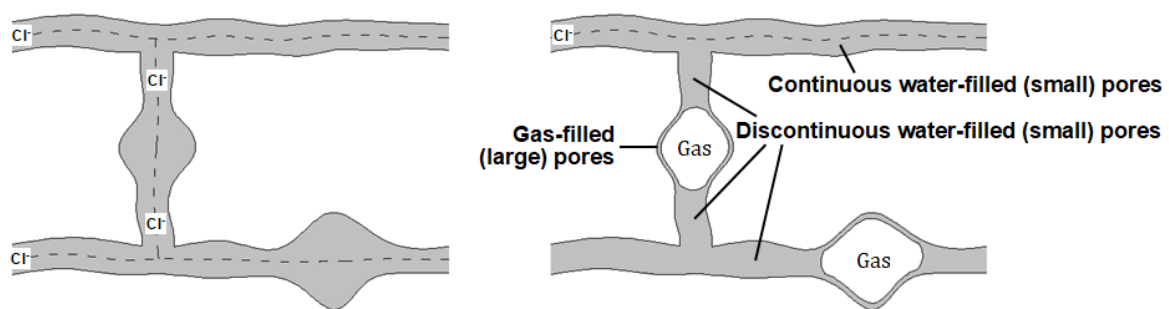


Fig. 3.11 Transport of chloride ions ( $Cl^-$ ) in saturated (left) and non-saturated (right) pore systems.

It is generally assumed that the ink-bottle pores remain filled with mercury after the 1<sup>st</sup> intrusion-extrusion cycle and no remaining mercury is expected when performing the 2<sup>nd</sup> cycle. Based on this assumption, mercury penetration with repeated intrusion-extrusion cycles can be effective to examine the ink-bottle effect. Moro et al. [2002] performed intrusion-extrusion cycles at pressures of 12.3, 25.6, 61.1 and 112.7 MPa. They found that each intrusion-extrusion cycle resulted in mercury entrapment. Zhou et al. [2010] carried out one hundred pressurization-depressurization cycles. In each cycle the pressure is first increased to  $P_n^{\text{in}}$  and then decreased to  $P_n^{\text{ex}}$ . Both pressures  $P_n^{\text{in}}$  and  $P_n^{\text{ex}}$  correspond to the same pore diameter by following the Washburn equation (Eq. (3.1)) with advancing and receding contact angles, respectively. Noteworthy, the measurement from Zhou et al. tends to underestimate throat pores and overestimate ink-bottle pores [Zhang et al. 2018].

In the present work the concept of intrusion-extrusion cycles will be further developed in order to better study the small (throat) pores and large (ink-bottle) pores. An alternative measurement, viz. IEC-MIP, will be described and evaluated in the following.

### 3.4 Intrusion-extrusion cyclic mercury porosimetry (IEC-MIP)

#### 3.4.1 Test sequence

Intrusion-extrusion cyclic mercury porosimetry (IEC-MIP) consists of a low pressure run from 0 to  $P_0$  (0.15 MPa) and step-by-step high pressure runs. The low pressure run is carried out in the same manner as that of standard MIP tests. For the step-by-step high pressure runs of IEC-MIP tests, an example is provided in Table 3.1, in which the 1<sup>st</sup> pressurization is divided into 19 steps and followed with the 2<sup>nd</sup> pressurization (20<sup>th</sup> step). Each high pressure step  $i$  ( $i = 1 \sim 20$ ) contains an intrusion procedure (from minimum  $P_0$  to  $P_i$ ) and an extrusion procedure (from  $P_i$  to  $P_0$ ), as indicated in Fig. 3.12a. The pressure  $P_i$  forces the mercury to intrude the pores with diameter  $d_i$  by following the Washburn equation (Eq. (3.1)).

*Table 3.1 Maximum applied pressure  $P_i$  and minimum intruded pore diameter  $d_i$  at each intrusion-extrusion step  $i$  ( $i=1 \sim 20$ ) in IEC-MIP tests (contact angle  $\theta_a = 138^\circ$  for intrusion). The 1<sup>st</sup> pressurization is divided into 19 steps*

Steps $i$	$P_i$ [MPa] ( $d_i$ [nm])	Steps $i$	$P_i$ [MPa] ( $d_i$ [nm])
1	3.4 (422.7)	11	77.7 (18.6)
2	5.6 (259.2)	12	95.7 (15.1)
3	10.4 (138.6)	13	109.9 (13.1)
4	15.8 (91.1)	14	117.8 (12.2)
5	20.8 (69.4)	15	126.3 (11.4)
6	25.6 (56.4)	16	135.4 (10.6)
7	31.5 (45.8)	17	166.8 (8.6)
8	33.9 (42.6)	18	178.7 (8.1)
9	41.6 (34.6)	19	210.0 (6.9)
10	58.9 (24.5)	20*	210.0 (6.9)

\* The intrusion procedure at step 20 represents the 2<sup>nd</sup> pressurization of MIP.

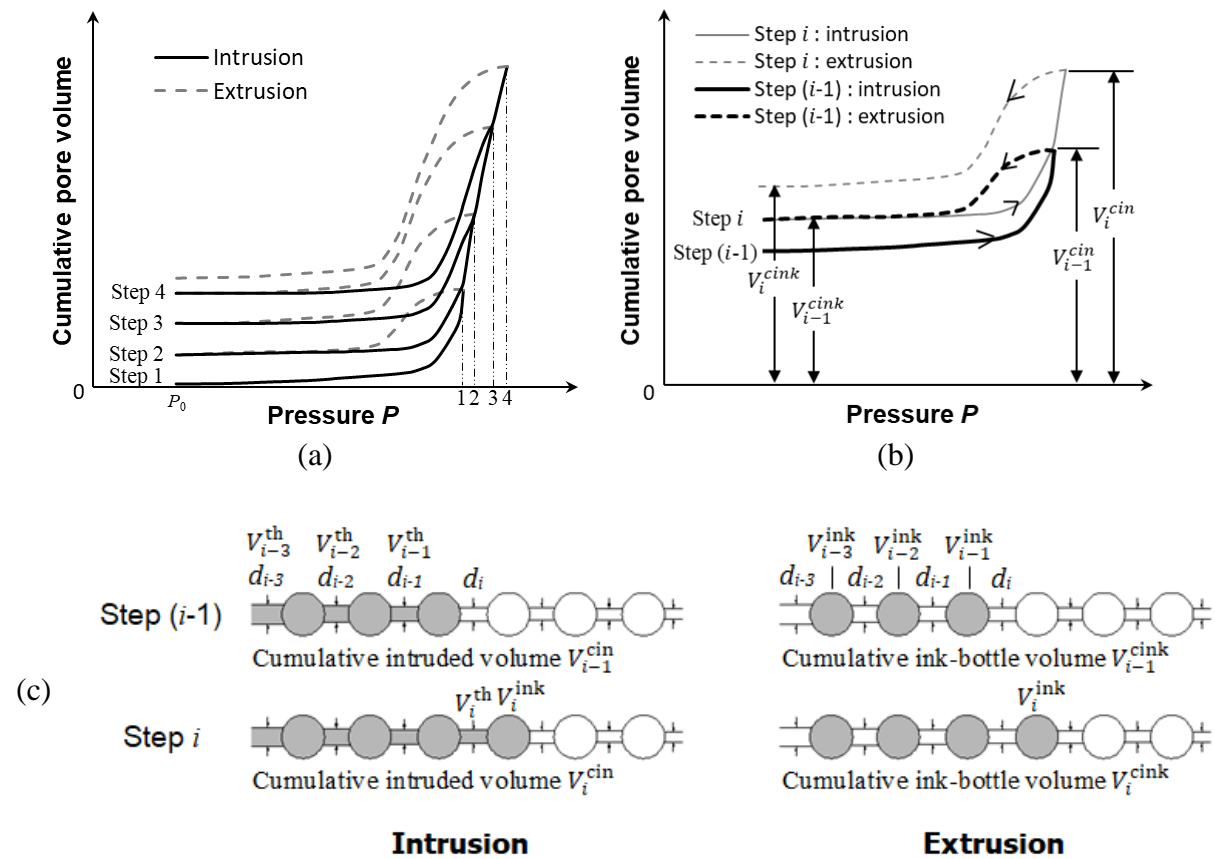


Fig. 3.12 (a) Illustration of IEC-MIP test sequence with repeated intrusion-extrusion cycles. (b) From step  $(i-1)$  to step  $i$ , the cumulative intruded volume increases from  $V_{i-1}^{cin}$  to  $V_i^{cin}$  and the cumulative ink-bottle volume increases from  $V_{i-1}^{cink}$  to  $V_i^{cink}$ . (c) Schematic representations of the mercury penetration in a pore system from step  $(i-1)$  to step  $i$ .

Figure 3.12a-c illustrates the IEC-MIP test sequence.

- At step 1, the pressure is first increased from the minimum  $P_0$  up to  $P_1$ , by which the throat pores (diameter  $d_1$  and volume  $V_1^{th}$ ) and their neighbouring ink-bottle pores (volume  $V_1^{ink}$ ) are filled with mercury. The pressure is then decreased from  $P_1$  down to the minimum  $P_0$ , by which mercury in the throat pores  $d_1$  is freely removed while mercury in the ink-bottle pores is entrapped.
- At step  $(i-1)$  ( $1 < i < 19$ ), the pressure is first increased from  $P_0$  to  $P_{i-1}$ , by which the throat pores (diameters  $d_1, d_2, \dots, d_{i-1}$ , volumes  $V_1^{th}, V_2^{th}, \dots, V_{i-1}^{th}$ ) and the ink-bottle pores (volumes  $V_1^{ink}, V_2^{ink}, \dots, V_{i-1}^{ink}$ ) are filled with mercury. The pressure is then decreased from  $P_{i-1}$  to  $P_0$ , by which mercury in the throat pores (diameters  $d_1, d_2, \dots, d_{i-1}$ ) is removed while mercury in the ink-bottle pores (volumes  $V_1^{ink}, V_2^{ink}, \dots, V_{i-1}^{ink}$ ) is entrapped.
- At step  $i$ , the pressure is first increased from  $P_0$  to  $P_i$ , by which the throat pores (diameters  $d_1, d_2, \dots, d_{i-1}, d_i$ , volumes  $V_1^{th}, V_2^{th}, \dots, V_{i-1}^{th}, V_i^{th}$ ) are filled with mercury. With the ink-bottle pores (volumes  $V_1^{ink}, V_2^{ink}, \dots, V_{i-1}^{ink}$ ) being mercury-

filled, the ink-bottle pores (volume  $V_i^{\text{ink}}$ ) connected with the throat pores  $d_i$  are further intruded with mercury. In the subsequent extrusion procedure from  $P_i$  to  $P_0$ , all throat pores are empty while the ink-bottle pores (volumes  $V_1^{\text{ink}}, V_2^{\text{ink}}, \dots, V_{i-1}^{\text{ink}}, V_i^{\text{ink}}$ ) are mercury-filled.

- At step 19, the pressure is increased the minimum  $P_0$  to the maximum  $P_{19}$ . All throat pores and ink-bottle pores are filled with mercury. In the subsequent extrusion procedure, all throat pores are empty while all ink-bottle pores remain mercury-filled.
- At the last step (step 20), the pressure is again increased up to the maximum ( $P_{20} = P_{19}$ ). Since all ink-bottle pores are mercury-filled, there is no ink-bottle effect when mercury penetrates the throat pores. The truthful throat pore size distribution is obtained.

Following the IEC-MIP test sequence, the mercury intrudes a pore system through throat pores to reach interior ink-bottle pores. From step  $(i-1)$  to  $i$ , the cumulative intruded volume increases by  $(V_i^{\text{cin}} - V_{i-1}^{\text{cin}})$  and the cumulative ink-bottle volume increases by  $(V_i^{\text{cink}} - V_{i-1}^{\text{cink}})$ , as indicated in Fig. 3.12b-c. When mercury penetrates the throat pores of a specific diameter  $d_i$ , the volume  $V_i^{\text{th}}$  of the throat pores and the volume  $V_i^{\text{ink}}$  of their neighbouring ink-bottle pores, as well as the pore entrapment  $\alpha_{\text{en},i}$ , can be expressed by Eqs. 3.7 (a), (b) and (c), respectively.

$$V_i^{\text{th}} = (V_i^{\text{cin}} - V_{i-1}^{\text{cin}}) - (V_i^{\text{cink}} - V_{i-1}^{\text{cink}}) \quad (3.7a)$$

$$V_i^{\text{ink}} = V_i^{\text{cink}} - V_{i-1}^{\text{cink}} \quad (3.7b)$$

$$\alpha_{\text{en},i} = V_i^{\text{ink}} / (V_i^{\text{th}} + V_i^{\text{ink}}) \quad (3.7c)$$

In the example shown in Table 3.1, the 1<sup>st</sup> pressurization is divided into 19 steps. An increase of the number of the total steps enables to obtain a more detailed picture of the ink-bottle pore geometry in porous systems.

### 3.4.2 Analysis of measurement data

The IEC-MIP shows a high reproducibility from measurements on five replicates (cement paste, w/c = 0.5, one-year-old). For any particular step  $i$  ( $i = 1 \sim 20$ ), the difference of the intruded volumes  $V_i^{\text{cin}}$  is within  $\pm 3\%$ . The difference of the total porosities  $\phi_t$  is within  $\pm 5\%$ .

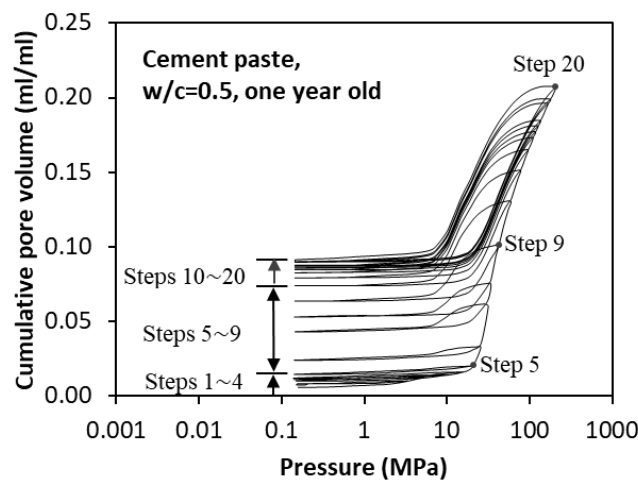
#### 3.4.2.1 Cumulative pore volume vs. pressure

Figure 3.13a gives an example of the cumulative pore volume obtained from IEC-MIP test. An intrusion-extrusion step  $i$  ( $i = 1 \sim 19$ ) always shows a hysteresis. The hysteresis, caused by ink-bottle effect, depends on the applied pressure and can be divided into three stages.

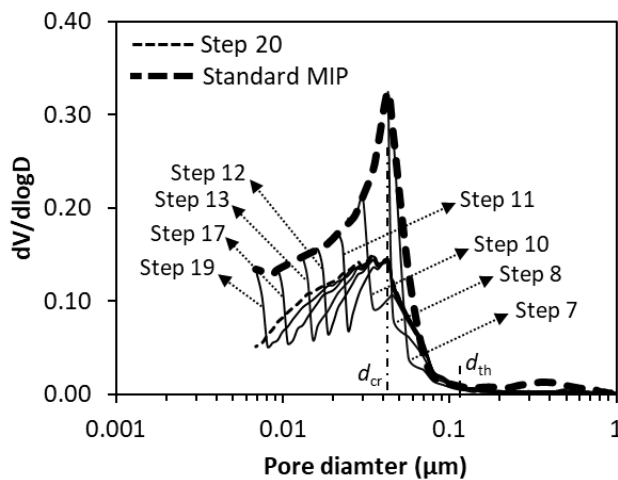
- 1) In the 1<sup>st</sup> stage (steps 1~4), mercury intrudes the surface of the specimen. Only a minor intrusion volume is detected.

- 2) In the 2<sup>nd</sup> stage (steps 5~9), the intruded volume increases abruptly when the threshold pores (diameter  $d_{th}$ ) are filled with mercury. Plenty of mercury is intruded within a narrow pore size range of 34.6~69.4 nm, but most of the intruded mercury is irreversibly entrapped. Obviously, the intruded pores are poorly connected.
- 3) In the 3<sup>rd</sup> stage (steps 10~20), after the critical pores (diameter  $d_{cr}$ ) are filled with mercury, a considerable amount of mercury continues to intrude the small pores. The majority of the intruded mercury is removable after the extrusion step. It is considered, therefore, that these small pores are highly interconnected.

Figure 3.13b shows the pore size distributions (PSD) obtained from the intrusion steps. For the sake of clarity, only eight intrusion steps are shown. By connecting the maximum points of the PSD curve at each step into a continuous curve, the PSD from standard MIP test can be simulated, as shown by the bold dotted line. No ink-bottle effect is observed in the intrusion-extrusion cycle at step 20. The PSD curve obtained from the 20<sup>th</sup> intrusion step, as indicated by the thin dotted line in Fig. 3.13b, represents the truthful size distribution of throat pores.



(a) Cumulative pore volume



(b) Differential pore size distribution at different intrusion steps

Fig. 3.13 Measurement data obtained by means of IEC-MIP tests.

3.4.2.2 Cumulative ink-bottle volume  $V_i^{cink}$

Figure 3.14 shows the cumulative ink-bottle volume  $V_i^{cink}$  as a function of the pore diameter measured by the IEC-MIP test. As expected, the  $V_i^{cink}$  increases with decreasing diameter of the pores intruded. At the smallest intrusion pore diameter, the  $V_i^{cink}$  value is equal to the ink-bottle porosity  $\phi_{ink}$  obtained from the standard MIP test, as indicated in Fig. 3.14.

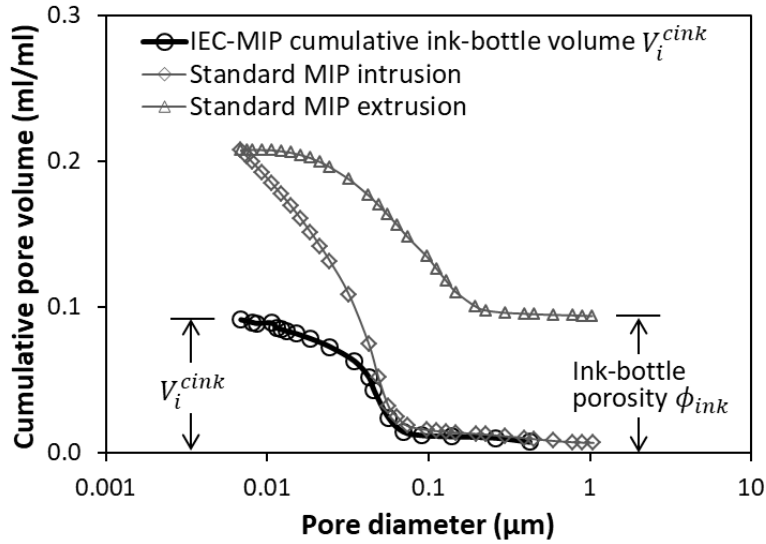


Fig. 3.14 Cumulative ink-bottle volume  $V_i^{cink}$  obtained from IEC-MIP tests and ink-bottle porosity  $\phi_{ink}$  obtained from standard MIP tests. Cement paste,  $w/c=0.5$ , one-year-old.

A differential curve of the  $V_i^{cink}$  is shown in Fig. 3.15. There is a main peak in the differential curve. The pore size corresponding to this peak is the critical diameter  $d_{cr}$ , above which a high ink-bottle volume is observed while below which comparatively low ink-bottle volume is observed.

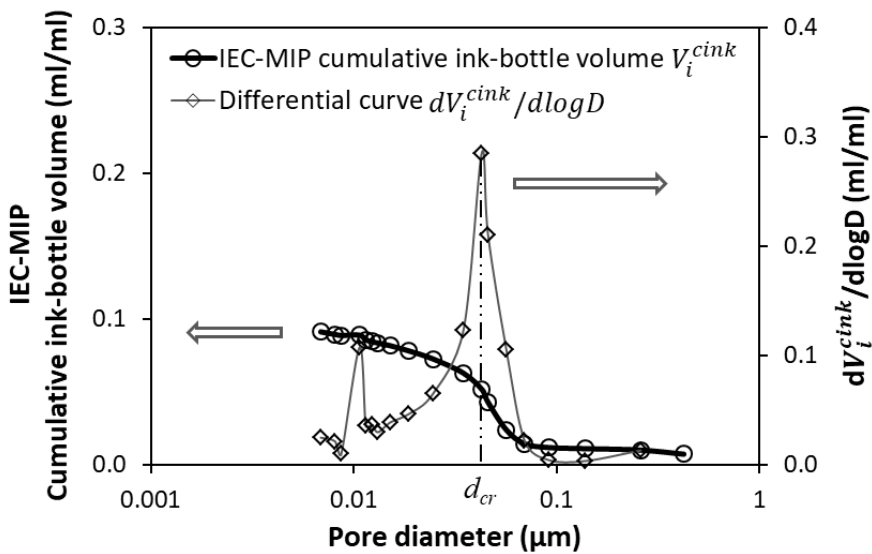


Fig. 3.15 Cumulative ink-bottle volume and its differential curve obtained from IEC-MIP test. Cement paste,  $w/c=0.5$ , one-year-old.

### 3.4.2.3 The distribution of pore entrapment $\alpha_{en}$ as a function of pore diameter $d$

A high ink-bottle volume does not necessarily ensure a strong ink-bottle effect in case the volume of throat pores is high. The term pore entrapment  $\alpha_{en}$  (defined by Eq. (3.6)) is adopted to indicate the ink-bottle effect. Based on the IEC-MIP tests and Eq. (3.7a-c), the distribution of pore entrapment  $\alpha_{en}$  as a function of pore diameter  $d_i$  can be determined. Figure 3.16a shows an example of the  $\alpha_{en}$ - $d$  plots when mercury penetrates the small capillary pores ( $d = 0.01 \sim 0.1 \mu\text{m}$ ).

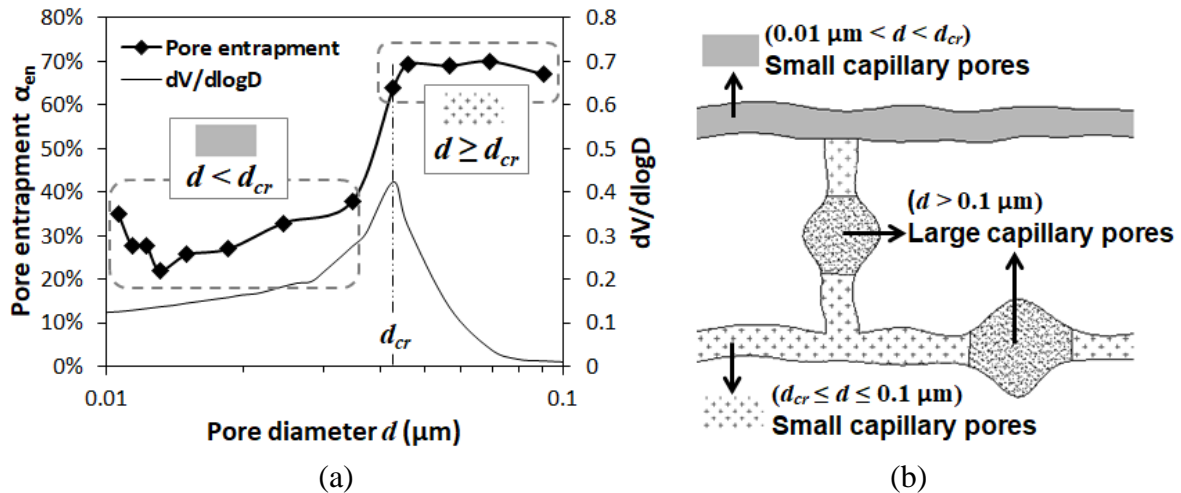


Fig. 3.16 (a) The  $\alpha_{en}$ - $d$  plots obtained from the IEC-MIP test of one-year-old cement paste ( $w/c = 0.5$ ).  $d_{cr}$  - critical pore diameter. (b) 2D representation of connections between small and large capillary pores based on the  $\alpha_{en}$ - $d$  plots shown in (a).

The  $\alpha_{en}$ - $d$  plots shown in Fig. 3.16a can be categorized into two groups according to the pore size  $d_i$  above or below the critical pore diameter  $d_{cr}$ .

- At  $d \geq d_{cr}$ , high  $\alpha_{en}$ -values ( $\approx 70\%$ ) are observed. This suggests that the small capillary pores ( $d_{cr} \leq d \leq 0.1 \mu\text{m}$ ) are highly connected with the large capillary pores ( $d > 0.1 \mu\text{m}$ ), as illustrated in Fig. 3.16b.
- At  $d < d_{cr}$ , low  $\alpha_{en}$ -values ( $\approx 30\%$ ) are observed. This suggests that the small capillary pores ( $0.01 \mu\text{m} < d < d_{cr}$ ) have little connection with the large capillary pores ( $d > 0.1 \mu\text{m}$ ) and instead they are highly interconnected, as illustrated in Fig. 3.16b.

The above analysis provides a basis for studying the continuity of water-filled pores in the porous system. At *high* water saturation levels, the gas phase tends to fill the large capillary pores (e.g.  $d > 0.1 \mu\text{m}$ ). The water-filled small pores ( $d_{cr} \leq d \leq 0.1 \mu\text{m}$ ) can readily become discontinuous, whereas the small pores ( $0.01 \mu\text{m} < d < d_{cr}$ ) can easily form continuous water-filled paths. At *low* water saturation levels, part of the small pores ( $0.01 \mu\text{m} < d < d_{cr}$ ) can be filled with the gas phase. However, the remaining smaller pores ( $0.01 \mu\text{m} < d < d_{cr}$ ) can still easily form continuous water-filled paths due to their high interconnectivity.

The distribution of pore entrapment, i.e.  $\alpha_{en}$ - $d$  plots, can be very different for different cementitious materials. More details will be presented in Chapter 4.

#### 3.4.2.4 Pore size distribution obtained from the 20<sup>th</sup> step of IEC-MIP test

Figure 3.17 shows the pore size distribution obtained from the intrusion-extrusion cycle at the 20<sup>th</sup> step of the IEC-MIP test. The data are taken from Fig. 3.13-left. The same contact angle (138°) is applied for both intrusion and extrusion procedures. The pore size distribution obtained from standard MIP test is also plotted for a comparison.

The extrusion curves from the standard MIP and the 20<sup>th</sup> step of IEC-MIP are almost overlapped. For the 20<sup>th</sup> intrusion-extrusion cycle, little mercury is entrapped. The hysteresis can be ascribed to the different contact angles between intrusion and extrusion. The 20<sup>th</sup> intrusion step, which has little ink-bottle effect, provides better estimates of the size distribution of small capillary pores (< 0.1  $\mu\text{m}$ ) than that obtained from the standard MIP test.

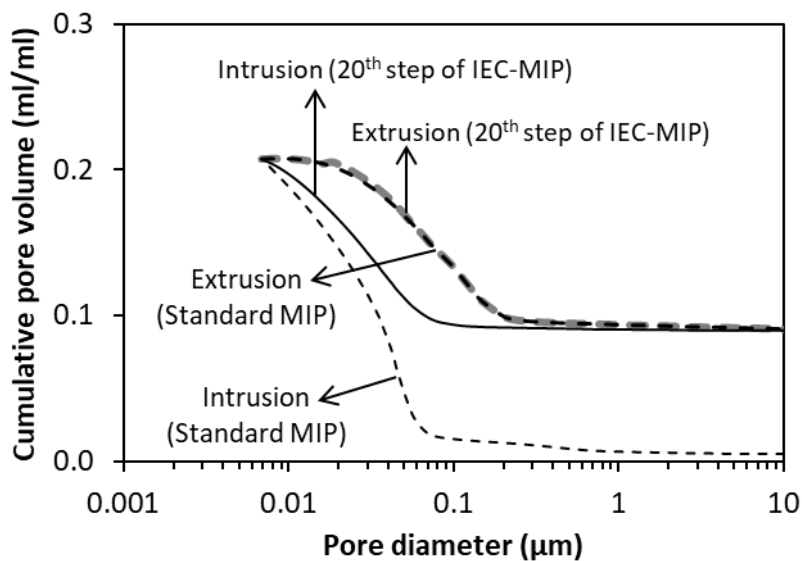


Fig. 3.17 Comparison of pore size distributions obtained from standard MIP test and from the intrusion-extrusion at the 20<sup>th</sup> step of IEC-MIP test. OPC paste,  $w/c = 0.5$ , one-year-old.

### 3.5 Conclusions

A novel measurement procedure, i.e. *intrusion-extrusion cyclic mercury porosimetry* (IEC-MIP), is proposed and evaluated. Compared to standard MIP tests, the IEC-MIP tests provide a more detailed picture of the *size distribution* and *connectivity* of small capillary pores. Both are essential factors influencing the moisture distribution and ionic transport in unsaturated pore systems.

## Chapter 4

# Analysis of Pore Structure in Blended Cement Pastes

---

### 4.1 Introduction

Ionic transport in unsaturated porous systems is controlled by the *continuous water-filled pores* (see Fig. 3.11-right). The continuous water-filled pores are highly influenced by the amount of small capillary pores and their connectivity with large capillary pores. Both can be well-examined by the IEC-MIP tests described in Chapter 3. The small pores and the large pores, as well as their connectivities, will change when OPC is partially replaced by SCMs.

In this chapter (see Fig. 4.1) the IEC-MIP tests are adopted to analyze the pore structures of cementitious pastes. Various pore features, such as porosity, pore size and pore connectivity, will be measured. The influencing factors, including w/b ratio (0.4~0.6), curing age (28~370 days) and SCMs (FA, BFS and LP), will be discussed. The pore structure determines the moisture distribution and chloride transport properties in cementitious materials.

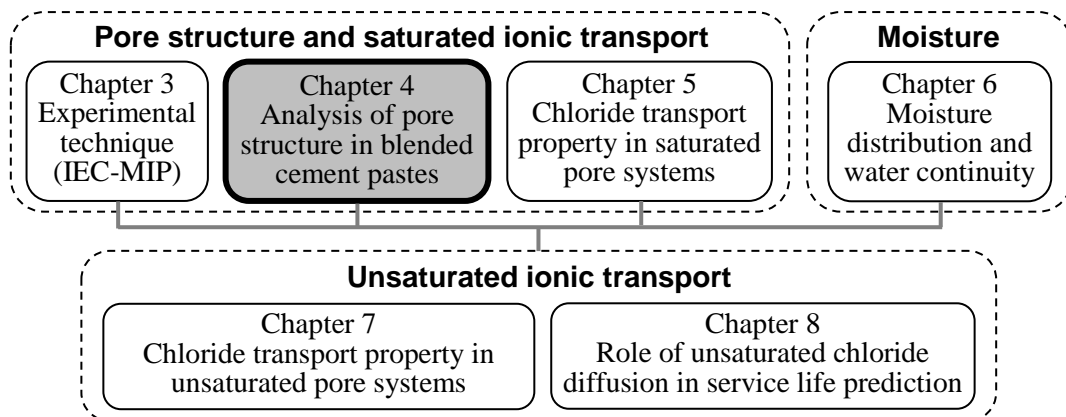


Fig. 4.1 Main chapters of the thesis.

## 4.2 Experimental program

### 4.2.1 Raw materials

Given that the paste matrix contributes most to the porosity of concrete [Kolias et al. 2005], this chapter focuses on analyzing the pore structure of paste specimens. The raw materials used for the specimens were OPC (CEM I 42.5N) and SCMs (low calcium FA, BFS and LP). The chemical compositions and the particle size distributions of the raw materials are given in Table 4.1 and Fig. 4.2, respectively. The mean particle sizes, measured by laser diffraction, were 24.1  $\mu\text{m}$  for OPC, 13.5  $\mu\text{m}$  for BFS, 25.0  $\mu\text{m}$  for FA and 33.5  $\mu\text{m}$  for LP. Based on X-ray diffraction the crystalline fraction of FA was about 42 wt.%, compared to only 2 wt.% in the BFS. The main component of the LP,  $\text{CaCO}_3$ , was around 98 wt.%.

Table 4.1 Chemical composition of OPC and SCMs by X-ray fluorescence (g/100g)

Item	OPC	FA	BFS	LP
CaO	64.495	5.537	41.398	-
SiO <sub>2</sub>	18.875	50.554	34.015	0.737
Al <sub>2</sub> O <sub>3</sub>	4.481	30.743	11.117	0.180
Fe <sub>2</sub> O <sub>3</sub>	3.686	6.301	0.529	0.073
MgO	2.012	1.009	8.284	0.523
K <sub>2</sub> O	0.508	1.109	0.398	0.026
Na <sub>2</sub> O	0.341	0.284	0.205	0.010
SO <sub>3</sub>	2.625	0.785	2.430	0.082
TiO <sub>2</sub>	0.319	2.362	1.027	0.020
CaCO <sub>3</sub>	1.185	-	-	98.316
Others	3.824	1.316	0.597	0.033
LOI	3.04	2.66	0.38	43.26
Specific gravity (g/cm <sup>3</sup> )	3.12	2.26	2.87	3.08

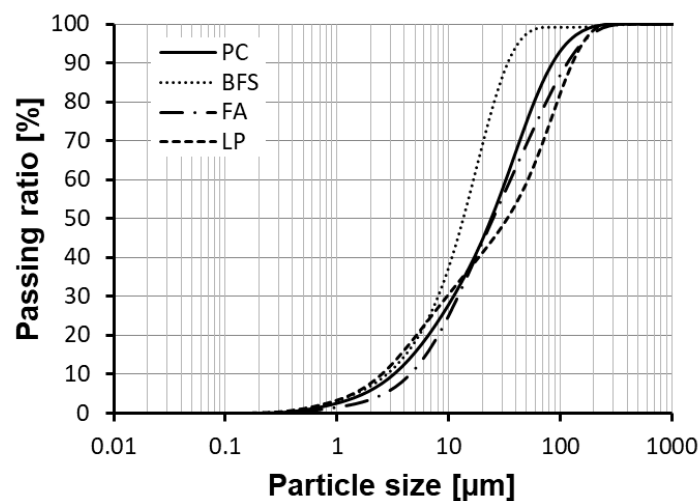


Fig. 4.2 Particle size distributions of various powders by laser diffractometry.

### 4.2.2 Sample preparation

Mixture compositions of paste samples are listed in Table 4.2. The blended mixtures were made with often-adopted replacement levels of 30% FA, 70% BFS and 5% LP. The powders and deionized water were mixed at low speed for 1 min and at high speed for another 2 min. The fresh pastes were poured into plastic bottles. The bottles were vibrated continuously to remove air bubbles and sealed with lids thereafter. To avoid bleeding, the paste samples were rotated for one day before placing them in the curing room at  $20 \pm 0.1$  °C. At the age of 28, 105, 182 and 370 days, the samples were taken out of the plastic bottles and crushed into small pieces (around  $1 \text{ cm}^3$ ). The pieces were immersed in liquid nitrogen at  $-195$  °C for 5 minutes, and then placed in a freeze-dryer with  $-24$  °C and under vacuum at 0.1 Pa. After the water loss was below 0.01% per day the paste pieces were ready for pore structure measurements.

Table 4.2 Mixtures for the paste samples

Binders	Raw materials and replacement (weight percentage)				w/b
	OPC	FA	BFS	LP	
P4	100%	-	-	-	0.4
P5	100%	-	-	-	0.5
P6	100%	-	-	-	0.6
PF5	70%	30%	-	-	0.5
PFL5	65%	30%	-	5%	0.5
PB4	30%	-	70%	-	0.4
PB5	30%	-	70%	-	0.5
PB6	30%	-	70%	-	0.6
PBL5	25%	-	70%	5%	0.5

### 4.2.3 Pore structure measurement

The pore structures of various paste specimens were measured by the IEC-MIP tests described in Chapter 3. The measurements were performed with Micromeritics PoreSizer 9320, which has a capacity of 210 MPa. The obtained pore structure parameters were porosity, pore size distribution, critical pore diameter, threshold pore diameter, pore connectivity and pore entrapment. All parameters were determined based on three parallel measurements.

## 4.3 Results and discussion

### 4.3.1 Porosity

#### 4.3.1.1 Total porosity $\phi_t$ in OPC pastes

The total porosity  $\phi_t$  of paste specimens was determined as the total intruded volume of mercury at the maximum pressure (210 MPa). For a specimen with hydration age  $t=0$ , the  $\phi_t$ -value, i.e. non-solid phase and no air volume considered, was estimated as:

$$\phi_t(t = 0) = \frac{w/b}{\frac{w}{b} + \frac{m_b}{\rho_b} + \frac{m_c}{\rho_c}} \tag{4.1}$$

where  $w/b$  is the water-to-binder ratio;  $m_c$  and  $m_b$  are the mass percentage of Portland cement and blended cement, respectively;  $\rho_c$  and  $\rho_b$  are the specific gravity of Portland cement and blended cement, respectively. For pure Portland cement pastes,  $m_b=0$ .

Figure 4.3-left shows the total porosity  $\phi_t$  of OPC pastes with  $w/b$  ratios of 0.4, 0.5 and 0.6. The  $\phi_t$ -value decreases sharply in the first 28 days, followed by a gradual slow decrease. An increase of the  $w/b$  ratio of 0.1 results in an increase of the  $\phi_t$ -value of around 5.4~7.2%, depending on the age (28~370 days). A lower  $w/b$  ratio or a higher age leads to a significant decrease of the effective porosity  $\phi_e$  (see Fig. 4.4-left). Both  $w/b$  ratio and age, however, play only a minor role in the ink-bottle porosity  $\phi_{ink}$  (see Fig. 4.4-right).

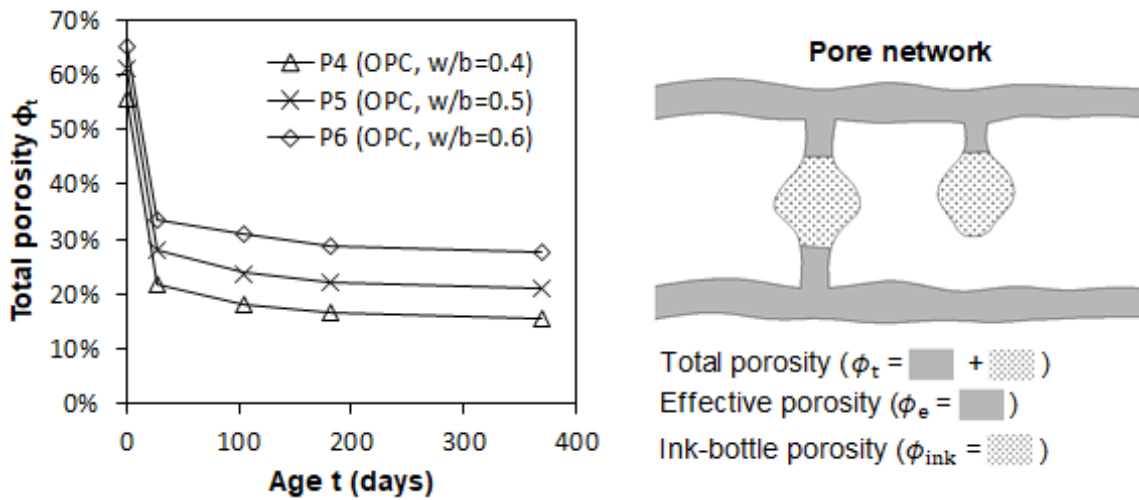


Fig. 4.3 (left) Total porosity of OPC pastes at different ages. (right) Schematic representation of pore network.

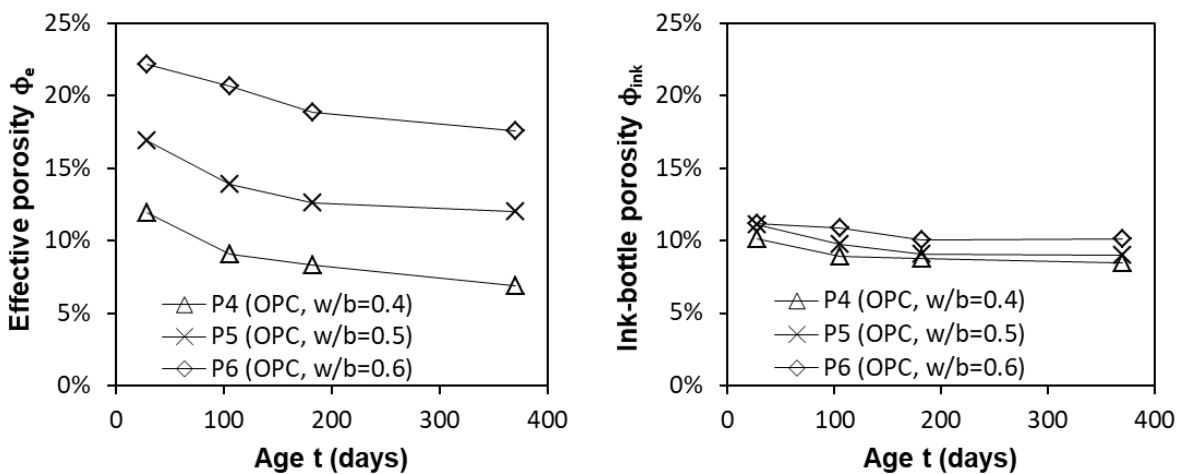


Fig. 4.4 Effective porosity (left) and ink-bottle porosity (right) in OPC pastes at different ages.

#### 4.3.1.2 Effect of reactive SCMs on total porosity (binary cement)

The effects of reactive SCMs, FA or BFS, on the total porosity  $\phi_t$  are shown in Fig. 4.5a-b. The initial total porosity ( $t=0$ ) was obtained by using Eq. (4.1).

Incorporating 30% FA (i.e. PF5) results in a higher total porosity  $\phi_t$  than that of the reference cement paste (i.e. P5) at all ages (see Fig. 4.5a). This is in agreement with the results reported by Chindaprasirt et al. [2005]. Partial replacement of OPC by FA leads to a relatively higher w/c ratio and lower gel-space ratio, resulting in a higher porosity [Chindaprasirt et al. 2009]. Herein, the gel-space ratio refers to the quotient of the volume of hydration products over the volume of both hydration products and capillary pores.

The paste containing 70% BFS (i.e. PB5) shows a lower total porosity  $\phi_t$  than the reference OPC paste P5 at all ages (see Fig. 4.5b). This suggests a strong chemical reactivity of the BFS used in this work. The strong reactivity of BFS is attributed to its fine particle size (see Fig. 4.2), as well as to its considerable amount of amorphous phases. The  $\phi_t$ -value of the BFS-blended pastes (PB4, PB5 and PB6) drops sharply in the first 28 days, followed by a clear decreasing trend until 105 days and a slow decline thereafter. For a given age a paste with lower w/b ratio shows a lower  $\phi_t$ . The decrease of the  $\phi_t$ -value with decreasing w/b ratio is particularly pronounced when the w/b ratio decreases from 0.5 (PB5) to 0.4 (PB4).

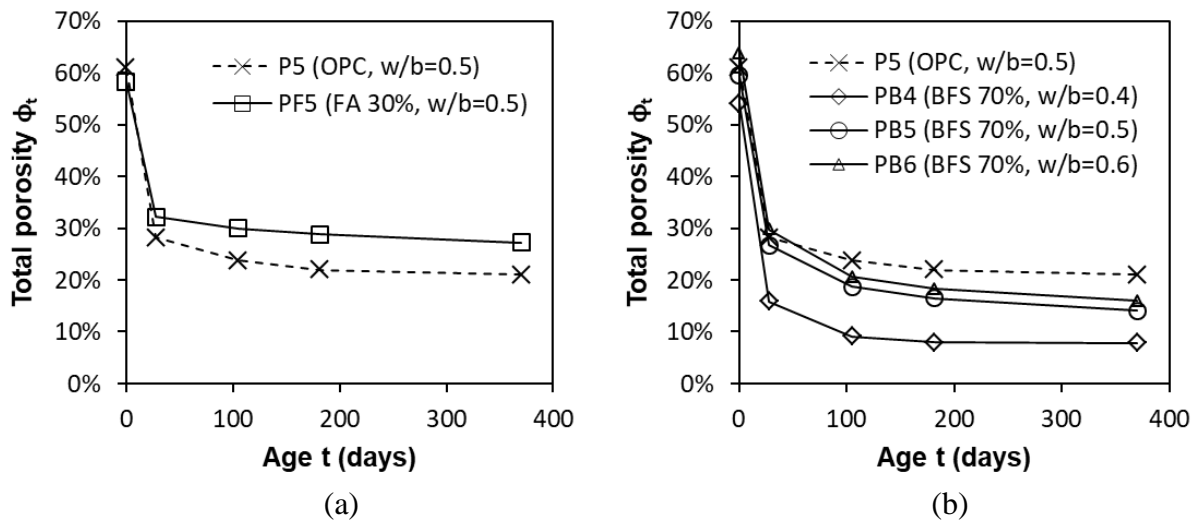


Fig. 4.5 Effect of FA (a) and BFS (b) on the total porosity of paste specimens.

#### 4.3.1.3 Effect of LP on total porosity (ternary cement)

Figure 4.6a shows the total porosity  $\phi_t$  of LP-filled ternary cement pastes (PFL5 and PBL5) and of LP-free binary cement pastes (PF5 and PB5). It is clear that the addition of LP 5% increases the total porosity. Such porosity increase can be ascribed to the dilution effect of LP in the paste systems. The porosity difference is noted as  $\Delta\phi_F$  between PFL5 and PF5, and as  $\Delta\phi_B$  between PBL5 and PB5. As seen from Fig. 4.6a, the  $\Delta\phi_F$  value is much smaller than the  $\Delta\phi_B$  value at all ages. This suggests a *synergistic effect* when LP is used in combination with FA. Such synergistic effect promotes the hydration of LP and can be ascribed to the high alumina content of FA grains (30.7 wt.%).

The presence of alumina-rich FA lowers the sulphate to alumina ratio and, therefore, impairs the transformation of ettringite (AFt) to monosulphate (Ms). AFt is more bulky than Ms:  $707 \text{ cm}^3/\text{mol}$  vs.  $309 \text{ cm}^3/\text{mol}$  at  $25 \text{ }^\circ\text{C}$  [Lothenbach et al. 2008]. The main component of LP is  $\text{CaCO}_3$  (CC). Combining FA with LP tends to form the alumina-carbonate compounds, i.e. hemicarboaluminate (Hc) or monocarboaluminate (Mc) [Kuzel 1991], as:



The Differential Thermogravimetric analysis (DTG) shown in Fig. 4.6b confirms the phase changes when LP is present, and also proves a much higher AFt content in PFL5 than in PBL5. These observations agree with the findings from de Weerd et al. [2011a].

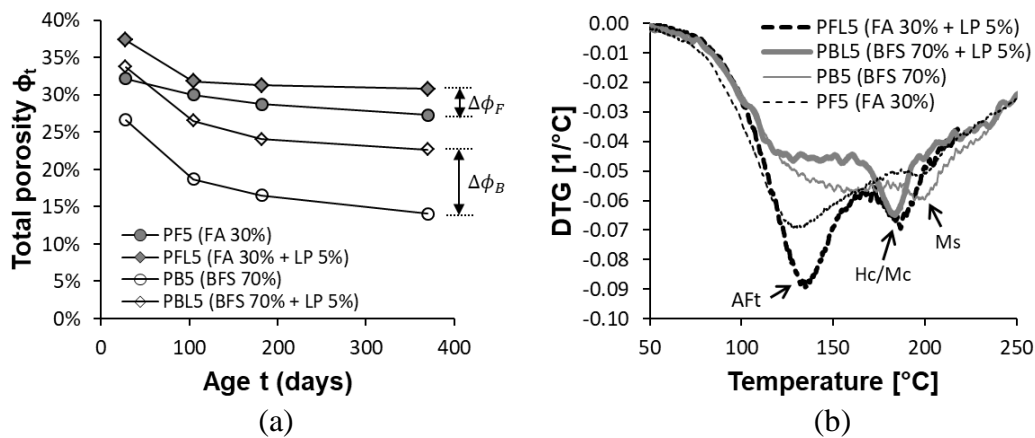


Fig. 4.6 Effect of LP on total porosity (a) and on Differential Thermogravimetric analysis (DTG) (b) in ternary pastes ( $w/b=0.5$ , age=370 days).

#### 4.3.1.4 Effect of SCMs on effective porosity

Figure 4.7 shows the relationships between effective porosities  $\phi_e$  and total porosities  $\phi_t$  in the OPC pastes and SCMs-blended pastes.

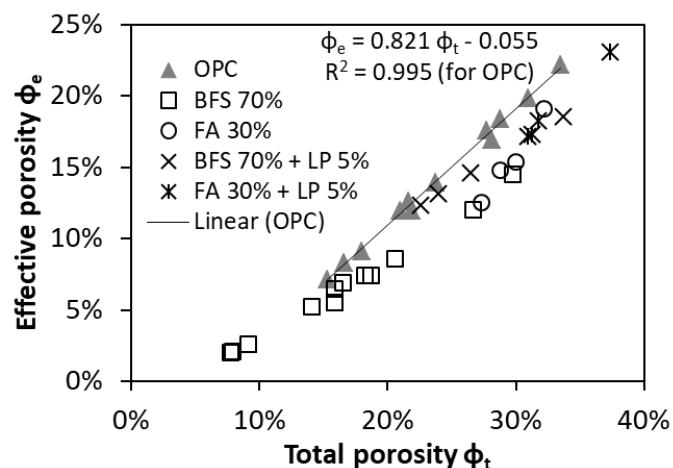


Fig. 4.7 The  $\phi_t$ - $\phi_e$  plots in the OPC and SCMs-blended pastes (age 28~370 days).

As indicated in Fig. 4.7 the effective porosity  $\phi_e$  tends to increase with increasing total porosity  $\phi_t$ . A nearly perfect linear  $\phi_t$ - $\phi_e$  relationship ( $R^2 = 0.9953$ ) can be obtained for the OPC pastes. For a given total porosity  $\phi_t$  the pastes containing BFS 70% or FA 30% exhibit lower effective porosities  $\phi_e$  (in other words, higher ink-bottle porosities  $\phi_{ink}$ ) than the OPC pastes. The LP-filled ternary paste (e.g. BFS 70% + LP 5%) shows a higher effective porosity  $\phi_e$  than the LP-free binary paste (e.g. BFS 70%) of the same total porosity  $\phi_t$ .

### 4.3.2 Pore size distribution

The IEC-MIP measurements consist of 20 intrusion-extrusion cycles (see Table 3.1). The first 19 intrusion-extrusion cycles show hysteresis (i.e. ink-bottle effect), which can be used to examine the connectivity between small pores and large pores, as will be presented in Section 4.3.4. The 20<sup>th</sup> intrusion-extrusion cycle shows little ink-bottle effect, and the 20<sup>th</sup> intrusion step is adopted to determine the (small) pore size distribution of cementitious pastes, as presented in the following.

#### 4.3.2.1 Pore size distribution of OPC pastes

Figure 4.8 shows the pore size distribution of OPC pastes. A higher w/c ratio from 0.4 to 0.6 substantially increases the effective porosity  $\phi_e$  at 28 days from 12.8% to 23.2% (see Fig. 4.8-left), but slightly increases the ink-bottle porosity  $\phi_{ink}$  at 28 days from 9.9% to 11.1%. When cement hydration continues from 28 to 370 days, the effective porosity  $\phi_e$  of the paste P4 decreases remarkably from 12.8% to 6.7% (see Fig. 4.8-right), while the ink-bottle porosity  $\phi_{ink}$  decreases slightly from 9.9% to 8.4%.

It is concluded that both w/b ratio and age influence the total porosity of OPC pastes ( $\geq 28$  days) *mainly* by altering the effective porosity, i.e. by changing the amount of small continuous pores ( $< 0.2 \mu\text{m}$ ).

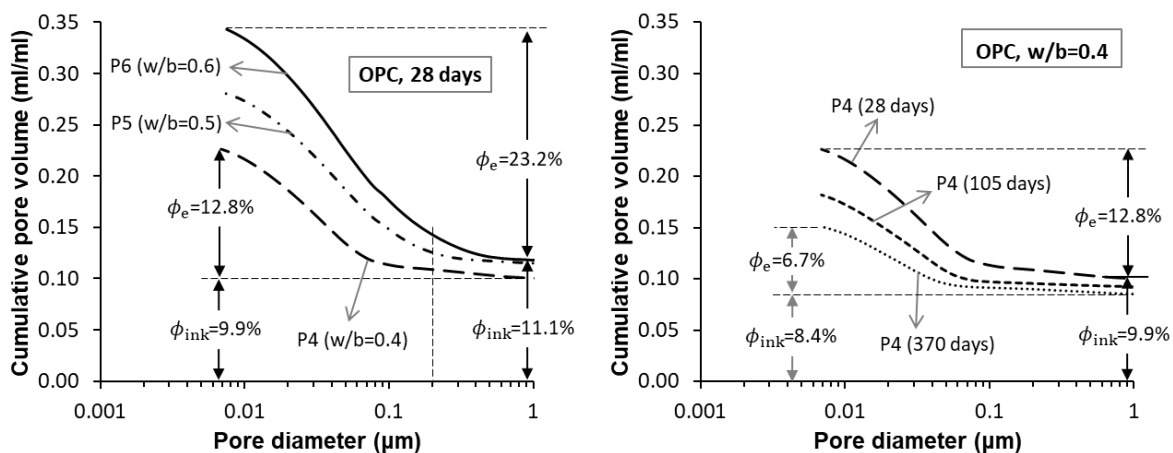


Fig. 4.8 Pore size distribution of OPC pastes obtained from the 20<sup>th</sup> intrusion step of IEC-MIP tests (pressure Table 3.1). (left) Effect of w/b ratio: 0.4, 0.5 and 0.6; (right) Effect of curing age: 28, 105 and 370 days.  $\phi_e$ -effective porosity;  $\phi_{ink}$ -ink-bottle porosity.

### 4.3.2.2 Effect of SCMs on pore size distribution

Figure 4.9 shows the effects of SCMs on the pore size distribution of cementitious pastes. The paste specimens were one-year-old and with the same w/b ratio of 0.5.

- Compared to the OPC paste P5, the addition of 70% BFS (PB5) results in a decrease of the effective porosity  $\phi_e$  by 6.0%, with the ink-bottle porosity  $\phi_{ink}$  almost unchanged. The decrease of the effective porosity  $\phi_e$  is caused by a decrease of small pores ( $< 0.08 \mu\text{m}$ ).
- Compared to the OPC paste P5, the addition of 30% FA (PF5) leads to a substantial increase of the ink-bottle porosity, i.e.  $\phi_{ink}=9.0\%$  (P5) vs.  $\phi_{ink}=14.7\%$  (PF5), with the effective porosity changing little, i.e.  $\phi_e=11.7\%$  (P5) vs.  $\phi_e=12.2\%$  (PF5). The increase of the ink-bottle porosity  $\phi_{ink}$ , mainly a result of the increase of large pores ( $> 0.08 \mu\text{m}$ ), may be explained by the presence of the hollow voids within the original boundary of the FA particles. Note that these hollow voids do not represent the originally water-filled spaces between cement grains, the accepted concept of the origin of “capillary pores” [Diamond 1999].
- Compared to the paste PF5, further addition of 5% LP (PFL5) increases the effective porosity  $\phi_e$ , but has little influence on the ink-bottle porosity  $\phi_{ink}$ . The increase of the effective porosity  $\phi_e$  is attributable to the increase of small pores ( $< 0.2 \mu\text{m}$ ).

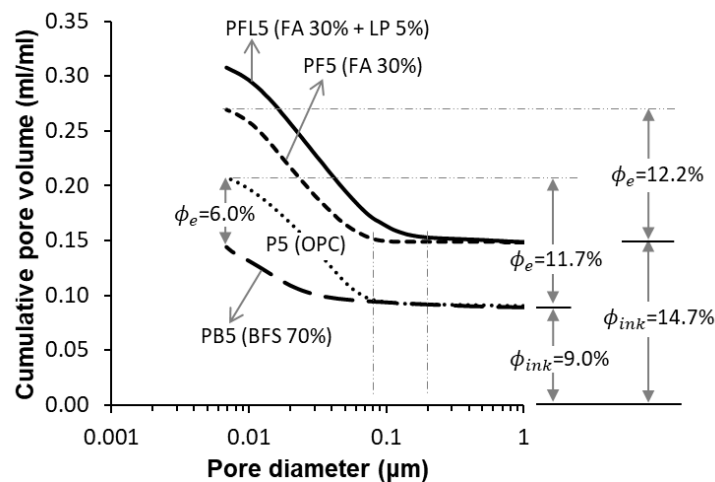


Fig. 4.9 Effect of SCMs on the pore size distribution of cementitious pastes (one-year-old, w/b = 0.5) obtained from the 20<sup>th</sup> intrusion step of IEC-MIP tests (pressure Table 3.1).

$\phi_e$ -effective porosity;  $\phi_{ink}$ -ink-bottle porosity.

### 4.3.3 Critical pore diameter $d_{cr}$ and threshold pore diameter $d_{th}$

#### 4.3.3.1 Critical pore diameter $d_{cr}$ in OPC pastes

The critical pore diameter  $d_{cr}$  is determined as the pore size corresponding to the peak of the differential pore size distribution curve, as illustrated already in Fig. 3.7-right. It is generally assumed that the mercury can penetrate through the specimen once the pressure corresponding to the critical pores is applied.

Figure 4.10 shows the critical pore diameters  $d_{cr}$  in OPC pastes with w/c ratios of 0.4, 0.5 and 0.6. The w/c ratio has a great influence on the  $d_{cr}$ -value at 28 days. With increasing age the  $d_{cr}$ -value tends to be less dependent on the w/c ratio. The three solid lines, obtained from regression analyses on the measured data, tend to intersect at one point (4 years, 22 nm). Obviously, if cement hydration continues up to a high degree, the critical pore diameter  $d_{cr}$  would reach a *constant* value of approximately 22 nm, regardless of the w/c ratio (0.4~0.6). Such constant critical pore diameter  $d_{cr}$  indicates the *characteristic pore size* in the clusters of hydrated cement gels.

The data from the literature provide a characteristic pore size of the same magnitude. By applying nuclear magnetic resonance, Halperin et al. [1994] reported that the pore diameters in fully hydrated cement pastes fall into 20~25 nm. Odler and R blier [1985] found the  $d_{cr}$ -value of mature cement pastes between 20~25 nm for w/c ratios from 0.22 to 0.52.

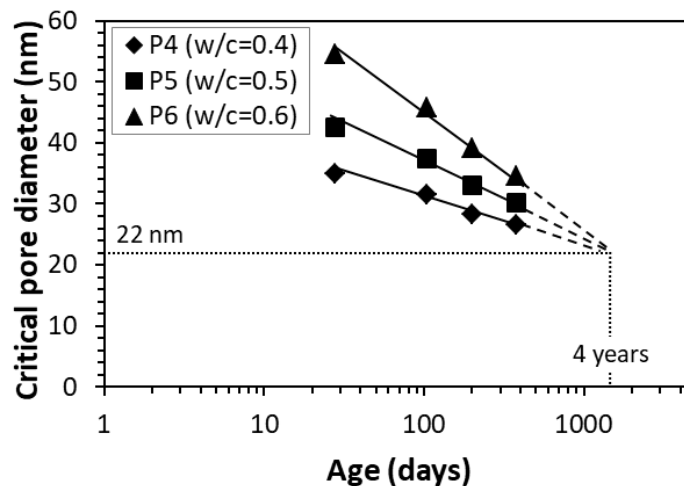


Fig. 4.10 Critical pore diameter of OPC pastes at different ages, w/c = 0.4, 0.5 and 0.6.

Three assumptions are made in order to explain the little dependency of the  $d_{cr}$ -value on the w/b ratios in mature cement pastes. *First*, the hydration products preferably precipitate in the vicinity of the dissolving cement grains. *Second*, both dissolution and growth process of the cement grains are assumed to occur concentrically until contact with each other. *Third*, the clusters of hydration products have a constant gel porosity.

The changing  $d_{cr}$ -value in a hydrating cement paste with increasing degree of cement hydration is illustrated in Fig. 4.11 (I-IV).

- I. When cement grains are mixed with water, the degree of cement hydration is initially zero ( $\alpha = 0$ ). In the hydrating system, only large capillary pores are present and they are all interconnected. The  $d_{cr}$ -value is determined by the distance between the cement grains during mixing. A higher w/c ratio thus results in a higher  $d_{cr}$ -value.
- II. At the early hydration stage, e.g.  $\alpha = 10\%$ , a small amount of hydrates is produced. There is limited contact between the hydrating cement grains. The large capillary pores can still form an interconnected network. The  $d_{cr}$ -value, still relying on the w/c ratio, will decrease continuously with the growth of hydrating cement grains.

- III. With further cement hydration, up to  $\alpha = 50\%$ , a large number of contact area is formed, either segmenting or clogging the large capillary pores. The  $d_{cr}$ -value refers to a particular size of the small capillary pores through which the majority of the large capillary pores can be connected. Since the small capillary pores represent the void space in the clusters of hydration products, the  $d_{cr}$ -values of cement pastes shall be less dependent on the w/c ratio.
- IV. For a mature cement paste, e.g.  $\alpha = 90\%$ , nearly all the hydrated cement grains are in good contact with neighbor particles. In an MIP test the main peak of the pore size distribution curve is created by the most frequently occurring pore size in the outer product zones, which is noted as the *characteristic pore size* for the void space formed in the clusters of hydration products and is independent of the w/c ratio.

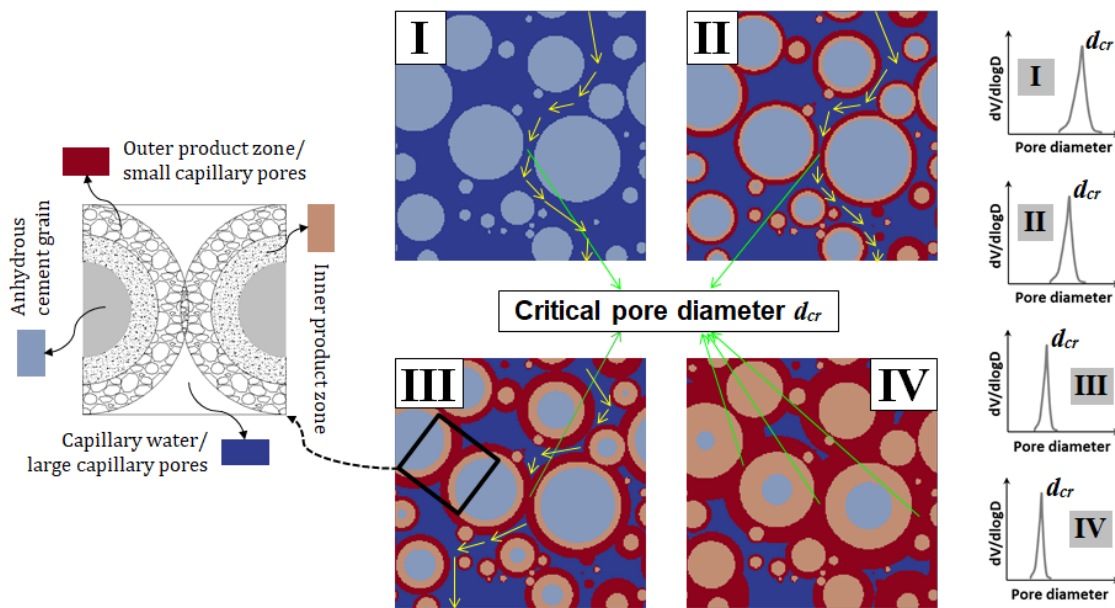


Fig. 4.11 Changes (decrease) of critical pore diameter  $d_{cr}$  with degree of cement hydration  $\alpha$ : (I)  $\alpha=0$ ; (II)  $\alpha=10\%$ ; (III)  $\alpha=50\%$ ; (IV)  $\alpha=90\%$ .

#### 4.3.3.2 Critical pore diameter $d_{cr}$ in blended pastes (FA, BFS and LP)

Compared to the reference OPC paste P5, the addition of FA decreases the critical pore diameter  $d_{cr}$  (see Fig. 4.12-left). The LP-filled paste (i.e. PFL5) shows a larger  $d_{cr}$  than the LP-free paste (i.e. PF5) at all ages (see Fig. 4.12-left). The  $d_{cr}$  in the BFS-blended pastes (see Fig. 4.12-right) is much smaller than that in the OPC paste P5 (see Fig. 4.12-left).

As indicated in Fig. 4.12-right, with progress of hydration the critical pore diameters  $d_{cr}$  of the BFS-blended pastes, regardless of the w/b ratio, tend to intersect at one point (7.5 nm, 14 years). The constant  $d_{cr}$ -value (7.5 nm) is associated with the constant packing density of the products formed due to hydrated slag. In the presence of BFS, the CH reacts with silica and transforms into secondary C-S-H gels, resulting in a higher packing density of hydration products compared to that in pure OPC pastes, i.e. 7.5 nm for BFS binder (Fig. 4.12b) vs. 22 nm for OPC binder (Fig. 4.10).

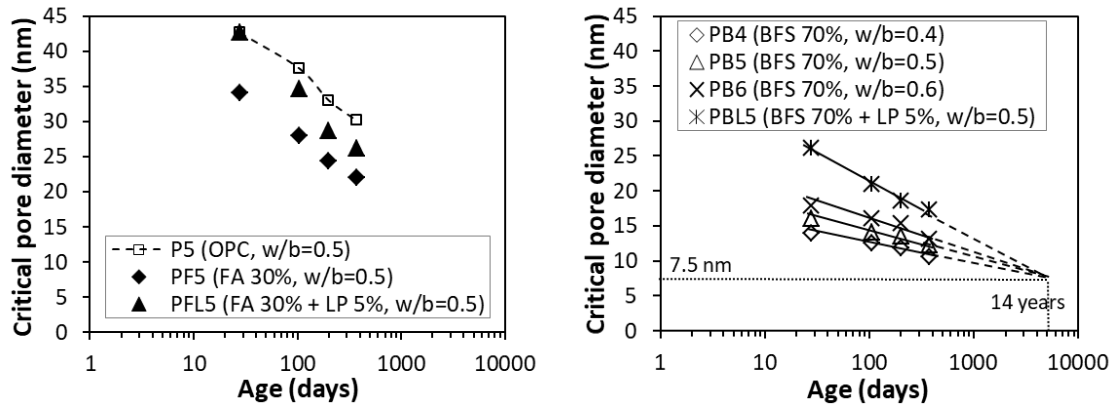


Fig. 4.12 Effects of FA and/or LP on the critical pore diameter of cementitious pastes (left) and effects of BFS and/or LP on the critical pore diameter of cementitious pastes (right).

4.3.3.3 Threshold pore diameter  $d_{th}$  in cementitious pastes

The threshold pore diameter  $d_{th}$  is the pore size below which the mercury intrusion increases abruptly, as illustrated already in Fig. 3.7-right. Figure 4.13 shows the  $d_{th}$  in various cementitious pastes. The  $d_{th}$ -values differ significantly, ranging from around 30 nm to more than 1000 nm. A lower w/b ratio results in a smaller  $d_{th}$  (Fig. 4.13-left). For a given w/b ratio the  $d_{th}$  decreases with age (Fig. 4.13-right). Compared to the OPC paste P5 of a particular age, the addition of BFS decreases the  $d_{th}$ , whereas the addition of FA and/or LP increases the  $d_{th}$  (Fig. 4.13-right).

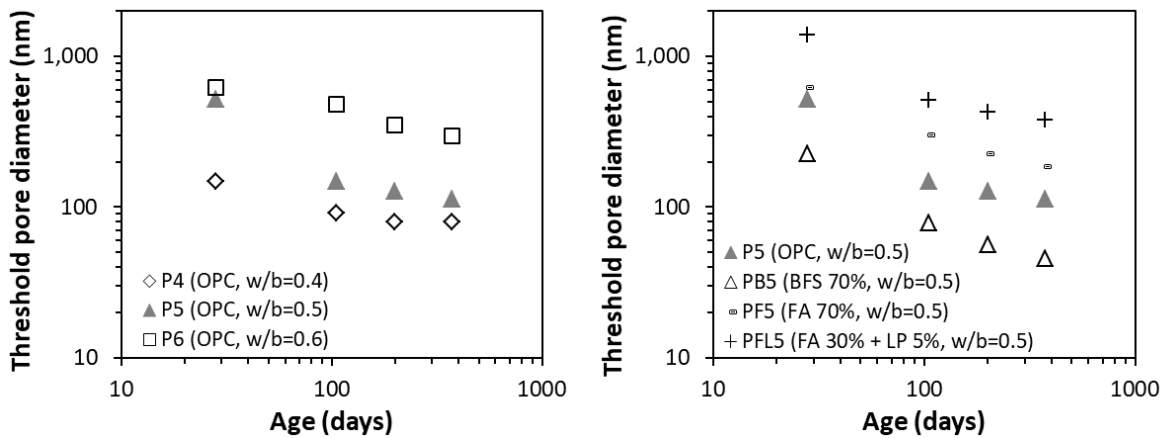


Fig. 4.13 Threshold pore diameters  $d_{th}$  in OPC pastes (left) and blended pastes (right).

4.3.4 Pore connectivity and distribution of pore entrapment

Pore connectivity  $\eta_p$ , a parameter representing the connectivity of pores of the entire pore structure, is commonly considered to play a significant role in the ionic transport in *saturated* porous systems. However, the distribution of pore entrapment  $\alpha_{en}$  as a function of pore diameter  $d$  enables a better understanding of the ionic transport in *unsaturated* porous systems, as noted already in Section 3.4.2.3. The pore connectivity  $\eta_p$  and pore entrapment ( $\alpha_{en}$  vs.  $d$ ) were determined from IEC-MIP measurements. Both results are presented in the following.

4.3.4.1 Pore connectivity  $\eta_p$  of cementitious pastes

Figure 4.14 shows the pore connectivity  $\eta_p$  in OPC pastes. A higher age or a lower w/b ratio results in a lower pore connectivity  $\eta_p$ . The  $\eta_p$ -value decreases slowly after 28 days, especially for the high w/b ratio cement pastes.

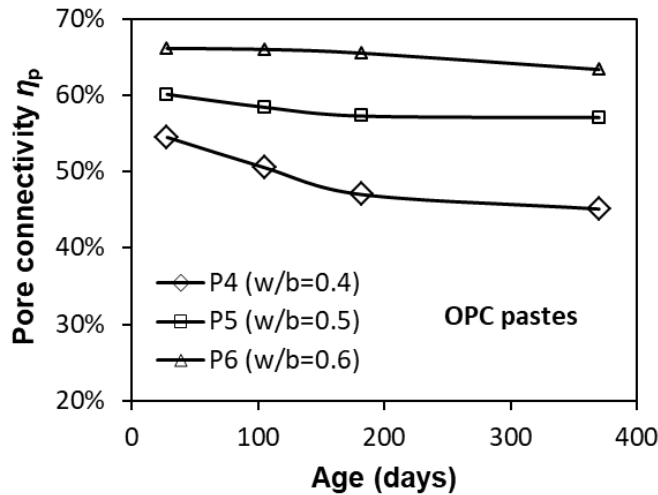


Fig. 4.14 Evolution of pore connectivity  $\eta_p$  in OPC pastes with different w/b ratios.

Figure 4.15-left shows the pore connectivity  $\eta_p$  in blended pastes. The  $\eta_p$ -value normally drops rapidly in the first 105 days, followed by a slow decrease thereafter. Compared with the reference OPC paste P5, all the blended pastes (except PFL5 at 28 days) exhibit lower pore connectivity  $\eta_p$ . Figure 4.15-right shows the effect of the w/b ratio on the pore connectivity  $\eta_p$ . At 370 days the  $\eta_p$  for w/b=0.4 is much lower than that for w/b=0.5 and w/b=0.6. This finding holds for both OPC pastes (P4, P5 and P6) and BFS-blended pastes (PB4, PB5 and PB6).

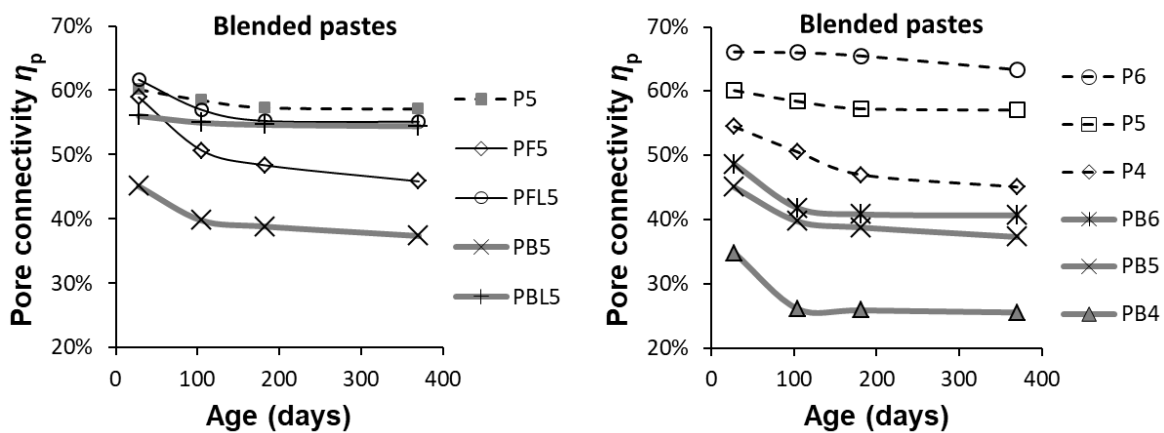


Fig. 4.15 Pore connectivity  $\eta_p$  in various blended pastes: (left) effect of SCMs and (right) effect of w/b ratio. P (OPC), B (BFS 70%), F (FA 30%), L (LP 5%), 4 (w/b = 0.4), 5 (w/b = 0.5) and 6 (w/b = 0.6).

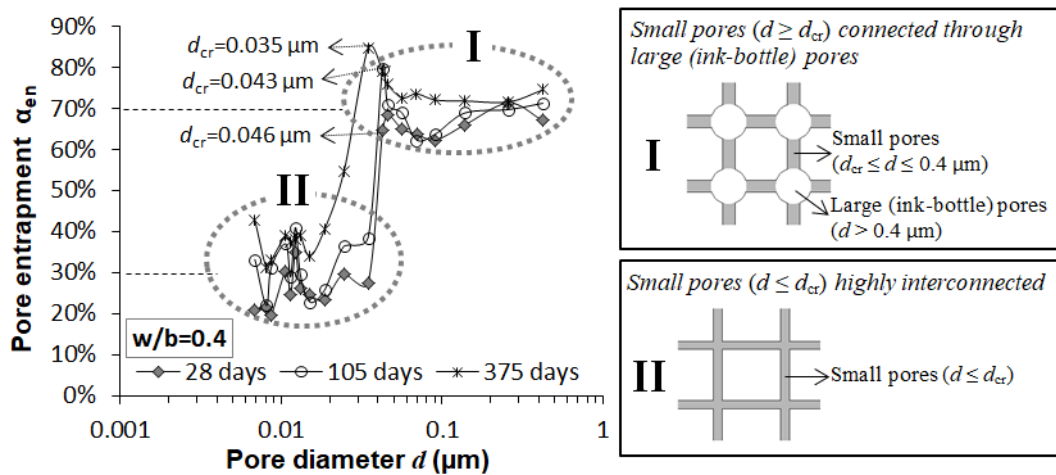
4.3.4.2 Distribution of pore entrapment ( $\alpha_{en}$  vs.  $d$ ) in cementitious pastes

The pore entrapment  $\alpha_{en}$  as a function of pore diameter  $d$  was measured by the IEC-MIP tests and using Eq. 3.7a-c. As shown below, the changes of the  $\alpha_{en}$  with the pore diameter varying in the range  $d \leq 0.4 \mu\text{m}$  are presented for cementitious pastes with and without SCMs.

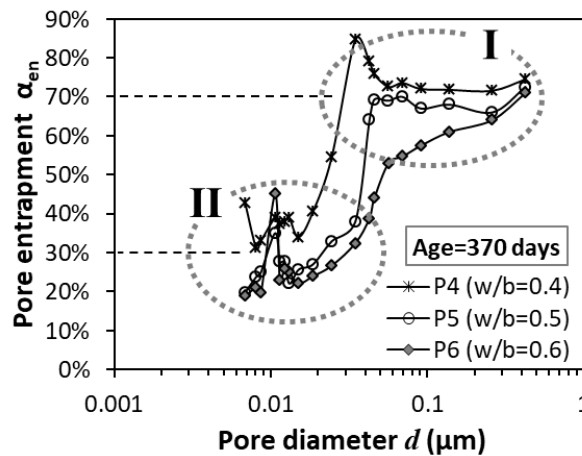
$\alpha_{en}$ - $d$  in OPC pastes

Increased age (Fig. 4.16a) or decreased w/b ratio (Fig. 4.16b) results in a higher  $\alpha_{en}$ -value in OPC pastes. Nevertheless, a common feature can be observed that all the  $\alpha_{en}$ - $d$  plots of OPC pastes can be divided into two groups (I and II) with pore diameter  $d$  above and below the critical pore diameter  $d_{cr}$ .

- 1) For  $d_{cr} \leq d \leq 0.4 \mu\text{m}$  (group I), the  $\alpha_{en}$ -values are generally high ( $\alpha_{en} \approx 70\%$ ), indicating that these small pores are highly connected with large (ink-bottle) pores.
- 2) For  $d < d_{cr}$  (group II), the  $\alpha_{en}$ -values are generally low ( $\alpha_{en} \approx 30\%$ ), indicating that these small pores are highly interconnected.



(a) Effect of age (28, 105 and 370 days) on distribution of pore entrapment ( $\alpha_{en}$ - $d$ ).



(b) Effect of w/b ratio (0.4, 0.5 and 0.6) on distribution of pore entrapment ( $\alpha_{en}$ - $d$ ).

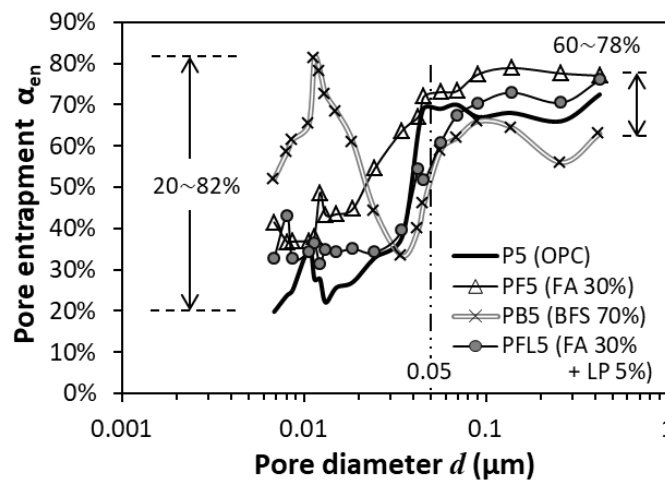
Fig. 4.16 Distribution of pore entrapment ( $\alpha_{en}$ - $d$ ) in OPC pastes obtained from IEC-MIP measurements.  $d_{cr}$  - critical pore diameter.

### $\alpha_{en}$ - $d$ in SCMs-blended pastes

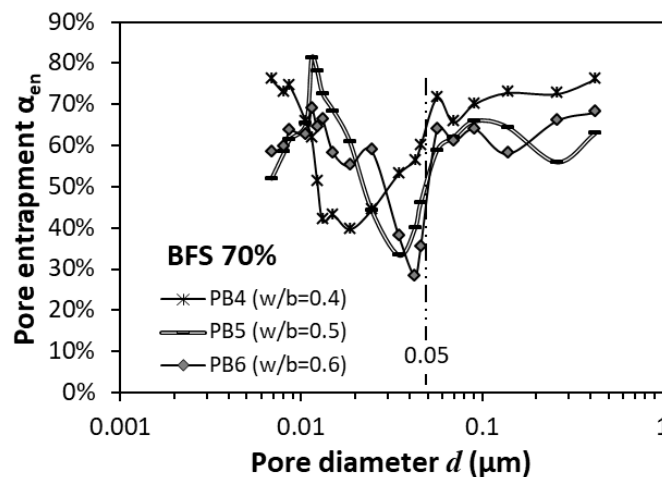
Figure 4.17a shows the  $\alpha_{en}$ - $d$  relations in pastes with different binders.

- For  $d \geq 0.05 \mu\text{m}$ , the  $\alpha_{en}$ -values are generally high and mostly lie in a narrow range 60~78%, regardless of the binders.
- For  $d < 0.05 \mu\text{m}$ , the  $\alpha_{en}$ -values differ significantly for different binders. Compared with the OPC binder (P5), the binders with FA or BFS show much higher  $\alpha_{en}$ -values for the small pores ( $d < 0.05 \mu\text{m}$ ). The LP-filled paste PFL5 shows lower  $\alpha_{en}$ -values than the LP-free paste PF5 in the whole pore size range tested.

The role of the w/b ratio (0.4~0.6) in the  $\alpha_{en}$ - $d$  relation is much less pronounced in BFS-blended pastes (Fig. 4.17b) than in OPC pastes (Fig. 4.16b).



(a) Effect of binder type (constant w/b = 0.5) on distribution of pore entrapment ( $\alpha_{en}$ - $d$ ).



(b) Effect of w/b ratio (0.4, 0.5 and 0.6) on the distribution of pore entrapment ( $\alpha_{en}$ - $d$ ) in BFS-blended pastes.

Fig. 4.17 Distribution of pore entrapment ( $\alpha_{en}$ - $d$ ) in blended pastes (one-year-old) obtained from IEC-MIP measurements.

## 4.4 Conclusions

The pore structures of cementitious pastes have been analyzed by IEC-MIP measurements. The effects of curing age (28~370 days), binder type and w/b ratio (0.4, 0.5 and 0.6) were studied. The main findings are as follows:

- 1) Combining the alumina-rich FA (30%) with LP (5%) shows a synergistic effect in filling the capillary pores due to the formation of carboaluminate and bulky ettringite.
- 2) In OPC pastes there is a linear relationship between total porosity and effective porosity. For a given total porosity, the pastes blended with BFS (70%) or FA (30%) generally exhibit a lower effective porosity than that of OPC pastes.
- 3) The w/b ratio and the curing age influence the total porosity mainly by altering the effective porosity.
- 4) If the cement and/or blended powders continue hydrating up to a high degree, the critical pore diameter tends to reach a constant, regardless of the w/b ratio. Such constant is found to be 22 nm for neat OPC pastes and 7.5 nm for BFS-blended pastes.
- 5) The large pores ( $\geq 50$  nm) are poorly interconnected in all cementitious pastes tested.
- 6) The small pores ( $< 50$  nm) of OPC pastes are highly interconnected. Partial replacement of OPC by reactive SCMs, either FA or BFS, substantially reduces the connectivity of small pores ( $< 50$  nm). The addition of LP increases the connectivity of small pores ( $< 50$  nm). The w/b ratio does not significantly affect the connectivity of small pores ( $< 50$  nm), regardless of OPC or BFS-blended binders.



## Chapter 5

# Chloride Transport Property in Saturated Cementitious Materials: Effect of Pore Structure

---

## 5.1 Introduction

Chloride ions diffuse in saturated concrete via its pore structure. Part of the chlorides will interact with pore walls. The interaction between chlorides and pore walls can be physical (chloride binding by surface forces on the pore walls) and/or chemical (chloride binding due to reaction with aluminate phases) [Glass et al. 2000]. In an accelerated test, i.e. rapid chloride migration test (RCM), the chloride binding effect plays a negligible role in the obtained chloride migration coefficient  $D_{RCM}$  [Spiesz et al. 2013]. The  $D_{RCM}$ -value is normally considered to be governed by the pore structure of the specimen tested, and it is widely used as a measure for the chloride diffusion coefficient in cementitious materials.

The pore structure of various cementitious binders has been analyzed in Chapter 4. The purpose of this chapter (see Fig. 5.1) is to understand the effect of the pore structure on the chloride transport property in saturated cementitious binders. The chloride transport property is indicated by the chloride migration coefficient  $D_{RCM}$  obtained from RCM tests performed on saturated mortar specimens made with and without SCMs. The roles of SCMs on the  $D_{RCM}$  obtained are analyzed. The effects of the often adopted pore structure parameters, viz. porosity, pore size and pore connectivity, on the  $D_{RCM}$  are discussed. The deficiency of these parameters in examining the saturated chloride transport property is pointed out. Another parameter, i.e. connectivity  $\eta_{sc}$  of small capillary pores, is described and a mathematical relationship between  $D_{RCM}$  and  $\eta_{sc}$  is established covering all mixtures studied.

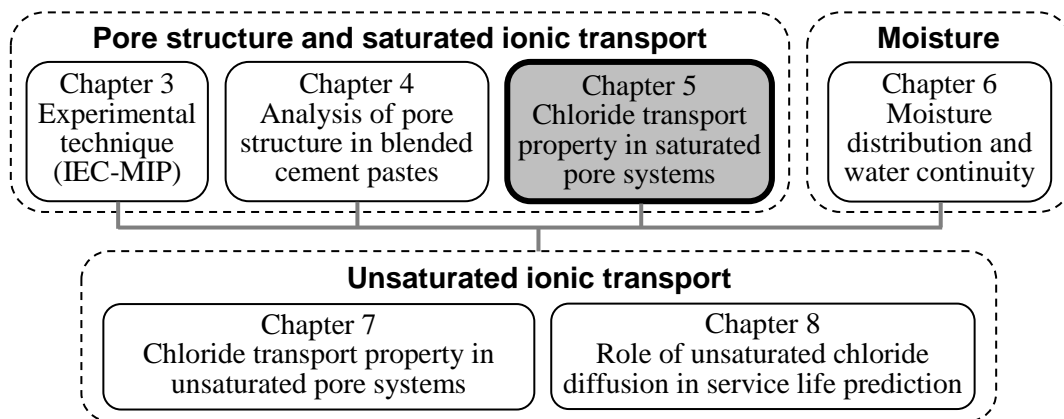


Fig. 5.1 Main chapters of the thesis.

## 5.2 Experimental program

### 5.2.1 Materials and samples preparation

Mortar samples were prepared for rapid chloride migration tests. The mixture proportions of the binders and the particle size distribution of the sand are given in Table 5.1. For all mortar samples the paste-sand ratio was kept constant as 1:3 by weight.

Cementitious powders and tap water were mixed at low speed for 30s. The sand was added during the next 30s and mixed at high speed for another 30s. Then the mixing stopped for 30s in order to scrape off the material that had adhered to the sides and bottom of the bowl. After that, the mixing continued for 90s. Cylindrical mortar samples ( $\phi 100 \times 80$  mm) were cast and demoulded after one day and then moved to a curing room ( $20 \pm 0.1$  °C, RH > 98%). At the age of 28, 105, 182, 370 and 730 days, both the top and bottom slices (15 mm thick) of the mortar samples were cut off. The middle part of the mortar samples (50 mm thick) were used for the rapid chloride migration tests.

Table 5.1 Mortar mixtures with constant paste-sand ratio of 1:3

Mortar mixtures	Binders and w/b ratios for paste					Particle size distribution of sand (mm)			
	OPC	FA	BFS	LP	W/b	1~2	0.5~1	0.25~0.5	0.125~0.25
M4	100%	-	-	-	0.4				
M5	100%	-	-	-	0.5				
M6	100%	-	-	-	0.6				
MF5	70%	30%	-	-	0.5				
MFL5	65%	30%	-	5%	0.5	40%	28%	11%	21%
MB4	30%	-	70%	-	0.4				
MB5	30%	-	70%	-	0.5				
MB6	30%	-	70%	-	0.6				
MBL5	25%	-	70%	5%	0.5				

### 5.2.2 Rapid chloride migration test

Figure 5.2 shows the set-up for rapid chloride migration (RCM) tests (according to NT Build 492 [1999]). The non-steady-state migration coefficient  $D_{RCM}$  [ $\times 10^{-12}$  m<sup>2</sup>/s] is calculated by using the simplified equation:

$$D_{RCM} = \frac{0.0239(237+T)L}{(U-2)t} (x_d - 0.0238 \sqrt{\frac{(237+T)Lx_d}{U-2}}) \quad (5.1)$$

where  $U$  [V] is the absolute value of the applied voltage;  $T$  [°C] is the average value of the initial and final temperatures in the anolyte solution;  $L$  [mm] is the thickness of the specimen;  $x_d$  [mm] is the average value of the penetration depths;  $t$  [hour] is the test duration.

The measured  $D_{RCM}$ -value is commonly used to indicate the capacity of saturated cementitious materials to resist chloride penetration.

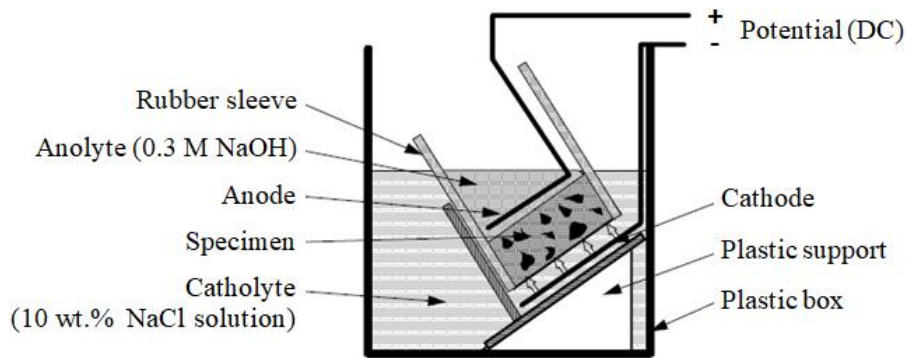


Fig. 5.2 Set-up for rapid chloride migration test (after NT Build 492 [1999]).

## 5.3 Experimental results

### 5.3.1 Chloride migration coefficient $D_{RCM}$ with age

Figure 5.3 shows the changes of the chloride migration coefficient  $D_{RCM}$  with the sample age from 28 days up to 2 years in the mortars made with and without SCMs. In general, the  $D_{RCM}$ -value is decreasing in the first 105 days. Particularly for the mortars containing 30% FA (i.e. MF5, MFL5), the  $D_{RCM}$  drops drastically during this period and their values at 105 days are almost five times smaller than those at 28 days. The mortars containing 70% BFS (i.e. MB4, MB5, MB6 and MBL5) exhibit high chloride resistance. Their  $D_{RCM}$ -values at 28 days are approximately four times smaller than those of OPC mortars (i.e. M4, M5 and M6).

For OPC mortars the  $D_{RCM}$ -values show a slight increasing trend after 182 days, while decreasing slowly again from one year onward. The reason for the increase of the  $D_{RCM}$ -value remains a pending issue. One possible explanation is the delayed ettringite formation (DEF) [Yu 2005]. It is noted that all the mortar specimens were cured in a humid climate ( $RH > 98\%$ ). Under such circumstances leaching of the alkali hydroxide from the mortar specimens into the surrounding water can take place and, therefore, reduces the alkali hydroxide concentration of the mortar pore solutions. The DEF process can be triggered as a consequence of such alkali leaching effect [Famy 1999, Diamond 2000b].

For all blended mortars the  $D_{RCM}$ -values decrease slowly after 182 days. At one year the mortars blended with 30% FA (i.e. MF5) or with 70% BFS (i.e. MB5) have an almost equal resistance to chloride penetration. By comparing the  $D_{RCM}$ -values in LP-filled ternary mortars (MFL5 and MBL5) and LP-free binary mortars (MF5 and MB5), it is found that the presence of 5% LP slightly reduces the  $D_{RCM}$ -value in the period from 28 days to 2 years. Attari et al. [2016] also observed a higher resistance to chloride penetration when BFS was used in combination with LP.

The roles of such parameters as w/b ratio, age and SCMs in the  $D_{RCM}$ -values are the result of their effects on the pore structure. Various pore features of cementitious pastes, including pore size, porosity and pore connectivity, have been analyzed in Chapter 4. The influences of these pore features on the  $D_{RCM}$ -values presented in Fig. 5.3 will be discussed hereafter.

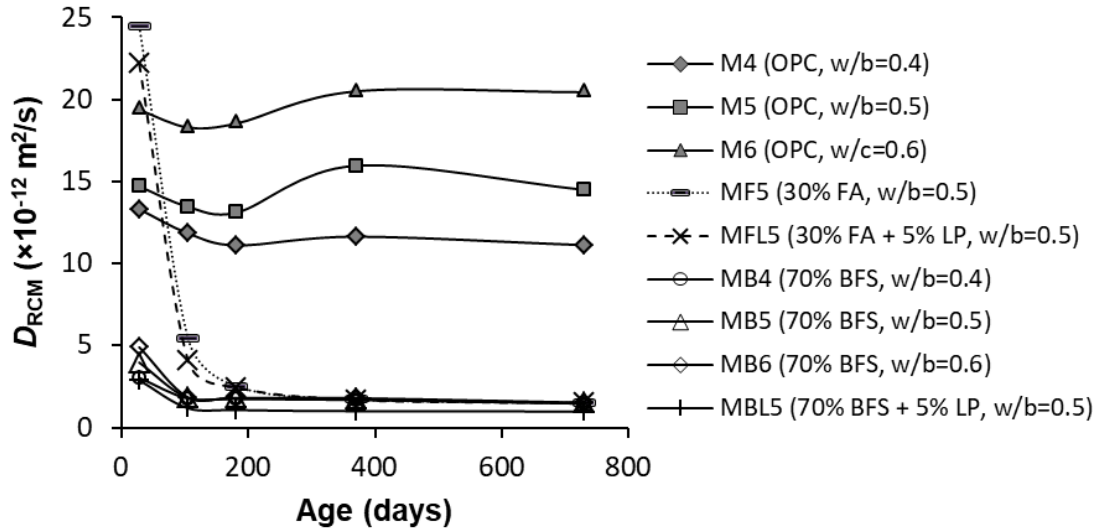


Fig. 5.3 Changes of chloride migration coefficient  $D_{RCM}$  with age from 28 days up to 2 years in the OPC and blended mortars.

### 5.3.2 Pore size effect on $D_{RCM}$

Figure 5.4 shows two porous systems (I and II) to explain the pore size effect on ionic transport. The interactions between pore walls and chlorides are not considered in the following.

The 1<sup>st</sup> system (Fig. 5.4-I) consists of one single big channel with a pore radius  $r_1$ . If this channel is saturated with water, the apparent ionic diffusion coefficient  $D_a$  and the intrinsic ionic diffusion coefficient  $D_0$  are correlated by [Garboczi 1995]:

$$D_a(I) = D_0 \cdot \frac{\pi r_1^2}{L^2} \quad (5.2)$$

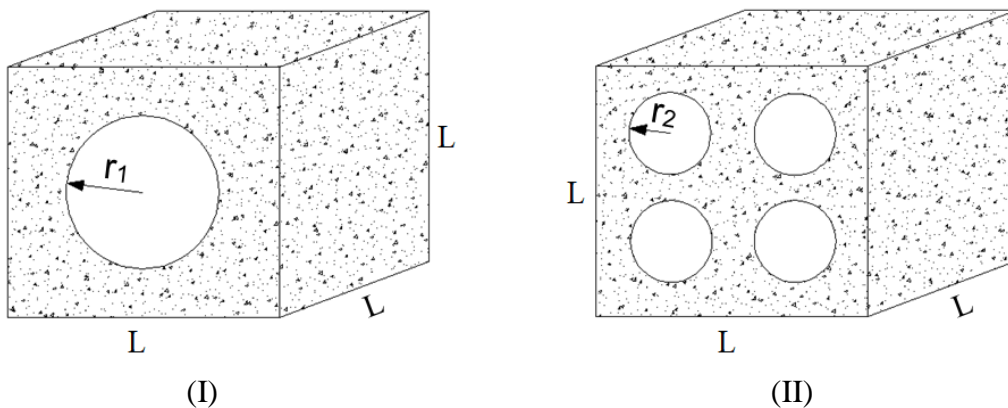


Fig. 5.4 Two porous systems with the same pore connectivity and porosity, but with different pore sizes: (I) a big channel with pore radius  $r_1$ ; (II) four small channels with pore radius  $r_2$  ( $r_2 = r_1/2$ ). If the two systems are saturated with water, their apparent ionic diffusion coefficients are the same when the interactions between pore walls and chlorides are not considered.

The 2<sup>nd</sup> system (Fig. 5.4-II) contains four parallel small channels. Each small channel has a pore radius  $r_2 = r_1/2$ . The 2<sup>nd</sup> system has the same porosity as the 1<sup>st</sup> one, i.e.  $\phi_t(\text{II}) = 4\pi r_2^2/L^2 = \pi r_1^2/L^2 = \phi_t(\text{I})$ . If the four small channels are saturated with water, the apparent ionic diffusion coefficient  $D_a(\text{II})$  is equal to that in the system I:

$$D_a(\text{II}) = D_0 \cdot \frac{4\pi r_2^2}{L^2} = D_a(\text{I}) \quad (5.3)$$

Note that Eq. (5.3) is very useful to study transport properties in the cases where the ionic diffusion process is the predominant mechanism for ionic penetration.

### 5.3.3 Porosity effect on $D_{\text{RCM}}$

Figure 5.5 shows the relationship between the chloride migration coefficient  $D_{\text{RCM}}$  and the total porosity  $\phi_t$ . The  $D_{\text{RCM}}$  values are taken from Fig. 5.3 and the  $\phi_t$  values from Figs. 4.3, 4.5 and 4.6. The specimens are 28, 105, 182 and 370 days old. The data ( $D_{\text{RCM}}$  vs.  $\phi_t$ ) can be categorized into two groups, except two (PF5 and PFL5 at 28 days). One group is for the specimens with *OPC binders*, where the  $D_{\text{RCM}}$ -value increases markedly with an increase of the total porosity  $\phi_t$ . The other group is for the specimens with *blended binders*, where the  $D_{\text{RCM}}$ -value shows little dependency on the total porosity  $\phi_t$ . In this respect more details will be discussed in Section 5.4.

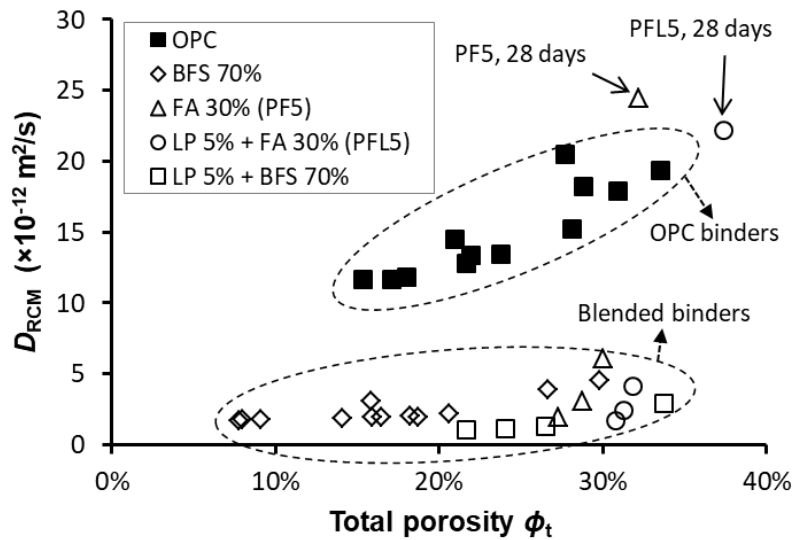


Fig. 5.5 Relationship between chloride migration coefficient  $D_{\text{RCM}}$  and total porosity  $\phi_t$  for different binders (28~370 days old). All  $D_{\text{RCM}}-\phi_t$  plots, except two (PF5 and PFL5 at 28 days), can be divided into two groups: one for OPC binders and the other for blended binders.

### 5.3.4 Pore connectivity effect on $D_{RCM}$

Figure 5.6 plots the relationship between chloride migration coefficient  $D_{RCM}$  and pore connectivity  $\eta_p$ . The  $D_{RCM}$  values are taken from Fig. 5.3 and the  $\eta_p$  values from Figs. 4.14-4.15. The specimens are 28, 105, 182 and 370 days old. All  $D_{RCM}$  vs.  $\eta_p$  plots, except two (PF5 and PFL5 at 28 days), can again be categorized into two groups and exhibit a similar trend as the  $D_{RCM}$  vs.  $\phi_t$  plots shown in Fig. 5.5. For the OPC binders a higher pore connectivity  $\eta_p$  tends to produce a higher  $D_{RCM}$ . For the blended binders, however, the  $D_{RCM}$ -value changes little when the  $\eta_p$ -value increases from 25% up to 58%.

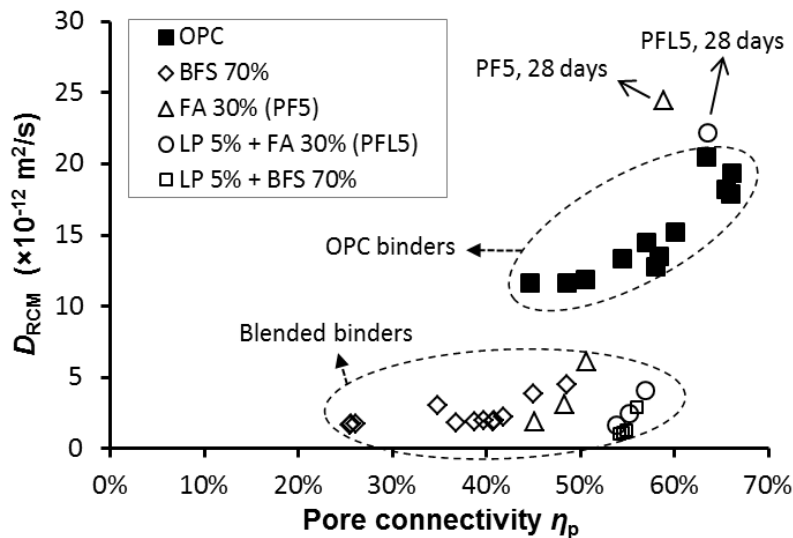


Fig. 5.6 Relationship between chloride migration coefficient  $D_{RCM}$  and pore connectivity  $\eta_p$  for different binders (28~370 days old). All  $D_{RCM}$ - $\eta_p$  plots, except two (PF5 and PFL5 at 28 days), can be divided into two groups: one for OPC binders and the other for blended binders.

From Figs. 5.5 and 5.6, it can be inferred that the total porosity  $\phi_t$  and the pore connectivity  $\eta_p$  are suitable parameters to predict the chloride transport property in saturated OPC mortars while, surprisingly, both  $\phi_t$  and  $\eta_p$  are not effective in judging the chloride transport property in saturated *blended* mortars. A discussion on this point follows below.

## 5.4 Discussion

### 5.4.1 Pore structure and transport property: role of small capillary pores

To understand the pore structure-related transport property in saturated porous systems, one needs to clarify two issues: (i) the pores all over the pore structure need to be subdivided into *one part* that contributes to ionic transport and *another part* that does not; (ii) the connectivity of the pores that contribute to ionic transport needs to be determined.

Figure 5.7 shows a sketch of the microstructure in hydrated cementitious systems, as previously described in Chapter 3. Different pore categories have different contributions to ionic transport.

- 1) The large capillary pores (I:  $d_{th} < d \leq 10 \mu\text{m}$ ) are mostly disconnected and have minor influence on the ionic transport property. An increase of the volume of the large capillary pores will result in a higher total porosity, but will not significantly affect the rate of ionic transport.
- 2) The small capillary pores (II:  $0.01 \mu\text{m} < d \leq d_{th}$ ) play a major role in the rate of ionic transport. The connectivity of small capillary pores and its relation to ionic transport will be quantitatively described in Sections 5.4.2 and 5.4.3.
- 3) Ionic transport in the gel pores (III:  $d \leq 0.01 \mu\text{m}$ ) is so slow that it is negligible compared to ionic transport in the capillary pores in range II.

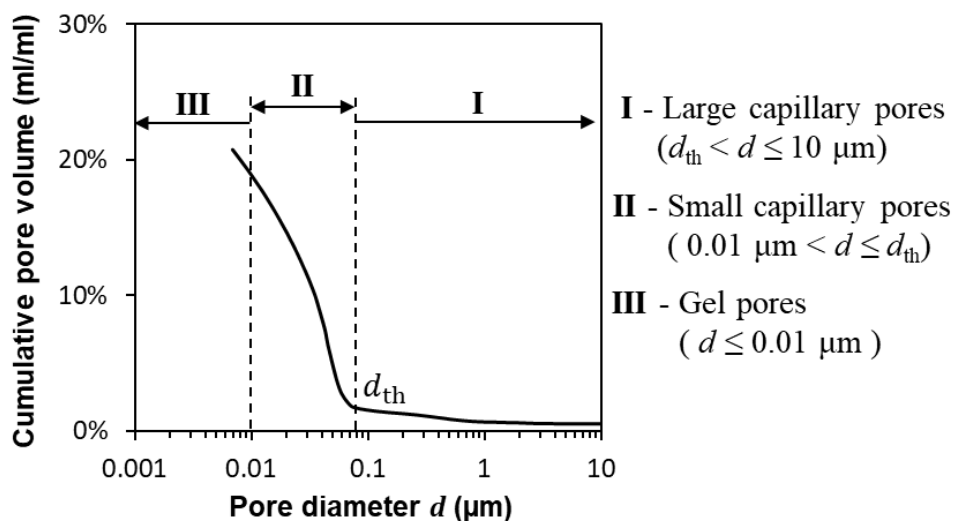
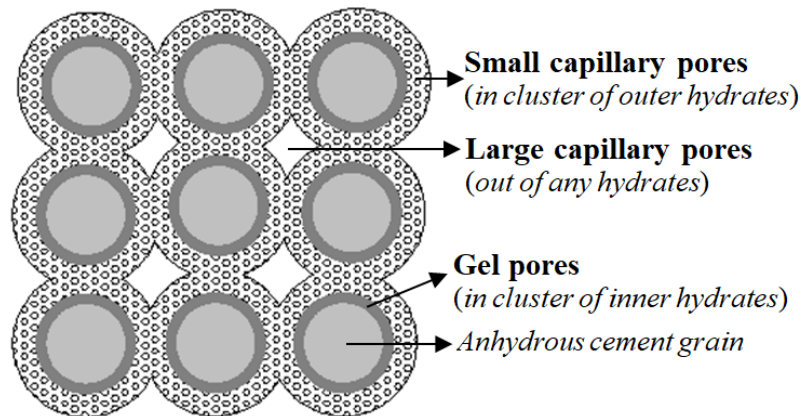


Fig. 5.7 (a) A sketch of the microstructure in hydrated cementitious systems.  
 (b) Three pore categories based on MIP-derived pore size distribution.  
 $d_{th}$  - threshold pore diameter.

### 5.4.2 Connectivity of small capillary pores ( $0.01 \mu\text{m} < d \leq d_{\text{th}}$ )

Two types of pore geometry of *small* capillary pores ( $0.01 \mu\text{m} < d \leq d_{\text{th}}$ , range II of Fig. 5.7b) can be distinguished: throat type (volume  $V_{\text{sc}}^{\text{th}}$ ) and ink-bottle type (volume  $V_{\text{sc}}^{\text{ink}}$ ). The connectivity of small capillary pores in range II,  $\eta_{\text{sc}}$ , is expressed as:

$$\eta_{\text{sc}} = \frac{V_{\text{sc}}^{\text{th}}}{V_{\text{sc}}^{\text{th}} + V_{\text{sc}}^{\text{ink}}} \quad (5.4)$$

The  $\eta_{\text{sc}}$ -value of each specimen can be determined based on IEC-MIP tests (pressure Table 3.1), where the 1<sup>st</sup> pressurization is divided into 19 steps and the 20<sup>th</sup> intrusion step has no ink-bottle effect. To understand the volume  $V_{\text{sc}}^{\text{ink}}$  of small capillary *ink-bottle* pores, differentiation between *small* capillary ink-bottle pores and *large* capillary ink-bottle pores is needed. This can be achieved by studying the distribution of pore entrapment ( $\alpha_{\text{en}}$  vs. diameter  $d$ ) measured from the first 19 intrusion-extrusion steps of the IEC-MIP test. Figure 5.8 shows an example of the  $\alpha_{\text{en}}-d$  plots which can be categorized into two groups:

- 1) At  $d_{\text{cr}} \leq d \leq d_{\text{th}}$ , mercury penetrates into both small (throat and ink-bottle) capillary pores and large (ink-bottle) capillary pores (Fig. 5.7a), resulting in strong ink-bottle effect ( $\alpha_{\text{en}} \approx 0.65$ ) (Fig. 5.8).
- 2) At  $0.01 \mu\text{m} < d \leq d_{\text{s,cr}}$ , mercury only penetrates into small capillary pores (Fig. 5.7a), including *throat* type and *ink-bottle* type, resulting in small ink-bottle effect ( $\alpha_{\text{en}} \approx 0.25$ ) (Fig. 5.8). The  $d_{\text{s,cr}}$  is the pore size smaller than, but close to, the critical pore diameter  $d_{\text{cr}}$ .

It is not easy to obtain the  $V_{\text{sc}}^{\text{ink}}$ -value directly from mercury intrusion-extrusion cycles at pore size range II ( $0.01 \mu\text{m} < d \leq d_{\text{th}}$ ). However, given that the pore entrapment  $\alpha_{\text{en}}$  is almost the same for small capillary pores in the range  $0.01 \mu\text{m} < d \leq d_{\text{s,cr}}$ , it is reasonable to assume that the connectivity  $\eta_{\text{sc}}$  of small capillary pores in range II ( $0.01 \mu\text{m} < d \leq d_{\text{th}}$ ) is equal to the connectivity  $\eta_{\text{s,cr}}$  of pores ( $0.01 \mu\text{m} < d \leq d_{\text{s,cr}}$ ). The  $\eta_{\text{s,cr}}$ -value is obtainable from mercury intrusion-extrusion cycles at pore size range  $0.01 \mu\text{m} < d \leq d_{\text{s,cr}}$ , and can be expressed as Eq. (5.5).

$$\eta_{\text{sc}} = \eta_{\text{s,cr}} = \frac{V_{\text{s}}^{\text{th}}}{V_{\text{s}}^{\text{in}}} \times 100\% \quad (5.5)$$

where  $V_{\text{s}}^{\text{th}}$  and  $V_{\text{s}}^{\text{in}}$  are the cumulative throat pore volume and the cumulative intrusion volume, respectively, when the mercury intrudes the pores with diameters from  $d_{\text{s,cr}}$  to  $0.01 \mu\text{m}$ . The  $V_{\text{s}}^{\text{th}}$ -value can be determined from the pore size distribution obtained by the 20<sup>th</sup> intrusion step of the IEC-MIP test. The  $V_{\text{s}}^{\text{in}}$ -value can be determined from the pore size distribution obtained by the 1<sup>st</sup> pressurization (which is identical to the standard MIP). Determinations of both  $V_{\text{s}}^{\text{th}}$ -value and  $V_{\text{s}}^{\text{in}}$ -value are illustrated in Fig. 5.8.

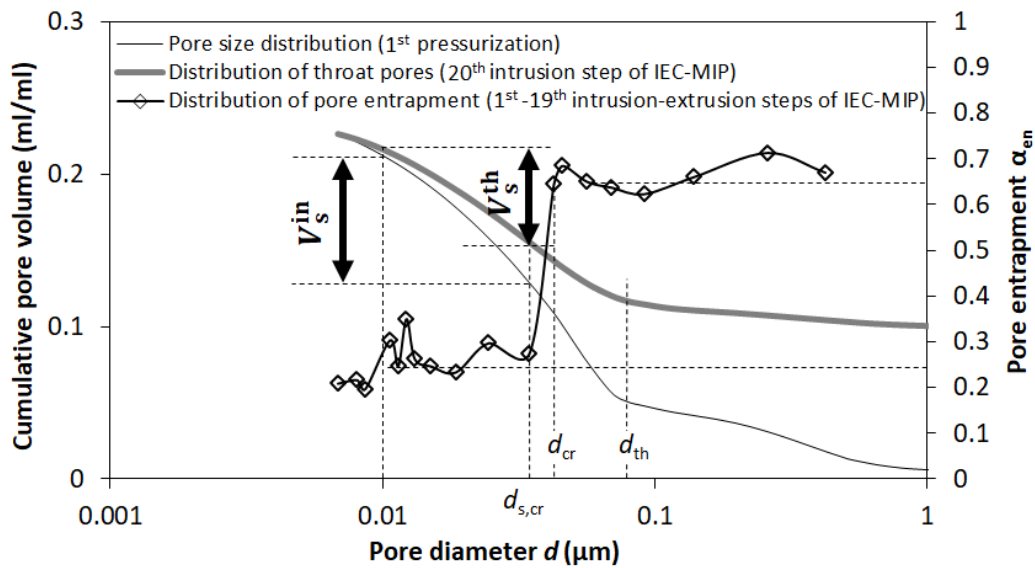


Fig. 5.8 Determination of the connectivity of small capillary pores (range II:  $0.01 \mu\text{m} < d \leq d_{th}$ ) in cement paste ( $w/c = 0.4$ , 28-day-old).  $d_{th}$  – threshold pore diameter;  $d_{cr}$  – critical pore diameter;  $d_{s,cr}$  is the pore diameter smaller than, but close to, the critical pore diameter  $d_{cr}$ .

### 5.4.3 Quantitative relationship between chloride transport and connectivity of small capillary pores

The connectivity  $\eta_{sc}$  of small capillary pores (range II:  $0.01 \mu\text{m} < d \leq d_{th}$ ) was determined with Eq. (5.5) for various mixtures. Figure 5.9 shows the  $D_{RCM}$  as a function of the  $\eta_{sc}$  for all mortar specimens. A power equation can be used to well describe the  $D_{RCM}$ - $\eta_{sc}$  relation covering the plots of all OPC and blended binders. The exponent of 4 suggests that the chloride transport property in saturated mortars significantly depends on the connectivity  $\eta_{sc}$  of small capillary pores. Note that the  $\eta_{sc}$ -values shown in Fig. 5.9 are generally higher than the  $\eta_p$ -values shown in Fig. 5.6.

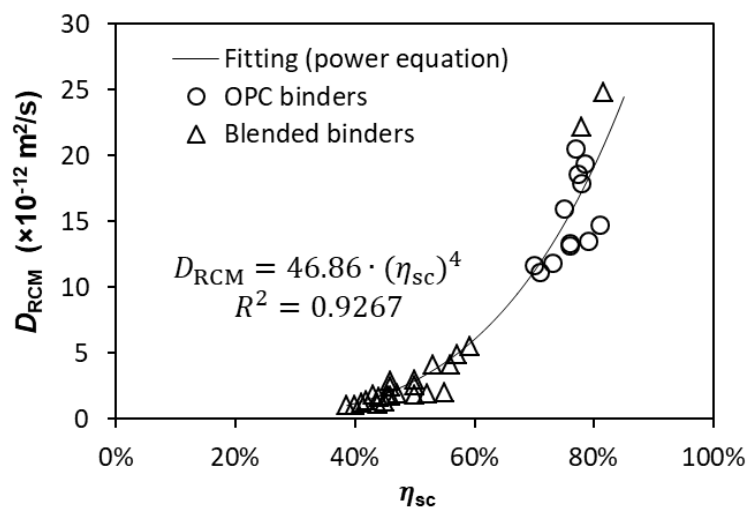


Fig. 5.9 Power relationship between chloride migration coefficient  $D_{RCM}$  and connectivity  $\eta_{sc}$  of small capillary pores ( $0.01 \mu\text{m} < d \leq d_{th}$ ), regardless of the binders (OPC, BFS, FA or LP).

## 5.5 Conclusions

The following conclusions are based on the experimental results reported in this chapter.

- 1) The chloride migration coefficient  $D_{RCM}$  shows a minor decrease for all saturated binders tested after one year.
- 2) A higher total porosity  $\phi_t$ , or a higher pore connectivity  $\eta_p$ , leads to a higher chloride migration coefficient  $D_{RCM}$  for OPC binders. This finding, however, does not hold for binders blended with FA or BFS.
- 3) A parameter, *connectivity*  $\eta_{sc}$  of *small capillary* pores ( $0.01 \mu\text{m} < d \leq \text{threshold pore diameter } d_{th}$ ), is utilized to describe the pore structure-related transport property in *saturated* cementitious materials. A power equation between  $D_{RCM}$  and  $\eta_{sc}$  is established, regardless of binders (OPC, BFS, FA and LP).

## Chapter 6

# Moisture Distribution and Water Continuity in Unsaturated Cementitious Materials

---

## 6.1 Introduction

In unsaturated porous systems the water tends to accumulate in small pores. Part of the water-filled small pores can form continuous paths for chloride transport while the other part cannot. The continuity of water-filled pores, in short water continuity, controls the chloride transport. The water continuity is dependent not only on the degree of water saturation but also on the pore structure.

In this chapter (see Fig. 6.1) the influence of the pore structure on the water continuity in unsaturated porous systems is dealt with. The effects of various pore features, viz. porosity, pore size, pore connectivity and tortuosity, on the moisture distribution as well as on the concept of water continuity are analyzed according to the Kelvin law. In parallel, experimental studies about the water vapour desorption isotherms (WVDIs) of cementitious mortars are carried out. The influence of the pore structure on the WVDIs is analyzed. Finally, the water continuity,  $\eta_w$ , is described as a function of the degree of water saturation  $S_w$ . The  $\eta_w$ - $S_w$  relationship will be used to quantitatively study the relative chloride diffusion coefficient  $D_{rc}$  in unsaturated cementitious materials (see Chapter 7).

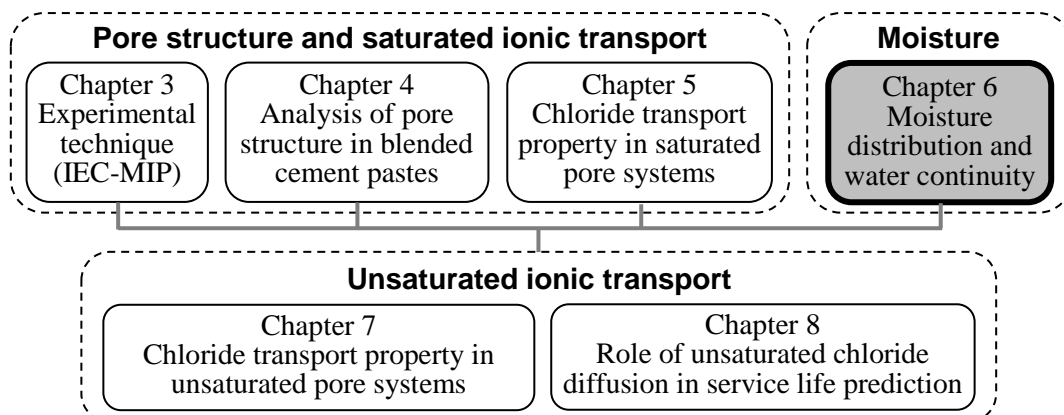


Fig. 6.1 Main chapters of the thesis.

## 6.2 Moisture distribution and water continuity

### 6.2.1 Effect of pore features on moisture distribution

#### 6.2.1.1 Moisture state in a pore

Figure 6.2a-c illustrates three typical moisture states in a pore (Note that the pore stands for a channel in 3D microstructure). Initially, the pore is *fully water-filled* (Fig. 6.2a). In a desorption process water loss starts from the central part of the pore and the gas phase gradually fills the pore. The pore becomes *partially water-filled* (Fig. 6.2b). The pore is considered *drained* if only an adsorbed water film is present (Fig. 6.2c). The thickness  $t$  of the water film depends on the relative humidity RH in the pore system.

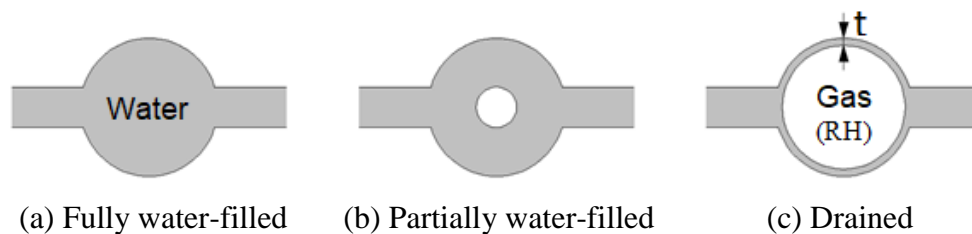


Fig. 6.2 Three moisture states in a pore. The pore is drained if only the thin water film (thickness  $t$ ) is present.

#### 6.2.1.2 Pore size effect on moisture distribution

Figure 6.3 illustrates the *idealised* moisture distribution in the pores of different sizes. According to the Kelvin-Cohan equation (Eq. (2.4)), each relative humidity RH corresponds to a particular pore radius  $r_p$ . The pores with radius  $r < r_p$  are saturated with water, whereas the pores with radius  $r > r_p$  are drained (only adsorbed water film is present).

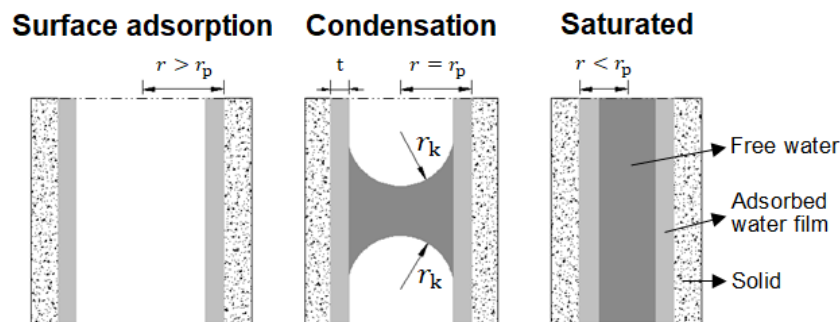


Fig. 6.3 Idealised moisture distribution in a pore system at a particular relative humidity.  $r_k$  - Kelvin radius,  $r_p$  - pore radius,  $t$  - thickness of water film.

#### 6.2.1.3 Pore constriction (or pore entrapment) effect

The idealised moisture distribution hardly exists in cementitious materials, since a desorption-absorption cycle often results in a moisture hysteresis because of the ink-bottle pore geometry, as illustrated in Fig. 6.4.

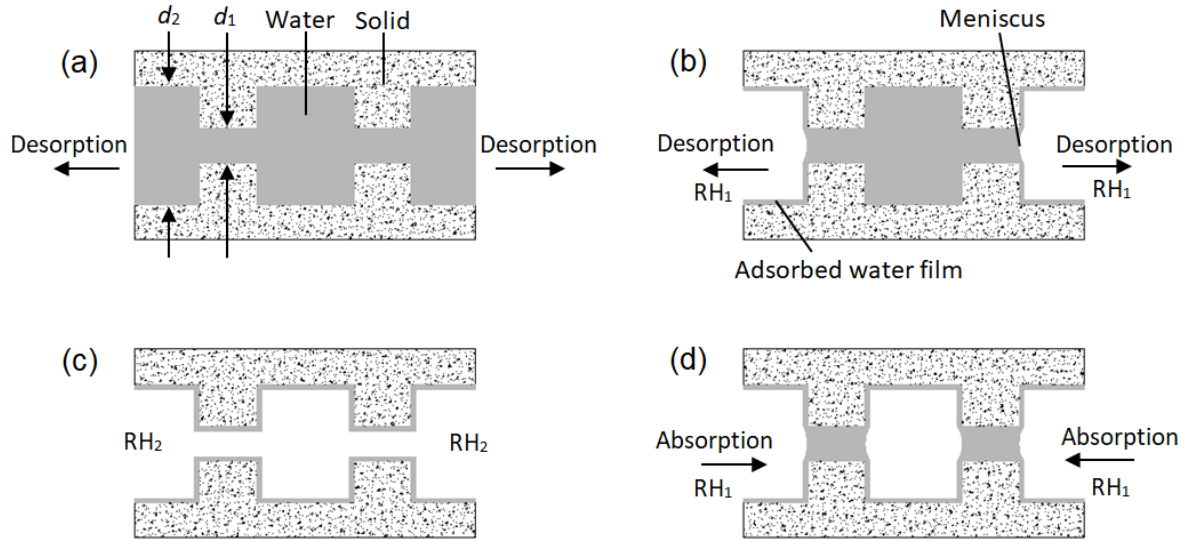


Fig. 6.4 Moisture hysteresis in a desorption-absorption cycle under isothermal condition: (a) saturated; (b) desorption to  $RH_1$ ; (c) further desorption to  $RH_2$ ; (D) absorption to  $RH_1$ .

Figure 6.4a shows a channel ( $d_1 < d_2$ ) initially saturated with water. Figure 6.4b shows water desorption from saturated state to  $RH_1$ . The pores  $d_2$  at the two ends are drained. Figure 6.4c shows further desorption from  $RH_1$  to  $RH_2$  ( $RH_2 < RH_1$ ). The whole channel is drained (only an adsorbed water film covers the pore walls). Figure 6.4d shows an absorption process from  $RH_2$  to  $RH_1$ . The throat pores  $d_1$  are fully filled with water while in the ink-bottle pores  $d_2$  only an adsorbed water film is present. With the same  $RH_1$  level the water contents present in Figs. 6.4b and 6.4d are different. Therefore, under isothermal condition cementitious materials with the same internal  $RH$  can have different water contents, depending on the dynamic moisture loading history and pore entrapment of the materials.

## 6.2.2 Effect of pore features on water continuity

### 6.2.2.1 Definition of water continuity

The continuity of water-filled pores, in short water continuity  $\eta_w$ , stands for the effect of the moisture distribution on ionic transport in a porous system. Ionic transport occurs only if a continuous water-filled path is present. The water continuity  $\eta_w$  can be expressed as:

$$\eta_w = \frac{N_w}{N_{Sat}} \quad (6.1)$$

where  $N_w$  and  $N_{Sat}$  represent the number of paths available for ionic transport in the porous system at a particular water saturation level and at saturated state, respectively.

Whether a channel is available for ionic transport depends on the moisture state in the pores. Ionic transport is possible in fully or partially water-filled pores (Fig. 6.2a-b), but is not possible in a drained pore (Fig. 6.2c).

Figure 6.5 schematically illustrates the changes of the water continuity  $\eta_w$  with decreasing degree of water saturation  $S_w$  in an imaginary pore system. There are small pores and large pores (radii  $r_1 > r_2 > r_3 > r_4$ ) in the system. The larger pores tend to be drained with lower  $S_w$ .

- At  $S_w = 100\%$  (Fig. 6.5a), all pores are fully water-filled. Four continuous water-filled paths are present, i.e.  $1 \rightarrow 3 \rightarrow 5$ ,  $1 \rightarrow 3 \rightarrow 6$ ,  $1 \rightarrow 3 \rightarrow 4 \rightarrow 7$  and  $2 \rightarrow 4 \rightarrow 7$ . It holds:  $N_w = N_{\text{Sat}} = 4$  and  $\eta_w = 1$ .
- At  $S_w = 80\%$  (Fig. 6.5b), the largest pores  $r_1$  are drained. The water in both paths  $1 \rightarrow 3 \rightarrow 5$  and  $1 \rightarrow 3 \rightarrow 6$  becomes discontinuous. The remaining two paths ( $1 \rightarrow 3 \rightarrow 4 \rightarrow 7$  and  $2 \rightarrow 4 \rightarrow 7$ ) are still intact. It holds:  $N_w = 2$  and  $\eta_w = 2/4$ .
- At  $S_w = 65\%$  (Fig. 6.5c), the pores  $r_1$  and  $r_2$  are both drained. Only one continuous water-filled path,  $2 \rightarrow 4 \rightarrow 7$ , is present. It holds:  $N_w = 1$  and  $\eta_w = 1/4$ .
- At  $S_w = 55\%$  (Fig. 6.5d), the pores  $r_1$ ,  $r_2$  and  $r_3$  are drained. However, draining of the dead-end pores  $r_3$  does not influence the water continuity. In this case the water continuity is  $\eta_w = 1/4$ , which is the same as that in the case of  $S_w = 65\%$ .
- At  $S_w = 45\%$  (Fig. 6.5e), the pores  $r_1$ ,  $r_2$ ,  $r_3$  and  $r_4$  are all drained. No continuous water-filled path is present. It holds:  $N_w = 0$  and  $\eta_w = 0$ .
- At  $S_w < 45\%$  (Fig. 6.5f), water loss takes place in the small pores. Further loss of water no longer alters the water continuity in the pore system.

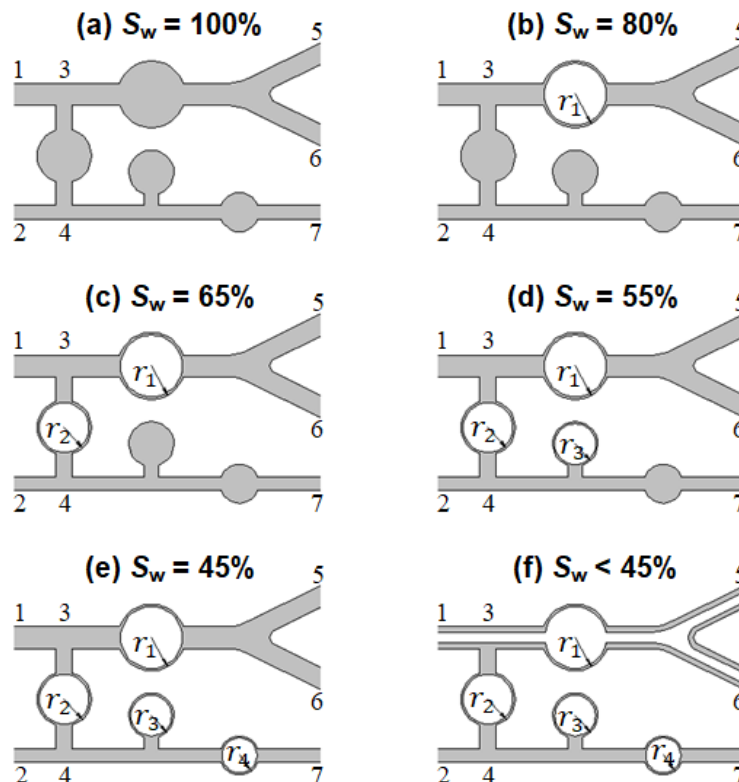


Fig. 6.5 Schematic illustration on the changes of water continuity with decreasing degree of water saturation  $S_w$ . Small pores and large pores (radii  $r_1 > r_2 > r_3 > r_4$ ) present in the pore system. The larger pores tend to be drained with lower  $S_w$ . There is no continuous water-filled path when the  $S_w$  is below a critical level.

For a given degree of water saturation  $S_w$  the water continuity  $\eta_w$  can differ significantly for different pore systems. The effects of various pore features, viz. porosity, pore size, pore connectivity and tortuosity, on water continuity  $\eta_w$  will be analyzed based on Kelvin's law.

### 6.2.2.2 Effect of porosity on water continuity

Figure 6.6 shows two porous systems, I and II, with different porosities (but with the same pore size distribution). System I has one channel (porosity  $\phi_I$ ) and system II has two channels (porosity  $\phi_{II} = 2\phi_I$ ). Each channel consists of small pores (diameter  $d_1$ ) and large pores (diameter  $d_2$ ).

- At saturated state, it holds:  $N_w(I) = 1$  and  $N_w(II) = 2$ ;  $\eta_w(I) = \eta_w(II) = 1$ .
- At unsaturated state, e.g.  $S_w = 70\%$ , systems I and II exhibit the same moisture distribution. The large pores  $d_2$  in both systems I and II are drained, i.e.  $N_w(I) = N_w(II) = 0$  and  $\eta_w(I) = \eta_w(II) = 0$ .

It is found that for a given degree of water saturation  $S_w$  the porous systems with varying porosities exhibit the same water continuity  $\eta_w$ . In other words, in this case the porosity has no influence on the  $\eta_w$  vs.  $S_w$  relationship.

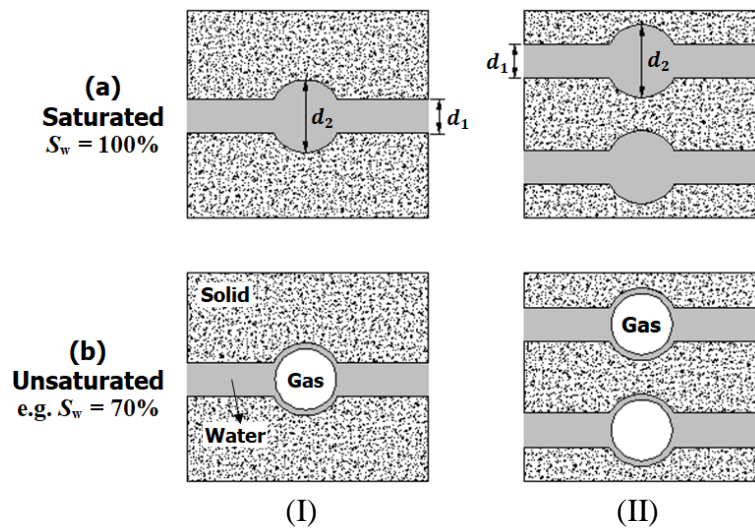


Fig. 6.6 With the same degree of water saturation  $S_w$ , the two porous systems with varying porosities ( $\phi_{II} = 2\phi_I$ ) exhibit the same moisture distribution and water continuity. Note that the pore size distribution and pore connectivity are the same for systems I and II.

### 6.2.2.3 Effect of pore size on water continuity

Figure 6.7 shows two porous systems, I and II, with different pore size distributions (but with the same porosity). System I has one channel consisting of large pores (diameter  $D_1$ ) and small pores (diameter  $D_2$ ). System II has two channels consisting of pores with diameters  $d_1 = D_1/2$ ,  $d_2 = \sqrt{3}D_1/2$ ,  $d_3 = D_2/2$  and  $d_4 = \sqrt{3}D_2/2$ .

- At  $S_w = 100\%$ ,  $\eta_w(I) = 1/1 = 1$  and  $\eta_w(II) = 2/2 = 1$ .
- At  $S_w = 70\%$ , the pores  $d_2$  in system II are drained, i.e.  $N_w(II) = 1$  and  $\eta_w(II) = 1/2$ . In

contrast, the pores  $D_1$  in system I remain partially water-filled, i.e.  $N_w(\text{I}) = 1$  and  $\eta_w(\text{I}) = 1$ .

- c) At  $S_w = 60\%$ , the pores  $D_1$  in system I become drained, and the pores  $d_1$  and  $d_2$  in system II are drained as well. It holds:  $\eta_w(\text{I}) = \eta_w(\text{II}) = 0$ .
- d) At low saturation levels, i.e.  $S_w < 60\%$ , further loss of water no longer influences the water continuity in both systems I and II. It holds:  $\eta_w(\text{I}) = \eta_w(\text{II}) = 0$ .

It is found that for a given degree of water saturation  $S_w$  the water continuity  $\eta_w$  tends to be lower in the system with a finer pore size distribution. The pore size effect on water continuity  $\eta_w$  is pronounced at high  $S_w$  levels, but becomes weak at low  $S_w$  levels.

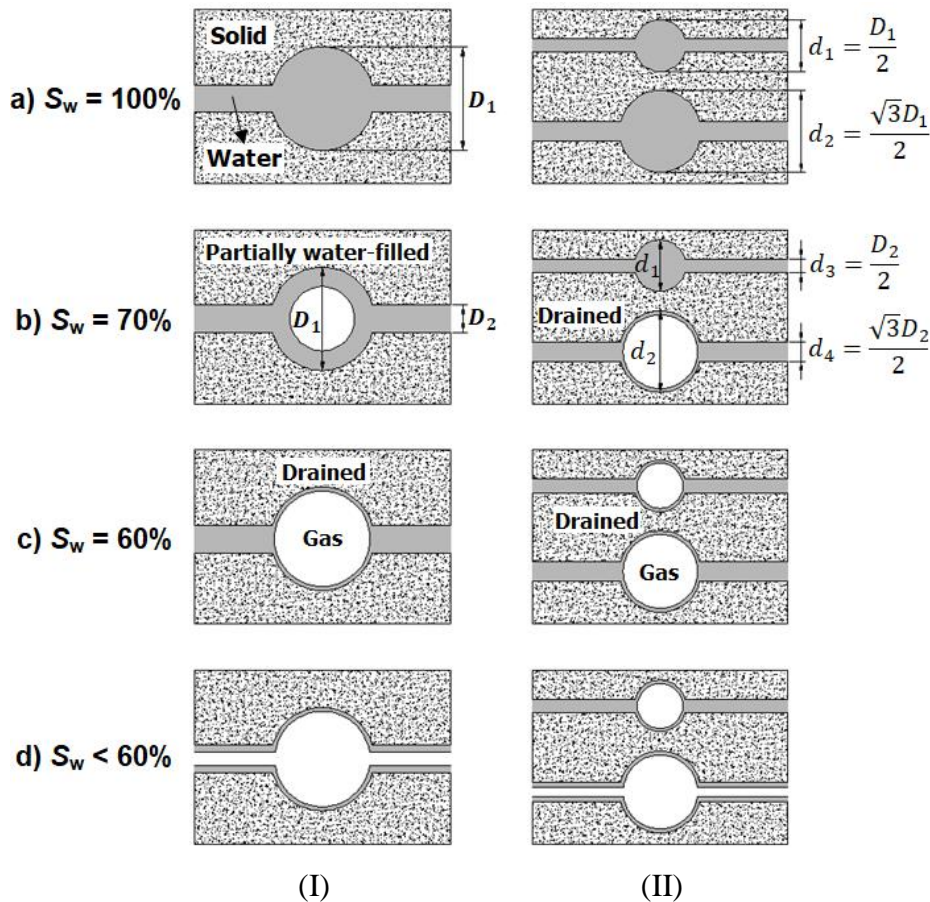


Fig. 6.7 Changes of water continuity with decreasing degree of water saturation  $S_w$  in two porous systems (I and II) with different pore sizes but with the same porosity ( $D_1^2 = d_1^2 + d_2^2$  and  $D_2^2 = d_3^2 + d_4^2$ ).

#### 6.2.2.4 Effect of pore connectivity (or pore entrapment) on water continuity

Figure 6.8 shows two porous systems I and II. Both consist of small pores (diameter  $d_1$ ) and large pores (diameter  $d_2$ ), but they have different pore connectivities. The water continuity differs when water loss takes place in the large pores in the two systems.

- In system I the small pores  $d_1$  are highly interconnected and they have no connection with the large pores  $d_2$ . The water-filled small pores  $d_1$  easily form continuous paths when water loss occurs in the large pores  $d_2$ .

- In system II the small pores  $d_1$  are connected through the large pores  $d_2$ . In the case of water loss in the large pores  $d_2$ , it is difficult for the water-filled small pores  $d_1$  to form a continuous path.

It is found that higher pore connectivity (Fig. 6.8-I) tends to result in higher water continuity  $\eta_w$  in unsaturated porous systems.

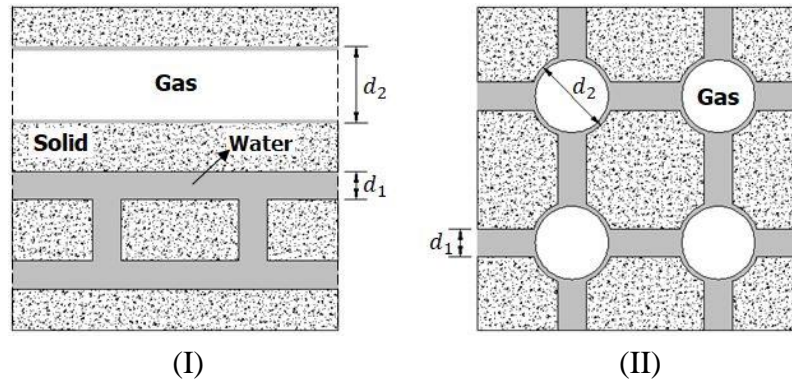


Fig. 6.8 Water continuity in two porous systems I and II, where the connections between small pores (diameter  $d_1$ ) and large pores (diameter  $d_2$ ) are different.

The pore connectivity (Eq. (3.5)) in a porous specimen can be determined by IEC-MIP tests as described in Chapter 3. High pore connectivity (Fig. 6.8-I) corresponds to a small ink-bottle effect (low pore entrapment, Eq. (3.6)). Low pore connectivity (Fig. 6.8-II) corresponds to a large ink-bottle effect (high pore entrapment). The pore entrapment  $\alpha_{en}$  of different cementitious materials was analyzed in Chapter 4. It has been shown in Fig. 4.17a that for pastes made with different binders the  $\alpha_{en}$  values for large pores (which tend to be drained at high water saturation levels) differ slightly from each other, but the  $\alpha_{en}$  values for small pores (which tend to be drained at low water saturation levels) can differ significantly. On this basis, the pore connectivity is a very effective index when comparing the water continuity of different cementitious materials at low water saturation levels.

#### 6.2.2.5 Effect of pore tortuosity on water continuity

Pore tortuosity, often noted as  $\tau$ , is a property of a transport channel being tortuous. In its simplest way, the tortuosity is estimated as the ratio of the length  $L$  of a channel to the straight distance  $C$  between the two ends of the channel, as  $\tau = L/C$ .

Figure 6.9a-b shows two channels I and II. Channel I has small pores (diameter  $d_1$ , volume  $v_1$ ) and large pores (diameter  $D_1$ , volume  $V_1$ ). Channel II consists of small pores (diameter  $d_2$ , volume  $v_2$ ) and large pores (diameter  $D_2$ , volume  $V_2$ ). Channel II has a higher tortuosity than channel I, i.e.  $\tau(\text{II}) > \tau(\text{I})$ , but the two channels have the same porosity ( $V_1 + v_1 = V_2 + v_2$ ) and the same pore entrapment, i.e.  $\alpha_{en}(\text{I}) = V_1/(v_1 + V_1) = V_2/(v_2 + V_2) = \alpha_{en}(\text{II})$ .

- In saturated state (Fig. 6.9a), the water continuity of channel I ( $\eta_w(\text{I}) = 1/1=1$ ) is equal to that of channel II ( $\eta_w(\text{II}) = 1/1=1$ ).

b) In non-saturated state (Fig. 6.9b), i.e.  $S_w = 70\%$ , the large pores in channels I and II are drained. The water in both channels becomes discontinuous, i.e.  $\eta_w(I) = \eta_w(II) = 0$ .

Therefore, the dependency of the water continuity on the pore tortuosity is insignificant since the water-filled pores in a channel, irrespective of its tortuosity, are no longer continuous only if one pore in the channel is drained (Fig. 6.9b).

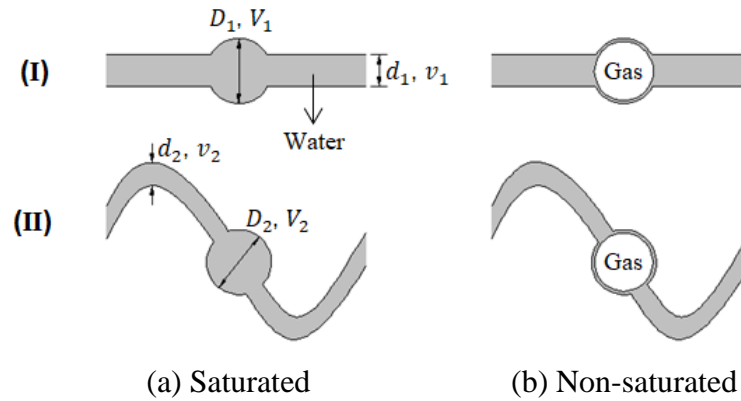


Fig. 6.9 The two channels with different pore tortuosities ( $\tau(II) > \tau(I)$ ) exhibit the same moisture distribution and water continuity.

#### 6.2.2.6 Summary

The analyses in Sections 6.2.2.1-6.2.2.5 reveal that the pore size distribution is a main indicator for water continuity  $\eta_w$  at high water saturation levels  $S_w$  (e.g.  $> 60\%$ ). The  $\eta_w$ - $S_w$  relation of SCMs-blended systems can be very different from that of OPC systems, because of their different pore size distribution. Compared to OPC systems the addition of SCMs, either FA or BFS, results in a finer pore size distribution, as already noted in Chapter 4. It is thus expected that systems FA-OPC or BFS-OPC exhibit lower water continuities than pure OPC systems of the same water saturation level  $S_w$  ( $> 60\%$ ). The addition of LP enlarges the pore size and, therefore, increases the water continuity  $\eta_w$ .

In unsaturated porous system the internal RH determines the smallest drained pore diameter  $d_p$  according to Eq. (2.6). The water-filled pores with diameter  $d \leq d_p$  dominate the water continuity  $\eta_w$  and unsaturated ionic transport. A reduction of the degree of water saturation  $S_w$  leads to a reduction of the internal RH. The RH- $S_w$  relation, often noted as water vapour desorption isotherm, will be obtained from experiments in order to quantitatively study the  $\eta_w$ - $S_w$  relationship of cementitious materials.

### 6.3 Experimental program: water vapour desorption isotherm

In the experimental program cementitious mortar samples were preconditioned to different uniform water content ( $S_w=18\sim 100\%$ , uniform RH). The RH value of these partially saturated mortar samples was measured. The obtained RH- $S_w$  plots were determined as the water vapour desorption isotherm (WVDI) of the mortars.

### 6.3.1 Materials and samples

Cylindrical mortar samples ( $\phi 100 \times 80$  mm) were cast for WVDI tests. For the details of mortar mixtures, see Table 5.1. The mortar samples were moist-cured ( $RH > 98\%$ ,  $20 \pm 0.1$  °C). After 370 days the top and bottom slices (15-mm thick) of the mortar samples were cut off. The middle part of each mortar sample (50-mm thick) was stored in lime water for one week, followed by sample preconditioning steps as described below.

### 6.3.2 Sample preconditioning for desired uniform water content

The saturated mortar samples were preconditioned to uniform water content ranging from 18 to 100%. The sample preconditioning proceeded in three steps.

*Step one: drying each sample at 50 °C to reach its desired  $S_w$ -value*

- 1) The lateral and bottom sides of the saturated mortar sample (50-mm thick) were sealed with isolating tape to avoid any multi-directional moisture transfer. Only the top side of the sample is left as drying surface.
- 2) The mortar sample was moved into a ventilated oven, which was heated gradually at a rate of 5 °C per hour up to 50 °C. A CO<sub>2</sub> absorbent (sodium hydroxide) was placed in the oven to minimize the carbonation effect.
- 3) The oven was evacuated until the pressure was below 50 Pa. The low pressure condition enables to dry the sample to a low water saturation level in a relatively short period.
- 4) The mass loss with time was recorded at frequent intervals during the first 6 hours, followed by one measurement per day later on. Figure 6.10 shows typical drying curves in an OPC mortar.

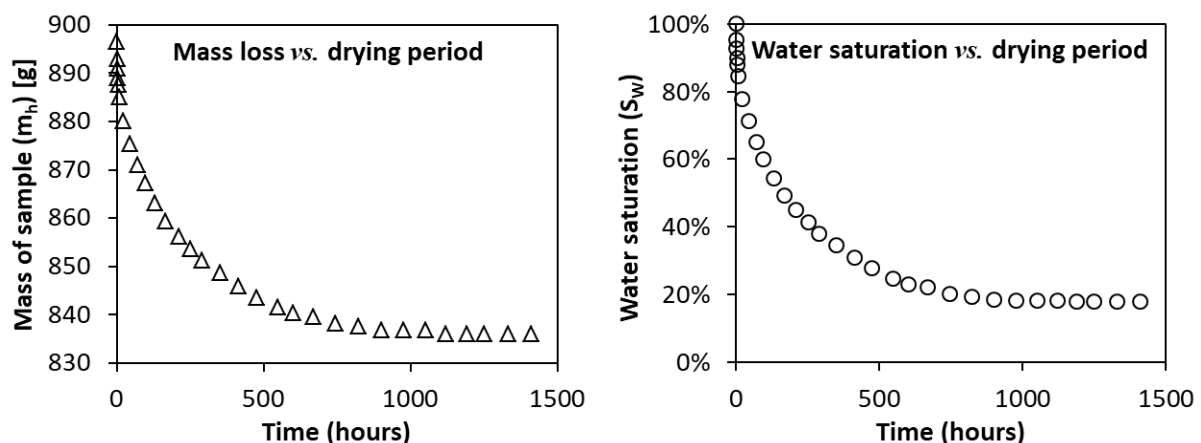


Fig. 6.10 Change of sample mass  $m_h$  (left) and related change of water saturation  $S_w$  (right) in an OPC mortar ( $w/c = 0.5$ , one-year-old) drying at 50 °C.

*Step two: monitoring moisture homogeneity by a moisture redistribution procedure*

Once the sample mass  $m_h$  corresponding to a given  $S_w$  level reaches its desired value, there may still exist a moisture gradient from the bottom to the top of the sample. A moisture

redistribution procedure is required to obtain homogeneous moisture distribution over the full height of the sample. To this end, all surfaces (top, bottom and lateral) of the sample were tightly sealed with isolating tape. The sample was then stored in a plastic bag at 50 °C for a certain period, i.e. 7~45 days, depending on the  $S_w$  level of the sample. During the storage period a great deal of moisture moved from the bottom to the top of the sample. Next the sample was gradually cooled down to  $30\pm 0.1$  °C.

The moisture homogeneity inside the sample was then monitored by using the set-up shown in Fig. 6.11 to measure the RH of the top and bottom of the sample.

- 1) The isolating tape on the top and bottom surfaces of the mortar sample was removed. The lateral side was still sealed.
- 2) The mortar sample was placed in a cylindrical chamber. The chamber was sealed with lid and maintained at  $30\pm 0.1$  °C. The RH changes with time at the top and bottom surfaces of the sample were monitored with two hygrometers. As expected, the RH-value on the top surface increased while that on the bottom surface decreased. Once the RH-values on both surfaces approached the same value (difference less than 1%), the moisture distribution inside the sample was considered homogeneous.
- 3) The sample was cooled down with 5 °C per hour to room temperature  $20\pm 0.1$  °C.
- 4) The sample was removed from the chamber. All the surfaces (top, bottom and lateral) of the sample were tightly sealed with isolating tape. The sample was then stored in a plastic bag to keep its specific water saturation level.

*Step three: evaluation on the preconditioned sample*

All preconditioned mortar samples were examined under an optical microscope with a magnification of  $\times 100$  to check the crack initiation. No micro-cracking was observed. By applying the preconditioning approach the water loss from mortar samples was found to be very slow when the internal RH of mortar samples approached 45%.

The RH of each mortar sample at its desired uniform water content  $S_w$  was recorded at  $20\pm 0.1$  °C by using the set-up shown in Fig. 6.11. The water vapour desorption isotherm (RH vs.  $S_w$ ) in the mortar samples with OPC and blended binders were determined.

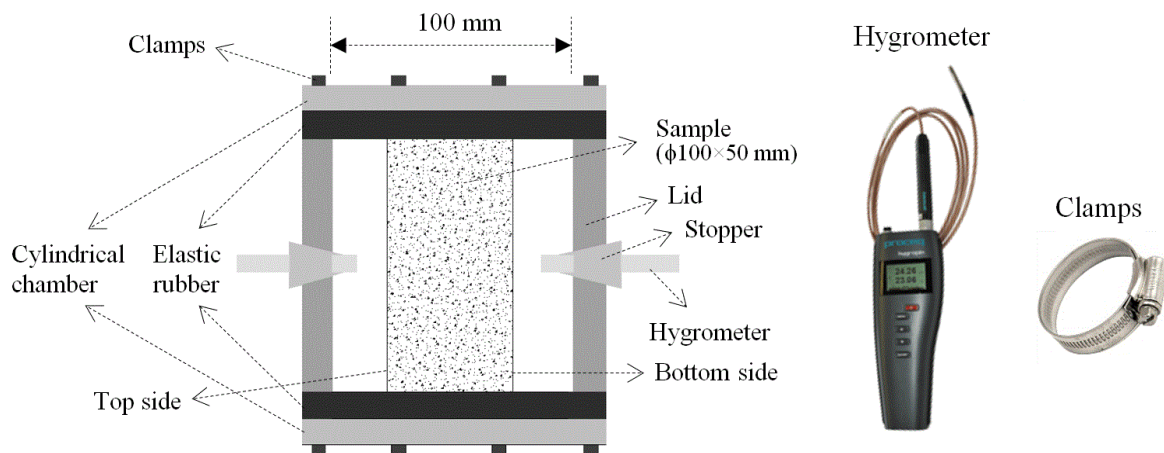


Fig. 6.11 Set-up for monitoring the moisture homogeneity inside unsaturated mortar sample.

## 6.4 Experimental results

### 6.4.1 Water vapour desorption isotherm (WVDI) in OPC mortars

Figure 6.12-left shows the water vapour desorption isotherms (WVDI) in one-year-old OPC mortars with w/c ratios of 0.4, 0.5 and 0.6. The degree of water saturation  $S_w$  drops when the RH decreases from 100 to 90%. Such drop is more significant for a higher w/c ratio. Almost linear RH- $S_w$  patterns are observed for all w/c ratios when the RH decreases from 90% ( $d_p = 21.8$  nm) to 50% ( $d_p = 4.0$  nm), where  $d_p$  is the smallest drained pore diameter by following Eq. (2.6). For a given saturation  $S_w$  a higher w/c ratio results in a higher RH. The RH- $S_w$  curves are more close to each other for w/c = 0.5 (M5) and w/c = 0.6 (M6), compared to that for w/c = 0.4 (M4). For instance, at RH=60%, the  $S_w$ -values are 54, 31 and 27% for M4, M5 and M6, respectively.

It is known that for a given saturation  $S_w$  the pore system with a finer pore size distribution (PSD) has a lower RH. Figure 6.12-right shows the PSD of 370-day-old cement pastes with w/c ratios of 0.4, 0.5 and 0.6. Obviously, a paste with lower w/c ratio shows a finer PSD. Each PSD curve contains a characteristic critical diameter  $d_{cr}$  and threshold diameter  $d_{th}$ . Both diameters for P6 are marked in Fig. 6.12-right. The pore size range from  $d_{cr}$  to  $d_{th}$  changes significantly with different w/c ratios. For small pores (diameter < 20 nm), the PSD curves for P5 and P6 are more close to each other than the PSD curve for P4.

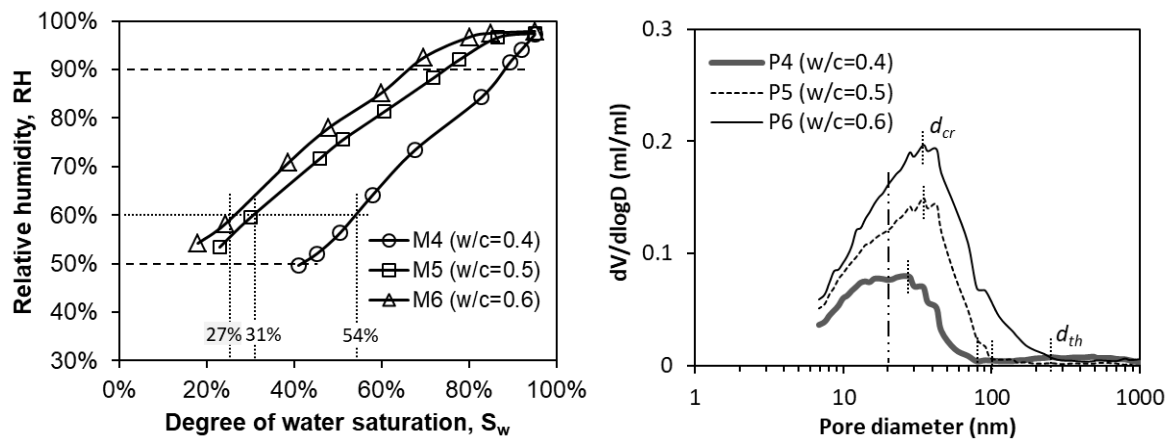


Fig. 6.12 (left) RH- $S_w$  relations in OPC mortars (370 days old). (right) Pore size distributions in OPC pastes (370 days old) by IEC-MIP tests (20<sup>th</sup> intrusion step of pressure Table 3.1).

### 6.4.2 Water vapour desorption isotherm (WVDI) in blended cement mortars

Figure 6.13-left shows the water vapour desorption isotherm (WVDI) in blended cement mortars (w/b = 0.5, one year old). Approximately linear RH- $S_w$  relations are observed in the blended mortars for  $S_w \leq 90\%$ . Compared to the reference OPC binder (M5), the binders incorporating FA (MF5) or BFS (MB5) show lower RH in the entire saturation range tested. The binders with LP, e.g. MFL5, show higher RH than the binders without LP, e.g. MF5.

Figure 6.13-right shows the pore size distributions in blended pastes ( $w/b = 0.5$ , one year old). In general, the binder with a finer pore size distribution tends to exhibit a lower RH. It is worthwhile to note that for mortar MB5 the RH changes in the range of 60~80% when the  $S_w$  varies in the wide range of 43~90%. The relatively small change of the RH in mortar MB5 is attributable to its narrow pore size distribution in the paste matrix PB5 (Fig. 6.13-right). The sharp drop of the RH in mortar MB5 when the  $S_w$  decreases in the high saturation levels ( $> 90\%$ ) can also be ascribed to the lack of large pores in the paste matrix PB5 (Fig. 6.13-right).

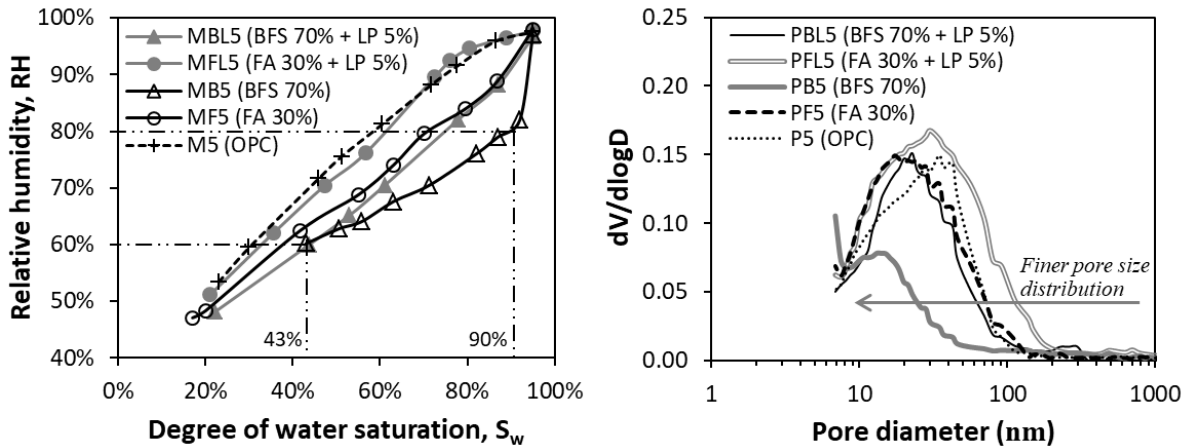


Fig. 6.13 (left) RH- $S_w$  relations in blended mortars (370 days old,  $w/b = 0.5$ ). (right) Pore size distributions in blended pastes (370 days old,  $w/b = 0.5$ ) by IEC-MIP tests ( $20^{\text{th}}$  intrusion step of pressure Table 3.1).

## 6.5 Discussion

### 6.5.1 Moisture distribution in unsaturated cementitious materials

For a given saturation level  $S_w$  there is a smallest drained pore diameter  $d_p$ . The  $d_p$ - $S_w$  plots are adopted to describe the moisture distribution in unsaturated cementitious materials. Figure 6.14 gives an example of the  $d_p$ - $S_w$  plots determined with the RH- $d_p$  relation (Eq. (2.6)) and the RH- $S_w$  relation (Fig. 6.12-left). The  $d_p$ -value drops rapidly when the  $S_w$  decreases in the range of high saturation levels (e.g.  $60\% \leq S_w \leq 100\%$ ), while it falls slowly with further decrease of the  $S_w$  (e.g.  $S_w < 60\%$ ). The  $d_p$ -value is larger for mixtures with a higher  $w/c$  ratio. The  $d_p$ - $S_w$  plots can be approximated with a power equation shown in Eq. (6.2), with correlation coefficients  $R^2$  of 0.96, 0.95 and 0.93 for M4, M5 and M6, respectively.

$$d_p = \frac{2c^2}{(1 - S_w)^2} \cdot d_0 \quad (6.2)$$

where  $d_0$  is the diameter for one-unit length pore ( $d_0 = 1$  nm);  $2c^2/(1 - S_w)^2$  is a moisture distribution factor. The coefficient  $c$  is related to the distribution of water-filled pores that depends primarily on the pore size distribution of the specimen. A smaller  $c$  value corresponds to a specimen with a finer pore size distribution.

To establish a quantitative relationship between coefficient  $c$  and pore size distribution, the *average pore diameter*  $d_a$  (defined by Eq. (3.3)) is used to characterize the fineness of pore size. Then the  $c$ -value shall be a function of  $d_a$ , as  $c = c(d_a)$ . The specific expression of  $c(d_a)$  will be determined based on experimental studies (see Chapter 7).

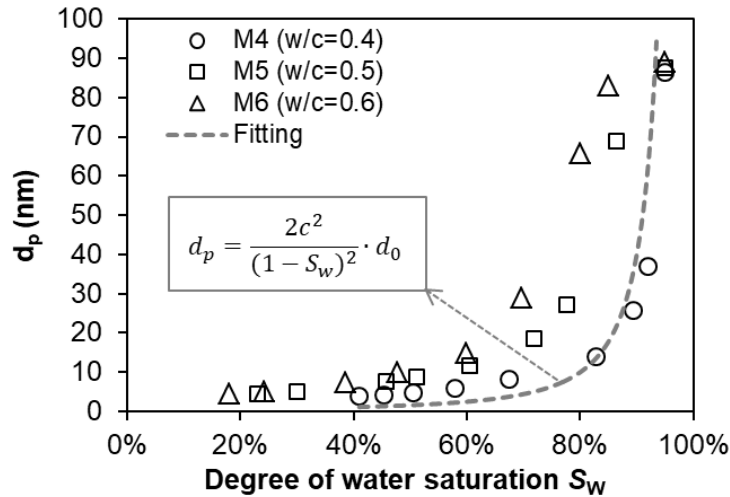


Fig. 6.14 Moisture distribution, i.e.  $d_p$ - $S_w$  plots, estimated from the water vapour desorption isotherm tests performed on cement mortars ( $w/c = 0.4, 0.5$  and  $0.6$ , one year old).  $d_p$  is the smallest drained pore diameter determined by the Kelvin law (Eq. (2.6)).

### 6.5.2 Water continuity in unsaturated cementitious materials

The water continuity  $\eta_w$  is determined primarily by the water-filled pores (diameter  $d \leq d_p$ ). A reduction of the degree of water saturation  $S_w$  results in a reduction of the  $d_p$ -value, and hence a reduction of the  $\eta_w$ -value. In a saturated pore system ( $S_w = 100\%$ ),  $d_p \rightarrow \infty$  and  $\eta_w = 1$ . When the pore system is drained ( $S_w$  approaching zero),  $d_p \rightarrow 0$  and  $\eta_w = 0$ . The  $\eta_w$ - $d_p$  relationship, which satisfies the two boundary conditions, can be described with an equation shown in Eq. (6.3).

$$\eta_w = e^{-\frac{d_0}{d_p}} \quad (6.3)$$

Combining Eqs. (6.2) and (6.3) leads to the expression for water continuity:

$$\eta_w = e^{-\frac{(1-S_w)^2}{2c^2}} \quad (6.4)$$

Equation (6.4) can be used to predict the water continuity  $\eta_w$  at various degrees of water saturation  $S_w$ , provided that the coefficient  $c$  of the material of interest is known. Equation (6.4) is a form of Gaussian function. The fact that the pore size distribution of cementitious materials estimated by MIP tests also shows a Gaussian distribution [Aligizaki 2006] confirms the pronounced dependence of the water continuity on the pore size distribution.

## 6.6 Conclusions

The moisture distribution and water continuity have been analyzed according to Kelvin's law and water vapour desorption isotherm in porous systems. The key findings are outlined as follows.

- 1) Moisture tends to accumulate in small pores. However, idealised moisture distribution hardly occurs in cementitious materials due to the presence of ink-bottle pore geometry.
- 2) In unsaturated pore systems the water-filled pores are divided into one part that has a continuity allowing ionic transport and the other part that does not. A mathematical relationship between water continuity  $\eta_w$  and degree of water saturation  $S_w$  has been established (Eq. (6.4)).
- 3) The water continuity  $\eta_w$  decreases with decreasing degree of water saturation  $S_w$ . The  $\eta_w$ - $S_w$  relationship is controlled by the pore structure. Porosity and tortuosity have little influence on the  $\eta_w$ - $S_w$  relationship. Finer pore size distribution or lower pore connectivity (i.e. higher pore entrapment) tends to result in lower water continuity  $\eta_w$ . The pore size effect on water continuity  $\eta_w$  is pronounced primarily at high water saturation levels. The water continuity  $\eta_w$  at low water saturation levels is dominated by the pore connectivity.
- 4) A sample preconditioning procedure has been described and utilized to prepare mortar samples with internal RH as low as 45%. The changes of internal RH with different  $S_w$  levels, i.e. water vapour desorption isotherm, are determined by the pore size distribution of the specimen. Incorporating FA (30%) or BFS (70%) results in *lower* RH, whereas the addition LP (5%) results in *higher* RH, compared to the reference OPC mortar of a given degree of water saturation  $S_w$ .

## Chapter 7

# Relative Chloride Diffusion Coefficient in Unsaturated Cementitious Materials

## 7.1 Introduction

In unsaturated cementitious materials the relative chloride diffusion coefficient  $D_{rc}$  is determined by the *continuous water*, which depends on the degree of water saturation  $S_w$  and water continuity  $\eta_w$  (see Fig. 7.1).

In this chapter (see Fig. 7.2) the concept shown in Fig. 7.1 is studied in detail. An analytical formula for predicting the  $D_{rc}$  at various degrees of water saturation  $S_w$  is developed

based on the Nernst-Einstein equation and conductivity of cementitious electrolyte. The conductivity is mathematically described as a function of the microstructure and moisture distribution (i.e. water continuity  $\eta_w$ ) in cementitious materials. In parallel, conductivity experiments are carried out and the data obtained are used to validate the formula developed. The effects of SCMs on the  $D_{rc}$ - $S_w$  relationship are emphasized. The formula is helpful for the designer to understand the actual serviceability of marine concrete structures.

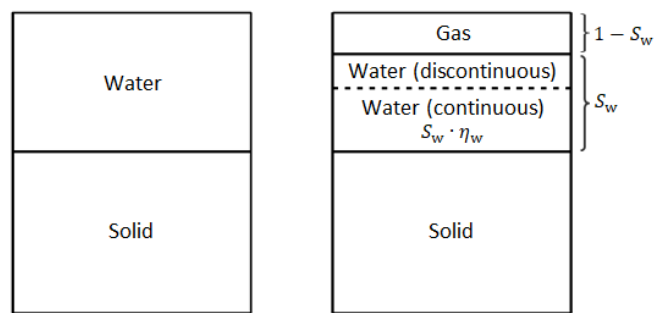


Fig. 7.1 Components in saturated (left) and unsaturated (right) cementitious materials.

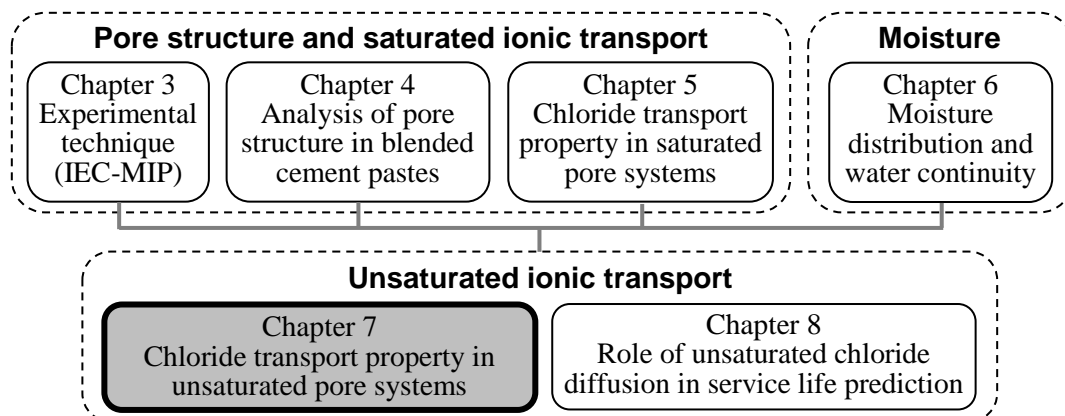


Fig. 7.2 Main chapters of the thesis.

## 7.2 Mathematical description of relative chloride diffusion coefficient

The water-filled pores in unsaturated cementitious materials are categorized into two parts. One part can form a continuous network allowing ionic transport while the other part cannot. The water continuity  $\eta_w$ , which has been described in Chapter 6, plays a significant role in the unsaturated chloride diffusion. To describe the relative chloride diffusion coefficient  $D_{rc}$ , a proper method for determining the mass transport property should be used. It is known that the chloride diffusion test is complicated when it comes to unsaturated cementitious materials, because of the fact that forcing chlorides into an unsaturated specimen may alter its interior moisture condition and/or microstructure and that testing the chloride diffusion in an unsaturated specimen is time consuming. The conductivity test, in contrast, has an obvious advantage because of its non-destructive and rapid nature. The latter approach will therefore be applied to determine the relative chloride diffusion coefficient  $D_{rc}$ .

In the mathematical descriptions three assumptions are made: (1) chloride binding and electrochemical effects on chloride diffusion are not taken into account; (2) cementitious system at any particular saturation level has a homogeneous moisture distribution; (3) all pore water is regarded as a solute.

### 7.2.1 Nernst-Einstein equation

The Nernst-Einstein equation (Eq. (7.1)) shows that the ratio of the conductivity  $\sigma_p$  of the pore solution to the conductivity  $\sigma$  [S/m] of the cementitious system is equal to the ratio of the chloride diffusion coefficient  $D_p$  in the pore solution to the chloride diffusion coefficient  $D$  [m<sup>2</sup>/s] in the cementitious system. In geoscience literature this ratio is defined as formation factor  $F_0$  [Manheim et al. 1974]:

$$F_0 = \frac{\sigma_p}{\sigma} = \frac{D_p}{D} \quad (7.1)$$

where the  $D_p$ -value is around  $1.5 \times 10^{-9}$  m<sup>2</sup>/s at room temperature when the chloride concentration of the pore solution is in the range of 0.1~1.0 mol/L [Weast 1976]. The  $\sigma_p$ -value is determined by the pore solution chemistry which changes with the degree of water saturation  $S_w$ . The  $D$ -value can be calculated from the  $\sigma$ -value, after correcting the  $\sigma_p$ -value for the water saturation level  $S_w$ .

### 7.2.2 Conductivity $\sigma$ of cementitious system

The conductivity  $\sigma$  of cementitious system is the inverse of its resistivity  $\rho$  [ $\Omega \cdot m$ ]:

$$\sigma = \frac{1}{\rho} = \frac{mL}{A} \cdot \frac{1}{R} \quad (7.2)$$

where  $m$  is the geometry factor of the specimen ( $m = 1$  for cylindrical specimen);  $L$  [m],  $A$  [m<sup>2</sup>] and  $R$  [ $\Omega$ ] represent the length, the cross sectional area and the electrical resistance, respectively. For direct current the resistance  $R$  is determined by Ohm's law and equal to the ratio of the voltage  $U$  applied to a specimen's ends over the current  $I$  passing through.

Figure 7.3-left schematically illustrates a cementitious system made of different phases in parallel layers. The parameters  $R_s$ ,  $R_p$  and  $R_v$  are the electrical resistance of the solid phase, the pore solution phase and the vapour phase, respectively. The parameters  $A_s$ ,  $A_p$  and  $A_v$  are the cross sectional area of the solid phase, the pore solution phase and the vapour phase, respectively. Figure 7.3-right shows the electrical model of the resistivity under direct current.

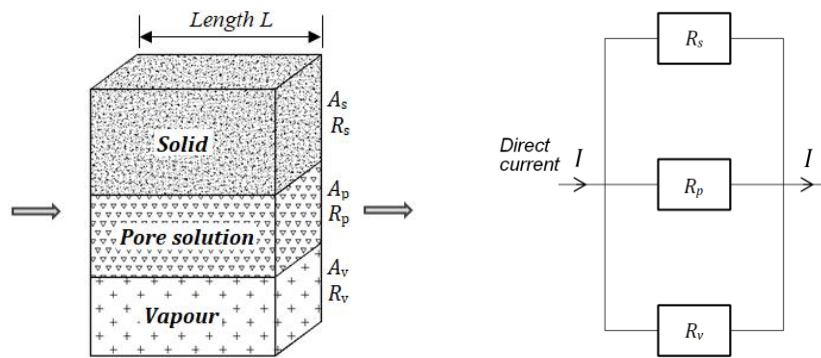


Fig. 7.3 (left) Schematic representation of a cementitious system made of different phases in parallel layers. For each phase layer,  $R_i$  and  $A_i$  are the electrical resistance and the cross sectional area, respectively. (right) Electrical model of resistivity under direct current.

The total resistance of the cementitious system,  $R$ , depends on the resistance of each phase:

$$\frac{1}{R} = \frac{1}{R_s} + \frac{1}{R_p} + \frac{1}{R_v} \quad (7.3)$$

Combining Eqs. (7.2) and (7.3) gives the expression for the conductivity  $\sigma$  of the system:

$$\sigma A = \sigma_s A_s + \sigma_p A_p + \sigma_v A_v \quad (7.4)$$

where  $\sigma_s$ ,  $\sigma_p$  and  $\sigma_v$  are the conductivity of the solid phase, the pore solution phase and the vapour phase, respectively;  $\sigma$  and  $A$  are the total conductivity and the total exposed surface area of the specimen, respectively; The  $A$ -value is expressed as  $A = A_s + A_p + A_v$ .

Multiplying both sides of Eq. (7.4) with the specimen length  $L$  yields:

$$\sigma V = \sigma_s V_s + \sigma_p V_p + \sigma_v V_v \quad (7.5)$$

where  $V_s$ ,  $V_p$  and  $V_v$  are the volume of the solid phase, the pore solution phase and the vapour phase, respectively. If the volume fraction of each phase is noted as  $\phi_i = V_i/V$ , where  $V$  is the total volume of the specimen, Eq. (7.5) can be written as Eq. (7.6).

$$\sigma = \sigma_s \phi_s + \sigma_p \phi_p + \sigma_v \phi_v \quad (7.6)$$

It is known that the different phases in cementitious system are not completely in parallel layers [Christensen 1993]. A structure factor  $\beta_i$  is introduced to allow for the effect of the actual structure of each phase on ionic conduction and Eq. (7.6) is thus replaced with Eq. (7.7).

$$\sigma = \sigma_s \phi_s \beta_s + \sigma_p \phi_p \beta_p + \sigma_v \phi_v \beta_v \quad (7.7)$$

where  $\beta_s$ ,  $\beta_p$  and  $\beta_v$  are the structure factor of the solid phase, the pore solution phase and the vapour phase, respectively.

In cementitious materials the conductivity of the pore solution phase,  $\sigma_p$ , is usually many orders of magnitude higher than that of the solid phase  $\sigma_s$  and vapour phase  $\sigma_v$  [Rajabipour 2006]. The  $\sigma_p$ -value is in the range of 1~20 S/m,  $\sigma_s$ -value is around  $10^{-9}$  S/m, and  $\sigma_v$ -value is in the order of  $10^{-15}$  S/m. Hence Eq. (7.7) can be approximated as:

$$\sigma \approx \sigma_p \phi_p \beta_p \quad (7.8)$$

The structure factor  $\beta_p$  of the pore solution phase is related to the interconnected water-filled capillary pores, which depend on the pore structure characteristics (indicated by a parameter  $\mu_p$  accounting for connectivity and tortuosity [Tumidajski et al. 1996]) and the moisture condition (indicated by water continuity  $\eta_w$ ).

At *saturated* state ( $S_w = 100\%$ ) the volume fraction  $\phi_p$  of the pore solution phase is equal to the total porosity  $\phi_t$  of the specimen and the structure factor  $\beta_p$  is determined by the pore structure parameter  $\mu_p$  alone. Equation (7.8) is rewritten as:

$$\sigma_{\text{Sat}} \approx \sigma_{p,\text{Sat}} \cdot \phi_t \cdot \mu_p \quad (7.9)$$

where  $\sigma_{\text{Sat}}$  is the conductivity of the specimen at saturated state;  $\sigma_{p,\text{Sat}}$  is the conductivity of the pore solution at saturated state. Combining Eqs. (7.1) and (7.9) leads to the expression of the formation factor for saturated specimen:

$$F_{0,\text{Sat}} = \frac{\sigma_{p,\text{Sat}}}{\sigma_{\text{Sat}}} \approx \frac{1}{\phi_t \cdot \mu_p} \quad (7.10)$$

At *non-saturated* state ( $S_w < 100\%$ ) the volume fraction  $\phi_p$  of the pore solution phase is equal to  $\phi_t S_w$  and the structure factor  $\beta_p$  is determined by both the pore structure parameter  $\mu_p$  and the water continuity  $\eta_w$ , as  $\beta_p = \mu_p \eta_w$ . Equation (7.8) is then modified as:

$$\sigma_{S_w} \approx \sigma_{p,S_w} \cdot \phi_t S_w \cdot \mu_p \eta_w \quad (7.11)$$

where  $\sigma_{S_w}$  is the conductivity of the specimen at a particular saturation  $S_w$ ;  $\sigma_{p,S_w}$  is the conductivity of the pore solution at a particular saturation  $S_w$ . Combining Eqs. (7.1) and (7.11) leads to the expression of the formation factor for non-saturated specimen:

$$F_{0,S_w} = \frac{\sigma_{p,S_w}}{\sigma_{S_w}} \approx \frac{1}{S_w \phi_t \cdot \mu_p \eta_w} \quad (7.12)$$

### 7.2.3 Relative chloride diffusion coefficient $D_{rc}$

The relative chloride diffusion coefficient  $D_{rc}$  is expressed as the ratio of the chloride diffusion coefficient  $D_{S_w}$  at a particular degree of water saturation over the chloride diffusion coefficient  $D_{Sat}$  at saturated state. Based on the Nernst-Einstein equation (Eq. (7.1)), the  $D_{S_w}$  and the  $D_{Sat}$  can be calculated with Eq. (7.13) and Eq. (7.14), respectively.

$$D_{S_w} = \frac{\sigma_{S_w}}{\sigma_{p,S_w}} \cdot D_p \quad (7.13)$$

$$D_{Sat} = \frac{\sigma_{Sat}}{\sigma_{p,Sat}} \cdot D_p \quad (7.14)$$

Then the relative chloride diffusion coefficient  $D_{rc}$  of cementitious material is expressed as:

$$D_{rc} = \frac{D_{S_w}}{D_{Sat}} = \frac{\sigma_{S_w}}{\sigma_{Sat}} \cdot \frac{\sigma_{p,Sat}}{\sigma_{p,S_w}} \quad (7.15)$$

Incorporating Eqs. (7.9) and (7.11) into Eq. (7.15) gives:

$$D_{rc} = \frac{D_{S_w}}{D_{Sat}} = S_w \cdot \eta_w \quad (7.16)$$

The water continuity  $\eta_w$ , as described with Eq. (6.4) in Chapter 6, is a function of the degree of water saturation  $S_w$ . Equation (7.16) is then rewritten as Eq. (7.17):

$$D_{rc} = \frac{D_{S_w}}{D_{Sat}} = S_w \cdot e^{-\frac{(1-S_w)^2}{2 \cdot c^2}} \quad (7.17)$$

where the coefficient  $c$  is related to the average pore diameter  $d_a$ , as already noted in Chapter 6. The  $c$ - $d_a$  relation can be determined from experimental studies (see Section 7.5.3). As will be shown, a larger  $d_a$ -value (i.e. a coarser pore size distribution) results in a larger  $c$ -value. For hydrated cementitious materials the  $c$ -value is usually in the range 0~0.45.

The parameters in Eq. (7.15),  $\sigma_{Sat}$ ,  $\sigma_{S_w}$ ,  $\sigma_{p,Sat}$  and  $\sigma_{p,S_w}$ , are obtainable from conductivity experiments. The experimental  $D_{rc}$ - $S_w$  data (Eq. (7.15)) can be used to validate the mathematical  $D_{rc}$ - $S_w$  relation (Eq. (7.17)). The details are given in Sections 7.3, 7.4 and 7.5. Figure 7.4 shows the  $D_{rc}$ - $S_w$  curves calculated by Eq. (7.17) with the coefficient  $c$  varying from 0.05 up to 0.9. At  $c = 0.05$  the  $D_{rc}$ -value highly depends on the degree of water saturation  $S_w$ . The dependence of the  $D_{rc}$ -value on the  $S_w$  is less pronounced in a cementitious material with higher  $c$ -value. The  $D_{rc}$ - $S_w$  relationship is almost linear for  $c \geq 0.7$ .

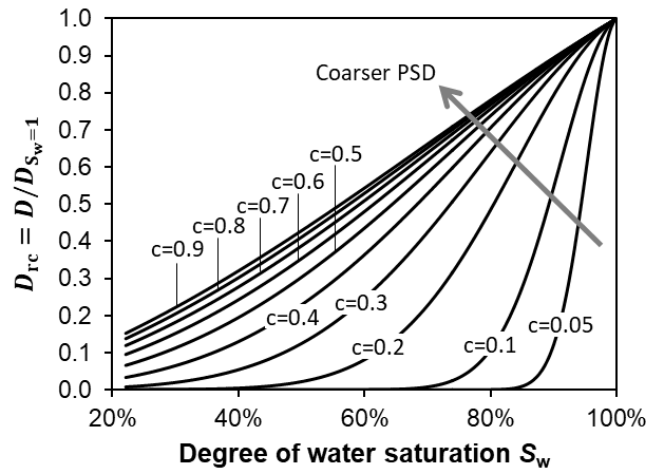


Fig. 7.4 The  $D_{rc}$ - $S_w$  curves calculated by Eq. (7.17) with the coefficient  $c$  varying in the range 0.05...0.9. A coarser PSD (pore size distribution) corresponds to a larger  $c$  value.

## 7.3 Experimental program

### 7.3.1 Sample preparation

Mortar samples were prepared for resistivity measurements and analyses of the pore solution chemistry. The details of the mortar mixtures were the same as those shown in Table 5.1. The saturated mortar samples ( $\phi 100 \times 50$  mm, one year old) were preconditioned to uniform water content  $S_w$  ranging from 18 to 100% by following the preconditioning procedures described in Section 6.3.2 (Chapter 6). Resistivity tests were then carried out on these mortar samples. Another series of saturated mortar samples ( $\phi 50 \times 100$  mm, one year old) was subjected to pressure up to 1000 MPa by following the method proposed by Barneyback et al. [1981]. The extracted pore solutions were collected and filtered using a  $0.45 \mu\text{m}$  pore size filter to remove the possible residual particles and then used for pore solution chemistry analyses.

### 7.3.2 Conductivity $\sigma_{p,S_w}$ of pore solution at various saturation levels

The conductivity  $\sigma_{p,S_w}$  of pore solution is governed mainly by the concentration of ions, viz. hydroxide ( $\text{OH}^-$ ) and alkalis ( $\text{Na}^+$ ,  $\text{K}^+$ ) [Snyder et al. 2003]. These ionic concentrations will be determined for mortar specimens at various saturation levels  $S_w$ .

The chemical composition of the pore solutions extracted from saturated mortars ( $S_w = 100\%$ ) was measured by Inductively coupled plasma atomic emission spectroscopy (ICP-OES) [Hou et al. 2000]. The concentrations of alkalis ( $\text{Na}^+$ ,  $\text{K}^+$ ) were obtained. The concentration of the  $\text{OH}^-$  was calculated as the sum of the concentrations of the alkalis ( $\text{Na}^+$ ,  $\text{K}^+$ ) [Taylor 1987]. A decrease of the saturation level  $S_w$  results in a *non-linear* increase of the alkali concentrations, because of the non-linear binding isotherm of the alkalis ( $\text{Na}^+$ ,  $\text{K}^+$ ) in cementitious materials. The relationship between bound alkalis (mainly by C-S-H) content and free alkalis (in pore solution) content can be described as [Chen et al. 2010]:

$$C_{\text{Na}} = \frac{n_{\text{Na}}^r}{\phi_t \cdot S_w + Rd \cdot m_{\text{C-S-H}}} \quad (7.18)$$

$$C_{\text{K}} \cdot \phi_t \cdot S_w + K_f \cdot (C_{\text{K}})^{0.24} \cdot m_{\text{C-S-H}} = n_{\text{K}}^r \quad (7.19)$$

where  $C_{\text{Na}}$  and  $C_{\text{K}}$  are the alkali concentration (mol/L) in the pore solution for  $\text{Na}^+$  and  $\text{K}^+$ , respectively;  $Rd$  is the distribution ratio ( $0.45 \times 10^{-3}$  L/g);  $K_f$  is the adsorption coefficient ( $0.20 \times 10^{-3}$  L/g);  $\phi_t$  is the total porosity;  $S_w$  is the degree of water saturation;  $m_{\text{C-S-H}}$  is the mass of C-S-H;  $n_{\text{Na}}^r$  and  $n_{\text{K}}^r$  are the moles of alkalis released during the hydration process for  $\text{Na}^+$  and  $\text{K}^+$ , respectively.

The  $m_{\text{C-S-H}}$  value was estimated by TGA/DSC with the assumption that the released water was from the thermal decomposition of C-S-H ( $105 \sim 1100$  °C) and calcium hydroxide ( $400 \sim 550$  °C) [Zhang 2013b]. The C-S-H is simplified as the composition of  $\text{C}_{1.7}\text{SH}_4$  for OPC binders and as  $\text{C}_{1.5}\text{SH}_{3.8}$  for FA/slag blended binders [Young et al. 1987]; At  $S_w = 100\%$ ,  $C_{\text{Na}}$  and  $C_{\text{K}}$  were measured from ICP-OES. Substituting the values of  $\phi_t$ ,  $m_{\text{C-S-H}}$ ,  $C_{\text{Na}}$ , and  $C_{\text{K}}$  into Eqs. (7.18) and (7.19) determines the values of  $n_{\text{Na}}^r$  and  $n_{\text{K}}^r$ . The parameters  $n_{\text{Na}}^r$ ,  $n_{\text{K}}^r$ ,  $K_f$ ,  $Rd$ ,  $\phi_t$  and  $m_{\text{C-S-H}}$  are considered constant for a given cementitious material. Hence the concentrations  $C_{\text{Na}}$  and  $C_{\text{K}}$  of the alkalis  $\text{Na}^+$  and  $\text{K}^+$  at different saturation levels  $S_w$  can be determined.

The pore solution chemistry of mortar specimens at various saturation levels ( $S_w < 100\%$ ) was predicted with Eqs. (7.18) and (7.19). Synthetic solutions were then prepared by mixing solids NaOH and KOH with distilled water in proper proportions to achieve the same chemical compositions as the concentrations of the ions  $\text{Na}^+$ ,  $\text{K}^+$  and  $\text{OH}^-$  at each saturation level  $S_w$ . The conductivities of the pore solution at various saturation levels, viz.  $\sigma_{p,S_w}$ -values, were obtained from conductivity tests performed on these synthetic solutions.

### 7.3.3 Conductivity $\sigma_{S_w}$ of mortar specimens at various saturation levels

Figure 7.5 illustrates the resistivity tests performed on mortar specimens. The electrical resistance  $R$  was measured with one stainless steel electrode covering each end of the specimen. A wet sponge was applied between specimen surface and each electrode to ensure the whole surface specimen under current flow. During the test the measured resistance  $R$  was found to decrease gradually with the testing time. This can be attributed to the moisture transfer from the wet sponge into the specimen. To minimize this effect, the result obtained from the first measurement of electrical resistance  $R$  was adopted. The resistivities ( $\rho$ -values), as well as the conductivities ( $\sigma_{S_w}$ -values), of the mortar specimens tested were calculated as a function of the measured resistances  $R$  by using Eq. (7.2).

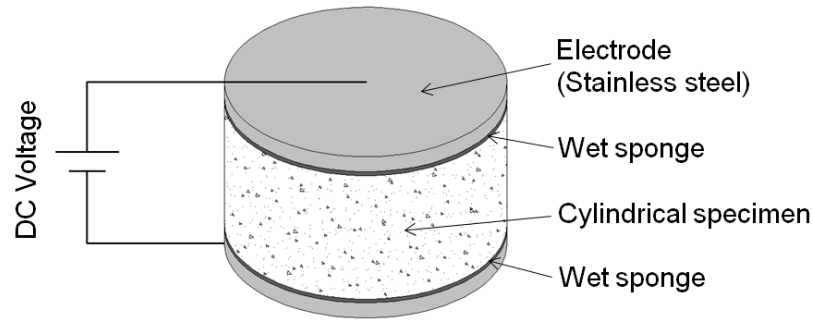


Fig. 7.5 Resistivity test on a cylindrical specimen under direct current (DC).

A summary of the experimental program is listed in Table 7.1.

Table 7.1 Summary of the experimental program

	Main contents	Remark
Materials & measurements	Materials	Table 5.1
	Mixture proportions	Subsection 6.3.2
	One-year-old unsaturated mortar samples	
	Pore solution chemistry and conductivity tests	Subsection 7.3.2
	Conductivity of unsaturated mortar specimens	Subsection 7.3.3
Experimental results of conductivity $\sigma$	Ionic concentration at various saturations	Subsection 7.4.1.1
	Conductivity $\sigma_{p,S_w}$ of pore solution at various saturations	Subsection 7.4.1.2
	Conductivity $\sigma_{S_w}$ of mortars at various saturations	Subsection 7.4.2.1
	Formation factor $F_{0,S_w}$ of unsaturated mortars	Subsection 7.4.2.2
Experimental results of relative chloride diffusion coefficient $D_{rc}$	$D_{rc}$ in OPC mortars	Subsection 7.4.3
	Effect of binder type on $D_{rc}$ - $S_w$ relation	Subsection 7.4.4.1
	Effect of w/b ratio on the $D_{rc}$ - $S_w$ relation in slag-blended binders	Subsection 7.4.4.2

## 7.4 Experimental results and discussion

### 7.4.1 Conductivity $\sigma_{p,S_w}$ of pore solution in unsaturated mortars

#### 7.4.1.1 Ionic concentrations at various saturation levels

The ionic concentrations in the pore solutions of cementitious mortars at different degrees of water saturation  $S_w$  were calculated with Eqs. (7.18) and (7.19). The results are shown in Fig. 7.6. The concentration of  $K^+$  is generally higher than that of  $Na^+$ , regardless of the binder type or saturation level  $S_w$ . The concentrations of the ions  $Na^+$ ,  $K^+$  and  $OH^-$  show a non-linear increasing trend with decreasing saturation level  $S_w$ . Compared to the OPC binders, the binders incorporating SCMs (FA, BFS or LP) exhibit lower ionic concentrations. The lowest ionic concentrations are observed in the BFS-blended binders.

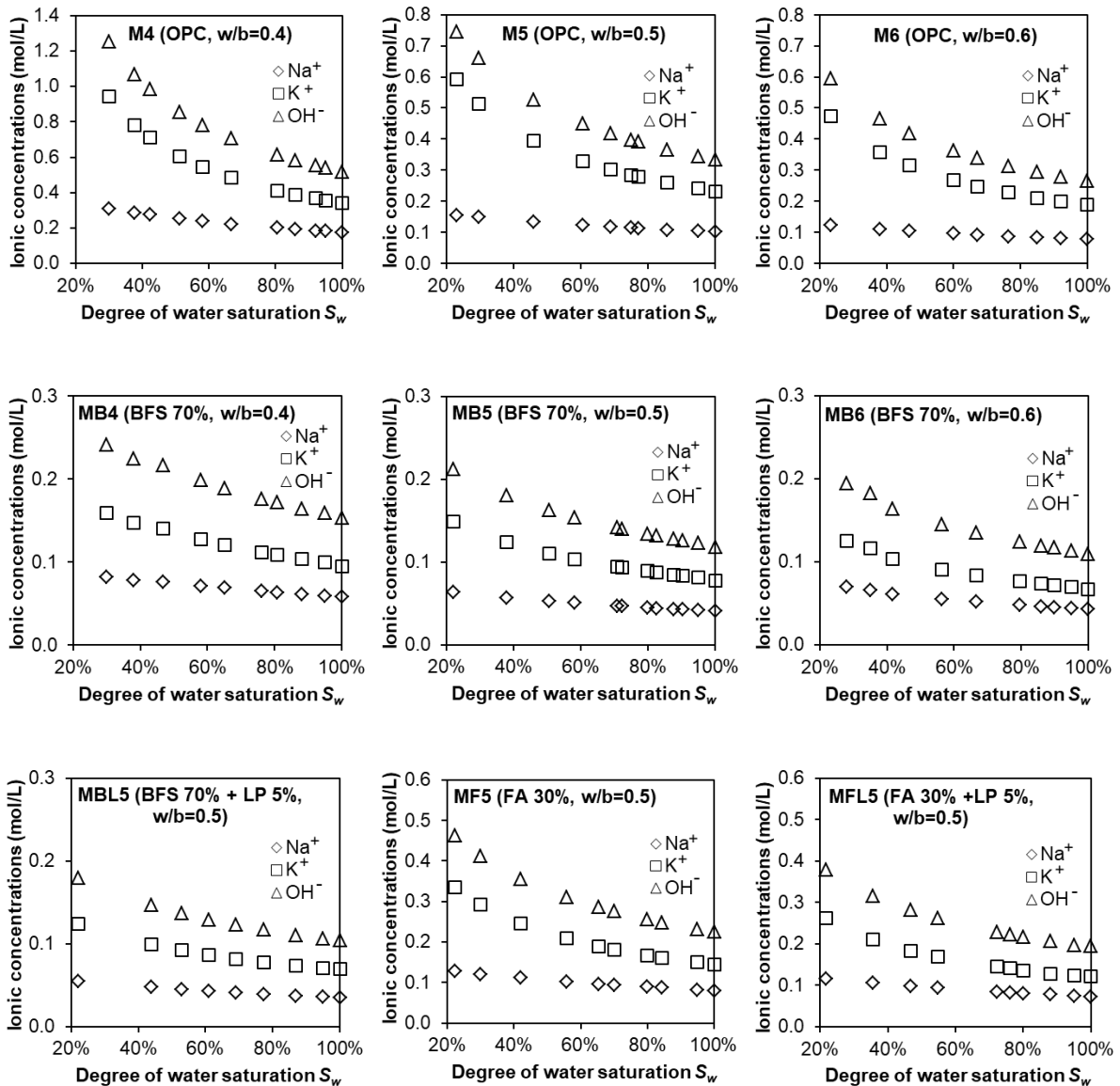


Fig. 7.6 Ionic concentrations in the pore solution at different degrees of water saturation  $S_w$  in one-year-old cementitious mortars made with different binders. Note that for clarity the vertical scales are different for different mixtures.

#### 7.4.1.2 Conductivity $\sigma_{p,S_w}$ of pore solution at various saturation levels

Figure 7.7 presents the conductivity  $\sigma_p$  of pore solution in unsaturated mortars at different degrees of water saturation  $S_w$ . For any particular  $S_w$  the binders blended with SCMs (FA, BFS or LP) generally show lower  $\sigma_p$ -values than the reference OPC binders. The lowest  $\sigma_p$ -values are found in the binders blended with 70% BFS. The  $\sigma_p$ -value increases non-linearly with decreasing  $S_w$ . Especially for  $S_w < 60\%$ , a relatively rapid increase of the  $\sigma_p$ -value is observed as the  $S_w$  further decreases. The  $\sigma_p$ -value is almost doubled when the  $S_w$  decreases from 100% to 30%, regardless of the w/b ratio or the type of cement.

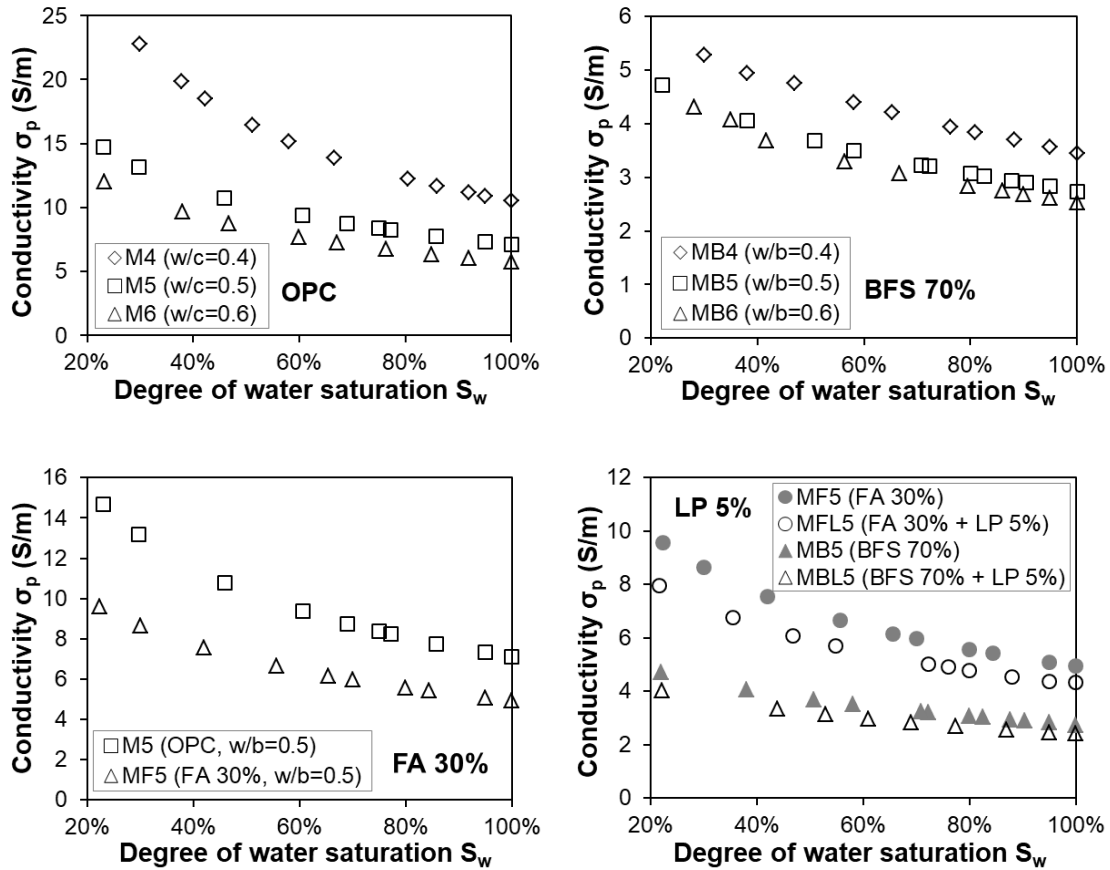


Fig. 7.7 Conductivity  $\sigma_p$  of pore solution at different degrees of water saturation  $S_w$  in one-year-old mortars made with different binders (OPC, BFS 70%, FA 30% and LP 5%).

#### 7.4.2 Conductivity $\sigma_{S_w}$ of unsaturated mortars

The relative conductivity  $\sigma_{S_w}/\sigma_{S_w=1}$  as a function of the degree of water saturation  $S_w$  was determined for one-year-old mortars mentioned in Table 7.1. Figure 7.8 presents an example of the relative conductivity for three different mortars. These mortars were made with a constant w/b ratio of 0.5, but with different binders. The relative conductivity shows an increasing trend with increasing saturation level  $S_w$ . For a given  $S_w$  the relative conductivity shows the lowest value in the mortar MB5 (BFS 70%), followed by mortar MF5 (FA 30%) and mortar M5 (OPC).

Figure 7.9 shows the formation factor  $F_0$  as a function of the degree of water saturation  $S_w$  for different mortars. The  $F_0$ -value is not a constant but increases with decreasing saturation level  $S_w$ . This is in line with the theoretical analysis described in Eq. (7.12), and also with the previous finding by Mercado-Mendoza et al. [2013]. The  $F_0$ -values are generally lower for the OPC binder M5 than for the blended binders, regardless of the  $S_w$ . The formation factor  $F_{0,S_w}$  enables us to obtain the ionic conductivity/diffusion coefficient in cementitious materials directly from the ionic conductivity/diffusion coefficient in the pore solution.

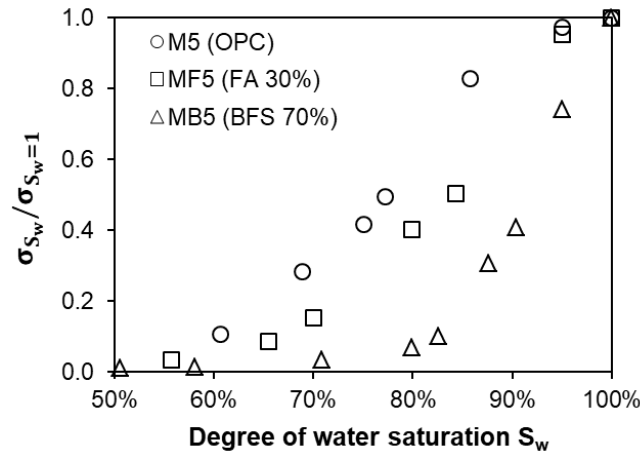


Fig. 7.8 Relative conductivity ( $\sigma_{S_w} / \sigma_{S_w=1}$ ) as a function of the degree of water saturation  $S_w$  in one-year-old mortars with the same w/b ratio of 0.5, but with different binders.

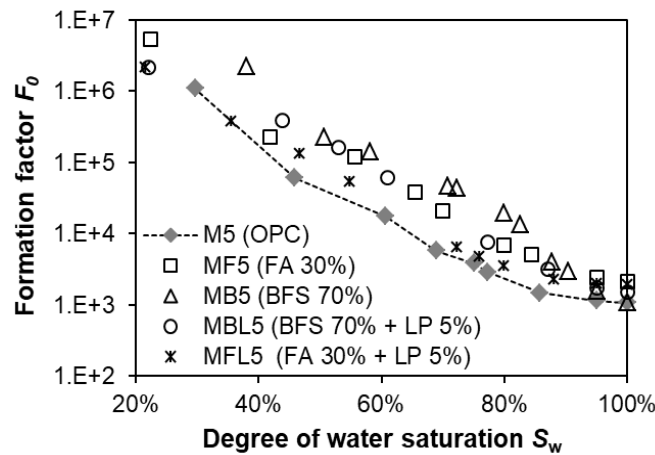


Fig. 7.9  $F_0$ - $S_w$  relation in different mortars (one-year-old, w/b = 0.5).

### 7.4.3 Relative chloride diffusion coefficient $D_{rc}$ in OPC mortars

Figure 7.10 presents the  $D_{rc}$ - $S_w$  relations in the OPC mortars with w/c ratios of 0.4, 0.5 and 0.6. The  $D_{rc}$  highly depends on the  $S_w$ , regardless of the w/c ratios. The change of the  $D_{rc}$  with decreasing  $S_w$  can be divided into three stages. An example of the three-stage  $D_{rc}$ - $S_w$  relation is marked for mortar M6 (w/c = 0.6). When the  $S_w$  starts to decrease from the saturated state the  $D_{rc}$ -value shows a slight decrease (stage I). There is a sharp drop in the  $D_{rc}$ -value when the  $S_w$  reduces from 90% to 60% (stage II), followed by only a slight decline in stage III. At each stage the saturation range differs for different w/c ratios. For w/c = 0.4 (M4), the stage II corresponds to the saturation range 65~95%.

At a particular  $S_w$  the  $D_{rc}$  is higher in the OPC mortars with a higher w/c ratio. For instance, at  $S_w = 80\%$  the  $D_{rc}$ -value is 0.34 for M4 (w/c = 0.4), compared to 0.58 and 0.67 for M5 (w/c = 0.5) and M6 (w/c = 0.6), respectively. The  $D_{rc}$ - $S_w$  curves for M5 and M6 are closer to each other, compared to the  $D_{rc}$ - $S_w$  curve for M4. It indicates that the role of the w/c ratio in the  $D_{rc}$ - $S_w$  relation becomes less pronounced with increasing w/c ratio.

The decrease of the  $D_{rc}$  against decreasing  $S_w$  can be ascribed primarily to three aspects:

- 1) The amount of water available for the ionic transport is lower;
- 2) The number of transport channels (i.e. continuous water-filled paths) becomes smaller;
- 3) The interaction forces between chloride ions and cement paste will increase due to the decreased thickness of the water layers adsorbed on the pore walls.

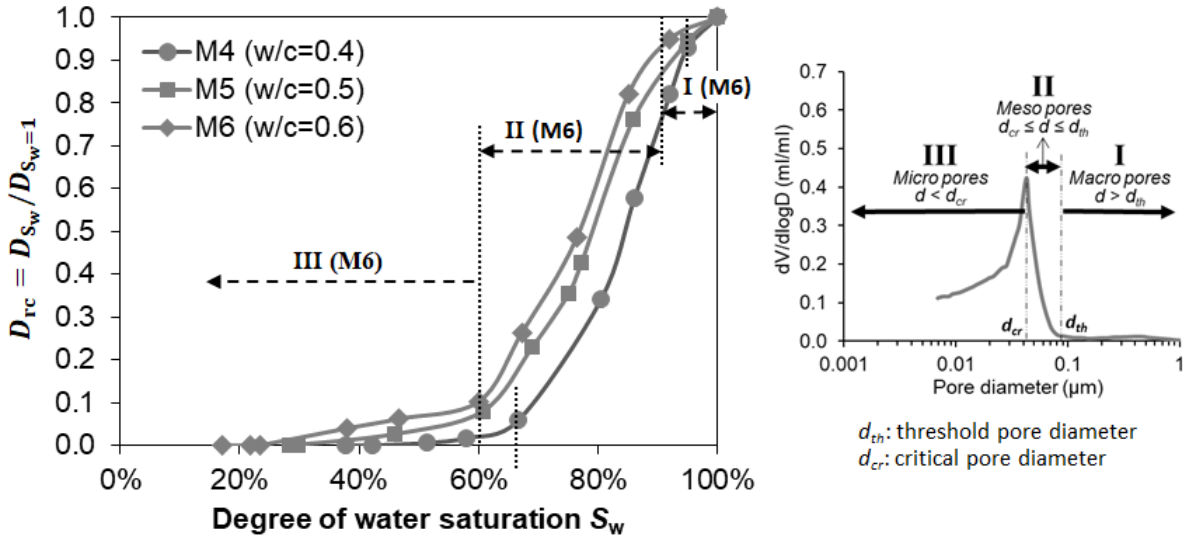


Fig. 7.10 (left)  $D_{rc}$ - $S_w$  relations in the OPC mortars (one-year-old,  $w/c = 0.4, 0.5$  and  $0.6$ ); (right) Three pore groups categorized based on MIP-derived pore size distribution.

These three aspects are closely related to the moisture distribution in the pore system. Note that the threshold pores  $d_{th}$  and critical pores  $d_{cr}$  are key factors influencing the percolation of the pore structure (see Fig. 7.10-right). The pore family can be categorized into three groups: macro pores ( $d > d_{th}$ ), meso pores ( $d_{cr} \leq d \leq d_{th}$ ) and micro pores ( $d < d_{cr}$ ).

Figure 7.11 shows a schematic pore network to explain the moisture distribution in cementitious systems. The macro pores and micro pores are both connected by the meso pores. The meso pores provide the main pathways for moisture transfer when the pore network is unsaturated. The three-stage  $D_{rc}$ - $S_w$  relationship (see Fig. 7.10-left) can be explained by the three-stage change of the moisture state in the meso pores (see Fig. 7.11):

- Stage I: All meso pores are saturated. When the  $S_w$  starts to decrease, the macro pores first lose water. The main pathways for ionic diffusion, viz. meso pores, are still fully water-filled. The  $D_{rc}$ -value is quite close to that in saturated condition.
- Stage II: The meso pores are partially saturated and gradually occupied with the gas phase which hinders the ionic diffusion to a great extent. As a result, the  $D_{rc}$ -value drops rapidly.
- Stage III: The meso pores are drained. Only nano-scale layers, consisting of water molecules and chemical compounds (e.g.  $\text{Ca}(\text{OH})_2$ ), are adsorbed on the walls of meso pores. In this stage the water loss in the micro pores starts. The ionic diffusion is quite slow, reflected by low  $D_{rc}$ -values.

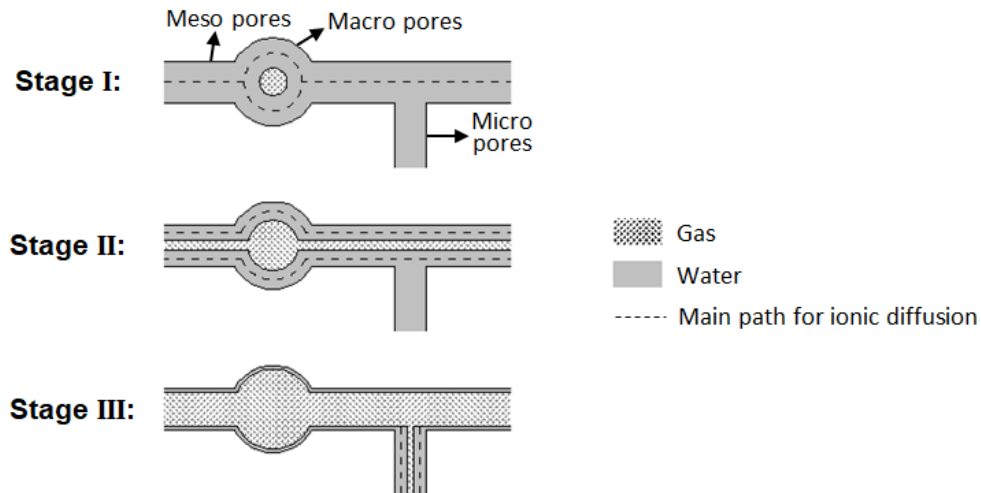


Fig. 7.11 Schematic representations of moisture distribution and ionic diffusion in the pore network with decreasing water saturation level.

#### 7.4.4 Relative chloride diffusion coefficient $D_{rc}$ in blended cement mortars

##### 7.4.4.1 Effect of binder type on $D_{rc}$ - $S_w$ relationship

Figure 7.12 shows the  $D_{rc}$ - $S_w$  relationship in mortar specimens made with different binders (same  $w/b = 0.5$ ). The addition of SCMs substantially influences the  $D_{rc}$ - $S_w$  relation. The presence of FA (binder MF5) reduces the  $D_{rc}$  to a great extent compared to the  $D_{rc}$  in the OPC binder M5 of the same  $S_w$ . At  $S_w = 80\%$  the  $D_{rc}$ -value of MF5 is approximately half that of M5. With addition of LP (binder MFL5) the  $D_{rc}$ -value abruptly increases compared to the binder MF5 in the entire saturation range. Of interest is that the  $D_{rc}$ -value of MFL5 is slightly higher than that of M5 at a given saturation level, e.g.  $S_w = 80\%$ . For the BFS-blended binder MB5 the  $D_{rc}$ -value at  $S_w = 80\%$  is almost twenty times smaller than that at  $S_w = 100\%$ .

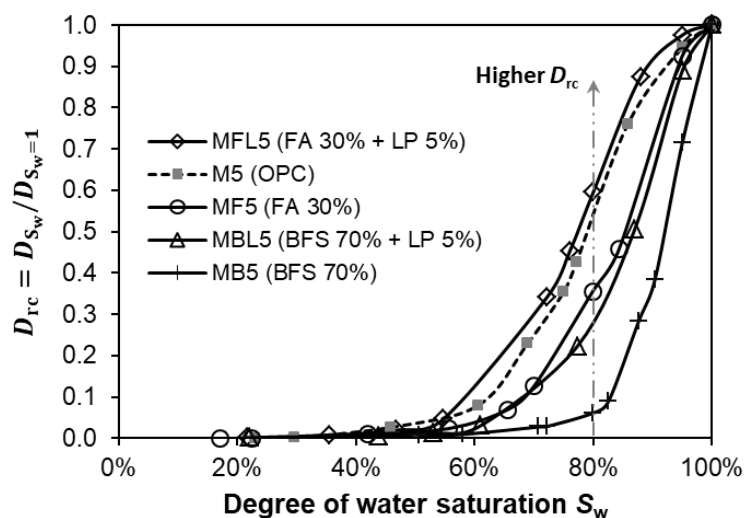


Fig. 7.12 Effect of binder type on  $D_{rc}$ - $S_w$  relations in one-year-old mortars ( $w/b = 0.5$ ).

The different  $D_{rc}$ - $S_w$  relation by adding SCMs is attributable to the influence of the SCMs on the pore structure and associated water continuity (see Section 6.2.2). In the high saturation levels, i.e.  $S_w = 60\sim 100\%$ , the  $D_{rc}$ -values of different binders show an ascending order as:  $D_{rc}$  (MB5) <  $D_{rc}$  (MBL5) <  $D_{rc}$  (MF5) <  $D_{rc}$  (M5) <  $D_{rc}$  (MFL5). The same ascending order also holds for the fineness of pore size in these binders (see Fig. 6.12-right).

#### 7.4.4.2 Effect of w/b ratio on $D_{rc}$ - $S_w$ relationship in BFS-blended binders

Figure 7.13 shows the  $D_{rc}$ - $S_w$  relations for w/b ratios of 0.4, 0.5 and 0.6. Different effects of the w/b ratio on the  $D_{rc}$ - $S_w$  relation exist between OPC binders (M4, M5 and M6) and BFS-blended binders (MB4, MB5 and MB6). The OPC binders with a higher w/b ratio show a higher  $D_{rc}$ -value for a given saturation level  $S_w$ . For BFS-blended binders, in contrast, the  $D_{rc}$ - $S_w$  relation changes little when the w/b ratio increases from 0.4 to 0.6.

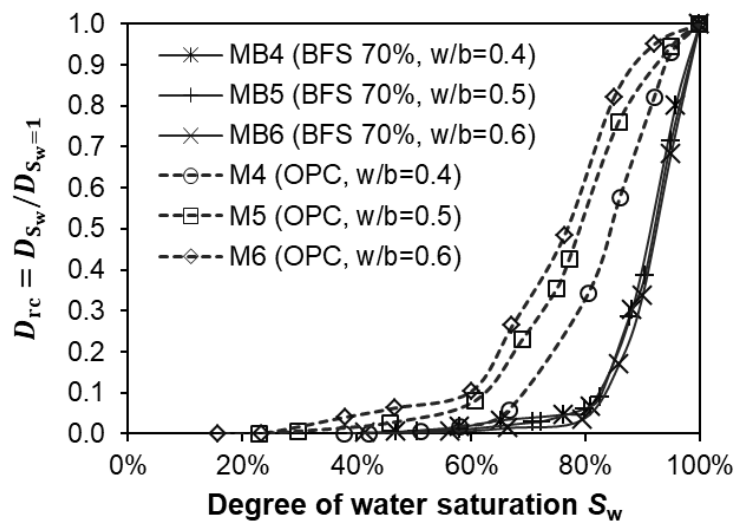


Fig. 7.13 Effect of w/b ratio (0.4, 0.5 and 0.6) on  $D_{rc}$ - $S_w$  relations in one-year-old OPC and BFS-blended mortars.

The role of the w/b ratio in the  $D_{rc}$ - $S_w$  relation stems from its effect on the pore structure and associated water continuity. As noted in Chapter 6, the pore size distribution affects the water continuity primarily at high saturation levels. At low saturation levels the water continuity is dominated by the pore entrapment. The pore structures of OPC and BFS-blended pastes have been analyzed by IEC-MIP tests (see Chapter 4). The effects of the w/b ratio on the pore size and pore entrapment of the two binders are summarized as follows:

- 1) The fineness of pore size is indicated by the average pore diameter  $d_a$  (Eq. (3.3)). The  $d_a$ -value of the mixtures (Fig. 7.13) is determined as 23.2, 24.5 and 27.6 nm for OPC pastes with w/b ratios of 0.4, 0.5 and 0.6, compared to 11.1, 11.6 and 11.9 nm for BFS-blended pastes with w/b ratios of 0.4, 0.5 and 0.6, respectively. It is clear that for OPC binders a lower w/b ratio significantly refines the pore structure. For BFS-blended binders, however, the w/b ratio does not affect the pore size fineness drastically.

- 2) At a given pore diameter the pore entrapment of OPC pastes is obviously higher for a higher w/c ratio (Fig. 4.16b), while the pore entrapment of BFS-blended pastes shows only a minor change when the w/b ratio increases from 0.4 to 0.6 (Fig. 4.17b).

## 7.5 Validation of the equation for relative chloride diffusion coefficient

With Eq. (7.17) the relative chloride diffusion coefficient  $D_{rc}$  is formulated as a function of the degree of water saturation  $S_w$ . Comparison of Eq. (7.17) with experimental data, including data derived in this work and those reported in literature, is carried out to test its reliability and efficiency. The coefficient  $c$  in Eq. (7.17) is determined from regression analyses. Equation (7.17) will then be able to predict the  $D_{rc}$  in non-saturated cementitious materials.

### 7.5.1 Validation of Eq. (7.17) with experimental data derived in this work

Calibration of Eq. (7.17) with the  $D_{rc}$ - $S_w$  plots (Figs. 7.10, 7.12 and 7.13) is performed for different mortars. An example of the regression curves is given in Fig. 7.14. Good agreement between experimental  $D_{rc}$ - $S_w$  plots and Eq. (7.17) is observed for all binders. The correlation coefficients are 0.989, 0.997, 0.992 and 0.997 for the binders M5, MF5, MB5 and MBL5, respectively. The values of the coefficient  $c$  in Eq. (7.17) are 0.214, 0.154, 0.077 and 0.135 for the binders M5, MF5, MB5 and MBL5, respectively.

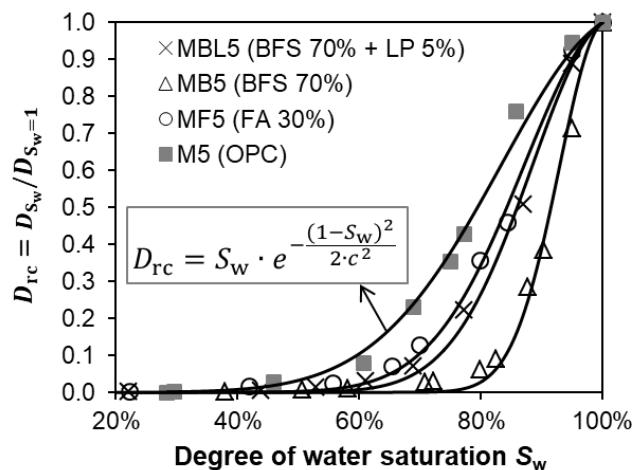


Fig. 7.14 Calibration of Eq. (7.17) with experimental  $D_{rc}$ - $S_w$  plots.

### 7.5.2 Validation of Eq. (7.17) with experimental data reported in literature

A series of previously published  $D_{rc}$ - $S_w$  data and details of the experiments are provided in Fig. 7.15 and Table 7.2, respectively. These data were obtained based on the Nernst-Einstein equation and conductivity experiments. Since the pore size distributions of the specimens were not available in these experimental studies, the porosities of the specimens are given instead. The values of the coefficient  $c$  and correlation coefficient  $R^2$  are obtained from

regression analyses. Figure 7.15 shows that Eq. (7.17) can describe these data series ( $D_{rc}$  vs.  $S_w$ ) quite well, regardless of cement types, w/b ratios or porosities of the specimens.

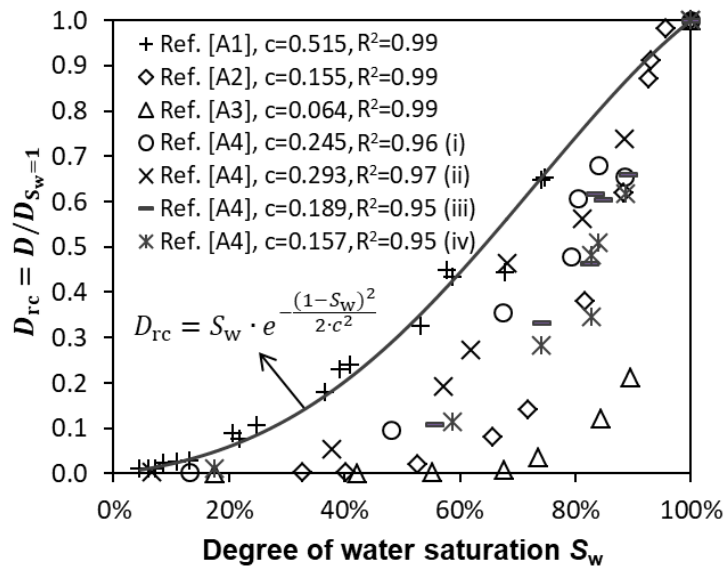


Fig. 7.15 Comparison between Eq. (7.17) and experimental  $D_{rc}$ - $S_w$  plots reported by different workers: A1-Buchwald [2000]; A2-Rajabipour [2006]; A3-Mercado-Mendoza et al. [2014]; A4-Olsson et al. [2018];

Table 7.2 Previous experimental studies on  $D_{rc}$ - $S_w$  relation in unsaturated porous materials

Authors	Binder type	Specimen	W/b	Porosity
Buchwald [2000]		Masonry materials		32%
Rajabipour [2006]	ASTM Type I	Concrete (18 months)	0.50	17.7%
Mercado-Mendoza et al. [2014]	CEM V (55% OPC + 22% Slag + 23% Fly ash)	Concrete (6 months)	0.41	14%
Olsson et al. [2018]	(i) OPC	Mortar (3 months)	0.38	15%
Olsson et al. [2018]	(ii) 95% OPC + 5% Silica fume	Mortar (3 months)	0.531	19%
Olsson et al. [2018]	(iii) 60% OPC + 40% Slag	Mortar (3 months)	0.386	16%
Olsson et al. [2018]	(iii) 30% OPC + 70% Slag	Mortar (3 months)	0.391	16%

### 7.5.3 Determination of coefficient $c$ and prediction of relative chloride diffusion coefficient $D_{rc}$

As shown in Figs. 7.14 and 7.15, Eq. (7.17) can describe the experimental  $D_{rc}$ - $S_w$  data quite well. Prediction of the relative chloride diffusion coefficient  $D_{rc}$  with Eq. (7.17) is possible once the coefficient  $c$  of the material of interest is known. Both the coefficient  $c$  and the average pore diameter  $d_a$  (defined by Eq. (3.3)) depend on *pore size distribution* of the material. There appears a strong correlation between the two quantities. Figure 7.16 depicts the coefficient  $c$  versus the average pore diameter  $d_a$  for all binders studied. A linear

relationship (Eq. (7.20)) with a correlation coefficient of 0.94 is obtained.

$$c(d_a) = k_1 \cdot d_a + k_2 \quad (R^2 = 0.94) \quad (7.20)$$

where  $k_1$  [ $\text{nm}^{-1}$ ] and  $k_2$  [-] are fitting parameters. Both are determined as  $k_1 = 0.01$  and  $k_2 = -0.05$  from the regression analysis shown in Fig. 7.16.

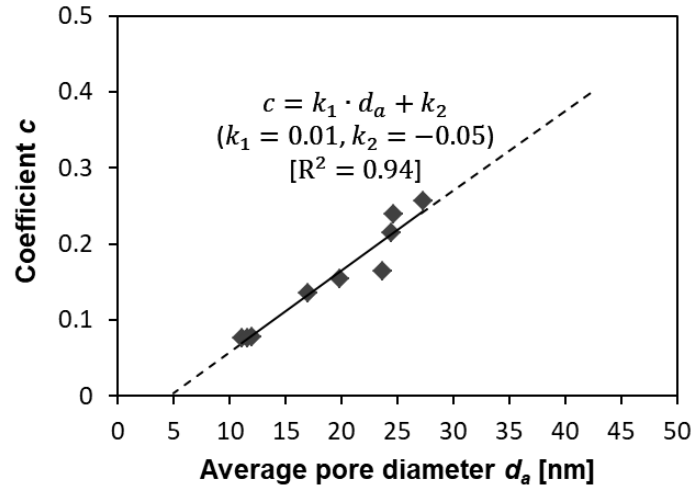


Fig. 7.16 Relationship between coefficient  $c$  and average pore diameter  $d_a$ .

According to Eq. (7.20) the coefficient  $c$  approaches zero at  $d_a \approx 5$  nm. Both  $\eta_w$  and  $D_{rc}$  are then determined as zero at  $d_a \leq 5$  nm. This is reasonable against the background of the microstructure of cementitious materials. At  $d_a > 5$  nm the microstructure contains both capillary pores ( $> 10$  nm) and gel pores ( $\leq 10$  nm). Whereas at  $d_a \leq 5$  nm there may be little capillary pores but only gel pores present in the microstructure and the chloride diffusion is then negligible [Mindess et al. 1981]. The linear  $c$ - $d_a$  relationship (Eq. (7.20)) also suggests that the coefficient  $c$  is around 0.45 at  $d_a \approx 50$  nm. For hydrated cementitious materials ( $> 28$  days old) the average pore diameter  $d_a$  rarely exceeds 50 nm [Ye 2003] and, therefore, the  $c$ -value is usually in the range 0~0.45.

Consequently, the relative chloride diffusion coefficient  $D_{rc}$  in unsaturated cementitious material can be predicted as:

$$D_{rc} = \frac{D_{S_w}}{D_{Sat}} = S_w \cdot e^{-\frac{(1-S_w)^2}{2 \cdot (0.01 d_a - 0.05)^2}} \quad (d_a > 5 \text{ nm}) \quad (7.21a)$$

$$D_{rc} = 0 \quad (d_a \leq 5 \text{ nm}) \quad (7.21b)$$

where  $D_{S_w}$  [ $\text{m}^2/\text{s}$ ] is the chloride diffusion coefficient at a particular degree of water saturation  $S_w$ ;  $D_{Sat}$  [ $\text{m}^2/\text{s}$ ] is the chloride diffusion coefficient at saturated state, which can be obtained from current test methods, e.g. resistivity measurements, steady-state diffusion or migration cell methods [Tang et al. 2012];  $d_a$  [nm] is the average pore diameter of the material estimated from MIP tests.

The linear relationship (Eq. (7.20)) was obtained based on the  $c-d_a$  plots of nine mixtures, covering different w/b ratios (0.4, 0.5 and 0.6) and cementing types (OPC, FA, BFS and LP). Natural and artificial blended materials have nowadays been widely used to partially or even entirely replace the OPC for hydraulic binders. More experimental investigations can be conducted to examine whether the linear equation (Eq. (7.20)), as well as the analytical tool (Eq. (7.21a-b)), is applicable for other hydraulic binders. *Improvement to Eq. (7.21), such as using a more effective relationship between the coefficient  $c$  and the microstructure information, is possible.*

From Eq. (7.21) the  $D_{rc}$  of any cementitious material can be predicted with two parameters as inputs,  $S_w$  and  $d_a$ . Fundamentally, the  $S_w$  depends on the w/b ratio, the degree of hydration and the moisture exchange between the material and ambient environment; the  $d_a$  is influenced by such factors as w/b ratio, type of cement, degree of hydration, etc. Accordingly, both  $S_w$  and  $d_a$  are not constant but time-dependent in practical. Simulation work can be done in future to obtain more details in that regards.

## 7.6 Conclusions

The main findings can be drawn as follows:

- 1) An analytical tool (Eq. (7.21)) has been developed, with which the chloride diffusion coefficient  $D_{S_w}$  at unsaturated state can be predicted based on the chloride diffusion coefficient  $D_{S_{at}}$  at saturated state, the degree of water saturation  $S_w$  and the average pore diameter  $d_a$  of the material.
- 2) The changes of the relative chloride diffusion coefficient  $D_{rc}$  with decreasing degree of water saturation  $S_w$  can be divided into three stages, i.e. a slight decrease (stage I), a sharp drop (stage II) and another slight decline (stage III). The  $D_{rc}$ - $S_w$  relationship depends on the water continuity in the pore systems. A pore network is put forward to explain the three-stage  $D_{rc}$ - $S_w$  relationship.
- 3) A finer pore size distribution or higher pore entrapment tends to result in a lower  $D_{rc}$  in cementitious materials.
- 4) The binder blended with 30% FA or 70% BFS exhibits a lower  $D_{rc}$  than the reference OPC binder of the same saturation level  $S_w$ . The addition of 5% LP increases the  $D_{rc}$  in the entire  $S_w$  range.
- 5) A higher w/b ratio (0.4~0.6) results in a higher  $D_{rc}$  for OPC binders of a given saturation level  $S_w$ . The w/b ratio, however, has little influence on the  $D_{rc}$ - $S_w$  relation for binders blended with 70% BFS. The different roles of the w/b ratio in the  $D_{rc}$ - $S_w$  relation arise from the different effects of the w/b ratio on the pore structure (including pore size fineness and pore entrapment) between OPC and BFS-blended binders.

## Chapter 8

# Effect of Unsaturated Chloride Diffusion on Service Life Prediction of Reinforced Concrete Structures

---

## 8.1 Introduction

To design new reinforced concrete structures or to plan a remedial maintenance, reliable models for predicting the long-term chloride diffusion into concrete should be invoked. Such models enable to determine the chloride profiles  $C(x, t)$  in the cover concrete. The chloride content at the surface of reinforcement is forecasted and then compared to the so called “critical chloride content” that determines the initiation of reinforcement corrosion. From that comparison the general service life of concrete structures can be predicted.

The unsaturated state of concrete plays a significant role in the chloride diffusion and hence in the service life of marine concrete structures. An analytical tool (Eq. (7.21)) for determining the unsaturated chloride diffusion coefficient has been developed in Chapter 7. That tool will be used in this chapter (see Fig. 8.1) to describe the evolution of the chloride diffusion coefficient in unsaturated cementitious materials. It is found that the long-term sharp decrease of the chloride diffusion coefficient is caused primarily by the decreasing degree of water saturation in cementitious materials.

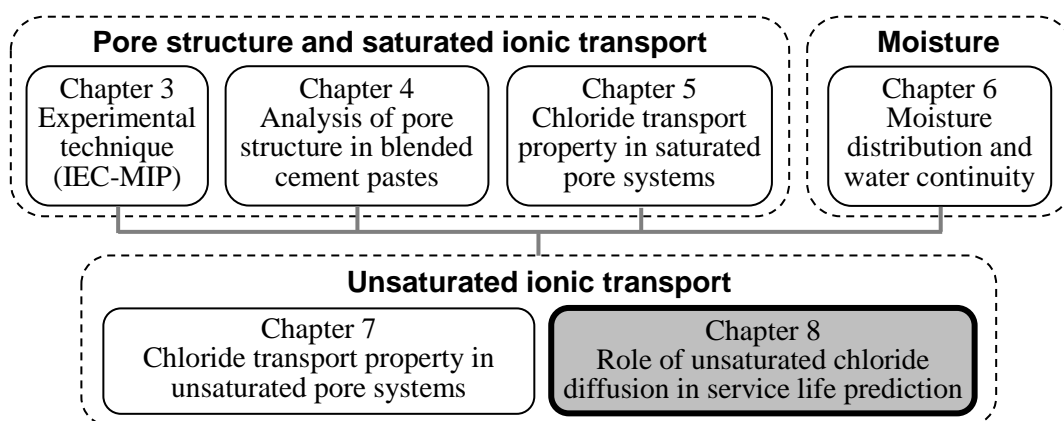


Fig. 8.1 Main chapters of the thesis.

## 8.2 Unsaturated chloride diffusion

Ionic diffusion in a cementitious system is largely determined by the degree of water saturation  $S_w$  and the microstructure (depending on the degree of hydration  $\alpha(t)$ ). In SCMs-blended systems the hydration process is complicated. Accurate determination of the hydration degree of each raw material is far from easy and requires advanced modeling [Gao 2018]. Nevertheless, the degree of hydration  $\alpha(t)$  in the entire cementitious system, by fitting against relative non-evaporable water content, can generally be formulated as [Jonasson 1984]:

$$\alpha(t) = \exp[-a(\ln t)^{-b}] \quad (8.1)$$

where  $t$  is the age;  $a$  and  $b$  are fitting parameters.

An example of the hydration curve according to Eq. (8.1) is shown in Fig. 8.2. The curve indicates that the degree of hydration  $\alpha(t)$  shows little change after a reference age  $t_{\text{ref}}$ . The change of the microstructure at later ages ( $t > t_{\text{ref}}$ ) is relatively small. In the following the evolution of the chloride diffusion will, therefore, not be described as a function of the degree of hydration  $\alpha(t)$ , but described instead as a function of the degree of water saturation  $S_w$ .

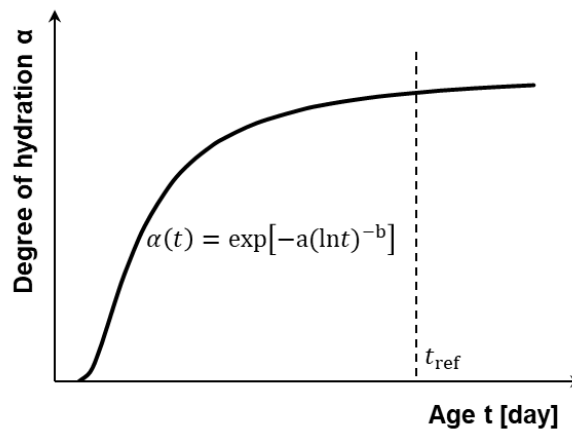


Fig. 8.2 Changes of the degree of hydration with age in cementitious systems.

The effect of the degree of water saturation  $S_w$  on chloride diffusion has been formulated in Chapter 7 (see Eq. (7.21)). If the material age  $t$  is taken into account, Eq. (7.21) can be extended into Eq. (8.2).

$$D(\alpha(t), S_w) = D_{\text{Sat}}(\alpha(t)) \cdot S_w(t) \cdot \exp \left[ \frac{(1-S_w)^2}{2 \cdot [0.01 d_a(\alpha(t)) - 0.05]^2} \right] \quad (8.2)$$

where:

- $D(\alpha(t), S_w)$  [ $\text{m}^2/\text{s}$ ] is the chloride diffusion coefficient in an unsaturated cementitious material.

- $D_{Sat}(\alpha(t))$  [ $m^2/s$ ] is the chloride diffusion coefficient of the cementitious material at saturated state, which can be obtained from resistivity measurements, steady-state diffusion or migration cell methods. The  $D_{Sat}$  value decreases with increasing degree of hydration  $\alpha(t)$  in the cementitious material.
- $S_w(t)$  [-] is the degree of water saturation at time  $t$ . The  $S_w$  value changes with self-desiccation and/or moisture exchange with ambient environment.
- $d_a(\alpha(t))$  [nm] is the average pore diameter, which can be obtained from mercury porosimetry measurements. The  $d_a$  value decreases with increasing degree of hydration  $\alpha(t)$  in the cementitious material.

Both  $D_{Sat}$  and  $d_a$  depend on the degree of hydration  $\alpha(t)$  in cementitious materials. From experimental studies the evolutions of  $D_{Sat}$  and  $d_a$  for different binders are given in Figs. 8.3 (a) and (b), respectively. Regardless of the binders, both  $D_{Sat}(\alpha(t))$  and  $d_a(\alpha(t))$  can be described with an exponential decay function:

$$D_{Sat}(\alpha(t)) = D_0 + A \cdot \exp\left(-\frac{t}{t_0}\right) \quad (t \geq 28 \text{ days}) \quad (8.3)$$

$$d_a(\alpha(t)) = d_0 + A \cdot \exp\left(-\frac{t}{t_0}\right) \quad (t \geq 28 \text{ days}) \quad (8.4)$$

where  $D_0$ ,  $d_0$ ,  $A$  and  $t_0$  are fitting parameters.

As can be deduced from Fig. 8.3 the changes of both  $D_{Sat}$  and  $d_a$  are very small after one year, regardless of the binders. This can be ascribed to the fact that for all binders tested the degree of hydration  $\alpha(t)$  changes only slightly after 1 year (i.e.  $t_{1 \text{ year}} > t_{ref}$ , see Fig. 8.2).

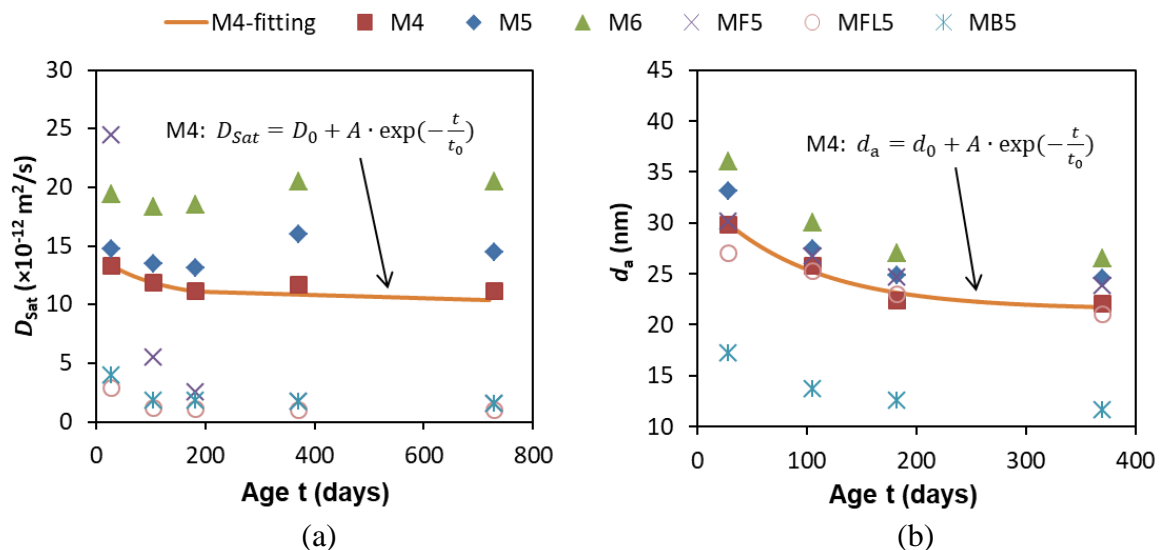


Fig. 8.3 (a) Evolution of the chloride diffusion coefficient  $D_{Sat}$  obtained from RCM tests on saturated specimens. (b) Evolution of the average pore diameter  $d_a$  obtained from MIP tests. Mixtures: M4 (OPC,  $w/b = 0.4$ ), M5 (OPC,  $w/b = 0.5$ ), M6 (OPC,  $w/b = 0.6$ ), MF5 (30% FA,  $w/b = 0.5$ ), MB5 (70% BFS,  $w/b = 0.5$ ), MFL5 (30% FA + 5% LP,  $w/b = 0.5$ ).

### 8.3 Role of unsaturated chloride diffusion in service life

#### 8.3.1 Evolution of unsaturated chloride diffusion coefficient $D(\alpha(t), S_w)$

The evolution of the chloride diffusion coefficient  $D(\alpha(t), S_w)$  with age (28 days  $\rightarrow$  50 years) at various degrees of water saturation  $S_w$  is predicted with Eq. (8.2), with  $D_{Sat}(\alpha(t))$  and  $d_a(\alpha(t))$  according to Eqs. (8.3) and (8.4), respectively. The predicted  $D(\alpha(t), S_w)$  values for different mortar mixtures are given in Fig. 8.4.

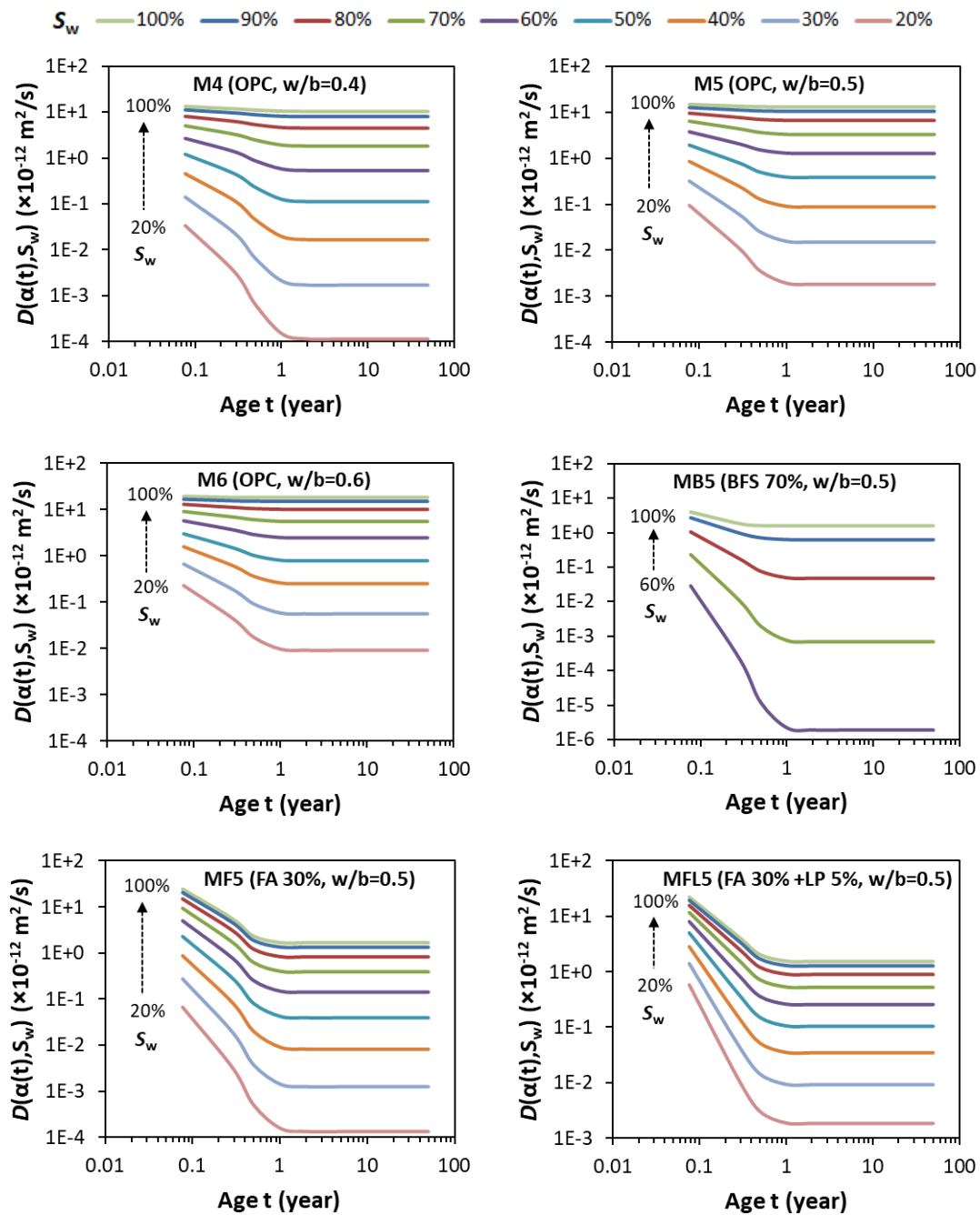


Fig. 8.4 Evolution of chloride diffusion coefficient  $D(\alpha(t), S_w)$  with age (28 days  $\rightarrow$  50 years) in the cementitious mortars at various degrees of water saturation  $S_w$ .

For all binders similar characteristics can be observed in Fig. 8.4. The chloride diffusion coefficient  $D(\alpha(t), S_w)$  generally decreases with age, especially in the 1<sup>st</sup> year. At saturated state ( $S_w = 100\%$ ) the diffusion coefficient  $D$  exhibits a relatively small decrease. The decrease of the diffusion coefficient  $D$ , however, becomes increasingly pronounced with decreasing saturation level  $S_w$ .

### 8.3.1.1 Effect of w/b ratio on $D(\alpha(t), S_w)$

Figure 8.5 presents the chloride diffusion coefficient  $D(\alpha(t), S_w)$  in the OPC mortars with w/b ratios of 0.4, 0.5 and 0.6. The data are taken from Fig. 8.4.

- At saturated state ( $S_w = 100\%$ ) the diffusion coefficient  $D$  decreases slightly with age after 28 days, whereas at unsaturated state ( $S_w = 60\%$ ) the diffusion coefficient  $D$  drops rapidly until the end of the 1<sup>st</sup> year.
- A higher w/b ratio results in a higher diffusion coefficient  $D$ , regardless of the degree of water saturation  $S_w$ . The effect of the w/b ratio on the  $D$  value, however, is much more significant in unsaturated mortars ( $S_w = 60\%$ ) than in saturated mortars ( $S_w = 100\%$ ). By increasing the w/b ratio from 0.4 (M4) to 0.6 (M6), the diffusion coefficient  $D$  is approximately 1.7 times higher for  $S_w = 100\%$ , compared to 4.3 times for  $S_w = 60\%$ .

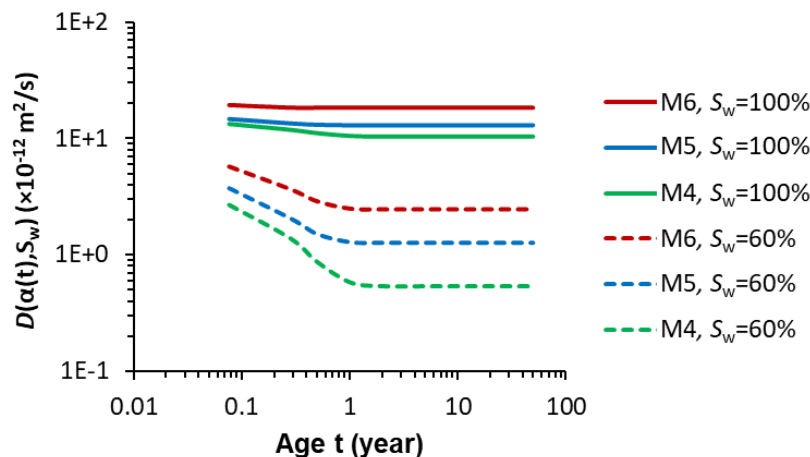


Fig. 8.5 Chloride diffusion coefficient  $D(\alpha(t), S_w)$  in the saturated ( $S_w = 100\%$ ) and unsaturated ( $S_w = 60\%$ ) OPC mortars with w/b ratios of 0.4 (M4), 0.5 (M5) and 0.6 (M6).

### 8.3.1.2 Effect of SCMs on $D(\alpha(t), S_w)$

Figure 8.6 shows the effect of SCMs on the chloride diffusion coefficient  $D(\alpha(t), S_w)$  for saturated ( $S_w = 100\%$ ) and unsaturated ( $S_w = 70\%$ ) mortar specimens. The data come from Fig. 8.4. A sharper decrease of the diffusion coefficient  $D$  with age is found for  $S_w = 70\%$  than for  $S_w = 100\%$ , regardless of the binders.

For a given water content, either saturated or unsaturated, the blended mortars (MF5, MB5 and MFL5) exhibit lower diffusion coefficient  $D$  than the OPC mortar (M5) after 1 year. At saturated state ( $S_w = 100\%$ ) the addition of 30% FA (MF5) or 70% BFS (MB5) results in almost the same diffusion coefficient  $D$  at an age of 1 year. At unsaturated state ( $S_w = 70\%$ ),

however, the diffusion coefficients  $D$  between mortars MF5 and MB5 differ significantly. Compared to mortar MF5, the mortar MFL5 shows slightly lower diffusion coefficient  $D$  at  $S_w = 100\%$  but much higher diffusion coefficient  $D$  at  $S_w = 70\%$ , regardless of the age.

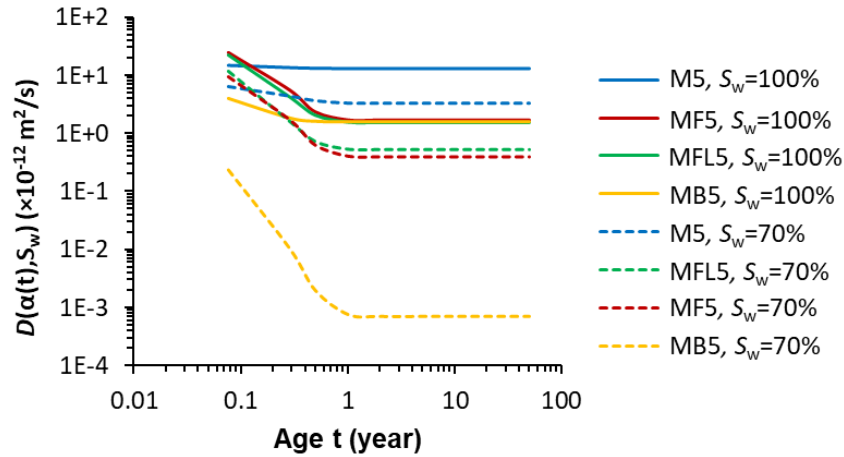


Fig. 8.6 Chloride diffusion coefficient  $D(\alpha(t), S_w)$  in saturated ( $S_w = 100\%$ ) and unsaturated ( $S_w = 70\%$ ) blended mortars. M5 (OPC,  $w/c = 0.5$ ), MF5 (30% FA,  $w/b = 0.5$ ), MB5 (70% BFS,  $w/b = 0.5$ ), MFL5 (30% FA + 5% LP,  $w/b = 0.5$ ).

Both Figs. 8.5 and 8.6 reveal that for a particular pore structure change, due to either hydration or varying  $w/b$  ratio or addition of SCMs, the change of  $D(\alpha(t), S_w)$  at *unsaturated* state is more pronounced than that at *saturated* state. This is reasonable in view of the main path for ionic diffusion in pore systems. When a slight change of pore structure (e.g. due to hydration) occurs in the saturated pore system (Fig. 8.7a), the rate of ionic diffusion changes slightly, resulting in a slight change of the diffusion coefficient  $D$ . However, when a slight change of pore structure occurs in the partially saturated pore system (Fig. 8.7b), the rate of ionic diffusion can be impaired significantly because of the decreased thickness (from  $t_1$  to  $t_2$ ) of the layers of capillary water adsorbed on the partially water-filled pores.

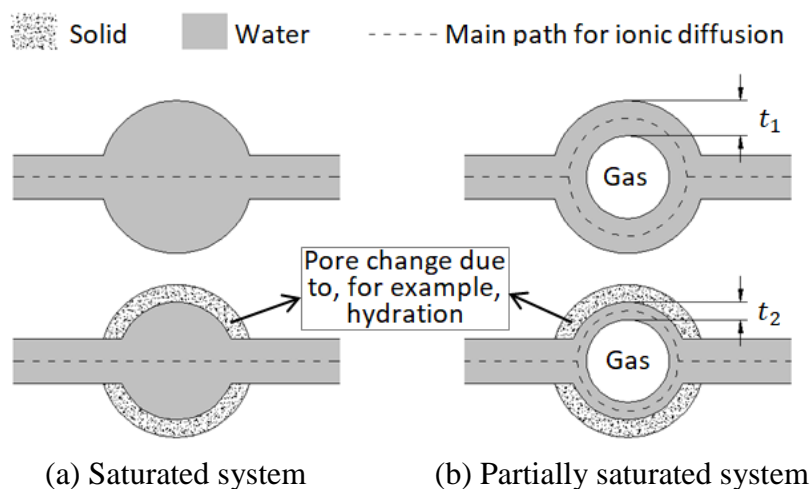


Fig. 8.7 Schematic illustrations on the effect of a minor pore structure change on ionic diffusion in (a) saturated and (b) partially saturated pore systems.

### 8.3.2 Chloride diffusion coefficient against internal relative humidity

Besides the degree of water saturation  $S_w$ , the relative humidity RH is another parameter used for determining the unsaturated chloride diffusion coefficient  $D$ . The moisture exchange between cementitious material and ambient environment highly depends on the ambient RH level. A lower ambient RH can result in a lower saturation level  $S_w$  of the material. By making use of the RH- $S_w$  relation, the  $D$ - $S_w$  relation can be converted into the  $D$ -RH relation. The  $D$ -RH relations of different mortar mixtures are given below.

#### 8.3.2.1 RH- $S_w$ relation

Figure 8.8 gives experimentally obtained RH- $S_w$  relations in the mortars made with different binders (see Chapter 6). At a particular RH, e.g. 80%, the saturation levels  $S_w$  of different mortars show an ascending order as  $S_w$  (M6) <  $S_w$  (M5) <  $S_w$  (MFL5) <  $S_w$  (MF5) <  $S_w$  (M4) <  $S_w$  (MB5). This order is consistent with the order of the fineness of pore size in the pastes made with the same binders (see Figs. 6.12-right and 6.13-right). The slag-blended mortar MB5 contains the highest content of small pores and its saturation level  $S_w$  shows only a slight change when the RH decreases from 98% to 80%.

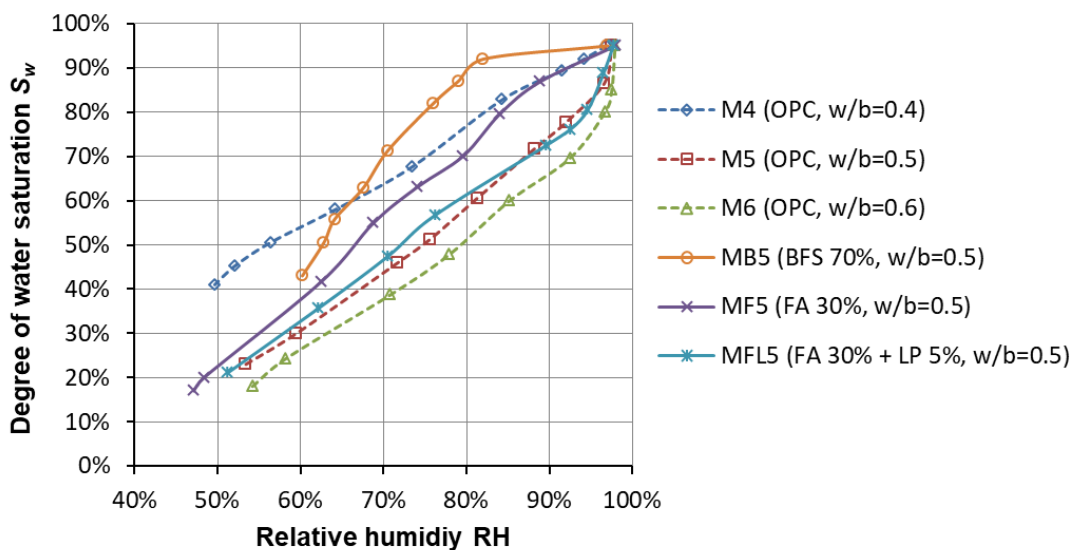


Fig. 8.8 RH- $S_w$  relations obtained from water vapour desorption isotherm tests performed on the one-year-old mortars made with different binders.

#### 8.3.2.2 D-RH relation

Figure 8.9 shows the  $D$ -RH relations in one-year-old OPC mortars. At high RH levels (> 95%) the diffusion coefficient  $D$  is higher in higher w/b ratio cement mortars. At low RH levels (< 85%), on the contrary, the higher diffusion coefficient  $D$  is found for lower w/b ratio cement mortars. This is reasonable against the background of the pore structure of paste matrixes formed with different w/b ratios. At high RH levels ionic diffusion in the large pores dominates the transport process. The cement mortar with a higher w/b ratio has more large pores, resulting in a larger  $D$ -value. The cement mortar with a lower w/b ratio has more small

pores. Below a certain RH level these small pores control the ionic transport process and the  $D$ -value can be larger in the lower  $w/b$  ratio cement mortar.

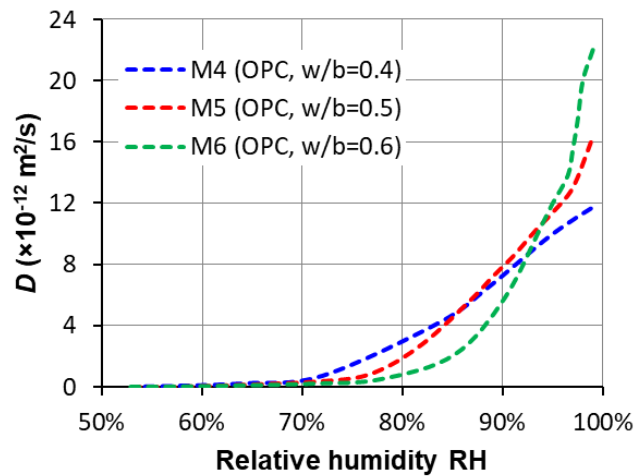


Fig. 8.9 Chloride diffusion coefficient  $D$  as a function of internal RH in one-year-old OPC mortars with different  $w/b$  ratios.

Figure 8.10a shows the  $D$ -RH relations of OPC (M5) and blended mortars (MB5, MF5 and MFL5). All mortars were made with a constant  $w/b$  ratio of 0.5. To clearly demonstrate the effect of blends, the  $D$ -RH plots in the range  $D = 0 \dots 2.0 \times 10^{-12} \text{ m}^2/\text{s}$  are shown in Fig. 8.10b at a different scale. The blended mortars generally show lower diffusion coefficient  $D$  than the OPC mortar M5 in the RH range of 60~98%. When the RH increases, the diffusion coefficient  $D$  increases rapidly in the OPC mortar M5 while it increases slowly in the blended mortars. Particularly for the slag-blended mortar MB5, the diffusion coefficient  $D$  shows little dependence on the RH for the RH above 83%, but it decreases drastically at lower RH. The pronounced influence of the SCMs on the  $D$ -RH relation is found mainly when  $\text{RH} > 60\%$ .

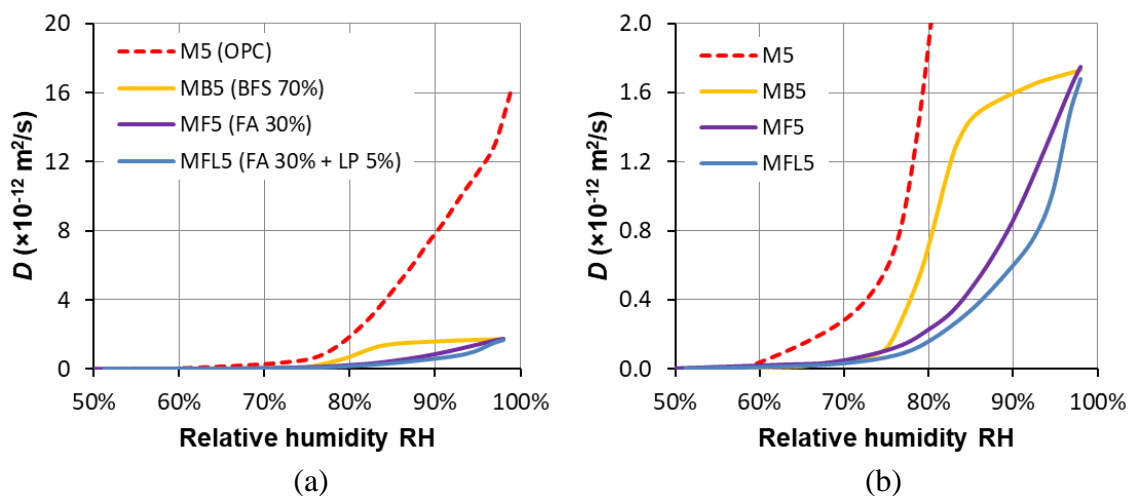


Fig. 8.10 (a) Chloride diffusion coefficient  $D$  as a function of RH in OPC and blended mortars ( $w/b = 0.5$ , one-year-old). (b) The  $D$ -RH relations in the range of  $0 \dots 2.0 \times 10^{-12} \text{ m}^2/\text{s}$  are plotted in a different scale.

## 8.4 Comparative study

A comparison on the evolution of the unsaturated chloride diffusion coefficient with age is made between the present approach (Eq. (8.2)) and the DuraCrete approach. The comparative study highlights the significance of the degree of water saturation in the service life prediction of concrete structures in chloride-laden environments.

### 8.4.1 Specimens and exposure condition

For sake of simplification, the study concerns two cementitious mortars exposed to atmospheric marine condition. Table 8.1 shows the mixtures and properties of the two mortars. The relative humidity RH of the atmospheric marine condition changes in the range of 65~90% within each year, with an average annual RH of 77.5% [Saetta et al. 1993].

Table 8.1 Details of two mortar mixtures;  $D_{RCM,28days}$  is the chloride diffusion coefficient obtained from RCM tests of 28-day-old saturated mortar specimens

Mortars	Binder	W/b	$D_{RCM,28days}$ ( $\times 10^{-12}$ m <sup>2</sup> /s)
M5	OPC	0.5	14.71
MB5	OPC 30% + BFS 70%		3.97

### 8.4.2 $D(t)$ by DuraCrete approach

In DuraCrete [2000] the service life of marine concrete structures highly relies on Eq. (8.5), which describes the changes of chloride diffusion coefficient  $D(t)$  with age  $t$ .

$$D(t) = D_0 \cdot k_c \cdot k_e \cdot \left(\frac{t_0}{t}\right)^n \quad (8.5)$$

where  $D_0$  [m<sup>2</sup>/s] is the chloride diffusion coefficient at a reference age  $t_0$ .  $k_c$  is the curing factor ( $k_c = 0.79$  when  $t_0 = 28$  days);  $n$  is the ageing factor.  $k_e$  is the environment factor, which depends on environment class  $k_{e,0}$  and type of cement  $k_{e,c}$ :

$$k_e = k_{e,0} \cdot k_{e,c} \quad (8.6)$$

The values of the ageing factor  $n$  and the sub-factors ( $k_{e,0}$  and  $k_{e,c}$ ) are presented in Table 8.2 [DuraCrete 2000]. DuraCrete follows a probabilistic method as well as partial factors to calculate the probabilities of failure. The details are out of the scope and will not be presented.

Figure 8.11 shows the evolution of the chloride diffusion coefficient  $D(t)$  with age for atmospheric OPC and slag-blended mortars determined using Eq. (8.5), with the  $D_0$  equal to the  $D_{RCM,28days}$  shown in Table 8.1. A long-term sharp decrease of the  $D(t)$  with age can be observed for both atmospheric OPC and slag-blended mortars. In contrast, the  $D(t)$  measured from RCM tests of *saturated* OPC mortar shows only a slight slow decrease with age. This indicates a significant influence of the unsaturated state on the  $D(t)$ .

Table 8.1 Characteristic values of the ageing factor  $n$  and the environment factors  $k_e$  ( $k_{e,0}$  and  $k_{e,c}$ ) [DuraCrete 2000]

	Condition	Characteristic values
Ageing factor $n$	OPC, Submerged	0.30
	OPC, Tidal and splash	0.37
	OPC, Atmospheric	0.65
	BFS, Submerged	0.71
	BFS, Tidal and splash	0.60
	BFS, Atmospheric	0.85
$k_{e,0}$ for environment class	Submerged	1.32
	Tidal zone	0.92
	Splash zone	0.27
	Atmospheric	0.68
$k_{e,c}$ for type of cement	OPC	1.0
	BFS	2.9

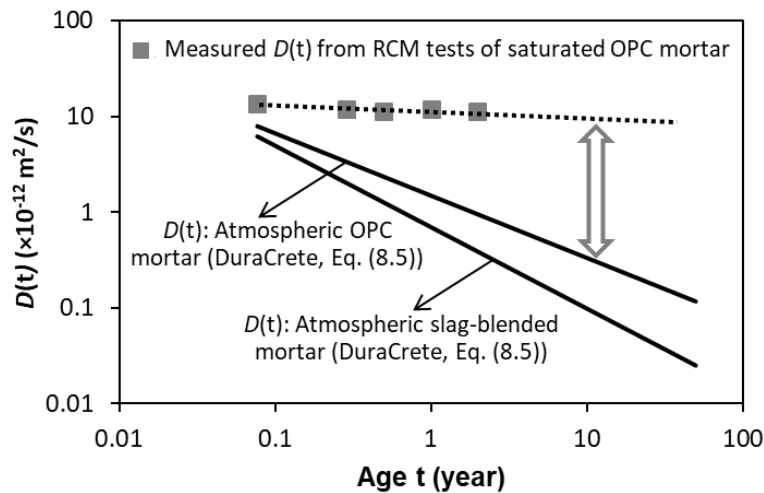


Fig. 8.11 Evolution of chloride diffusion coefficient  $D(t)$  with age according to DuraCrete.

### 8.4.3 $D(\alpha(t), S_w)$ by present approach

In the present approach the evolution of the unsaturated chloride diffusion coefficient  $D(\alpha(t), S_w)$  with age is determined with Eq. (8.2), with the values of  $D_{\text{Sat}}(t)$  and  $d_a(t)$  are taken from Fig. 8.3. The degree of water saturation  $S_w$  is supposed to change with time  $t$  when the mortars are exposed to atmospheric marine condition. Assuming a service life of 50 years, Eq. (8.7a-c) is adopted to describe the time-related saturation level  $S_w(t)$ :

- 1) In the first 28 days the mortar specimens are saturated ( $S_w = 100\%$ ) (Eq. (8.7a));
- 2) In the service period (28 days  $\rightarrow$  50 years), the degree of water saturation  $S_w$  of the mortar specimens decreases with time (Eq. (8.7b)).
- 3) At an age of 50 years, each mortar specimen reaches its equilibrium water saturation level,  $S_{w,e}$ , which corresponds to the equilibrium humidity level approximately the

same as the average annual RH of the atmospheric air, i.e. 77.5% RH. At this RH level the equilibrium water saturation level  $S_{w,e}$  can be estimated from the water vapour desorption isotherm of each mortar (see Fig. 8.8). The  $S_{w,e}$  values are 55% and 83% for mortars M5 and MB5, respectively.

$$S_w(t) = 100\% \quad 0 \leq t \leq 0.0767 \text{ year (28 days)} \quad (8.7a)$$

$$S_w(t) = \left(\frac{0.0767}{t}\right)^m \quad 0.0767 < t < 50 \text{ years} \quad (8.7b)$$

$$S_w(t) = S_{w,e} \quad t = 50 \text{ years} \quad (8.7c)$$

where  $m$  is a constant. By combining Eq. (8.7c) with Eq. (8.7b), the  $m$ -values are determined as 0.092 and 0.029 for mortars M5 and MB5, respectively. Figure 8.12 shows the time-related saturation  $S_w(t)$  obtained with Eqs. 8.7 (a), (b) and (c) for OPC and slag-blended mortars.

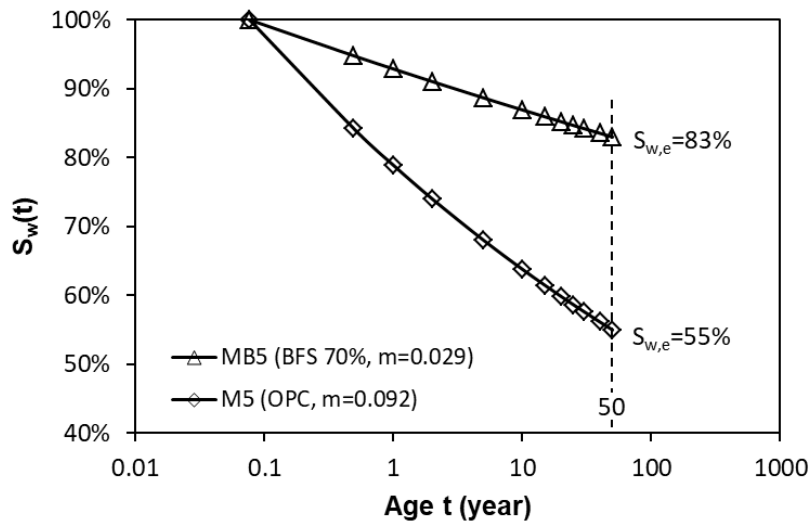


Fig. 8.12 Time-related saturation  $S_w(t)$  for atmospheric OPC and slag-blended mortars.

Figures 8.13 (a) and (b) present the  $D(\alpha(t), S_w)$  at different saturation levels  $S_w$  for OPC mortar M5 and slag-blended mortar MB5, respectively. The data come from Fig. 8.4. In the case when the saturation level  $S_w$  decreases with time by following Eq. (8.7), the evolution of  $D(\alpha(t), S_w)$  is replotted in Figs. 8.13 (a) and (b) with the dotted black lines. It is shown that the  $D(\alpha(t), S_w)$  value, with the  $S_w$  decreasing with time, drops much more significantly with age compared to that obtained based on saturated mortars ( $S_w = 100\%$ ).

For a comparative study the time-dependent  $D(t)$  recommended in DuraCrete (Eq. (8.5)) is also presented in Figs. 8.13 (a) and (b) with the solid black lines. At any particular age the  $D(t)$  value from Eq. (8.5) is in the same order of magnitude as that determined from Eq. (8.2). This holds for both OPC and slag-blended binders. The significant influence of the degree of water saturation on chloride diffusion, hidden behind but not explicitly addressed in DuraCrete, can therefore be clearly demonstrated by Eq. (8.2) proposed in the present work.

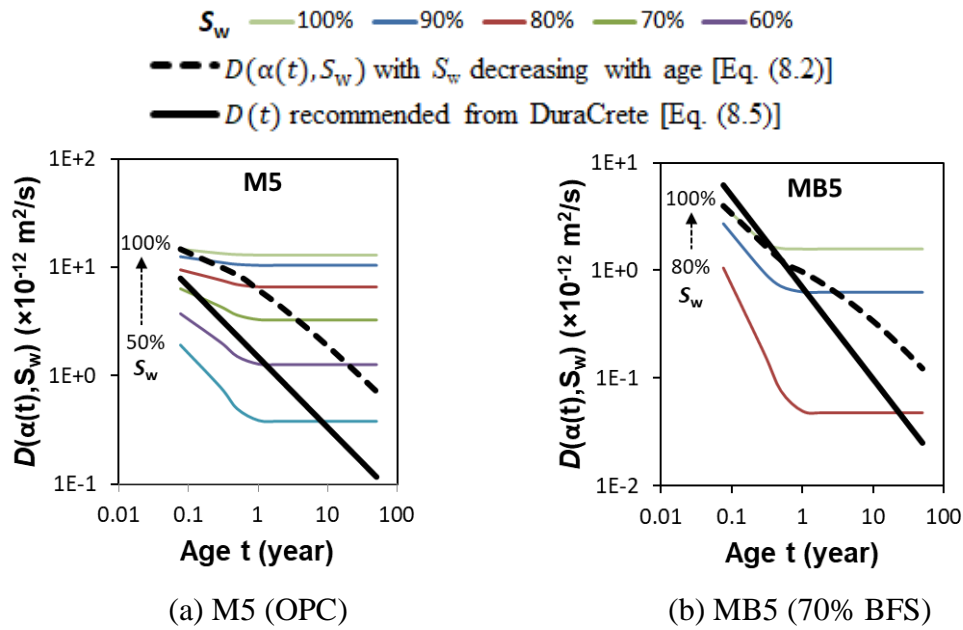


Fig. 8.12 Evolution of unsaturated chloride diffusion coefficient  $D(\alpha(t), S_w)$ .

## 8.5 Conclusions

- 1) A formula for determining the evolution of the chloride diffusion coefficient in unsaturated cementitious materials is proposed (Eq. (8.2)). The significant influence of the degree of water saturation  $S_w$  on chloride diffusion, hidden behind but not explicitly addressed in DuraCrete, has been substantiated by Eq. (8.2).
- 2) The effects of factors, such as w/b ratio and SCMs, on the chloride diffusion coefficient are relatively small when the cementitious materials are at saturated state, but become increasingly pronounced with decreasing degree of water saturation  $S_w$ .
- 3) The ageing factor  $n$ , representing the time-dependency of chloride diffusion coefficient, is influenced primarily by the degree of water saturation, rather than by long-term hydration, in the cementitious materials. It is not correct to judge the durability of marine concrete structures merely based on the chloride diffusion coefficient of saturated specimens.

## Chapter 9

# Retrospection, Conclusions and Prospects

---

### 9.1 Retrospection

Supplementary cementitious materials (SCMs), such as fly ash, slag, limestone powder, etc., are widely used in concrete mixtures. The transport-related durability of concretes made with these blended materials, however, is not completely clear yet. Chloride diffusion in unsaturated concretes is a major durability issue of reinforced concrete structures in marine environment. Prediction of the chloride diffusion in unsaturated blended cement concretes was the main reason to initiate this research project.

The relative chloride diffusion coefficient  $D_{rc}$ , a parameter often adopted for describing the chloride diffusion in unsaturated pore systems, has been investigated in only a small number of studies yet. A few expressions for determining the  $D_{rc}$ -value at different degrees of water saturation  $S_w$  were reported in the last two decades. These expressions, however, are mainly phenomenological calculation procedures. The pore structure, a fundamental factor influencing the moisture distribution and ionic diffusion, was not explicitly addressed in these expressions.

The final goal of this thesis was to develop a tool, with which the relative chloride diffusion coefficient of an arbitrary cementitious material can be predicted based on the degree of water saturation and the pore structure characteristics of the material. A couple of research steps were made in order to reach that goal.

The first step was to analyze the pore structure of cement pastes made with and without SCMs. Ionic transport in unsaturated pore systems is controlled by the *continuous water-filled pores*, which highly depend on the amount of small capillary pores ( $\leq$  threshold diameter  $d_{th}$ ) and their connectivity with large capillary pores ( $>$  threshold diameter  $d_{th}$ ). It is known that the standard mercury intrusion porosimetry tests cannot identify the large (ink-bottle) capillary pore sizes and tend to overestimate the small (throat) capillary pore sizes. Inspired by the pressurization-depressurization concept [Zhou et al. 2010], an alternative measurement procedure, viz. *intrusion-extrusion cyclic mercury porosimetry* (IEC-MIP), was proposed. The IEC-MIP tests enable to distinguish between small and large capillary pores. The effects of various SCMs on the structure of small capillary pores were analyzed.

The second step was to evaluate the influence of the pore structure on ionic transport property in saturated pore systems. The relationships between the traditional pore structure

parameters (porosity, pore size and pore connectivity) and the chloride migration coefficients, estimated from rapid chloride migration (RCM) tests performed on saturated cementitious mortars, were investigated. Besides, the relationship between the *connectivity of small capillary pores* and the chloride migration coefficient was discussed.

The third step concerned the study of influences of the pore structure on the moisture distribution, as well as on the continuity of water-filled pores (i.e. water continuity  $\eta_w$ ), in unsaturated pore systems. The effects of various pore features (porosity, pore size, pore connectivity and tortuosity) on water continuity were analyzed. In parallel, a sample preconditioning approach was proposed to prepare cementitious specimens with desired uniform water content. The relative humidity RH of mortars at different degrees of water saturation  $S_w$  was measured. The effect of pore structure characteristics on the RH- $S_w$  relationship was discussed. The water continuity  $\eta_w$  was then determined as a function of the degree of water saturation  $S_w$ .

In the fourth step an analytical tool for predicting the relative chloride diffusion coefficient  $D_{rc}$  at different degrees of water saturation  $S_w$  was developed. The  $D_{rc}$ - $S_w$  relation was determined by the Nernst-Einstein equation and conductivity of cementitious electrolyte. The conductivity was quantified based on the microstructure and moisture distribution in cementitious materials. Validation of the analytical tool with experimental data was performed. The effects of SCMs on the  $D_{rc}$ - $S_w$  relations were analyzed.

Finally the changes of the chloride diffusion coefficient in unsaturated cementitious materials at long ages were discussed. The analytical tool developed in the fourth step was extended and a formula for describing the evolution of the unsaturated chloride diffusion coefficient  $D(\alpha(t), S_w)$  was then established. The role of the degree of water saturation  $S_w$  in the  $D(\alpha(t), S_w)$  was analyzed for different cementitious materials. The  $D(\alpha(t), S_w)$  predicted with the formula was compared to that recommended with DuraCrete [2000].

## 9.2 Conclusions

Experiments were carried out to study the pore structure, the moisture distribution and the chloride transport properties in saturated and unsaturated cementitious materials. Specimens were made with different w/b ratios (0.4, 0.5 and 0.6) and supplementary cementitious materials (SCMs), such as fly ash (FA), slag (BFS) and limestone powder (LP). All specimens used in the experimental tests were more than 28-day-old. The key findings are summarized as follows:

- 1) Small pores (0.05~0.1  $\mu\text{m}$ ) are connected by the large pores (0.1~10  $\mu\text{m}$ ). In OPC pastes small pores in the range 0.01~0.05  $\mu\text{m}$  are highly interconnected. Partial replacement of OPC by reactive SCMs, either FA or BFS, significantly *reduces* the connectivity of the small pores (0.01~0.05  $\mu\text{m}$ ). Substitution of OPC by LP *increases* the connectivity of the small pores (0.01~0.05  $\mu\text{m}$ ).

- 2) The addition of BFS or FA refines the pore structure and, therefore, increases the degree of water saturation compared to the OPC system of a given internal relative humidity RH. Utilization of BFS or FA enables to gain a higher resistivity to chloride penetration in *saturated* cementitious materials. This advantage persists but is less pronounced for cementitious materials exposed to *unsaturated* humidity circumstances (60~100% RH).
- 3) In cementitious materials the pores larger than the threshold diameter  $d_{th}$  are poorly connected and hence they have only a minor influence on ionic transport. The chloride diffusion coefficient  $D_{Sat}$  of *saturated* cementitious materials strongly depends on the connectivity  $\eta_{sc}$  of capillary pores smaller than the threshold diameter  $d_{th}$ .
- 4) The chloride diffusion coefficient  $D_{S_w}$  of *unsaturated* cementitious materials can be predicted based on the chloride diffusion coefficient at *saturated* state  $D_{Sat}$ , the degree of water saturation  $S_w$  and the average pore diameter of the material. For a given  $S_w$  the relative chloride diffusion coefficient  $D_{rc}$  ( $D_{rc} = D_{S_w}/D_{Sat}$ ) is lower in the BFS or FA-blended system than in the neat OPC system.
- 5) The long-term sharp decrease of the chloride diffusion coefficient  $D_{S_w}$  at later ages is not primarily caused by densification of the microstructure, but by the decreasing degree of water saturation in the cementitious materials. It is not correct to judge the durability of marine concrete structures merely based on the chloride diffusion coefficient  $D_{Sat}$  of saturated specimens.

### 9.3 Contributions to science and engineering

- 1) A pore structure measurement procedure, viz. intrusion-extrusion cyclic mercury porosimetry (IEC-MIP), is proposed. The IEC-MIP measurements enable to determine the *distribution of pore entrapment* and the *structure of small capillary pores*. Both are essential factors for interpreting the ionic transport in unsaturated cementitious materials.
- 2) The connectivity  $\eta_{sc}$  of small capillary pores ( $0.01 \mu\text{m} < d \leq d_{th}$ ) is determined by the IEC-MIP measurements. Compared to the traditional concept of pore connectivity  $\eta_p$ , the connectivity  $\eta_{sc}$  of small capillary pores is a more effective parameter for predicting the ionic transport in cementitious materials, regardless of saturated or unsaturated state.
- 3) A sample preconditioning approach for preparing cementitious specimens with uniform water content is described. The sample is firstly oven-dried at 50 °C to obtain a desired degree of water saturation. The moisture homogeneity inside the sample is monitored by measuring the RH of both ends of the sample. The sample preconditioning approach enables to prepare cementitious specimens with internal RH as low as 45%.

- 4) A mathematical relationship between water continuity  $\eta_w$  and degree of water saturation  $S_w$  is established. The relationship is very useful for studying mass transport properties in unsaturated cementitious materials.
- 5) An analytical tool for determining the chloride diffusion coefficient in unsaturated cementitious materials is developed. The tool provides a better basis for predicting the long-term chloride transport and helps the designer to understand the actual serviceability of marine concrete structures.

## 9.4 Prospects

In concrete mixture design supplementary cementitious materials (SCMs) are selected largely on the basis of the contribution they can make to reach durability requirements. The transport-related durability issues are significantly influenced by the degree of water saturation in concrete. Particular attention should be given to the moisture-related properties of concrete in order to make a reliable durability assessment of structures made with different cementitious materials.

A few aspects are recommended for further research:

- Different SCMs, reactive or inert, have different contributions to the refinement of the pore structure. Composite cements, consisting of two or more types of SCMs, are worth to be developed based on the so called “synergistic effect” (see Chapter 3).
- Marine concretes are often unsaturated (only outer layers can be saturated). For blended cement pastes cured under *unsaturated* moisture condition, the mechanisms of cement hydration and pozzolanic reactions, including the long-term microstructure development, need to be studied.
- The pore solution chemistry influences the ionic transport in unsaturated pore systems. Experimental methods for effectively measuring the concentrations of alkalis in unsaturated concretes are needed.
- Reliable experimental techniques need to be developed to measure the unsaturated chloride diffusion coefficient with and without chloride binding.
- The influences of water absorption, as well as absorption-desorption cycles, on the moisture distribution and associated water continuity in unsaturated cementitious materials can be investigated.
- This thesis focused on studying the chloride diffusion in cementitious materials with uniform moisture content. Note that the moisture distribution in real concrete structures is rarely homogeneous. Studies of the coupled chloride-moisture transport should be carried out.

## References

---

- AASHTO T259-80 (1980), 'Standard Method of Test for Resistance of Concrete to Chloride Ion Penetration (Salt Ponding Test). *American Association of State Highway and Transportation Officials*, Washington, D.C., U.S.A.
- AASHTO T277-93 (1983), 'Electrical Indication of Concrete's Ability to Resist Chloride', *American Association of State Highway and Transportation Officials*, Washington D.C., U.S.A.
- Aligizaki K.K. (2006), 'Pore Structure of Cement-Based Materials: Testing, Interpretation and Requirements', CRC Press, Taylor & Francis.
- Antón C., Climent M.A., de Vera G., Sánchez I. and Andrade C. (2013), 'An improved procedure for obtaining and maintaining well characterized partial water saturation states on concrete samples to be used for mass transport tests. *Materials and Structures*, 46:1389-1400.
- Asbridge A.H., Chadbourn G.A., Page C.L. (2001), 'Effects of metakaolin and the interfacial transition zone on the diffusion of chloride ions through cement mortars'. *Cement and Concrete Research*, 31(11):1567-1172.
- ASTM C1760-12 (2013), 'Standard Test Method for Bulk Electrical Conductivity of Hardened Concrete'. April.
- ASTM C642-13 (2013), 'Standard Test Method for Density, Absorption, and Voids in Hardened Concrete'. February.
- Atkinson A., Nickerson A.K. (1984) 'The diffusion of ions through water-saturated cement, *Journal of Materials Science*, 19: 3068–3078.
- Attari A., McNally C. and Richardson M.G. (2016), 'A probabilistic assessment of the influence of age factor on the service life of concretes with limestone cement/GGBS binders', *Construction and Building Materials*, 111:488–494.
- Badmann R., Stockhausen N. and Setzer M.J. (1981), 'The statistical thickness and the chemical potential of adsorbed water films', *Journal of Colloid and Interface Science*, 82:534-542.
- Barneyback Jr. R.S., Diamond S. (1981) 'Expression and analysis of pore fluids from hardened cement pastes and mortars', *Cement and Concrete Research*, 11(2): 279-285.
- Baroghel-Bouny V, Nguyen TQ, Dangla P. (2009), 'Assessment and prediction of RC structure service life by means of durability indicators and physical/chemical models. *Cement and Concrete Composite*, 31:522-534.
- Baroghel-Bouny V., Thiéry M. and Wang X. (2011), 'Modelling of isothermal coupled moisture-ion transport in cementitious materials', *Cement and Concrete Research*, 41: 828-841.

- Benhelal E., Zahedia G., Shamsaei E. and Bahadori A. (2013), 'Global strategies and potentials to curb CO<sub>2</sub> emissions in cement industry', *Journal of Cleaner Production*, 51:142-161.
- Bijen J. (1996), 'Benefits of slag and fly ash', *Construction and Building Materials*, 10(5):309-314.
- Bockris J.O.M., Reddy A.K.N. (1970), 'Modern Electrochemistry, Vol. 1, Section 4.4, Plenum, New York.
- Brunauer S. (1943), 'The adsorption of gases and vapors', *Physical Adsorption*, Volume I, Princeton University Press, Princeton.
- Buchwald A. (2000), 'Determination of the ion diffusion coefficient in moisture and salt loaded masonry materials by impedance spectroscopy', *Proceedings third international PhD symposium*, Vienna, Austria, 475-482.
- CEB Bulletin d'information No. 182, (1989), 'Durable Concrete Structures, CEB Design Guide, CEB.
- Chatterji S (1994) Migration of ions through cement based materials Part I. *Cem Concr Res* 24:907-912.
- Chatterji S. (2004), 'An explanation for the unsaturated state of water stored concrete', *Cement and Concrete Composite*, 26(1): 75-79.
- Chaussadent T., G Arliguie. (1999), 'AFREM test procedures concerning chlorides in concrete: extraction and titration methods', *Materials and Structures*, 32 (217): 230-234.
- Chen W. (2006), 'Hydration of slag cement: theory, modeling and application'. PhD thesis, University of Twente.
- Chen W. and Brouwers H.J.H. (2010), 'Alkali binding in hydrated Portland cement paste', *Cement and Concrete Research*, 40:716-722.
- Chindaprasirt P., Jaturapitakkul C. and Sinsiri T. (2005), 'Effect of fly ash fineness on compressive strength and pore size of blended cement paste', *Cement and Concrete Composite*, 27(4):425-428.
- Chindaprasirt P. and Rukzon S. (2009), 'Pore structure changes of blended cement pastes containing fly ash, rice husk ash, and palm oil fuel ash caused by carbonation', *Journal of Materials in Civil Engineering*. 666-671.
- Christensen B.J. (1993), 'Microstructure studies of hydrating Portland cement-based materials using impedance spectroscopy', Ph.D. Dissertation, Northwestern University, Evanston, Illinois.
- Christensen B.J., Coverdale R.T., Olson R.A., Ford S.J., Garboczi E.J., Jennings H.M. and Mason T.O. (1994), 'Impedance spectroscopy of hydrating cement-based materials: measurement, interpretation, and application', *Journal of the American Ceramic Society*, 77(11):2789-2802.
- Climent M.A., de Vera G., Lopez J.F., Viqueira E. and Andrade C. (2002), 'A test method for measuring chloride diffusion coefficients through non-saturated concrete: Part I. The instantaneous plane source diffusion case', *Cement and Concrete Research*, 37:714-724.
- Climent M.A., de Vera G., Viqueira E., López M.M. (2004), 'Generalization of the possibility of eliminating the filtration step in the determination of acid-soluble chloride content in

- cement and concrete by potentiometric titration', *Cement and Concrete Research* 34 (12): 2291–2295.
- Cook R.A. and Hover K.C. (1993), 'Mercury porosimetry of cement-based materials and associated correction factors', *Construction and Building Materials*, 7(4):231–240.
- De Vera G., Climent M.A., Viqueira E., Antón C. and Andrade C. (2007), 'A test method for measuring chloride diffusion coefficients through partially saturated concrete. Part II. The instantaneous plane source diffusion case with chloride binding consideration'. *Cement and Concrete Research*, 37:714–724.
- De Weerd, K., Justnes, H., Kjellsen, K. O. and Sellevold, E. (2010), 'Fly ash-limestone ternary composite cement: synergetic effect at 28 days', *Nordic Concrete Research*, 42: 51-70.
- De Weerd K., Ben Haha M., Le Saout G. Le Saout, Kjellsen K.O., Justnes H. and Lothenbach B. (2011), 'Hydration mechanisms of ternary Portland cements containing limestone powder and fly ash', *Cement and Concrete Research*, 41:279–291.
- Diamond S. (1999), 'Aspects of concrete porosity revisited', *Cement and Concrete Research*, 29 (8):1181-1188.
- Diamond S. (2000a), 'Mercury porosimetry: an inappropriate method for the measurement of pore size distributions in cement-based materials', *Cement and Concrete Research*, 30(10):1517-1525.
- Diamond S. (2000b), The relevance of laboratory studies on delayed ettringite formation to DEF in field concretes. *Cement and Concrete Research*, 30 (12):1987-1991.
- DIN 50008, (1981), 'Part 1. Standard Atmospheres Over Aqueous Solutions', Deutsches Institut für Normung (DIN), Berlin, Germany.
- DuraCrete R17 (2000), 'DuraCrete Final Technical Report, The European Union – Brite EuRam III, DuraCrete – Probabilistic Performance based Durability Design of Concrete Structures', Document BE95-1347/R17, May; CUR, Gouda, The Netherlands.
- EN 196-1 (2002). Methods of testing cement - Determination of strength. European standard.
- EN 197-1 ed. 2 (2011) Cement - Part 1: Composition, specifications and conformity criteria for common cements.
- Escalante G.J.I. and Sharp J.H. (2004), 'The chemical composition and microstructure of hydration products in blended cements', *Cement and Concrete Composites*, 26:967–976.
- Famy C. (1999), 'Expansion of heat-cured mortars', PhD thesis, Imperial College of Science, Technology, and Medicine.
- Fraj B.A., Bonnet S, Khelidj A. (2012), 'New approach for coupled chloride/moisture transport in non-saturated concrete with and without slag', *Construction and Building Materials*, 35:761-771.
- Feldman R. F. and Sereda P. J. (1970), 'A new model for hydrated Portland cement and its practical implications', *Engineering Journal of Canada*, 53 (8-9):53-59.
- Fisher L.R. (1981), 'Experimental studies on the applicability of the Kelvin equation to highly curved concave menisci', *Journal of Colloid and Interface Science*, 80:528-541.
- Gallé C. and Daian J.F. (2000), 'Gas permeability of unsaturated cement-based materials: application of a multi-scale network model', *Magazine of Concrete Research*, 52:251-263.

- Gallé C. (2001), 'Effect of drying on cement based materials pore structure as identified by mercury intrusion porosimetry – a comparative study between oven, vacuum and freeze drying', *Cement and Concrete Research*, 31:1467-1477.
- Gao P. (2018), 'Simulation of hydration and microstructure development of blended cements', PhD thesis, Delft University of Technology, The Netherlands.
- Gao Y., De Schutter G., Ye G., Tan Z. and Wu K. (2014), 'The ITZ microstructure, thickness and porosity in blended cementitious composite: Effects of curing age, water to binder ratio and aggregate content', *Composites Part B: Engineering*, 60:1-13.
- Garboczi, E.J. (1990), 'Permeability, diffusivity, and microstructural parameters: A critical review'. *Cement and Concrete Research*, 20: 591-601.
- Garboczi, E.J. (1995), 'Performance Criteria for Concrete Durability', edited by J. Kropp and H.K. Hilsdorf. E & FN Spon, London.
- Glass G.K. and Buenfeld N.R. (2000), 'The influence of chloride binding on the chloride induced corrosion risk in reinforced concrete', *Corrosion Science*, 42:329-344.
- Guimarães A.T.C., Climent M.A., de Vera G., Vicente F.J., Rodrigues F.T. and Andrade C. (2011), 'Determination of chloride diffusivity through partially saturated Portland cement concrete by a simplified procedure', *Construction and Building Materials*, 25:785-790.
- Halperin W.P., Jehng J.Y. and Song Y.Q. (1994), 'Application of spin-spin relaxation to measurement of surface area and pore size distributions in a hydrating cement paste', *Magnetic Resonance Imaging*, 12(2):169-173.
- Huang H.L. (2014), 'Thermodynamics of Autogenous Self-healing in Cementitious Materials', PhD thesis, Delft University of Technology, The Netherlands.
- Horvath A.L. (1985), 'Handbook of Aqueous Electrolyte Solutions', Wiley, New York.
- Hou X.D and Jones B.T. (2000), 'Inductively Coupled Plasma/Optical Emission Spectrometry', John Wiley & Sons Ltd, Chichester.
- Jennings H.M. (2008), 'Refinements to colloid model of C-S-H in cement: CM-II', *Cement and Concrete Research*, 38:275-289.
- Jensen O.M. (1993), 'Autogenous deformation and RH-change—self-desiccation and self-desiccation shrinkage', Appendix-measurements and notes (in Danish), Building Materials Laboratory, The Technical University of Denmark, Lyngby, Denmark, TR 285/93.
- Jonasson J.-E. (1984), 'Slipform construction - calculations for assessing protection against early freezing'. Swedish Cement and Concrete Research Institute, Fo 4:84, Stockholm.
- Juenger M.C.G., Winnefeld F., Provis J.L. and Ideker J.H. (2011), 'Advances in alternative cementitious binders', *Cement and Concrete Research*, 41:1232-1243.
- Kaufmann J., Loser R. and Leemann A. (2009), 'Analysis of cement-bonded materials by multi-cycle mercury intrusion and nitrogen sorption', *Journal of Colloid and Interface Science*, 336:730-737.
- Kayyali O.A. and Haque M.N. (1995), 'The Cl<sup>-</sup>/OH<sup>-</sup> ratio in chloride-contaminated concrete – a most important criterion', *Magazine of Concrete Research*, 47:235-242.
- Khalil KA. (1996), 'Pore structure and surface area of hardened cement pastes containing silica fume', *Materials Letters*, 26(4):259-264.

- Köhler H. (1936), 'The nucleus in and the growth of hygroscopic droplets', *Transactions of the Faraday Society*, 32:1152–1161.
- Kolias S. and Georgiou C., (2005) 'The effect of paste volume and of water content on the strength and water absorption of concrete', *Cement and Concrete Composites*, 27:211–216.
- Kuzel H. J. and Pollmann H. (1991). 'Hydration of  $C_3A$  in the presence of  $Ca(OH)_2$ ,  $CaSO_4 \cdot 2H_2O$  and  $CaCO_3$ '. *Cement and Concrete Research*, 21:885–895.
- Larbi J.A. (1991), 'The cement paste-aggregate interfacial zone in concrete', PhD thesis, Delft University of Technology, The Netherlands.
- Li K., Li C. and Chen Z. (2009), 'Influential depth of moisture transport in concrete subject to drying–wetting cycles', *Cement and Concrete Composite*, 31(10):693–698.
- Life 365 (2001), 'Service life prediction—state-of-the-art report', Manual of Concrete Practice, *ACI Committee 365*. 1R-00-44.
- López W., González J.A. (1993), 'Influence of the degree of pore saturation on the resistivity of concrete and the corrosion rate of steel reinforcement', *Cement and Concrete Research*, 23 (2):368–376.
- Lothenbach B., Le Saout G., Gallucci E. and Scrivener K. (2008), 'Influence of limestone on the hydration of Portland cements', *Cement and Concrete Research*, 38:848–860.
- Lowell S. and Shields J.E. (1981), 'Hysteresis, Entrapment, and Wetting Angle in Mercury Porosimetry', *Journal of Colloid and Interface Science*, 83(1):273–278.
- Ma Y, Ye G. (2015), 'The shrinkage of alkali activated fly ash', *Cement and Concrete Research*, 68:75–82.
- Manheim F.T., Waterman L.S. (1974), Initial Reports of the Deep Sea Drilling Project, 22:663–670.
- McCarter W.J. and Garvin S. (1989), 'Dependence of electrical impedance of cement-based materials on their moisture condition', *Journal of Physics D: Applied Physics*, 22:1773–1776.
- McCarter W.J. (1996), 'Monitoring the influence of water and ionic ingress on cover-zone concrete subjected to repeated absorption', *Cement, Concrete and Aggregates*, 18(1):55–63.
- McKee R. A. (1981), 'A generalization of the Nernst-Einstein equation for self-diffusion in high defect concentration solids', *Solid State Ionics*, 5:133–136.
- Mercado-Mendoza H., Lorente S. and Bourbon X. (2013), 'The diffusion coefficient of ionic species through unsaturated materials', *Transport in Porous Media*, 96:469–481.
- Mercado-Mendoza H., Lorente S. and Bourbon X. (2014), 'Ionic aqueous diffusion through unsaturated cementitious materials – A comparative study', *Construction and Building Materials*, 51(31):1–8.
- Mindess S. and Young J.F. (1981), 'Concrete', Prentice Hall, Pearson Education, Inc. Upper Saddle River, NJ 07458.
- Moro F. and Böhni H. (2002), 'Ink-Bottle Effect in Mercury Intrusion Porosimetry of Cement-Based Materials', *Journal of Colloid and Interface Science*, 246: 135–149.

- Mustafa M.A., Yusof K.M. (1994), 'Atmospheric chloride penetration into concrete in semitropical marine environment', *Cement and Concrete Research*, 24:661-670.
- Neimark A.V., Ravikovitch P.I. and Vishnyakov A. (2003), 'Bridging scales from molecular simulations to classical thermodynamics: density functional theory of capillary condensation in nano pores', *Journal of Physics: Condensed Matter*, 15:347-365.
- Neville A.M. (1981), 'Properties of Concrete', Pitman Publishing Limited, London.
- Nielsen E.P. and M.R. Geiker (2003), 'Chloride diffusion in partially saturated cementitious material', *Cement and Concrete Research*, 33:133-138.
- Nilsson L.O. (2006), 'Present limitations of models for predicting chloride ingress into reinforced concrete structures. J. Phys. IV France, 136:123-130.
- NT Build 208 – Nordtest Method (1996), 'Concrete, Hardened: Chloride diffusivity by Volhard Titration.
- NT Build 443 – Nordtest Method (1995), 'Concrete, Hardened: Accelerated chloride penetration'.
- NT Build 492 – Nordtest Method (1999), 'Chloride migration coefficient from non-steady state migration experiments'.
- Odler I., and Röbler M. (1985), 'Investigations on the relationship between porosity, structure and strength of hydrated Portland cement pastes: II. Effects of pore structure and degree of hydration'. *Cement and Concrete Research*, 15:401-410.
- Olsson N., Baroghel-Bouny V., Nilsson L.O. and Thiery M. (2013), 'Non-saturated ion diffusion in concrete – A new approach to evaluate conductivity measurements', *Cement and Concrete Composite*, 40:40-47.
- Olsson N., Lothenbach B., Baroghel-Bouny V., and Nilsson L.O. (2018), 'Unsaturated ion diffusion in cementitious materials – The effect of slag and silica fume', *Cement and Concrete Research*, 108:31-37.
- Olsson N. (2018), 'Experimental studies of ion transport in cementitious materials under partially saturated conditions', PhD thesis Unversite Paris-Est and Lund University, ISBN 978-91-7753-667-3.
- Parrott L.J. (1994), 'Moisture conditioning and transport properties of concrete test specimens', *Materials and Structures*, 27:460-468.
- Persson B. (1997), 'Self-desiccation and its importance in concrete technology', *Materials and Structures*, 30(5):293-305.
- Ping D., Shui Z., Chen W. and Shen C. (2013), 'Enhancing microstructure and durability of concrete from ground granulated blast furnace slag and metakaolin as cement replacement materials', *Journal of Materials Research and Technology*, 2(1):52-59.
- Polder R.B. (2001), 'Test methods for onsite measurement of resistivity of concrete – a RILEM TC-154 technical recommendation'. *Construction and Building Materials*, 15:125-131.
- Polder R.B. (2012), 'Effects of slag and fly ash on reinforcement corrosion in concrete in chloride environment - Research from the Netherlands', *Heron*, 57 (3):197-210.
- Powers T.C. and Brownyard T.L. (1946), 'Studies of the physical properties of hardened Portland cement paste, *Proceedings Journal - American Concrete Institute*, 43-262.

- Powers T.C. (1945), 'Studies of water vapour adsorption of hardened Portland cement paste', Research Laboratories of the Portland Cement Association, *Bulletin*, vol. 22.
- Powers T.C. and Brownyard T.L. (1947), 'Studies of the physical properties of hardened Portland cement paste. Part 2. Studies of water fixation', *Journal - American Concrete Institute*, 18 (3):249–303.
- Powers, T.C. (1960). 'Physical properties of cement paste', Proceedings 4<sup>th</sup> ISCC, National Bureau of Standards, Washington, D.C. U.S., 2:577–613.
- Poulsen E., Mejlbro L. (2006), 'Diffusion of chloride in concrete: Theory and Application', Taylor & Francis, London & New York.
- Rajabipour F. (2006), 'In situ electrical sensing and material health monitoring of concrete structures', PhD thesis, Purdue University, USA.
- Rajabipour F. and Weiss J. (2007), 'Electrical conductivity of drying cement paste', *Materials and Structures*, 40:1143–1160.
- Ramachandran V.S. and Beaudoin J.J. (2001) *Handbook of Analytical Techniques in Concrete Science and Technology Principles, Techniques, and Applications*, Noyes/William Andrew, New York.
- Ranaivomanana H., Verdier J., Sellier A. and Bourbon X. (2011), 'Toward a better comprehension and modeling of hysteresis cycles in the water sorption–desorption process for cement based materials', *Cement and Concrete Research*, 41:817–827.
- RILEM TC 116-PCD. (1999), 'Permeability of Concrete as a Criterion of its Durability - Recommendations', *Materials and Structures*, 32:174-179.
- Ritter H.L. and Drake L.C. (1945), 'Pressure Porosimeter and Determination of Complete Macropore-Size Distributions. Pressure Porosimeter and Determination of Complete Macropore-Size Distributions', *Industrial and Engineering Chemistry, Analytical Edition*, 17(12):782–786.
- Saetta A.V., Scotta R.V. and Vitaliani R.V. (1993), 'Analysis of Chloride Diffusion into Partially Saturated Concrete', *American Concrete Institute Materials Journal*, 90:441-451.
- Sánchez I., Antón C., de Vera G., Ortega J.M. and Climent M.A. (2013), 'Moisture distribution in partially saturated concrete studied by impedance spectroscopy'. *Journal of Non-destructive Evaluation*, 32:362-371.
- Saraswathy V. and Song H.W. (2006), 'Corrosion performance of fly ash blended cement concrete: a state-of-art review', *Corrosion Reviews*, 24(1-2):87-122.
- Selvaraj R., Muralidharan S. and Srinivasan S. (2003), 'The influence of silica fume on the factors affecting the corrosion of reinforcement in concrete: a review', *Structural Concrete*, 4(1):19-23.
- Scrivener K.L. (2004), 'Backscattered electron imaging of cementitious microstructures: understanding and quantification', *Cement and Concrete Composite*, 26:935-945.
- Scrivener K.L. Nonat A. (2011), 'Hydration of cementitious materials, present and future', *Cement and Concrete Research*, 41(7):651-665.
- Sicat E., Gong .F, Ueda T. and Zhang D. (2014), 'Experimental investigation of the deformational behavior of the interfacial transition zone (ITZ) in concrete during freezing and thawing cycles', *Construction and Building Materials*, 65:122-131.

- Snyder K.A. (2001), 'The relationship between the formation factor and the diffusion coefficient of porous materials saturated with concentrated electrolytes: theoretical and experimental considerations', *Concrete Science and Engineering Journal*, 3(12):216–224.
- Snyder K.A., Feng X., Keen B.D. and Mason T.O. (2003), 'Estimating the electrical conductivity of cement paste pore solutions from OH<sup>-</sup>, K<sup>+</sup> and Na<sup>+</sup> concentrations', *Cement and Concrete Research*, 33:793-798.
- Spitzer Z. (1981), 'Mercury porosimetry and its application to the analysis of coal pore structure', *Powder Technology*, 29 (1): 177-186.
- Spiesz P. and Brouwers H.J.H. (2013), 'The apparent and effective chloride migration coefficients obtained in migration tests', *Cement and Concrete Research*, 48:116-127.
- Spraag R.P., Castro J., Li W., Pour-Ghaz M., Huang P.T. and Weiss J. (2011), 'Wetting and drying of concrete using aqueous solutions containing deicing salts', *Cement and Concrete Composite*, 33(5):535-542.
- Stark J. (2011), 'Recent advances in the field of cement hydration and microstructure analysis', *Cement and Concrete Research*, 41:666–678.
- Stratfull R.F. (1968), 'How Chlorides affect concrete used with Reinforcing Steel', *Materials Protection*, 7 (3):29-34.
- Tang L.P. and Nilsson L.O., (1992), 'Rapid determination of the chloride diffusivity in concrete by applying an electrical field', *American Concrete Institute materials journal*, 89 (1):49-53.
- Tang L.P. and Nilsson L.O. (1993), 'Chloride binding capacity and binding isotherms of OPC pastes and mortars', *Cement and concrete research*, 23:242-253.
- Tang L.P. (1996), 'Chloride Transport in Concrete - Measurement and Prediction', *Doctoral thesis*, Publication P-96:6, Development of Building Materials, Chalmers University of Technology, Gothenburg.
- Tang L.P. Nilsson L.O. and Basheer P.A.M. (2012), 'Resistance of Concrete to Chloride Ingress: Testing and Modelling', Spon Press.
- Taylor H.F.W. (1987), 'A method for predicting alkali ion concentrations in cement pore solutions', *Advances in Cement Research*, 1:5-16.
- Taylor H.F.W. (1990), 'Cement Chemistry', Academic Press, New York.
- Tennis P.D. and Jennings H.M. (2000), 'A model for two types of calcium silicate hydrate in the microstructure of Portland cement paste', *Cement and Concrete Research*, 30:855-863.
- Tumidajski P.J., Schumacher A.S., Perron S., Gu P., Beaudoin J.J. (1996), 'On the relationship between porosity and electrical resistivity in cementitious systems', *Cement and Concrete Research*, 26(4):539-544.
- Tuutti K. (1982), 'Corrosion of steel in concrete', *Swedish Cement and Concrete Research Institute*, Stockolom.
- Van Breugel K. (1991), 'Numerical simulation of hydration and microstructural development in hardening cement-based materials', PhD thesis, Delft University of Technology, Delft.
- Washburn E.W. (1921), 'The dynamics of capillary flow', *Physical Review*, 17:273-283.
- Weast, R.C. (1975), 'Handbook of Chemistry and Physics', 57th edition, CRC Press, Cleveland.

- Vedalakshmi R., Devi R.R., Emmanuel B. and Palaniswamy N. (2008), 'Determination of diffusion coefficient of chloride in concrete: an electrochemical impedance spectroscopic approach', *Materials and Structures*, 41:1315-1326.
- Weerdt, K. De, Justnes, H., Kjellsen, K. O. and Sellevold, E. (2010), 'Fly ash-limestone ternary composite cement: synergetic effect at 28 days', *Nordic Concrete Research*, 42:51-70.
- Weerdt, K. De, Haha, M. Ben., Saout, G. Le., Kjellsen, K.O., Justnes, H. and Lothenbach, B. (2011a), 'Hydration mechanisms of ternary Portland cements containing limestone powder and fly ash', *Cement and Concrete Research*, 41:279–291.
- Weerdt, K. De, Kjellsen, K.O., Sellevold, E. and Justnes, H. (2011b), 'Synergy between fly ash and limestone powder in ternary cements', *Cement and Concrete Composites*, 33:30–38.
- Weiss J., Snyder K., Bullard J. and Bentz D. (2013), 'Using a saturation function to interpret the electrical properties of partially saturated concrete', *Journal of Materials in Civil Engineering*, 25(8):1097-1106.
- Willis K.L., Abell A.B. and Lange D.A. (1998), 'Image-based characterization of cement pore structure using wood's metal intrusion', *Cement and Concrete Research*, 28(12):1695-1705.
- Ye G. (2003), 'Experimental study and numerical simulation of the development of the microstructure and permeability of cementitious materials', PhD Thesis, Delft University of Technology, The Netherlands.
- Yu Z.Q. (2015), 'Microstructure Development and Transport Properties of Portland Cement-fly Ash Binary Systems-in view of service life predictions', PhD Thesis, Delft University of Technology, The Netherlands.
- Zhang M., Ye G. and van Breugel K. (2012), 'Modelling of ionic diffusivity in non-saturated cement-based materials using lattice Boltzmann method', *Cement and Concrete Research*, 42:1524-1533.
- Young J.F., Hansen W. (1987), 'Volume relationship for C-S-H formation based on hydration stoichiometry', Materials Research Society symposium proceedings of Microstructural development during hydration of cement, Boston, Massachusetts, U.S.A. 85:313-322.
- Zhang M. (2013a), 'Multi-scale lattice Boltzmann finite element modelling of transport properties in cement-based materials', PhD thesis, Delft University of Technology, The Netherlands.
- Zhang Q. (2013b), 'Microstructure and deterioration mechanisms of portland cement paste at elevated temperature', PhD thesis, Delft University of Technology, The Netherlands.
- Zhang Y. and Ye G. (2015), 'Chloride Transport in Partially Saturated Mortar Made of Blended Cement', 14th International Congress on the Chemistry of Cement, Beijing, China.
- Zhang Y. and Ye G. (2018), 'A discussion of the paper "Characterization of pore structure in cement-based materials using pressurization–depressurization cycling mercury intrusion porosimetry (PDC-MIP)" by Zhou et al.', *Cement and Concrete Research*, under review.
- Zhang Y., Ye G. (2018), 'A model for predicting the relative chloride diffusion coefficient in unsaturated cementitious materials', *Cement and Concrete Research*, under review.

- 
- Zhang Y. and Zhang M.Z. (2014), ‘Transport properties in unsaturated cement-based materials – A review’, *Construction and Building Materials*, 72:367–379.
- Zhou J., Ye G. and van Breugel K. (2010), ‘Characterization of pore structure in cement-based materials using pressurization–depressurization cycling mercury intrusion porosimetry (PDC-MIP)’, *Cement and Concrete Research*, 40:1120–1128.

# Summary

---

Chloride-induced reinforcement corrosion is a major durability problem of concrete structures. The *chloride diffusion coefficient* is commonly adopted to describe the capacity of concrete to resist chloride diffusion. Chloride diffusion is significantly influenced by the moisture content and its distribution in the pore structure. Partial replacement of ordinary Portland cement (OPC) by supplementary cementitious materials (SCMs), such as fly ash (FA), ground granulated blast furnace slag (BFS), limestone powder (LP), etc., will inevitably alter the chloride diffusion process, because of the changes in the microstructure formation and associated changes in the moisture distribution. In the absence of sufficient knowledge about the *moisture-dependent chloride diffusion*, current concepts for concrete mixture design and for service life prediction are generally based on the understanding of the chloride diffusion coefficient of saturated concrete. This will introduce uncertainties and give rise to misjudgement of the actual serviceability of reinforced concrete structures, especially when SCMs are added in the concrete mixture.

This thesis aims to develop a tool for predicting the chloride diffusion coefficient at different degrees of water saturation, and hence to provide a basis for service life design based on the chloride diffusion in unsaturated cementitious materials. The influences of SCMs on the pore structure and moisture distribution as well as on the unsaturated chloride diffusion are given due attention.

Experimental studies were carried out. In unsaturated pore systems the water-filled pores that allow ionic transport tend to be small in size and, therefore, characterization of the structure of small capillary pores becomes a prerequisite. A technique, viz. *intrusion-extrusion cyclic mercury porosimetry* (IEC-MIP), was proposed to distinguish between small pores and large pores in the paste specimens made with and without SCMs. The water vapour desorption isotherm of mortar specimens was measured and its relation to the pore structure of paste specimens was analyzed, which provided a basis for examining the continuity of water-filled pores. The relative chloride diffusion coefficient at various degrees of water saturation was determined based on the Nernst-Einstein equation and conductivity measurements. Finally, the role of unsaturated chloride diffusion in the service life of reinforced concrete structures was discussed in depth.

## Experimental results

The effects of factors, viz. curing age (28~370 days), w/b ratio (0.4, 0.5 and 0.6) and SCMs (FA, BFS and LP), on *pore structure* features were analyzed using the IEC-MIP tests. The experimental results indicate that these factors have a great influence on the *structure of small capillary pores*, but a limited influence on the *structure of large capillary pores*. The large capillary pores are, in general, poorly connected, regardless of age, w/b ratio or cement type.

The small capillary pores are highly interconnected in OPC pastes. Partial replacement of OPC by reactive SCMs, either 30% FA or 70% BFS, significantly reduces the connectivity of small capillary pores. Incorporating 5% LP increases the connectivity of small capillary pores. The pore size distribution of cement paste with the addition of FA or BFS is finer, but becomes coarser with the addition of LP. The *connectivity of small capillary pores* and chloride migration coefficient can be well described with a power equation, regardless of the age, w/b ratio or cement type.

The continuity of water-filled pores, in short *water continuity*, depends on the degree of water saturation and pore structure. The water continuity was evaluated based on the Kelvin law and water vapour desorption isotherm. It is found that a finer pore size distribution or lower pore connectivity tends to result in a lower water continuity. The effect of the pore size fineness on water continuity is pronounced primarily at high water saturation levels. The water continuity at low water saturation levels is dominated by the pore connectivity. A quantitative relationship between water continuity and degree of water saturation is proposed.

An analytical tool for predicting the *relative chloride diffusion coefficient*  $D_{rc}$  at various degrees of water saturation  $S_w$  was developed based on the Nernst-Einstein equation and conductivity of cementitious electrolyte. The tool accounts for the microstructure and moisture distribution in cementitious materials. With decreasing  $S_w$  the  $D_{rc}$ -value shows three-stage change, i.e. a slight decrease at stage I, a sharp drop at stage II and another slight decline at stage III (Chapter 7). The three-stage  $D_{rc}$ - $S_w$  relationship is controlled by the water continuity. For a given  $S_w$ , the  $D_{rc}$ -value is smaller in the binders blended with 30% FA or 70% BFS, but larger in the binders with 5% LP, than that in the reference OPC binders (one-year-old).

The analytical tool was extended and a formula for describing the evolution of the chloride diffusion coefficient  $D(\alpha(t), S_w)$  in unsaturated cementitious materials was then established. It is indicated that the long-term sharp decrease of the chloride diffusion coefficient is not caused by densification of the microstructure due to continuous hydration, but influenced primarily by the decreasing degree of water saturation. The effects of the w/b ratio and SCMs on the chloride diffusion coefficient are relatively small when the cementitious materials are at saturated state, but become increasingly pronounced with decreasing degree of water saturation. At saturated state the mortars including 70% BFS or 30% FA have almost equal resistance to chloride diffusion. At unsaturated state, however, the mortar with 70% BFS shows much slower chloride diffusion than the mortar with 30% FA. It is well-worth examining the chloride diffusion coefficient at unsaturated state, rather than at saturated state, in order to more effectively utilize the supplementary cementitious materials in concrete mixture design.

# Samenvatting

---

Chloride geïnitieerde wapeningscorrosie is een belangrijk duurzaamheidsprobleem van betonconstructies. De chloride diffusiecoëfficiënt wordt doorgaans gebruikt om de weerstand tegen chloride indringing te beschrijven. Chloridediffusie wordt significant beïnvloed door het vochtgehalte en de verdeling ervan in de poriestructuur. Gedeeltelijke vervanging van Portland-cement (OPC) door aanvullende bindmiddelen (SCMs), zoals vliegashuis (FA), gemalen gegraneerde hoogovenslakken (BFS), kalksteenmeel (LP), enz., zal bijgevolg het chloridediffusieproces beïnvloeden, vanwege de veranderingen in de microstructuurformatie en daarmee samenhangende de vochtverdeling in de poriën. Door onvoldoende kennis over de aanwezigheid van vocht in de poriën, zijn de huidige concepten voor het ontwerp van het betonmengsel en bijbehorende levensduurvoorspelling in het algemeen gebaseerd op een chloride diffusiecoëfficiënt van verzadigd beton. Dit zal onzekerheden introduceren en aanleiding geven tot een verkeerde inschatting van de daadwerkelijke bruikbaarheid van gewapende betonconstructies, vooral wanneer bindmiddelen aan het betonmengsel worden toegevoegd.

Dit proefschrift heeft als doel een hulpmiddel te ontwikkelen voor het voorspellen van de chloridediffusiecoëfficiënt bij verschillende percentages van waterverzadiging, om daarmee een basis te bieden voor levensduurontwerp op basis van chloridediffusie in onverzadigde cementachtige materialen. De invloed van bindmiddelen op de poriestructuur en de bijbehorende vochtverdeling zijn uitvoerig onderzocht.

Experimenteel onderzoek is uitgevoerd en daarbij is geconstateerd dat in onverzadigde poriesystemen, de met water gevulde poriën die verantwoordelijk zijn voor ionen transport maken, een kleine bijdrage leveren, daarom is de karakterisering van de structuur van de kleinere capillaire poriën een vereiste. Een techniek, namelijk cyclische intrusie-extrusie kwikporosimetrie (IEC-MIP), is gebruikt om onderscheid te maken tussen de kleine poriën en grote poriën in proefstukken van pasta, bestaande uit; met en zonder toegevoegde bindmiddelen. De waterdampdesorptie-isotherm van mortelproefstukken zijn bepaald en de relatie met de poriestructuur van pasta proefstukken is daarbij geanalyseerd, wat een basis vormde voor het onderzoeken van de continuïteit van met water gevulde poriën. De relatieve chloride diffusiecoëfficiënt bij verschillende percentages van waterverzadiging werd bepaald op basis van de Nernst-Einstein-vergelijking en geleidbaarheidsmetingen. Ten slotte is de rol van onverzadigde chloridediffusie met het oog op levensduur (voorspellingen) van gewapende betonconstructies uitvoerig besproken.

## Experimentele resultaten

De effecten van diverse factoren zoals, uithardingstijd (28~370 dagen), w/b factor (0,4, 0,5 en 0,6) en de bindmiddelen (vliegas, hoogovenslak en kalksteenmeel), op poriestructuurkenmerken werden geanalyseerd met behulp van IEC-MIP tests. De experimenteel verkregen resultaten geven aan dat deze factoren een grote invloed hebben op de structuur van de kleinere capillaire poriën, maar een beperkte invloed hebben op de structuur van de grotere capillaire poriën. De grotere capillaire poriën zijn over het algemeen slecht verbonden, ongeacht de leeftijd, w/b factor of het toegepaste cementtype. De kleine capillaire poriën zijn sterk met elkaar verbonden in Portland cement pasta's. Gedeeltelijke vervanging van Portland door reactieve bindmiddelen, 30% vliegas of 70% hoogovenslak, vermindert de connectiviteit van de kleinere capillaire poriën aanzienlijk. Het opnemen van 5% kalksteenmeel verhoogt echter de connectiviteit van de kleinere capillaire poriën. De poriegrootteverdeling van cementpasta met de toevoeging van vliegas of hoogovenslak is fijner, maar wordt grover door toevoeging van kalksteenmeel. De connectiviteit van de kleine capillaire poriën en chloride migratiecoëfficiënt kan goed worden beschreven met een tot de macht vergelijking, ongeacht de leeftijd, w/b of het cementtype.

De continuïteit van met water gevulde poriën, in korte watercontinuïteit, hangt af van de mate van waterverzadiging en poriënstructuur. De watercontinuïteit werd geëvalueerd op basis van de Kelvin-wet en waterdamp desorptie proces. Er is gevonden dat een fijnere poriegrootte verdeling of lagere porieverbinding de neiging heeft te resulteren in een lagere watercontinuïteit. Het effect van poriegroottefijnheid op de watercontinuïteit wordt vooral gevonden bij hogere waterverzadigingsniveaus. De watercontinuïteit bij lage waterverzadigingsniveaus wordt gedomineerd door de poriënconnectiviteit. Een kwantitatieve relatie tussen watercontinuïteit en mate van waterverzadiging is vastgesteld.

Een analytisch hulpmiddel voor het voorspellen van de relatieve chloride diffusiecoëfficiënt  $D_{rc}$  bij verschillende percentages van waterverzadiging  $S_w$  werd ontwikkeld op basis van de Nernst-Einstein-vergelijking en de geleidbaarheid van de cementachtige elektrolyt. De tool is bruikbaar voor de microstructuur en vochtverdeling in cementachtige materialen. Bij afnemende  $S_w$  toont de  $D_{rc}$ -waarde een drietrapsverandering, d.w.z. een lichte afname in stadium I, een scherpe daling in stadium II en een verdere lichte afname in stadium III (Hoofdstuk 7). De driefase  $D_{rc}$ - $S_w$  relatie wordt aangestuurd door de watercontinuïteit. Voor een vaste waarde van  $S_w$ , blijkt de  $D_{rc}$ -waarde kleiner te worden in de bindmiddelen vermengd met 30% vliegas of 70% hoogovenslak, maar juist groter in de bindmiddelen met 5% kalksteenmeel, dan in de referentie Portland gebaseerde proefstukken (één jaar oud).

De analyse tool werd verder uitgebreid om vervolgens een formule te beschrijven voor de evolutie van de chloride diffusiecoëfficiënt  $D(\alpha(t), S_w)$  in onverzadigde cementachtige materialen. Daarbij moet worden aangegeven dat de lange termijn afname van de chloride diffusiecoëfficiënt niet wordt veroorzaakt door verdichting van de microstructuur als gevolg van voortgaande hydratatie, maar voornamelijk wordt beïnvloed door de afnemende mate van waterverzadiging. Het effect van de w/b factor en bindmiddelen op de chloride diffusiecoëfficiënt zijn relatief klein wanneer de cementachtige materialen in verzadigde toestand zijn, maar nemen juist toe bij afnemende waterverzadiging. In verzadigde toestand hebben de mortels waaronder die met 70% hoogovenslak of 30% vliegas bijna dezelfde

weerstand tegen chloridediffusie. In onverzadigde toestand vertoont de mortel met 70% hoogovenslak echter een veel tragere chloridediffusie dan de mortel met 30% vliegias. Het is verstandig om de chloride diffusiecoëfficiënt in onverzadigde toestand nader te onderzoeken in plaats van in verzadigde toestand, om cementachtige materialen effectiever in het ontwerp van een betonmengsel te gebruiken.

